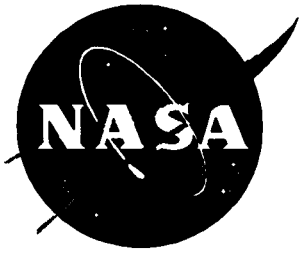

NASA Conference Publication 3311
Part 1

Mechanics of Textile Composites Conference

Edited by
Clarence C. Poe, Jr. and Charles E. Harris

Proceedings of a conference sponsored by the
National Aeronautics and Space Administration,
Washington, D.C., and held in
Hampton, Virginia
December 6–8, 1994

October 1995

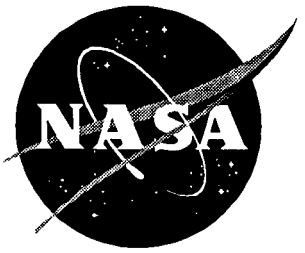

NASA Conference Publication 3311
Part 1

Mechanics of Textile Composites Conference

Edited by
Clarence C. Poe, Jr. and Charles E. Harris
Langley Research Center • Hampton, Virginia

Proceedings of a conference sponsored by the
National Aeronautics and Space Administration,
Washington, D.C., and held in
Hampton, Virginia
December 6–8, 1994

National Aeronautics and Space Administration
Langley Research Center • Hampton, Virginia 23681-0001

October 1995

This publication is available from the following sources:

NASA Center for AeroSpace Information
800 Elkridge Landing Road
Linthicum Heights, MD 21090-2934
(301) 621-0390

National Technical Information Service (NTIS)
5285 Port Royal Road
Springfield, VA 22161-2171
(703) 487-4650

PREFACE

This document is a compilation of papers presented at the Mechanics of Textile Composites Conference in Hampton, Virginia December 6-8, 1994. This conference was the culmination of a three-year program that was initiated by NASA late in 1990 to develop mechanics of textile composites in support of the NASA Advanced Composites Technology Program (ACT). The goal of the program was to develop mathematical models of textile preform materials to facilitate structural design and analysis. Participants in the program were from NASA, academia, and industry.

The use of trademarks or manufacturers' names in this publication does not constitute endorsement, either expressed or implied, by the National Aeronautics and Space Administration.

Clarence C. Poe, Jr.
Charles E. Harris
NASA Langley Research Center

CONFERENCE ORGANIZATION

Sponsored By

Mechanics of Materials Branch
NASA Langley Research Center
Hampton, Virginia 23681-0001

General Chairman	Conference Coordinator and Organizer	Administrative Assistant
Charles E. Harris NASA Langley Research Center	C. C. Poe, Jr. NASA Langley Research Center	Josephine L. Sawyer NASA Langley Research Center

CONTENTS

Part 2*

SESSION 2
STANDARD TEST METHODS

SESSION 3
ANALYTICAL MECHANICS

*Presented under separate cover

Role of Mechanics of Textile Preform Composites in the NASA Advanced Composites Technology Program

by

Charles E. Harris
Assistant Chief, Materials Division
and
C. C. Poe, Jr.

NASA Langley Research Center
Hampton, VA 23662

The Advanced Composites Technology Program

The Advanced Composites Technology Program was initiated by NASA as a partnership with the United States aeronautical industry in fiscal year 1989. The broad objective of the Program was to develop the technology to design and manufacture cost-effective and structurally optimized light-weight composite airframe primary structure. Phase A of the Program, 1989-1991, focused on the identification and evaluation of innovative manufacturing technologies and structural concepts. The prime contractors, Boeing, McDonnell-Douglas, and Lockheed, formed concurrent engineering teams to explore various innovative ideas and to begin the development and evaluation of the structural design concepts. At the end of Phase A, the leading wing and fuselage design concepts were down-selected for further development in Phase B of the Program, 1992-1995. (References 1-3 should be consulted for more details concerning the accomplishments in Phase A of the ACT Program.) Three major fabrication technologies emerged from Phase A as the most promising approaches to manufacturing cost-effective composite primary structures. These three approaches were the stitched dry preform, textile preform, and automated tow placement manufacturing methods. Each method emphasized rapid fiber placement, near net-shape preform fabrication, part count minimization, and matching the technologies to the specific structural configurations and requirements. The objective of Phase B was to continue the evolution of design concepts using the concurrent engineering process, down-select to the leading structural concept, and design, build, and test subscale components. Boeing and Lockheed were teamed together to focus on fuselage components, and McDonnell-Douglas was the prime contractor for wing components.

The issue of affordability of composite structure has emerged as a major technology challenge for the ACT Program. Because of the current poor

economic climate within the airline industry, most decisions regarding new airplane purchases are based on initial acquisition costs. Therefore, the widespread use of composite materials in primary structure will only occur if the cost of manufacturing a composite structure is lower than the cost of the corresponding metallic structure. Even though the cost per pound of the composite constituents may always be higher than aluminum, it is the cost of the finished structure that matters. Current state-of-the-art production costs of composite structure is almost twice the costs of corresponding aluminum airframe structure. However, the results from ACT Phase B are clearly indicating that composites can be cost competitive with metallic structure if cost efficiencies are achieved through innovative design and manufacturing technologies. (References 4-5 should be consulted for more details concerning the accomplishments in Phase B of the ACT Program.) The cost goal for ACT Phase C has been set at a 25% reduction in costs below that of corresponding aluminum structure.

Phase C of the ACT Program, 1995-2002, is a critical element of the NASA Advanced Subsonic Technology Program and has been approved for implementation beginning in 1995. The objective of Phase C is to design, build, and test major components of the airframe to demonstrate the technology readiness for applications in the next generation subsonic commercial transport aircraft. Part of the technology readiness demonstration will include a realistic comparison of manufacturing costs and an increased confidence in the ability to accurately estimate the costs of composite structure. The Program Plan calls for the structural components to be a complete fuselage barrel with a window-belt and a wing box at the wing/fuselage intersection. Proposals have been solicited from the major manufacturers to design, build, and test these composite structures. The procurement schedule calls for the prime contractors to be selected and the contracts awared by the end of fiscal year 1995. After the major contracts are awarded, the complete industry-University-NASA partnership will be completed with other program elements and team members being selected to support the activities of the prime contractors.

Subelement on Mechanics of Textile Preform Composites

Textile preform composites (braids and weaves) were the leading material form for the fuselage circumferential frames, window-belt reinforcements, and selected components in the keel of the fuselage. In addition, McDonnel-Douglas selected a knitted preform for the stitching technology for the wing components. To complete the development of the basic science underpinning to textile preform composites, the NASA Langley in-house team planned and implemented program elements focusing on fabrication technology, material system characterization, and mechanics-based design methodology. These

program elements were integrated with the programs of the prime contractors and became critical elements in the Phase B Program.

The Mechanics of Textile Preform Composites Program element had three primary objectives. First, test methods needed to be developed or modified to establish a set of test standards for measuring material properties and design allowables for textile preform composites. The standard test methods for tension, compression, and shear properties of laminated composites were evaluated and specialized for braided and woven preform composites. New test methods were developed to measure impact damage resistance and through-the-thickness strength. Second, mechanics models needed to be developed to predict the effects of the fiber preform architecture and constituent properties on engineering moduli, strength, damage resistance, and fatigue life. Micromechanics models were developed to predict the effects of the fiber architecture on local stress and strain behavior. The stress field results provided the basis for predicting the onset of various damage mechanisms and the strain field data were used to develop homogeneity methods for predicting the engineering elastic moduli of the composites. Third, an extensive experimental program was conducted to identify damage mechanisms and document damage progression and failure. A variety of loading histories were investigated including tension and compression strength of unnotched coupons, open-hole coupons and tubes with biaxial loadings, tension-tension and compression-compression fatigue, impact damage, post-impact residual strength, and post-impact fatigue. The experimental program led to the development of semi-empirical methods for predicting strength and fatigue life. More rigorous progressive damage models based on global-local analysis strategies were also developed for estimating strength and damage development due to impacts. However, these methods have limited capability and have not been experimentally verified.

The program objectives have been accomplished and the detailed results are presented by the Principal Investigators in this Proceedings. By the end of fiscal year 1995, the results will be integrated together into engineering design guidelines and a material property database will be assembled for all textile composites investigated in the Phase B Program. Taken together, the database and design guidelines will form the engineering basis for the detailed design of structural components using textile preform composites in Phase C of the ACT Program.

References

1. First NASA Advanced Composites Technology Conference, NASA CP 3104, compiled by John G. Davis and Herman L. Bohon, 1991.

2. Second NASA Advanced Composites Technology Conference, NASA CP 3154, compiled by John G. Davis and Herman L. Bohon, 1992.

3. Third NASA Advanced Composites Technology Conference, NASA CP 3178, compiled by John G. Davis and Herman L. Bohon, 1992.

4. Fourth NASA/DoD Advanced Composites Technology Conference, NASA CP 3229, compiled by John G. Davis, James E. Gardner, and Marvin B. Dow, 1993.

5. Fifth NASA/DoD Advanced Composites Technology Conference, NASA CP 3xxx, compiled by John G. Davis, James E. Gardner, and Marvin B. Dow, (1994).

EFFECTS OF NESTING ON COMPRESSION-LOADED 2-D WOVEN TEXTILE COMPOSITES

Daniel O'Hare Adams
Kurtis B. Breiling
Mark A. Verhulst
Department of Aerospace Engineering and Engineering Mechanics
Iowa State University
Ames, IA 50011

ABSTRACT

Layer nesting was investigated in five harness satin weave textile composite laminates under static compression loading. Two carbon/epoxy material systems, AS4/3501-6 and IM7/8551-7A were considered. Laminates were fabricated with three idealized nesting cases: stacked, split-span and diagonal. Similar compression strength reductions due to the effects of idealized nesting were identified for each material. The diagonal nesting geometry produced the largest reduction in static strength when compared to the compression strength of a conventional textile composite. All three nesting cases produced reductions in strength and ultimate strain due to the effects of idealized nesting. Finite element results showed consistent strength reduction trends for the idealized nesting cases, however the magnitudes of compressive strengths were overpredicted.

INTRODUCTION

Woven textile composite materials are attractive candidates for a variety of structural applications due to their ease in handling and economical fabrication. However, the advantages of these materials come at the expense of reduced in-plane stiffness and strength due to the undulating fibers inherent in woven textiles. Photomicrographs of 2-D woven composites reveal randomly scattered fiber tow waves throughout the laminate cross section as shown in Figure 1. These waves are inherent to the woven material, produced by the interlacing of warp and fill tows. In many applications, woven fabric is laid-up in warp-aligned laminates in which the direction of warp fibers is the same for each layer. The interaction between neighboring fabric layers is known as *nesting*. The effects of nesting on stiffness, compression strength and failure modes of 2-D woven composites are addressed in this study.

Although an idealized nesting configuration is usually assumed in analytical and numerical models, the effects of layer nesting have received very little attention to date. Jortner [1] addressed the effects of nesting on the stiffness of plain weave textile composites. A two-dimensional numerical model was developed to calculate the effective engineering constants for four different

nesting cases. The results showed that these constants can be significantly affected by the variations in nesting of fabric layers. The effects of nesting were found to be greater for the shear moduli than for Young's moduli. Naik and Shembekar [2] investigated optimum nesting patterns for plain weave fabrics. Numerical models that accounted for the differences in fabric geometry due to nesting were used to predict elastic constants. The authors concluded that it is possible to obtain a nesting configuration in plain weave textile composites that maximizes the elastic moduli and lowers Poisson's ratios. They also concluded that for a given fiber volume, the ability to control the nesting of individual lamina could produce in-plane elastic properties similar to that of a symmetric unidirectional cross-ply laminate.

The objective of this investigation was to fabricate idealized nesting cases in five harness satin weave textile composites. Three idealized nesting cases were fabricated so that the warp fiber waves of each layer nest in a particular pattern throughout an entire laminate in both the warp and fill directions. These nesting cases were defined as stacked, split-span, and diagonal, which are shown in Figure 2 for a five-harness satin weave. The stacked nesting case is characterized by the collimated arrangement of warp tow waves present throughout the laminate. Each layer exhibits the same warp wave pattern in both the warp and fill directions. The split-span case is defined by the split-collimated arrangement of warp tow waves. Every other layer in this geometry exhibits the same warp wave pattern. The diagonal case is characterized by the diagonal pattern of warp tow waves present throughout the laminate. Each fabric layer in these laminates is shifted one fill tow width as the thickness of the laminate is progressed.

Static compression tests were performed on specimens representing each of the three idealized nesting cases. These results were then compared to those obtained from randomly nested specimens produced using conventional fabrication methods. Two-dimensional finite element analyses were performed to identify possible failure modes and locations for each of the nesting cases. These efforts, both experimental and numerical, are directed toward developing an understanding of the effects of nesting on the stiffness and compression strength of textile composites.

FABRICATION PROCEDURE

Two carbon/epoxy materials were investigated: AS4/3501-6 and IM7/8551-7A. Both materials were supplied as 6K tow, five-harness satin weave prepreg. From each material, 6 in. (152.4 mm) square laminates were fabricated with the three idealized nesting cases shown in Figure 2. Each laminate was produced by first cutting a length of prepreg fabric slightly wider than 6.0 in. (152 mm), cutting along the edge of a fiber tow. Perpendicular cuts were made at slightly greater than 6.0 in. (152 mm) intervals, again following the edge of a fiber tow. From these two perpendicular edges, fabric squares were cut, measuring one fiber tow less than 6.0 in. (152 mm) in each direction. In some instances, the fabric had a slight degree of distortion, such that the cut pieces needed to be realigned. Extreme care was taken to ensure that the edges of the squares followed the edges of fiber tows. Depending on the idealized nesting case desired, the fabric

squares were cut in different relative positions with respect to the five-harness satin weave pattern. The fabric squares were then stacked in the proper orientation, making sure to align the fiber tows in the desired manner around the circumference. To maintain alignment, an alignment jig was designed with four needles protruding upward through a corkboard near the corners of the fabric squares. The corkboard was covered with teflon-coated fiberglass cloth. Thus, the fabric squares were punched over the corner needles and aligned with the layer below. A total of 16 prepreg layers were used to produce laminates of approximately 0.2 in. (5 mm) thick. After the last layer had been punched and aligned, the corners were stitched with Kevlar thread to prevent the layers from shifting during handling and curing.

The stitched assembly was placed in a 6 in. (152 mm) square steel well-and-plunger mold for curing. The mold was sealed using a thin bead of vacuum sealant around the periphery of the plunger. The mold was then placed into a heated press and consolidated. The temperature was slowly raised to 250 °F (121 °C) and held for one hour, then increased to 350° (177 °C) and held for two additional hours. The pressure was held at 100 psi (0.68 MPa) for the duration.

Three idealized nesting cases, stacked, split-span, and diagonal, were fabricated from each of the five-harness satin weave materials. All three nesting cases are readily identifiable from photomicrographs of the laminate cross sections as shown in Figure 3. The nesting patterns in each laminate were found to be very consistent throughout the entire laminate.

Conventional "randomly nested" laminates were manufactured following the same general procedure. These laminates were constructed by cutting 6.0 in. (152 mm.) squares from the prepreg fabric without concern as to the weave pattern contained. The well-and-plunger mold and curing procedure used were the same as for the idealized nesting cases. After curing, ultrasonic C-scans were performed on all of the laminates to ensure acceptable quality.

COMPRESSION TESTING

Static compression testing was performed to determine the stiffness and compression strength of 2-D woven textile composites with idealized layer nesting. Randomly nested specimens, considered the control case, were also tested. The compression strengths of the idealized nesting cases are compared to the randomly nested case, identifying changes in stiffness and strength due to the idealized nesting.

Test Preparation

The NASA short block compression test was chosen for this investigation primarily due to the small specimen size required. The fixture is composed of two hardened steel plates with sliding clamps attached to support the specimen during testing as shown in Figure 4. The fixture utilizes

an end loading configuration and allows for an adustable-pressure clamping support near the specimen ends. To further reduce out-of-plane bending in the specimen, a pivot stage was designed to be used during compression testing as shown in Figure 5.

A water-cooled diamond saw was used to cut the 6.0 in (152 mm) square laminates into short block test specimens of dimensions 1.25 in. (32 mm) wide by 1.5 in. (38 mm) long. After cutting, the specimen ends were machined using a surface grinder to ensure that they were flat and parallel for uniform end loading.

End brooming, a premature failure associated with load introduction through the specimen ends, was a concern with the NASA short block test. Several trial tests were run using this fixture to find the required clamping pressure needed to prevent end brooming and produce gage section failures. Excessive clamping pressure produced stress concentrations in the specimens at the clamp termination points. A moderate clamping pressure was used to allow Poisson expansion to occur during compression loading. Once an acceptable clamping pressure was found, nearly all specimens failed in the test sections. The remaining specimens failed at the ends, usually shearing off one of the corners.

An MTS servo-hydraulic testing machine was used to load the specimens at a constant displacement rate of 0.05 in/min (1.27 mm/min), consistent with the ASTM standard for compression testing [3]. A dual-measurement extensometer was used to record back-to-back strains during loading. These strains were used to detect bending during loading and to determine the stiffness and strain to failure. Specimens were preloaded to approximately 10 percent of ultimate strength and the pivot stage was adjusted to eliminate any bending detected. Once the out-of-plane bending was eliminated, the pre-load was removed and the compression test to failure was initiated. A data acquisition system collected load as well as back-to-back strain data throughout the entire test. The stress versus strain curves showed only slight nonlinearity as shown in Figure 6.

Test Results

The results of the static compression tests for the AS4/3501-6 and IM7/8551-7A materials are presented in Tables 1 and 2, respectively. The compression strength, stiffness, and ultimate strain are tabulated for each specimen and averaged for each nesting case. In order for comparisons to be made between the compression strengths and stiffness for each of the nesting cases, scale factors for thickness variations were required. Compression strength and stiffness scaling factors were calculated as the ratio of the average thickness of the random nested specimens to the thickness of the particular idealized nested specimen. Thus, all compression strength and stiffness values presented in Tables 1 and 2 are scaled to the average thickness of the random nested specimens for the particular material.

A reduction in compression strength due to idealized nesting may be identified by comparing the average compression strength results of each idealized nesting case to the results from the random case. The average compression strengths are plotted for the two materials in Figures 7 and 8. For the AS4/3501-6 material (Figure 7), strength reductions were 26.8, 28.6, and 39.4 percent for the split-span, stacked and diagonal nesting cases, respectively. For the IM7/8551-7A material (Figure 8), strength reductions were 7.7, 10.9 and 11.6 percent for the split-span, stacked and diagonal nesting cases, respectively. Thus for all cases, a reduction in compression strength resulted due to idealized nesting. Since the same fabrication method was used to create all the laminates tested, these compression strength reductions are attributed to the effects of idealized nesting.

The average stiffness value for each specimen was based on the average of the back-to-back strain readings between 0.1 and 0.3 percent strain. Figures 9 and 10 present the average stiffness for the AS4/3501-6 and IM7/8551-7A materials, respectively. For both materials, no appreciable change in average stiffness was experienced by any of the idealized nested specimens when compared to the average stiffness of the randomly nested case. Thus it is concluded that layer nesting does not have a significant effect on laminate stiffness.

The average ultimate strains are plotted for the two materials in Figures 11 and 12. The ultimate strain value for each specimen was based on an average of the back-to-back strain readings at ultimate load. The reduction trends revealed by the compression strength results were also present in the average ultimate strain results. For the AS4/3501-6 material (Figure 11), reductions in ultimate strain of 29.5, 32.0 and 40.1 percent were measured for the split-span, stacked and diagonal cases, respectively. For IM7/8551-7A (Figure 12), reductions in ultimate strain of 10.3, 14.0 and 16.2 percent were measured for the split-span, stacked and diagonal cases, respectively. Similar to the conclusion made for the average compression strength results, a reduction in ultimate strain exists due to the effects of the idealized nesting for both materials.

Observations From Failed Specimens

In all of the short block compression tests performed sudden fracture occurred without prior detection either visibly, audibly or by strain or load measurements. The inability to detect failure initiation prior to catastrophic failure made determining the initial failure modes impossible. Two variations of catastrophic failures were observed in the tests: straight and wedge shear failures. The straight shear failure is characterized by an angled fracture plane that spans through the specimen thickness as shown in Figure 13. The second variation, the wedge shear failure, is shown in Figure 14. Although the final condition of specimens suggested these two classifications, there was no evidence to suggest any difference in specimen quality or failure initiation.

FINITE ELEMENT ANALYSIS

The purpose of the finite element analysis was to identify the differences in stress distributions associated with the different idealized nesting cases and to predict the compression strength and probable modes of failure for these materials. A two-dimensional, plane strain model, subjected to a compression loading condition, was created for each nesting case. A maximum stress failure theory was applied to the models to predict compression strengths. These compression strengths were then compared to those obtained from static compression testing. Analyses were performed for both the AS4/3501-6 and the IM7/8551-7A materials tested.

Model Development

Photomicrographs of the idealized nesting cases were used in modeling the actual geometries of the materials. The two-dimensional unit cell used to model the five harness satin fabric is shown in Figure 15. The dimensions of the unit cell, including the amplitudes and wavelengths of the undulating warp tows, were obtained by measurements taken from photomicrographs of actual specimens. A wave severity parameter (δ/λ) was defined to compare the severity of the undulations in the warp fibers inherent to each nesting case. The wave severity parameters calculated for the different nesting cases were all within 7 percent of the average value, $\delta/\lambda = 0.0455$. Thus, this value was used to define a unit cell geometry for all three nesting cases. A total of ten repeating unit cells were modeled for each nesting geometry. The three model meshes used in the analysis are shown in Figure 16.

Loading and Boundary Conditions

The boundary conditions applied to each of the idealized nesting models are shown in Figure 17. These conditions produce symmetry about the global X and Y axes. Although none of the nesting geometries investigated in this study were symmetric with respect to the X axis, this boundary condition was applied to simulate a thick laminate. When the models were run without the enforced symmetry condition, out-of-plane bending was produced due to modeling a thin unsymmetric laminate. By simulating a thicker symmetric laminate using symmetry conditions, out-of-plane bending was eliminated. The effects of this applied boundary condition on the stress distributions did not progress more than one unit cell into the model leaving the central layer of interest unaffected. This result is consistent with those of Whitcomb [4] from a two-dimensional analysis of a plain weave.

A compressive load was applied through the use of a uniform displacement boundary condition. A displacement of 0.00375 in. (0.0293 mm) was chosen to simulate a 0.5 percent strain level in each model. Since the analysis was linear elastic, any substantial amount of load could have been applied to the models for obtaining the desired results.

Material property data for AS4/3501-6 and IM7/8551-7A prepreg tape obtained from references [5,6] were used. The warp and fill tows were treated as transversely isotropic in the 2-3 plane (perpendicular to the fiber orientation). Thus,

$$E_3 = E_2 \quad (1)$$
$$\upsilon_{13} = \upsilon_{12} \quad (2)$$
$$G_{13} = G_{12} \quad (3)$$
$$G_{23} = E_2/2(1+\upsilon_{23}) \quad (4)$$

The out of plane Poisson's ratio, υ_{23}, was estimated based on the ratio of υ_{23} to υ_{12} for carbon/epoxy materials obtained from reference [7]. The relation used for υ_{23} for the analysis was

$$\upsilon_{23} = 1.4\ (\upsilon_{12}). \quad (5)$$

The elastic material properties for the AS4/3501-6 and IM7/8551-7A carbon/epoxy materials used in the analyses are presented in Table 3.

Failure Prediction Results For AS4/3501-6 AND IM7/8551-7A

A maximum stress theory of failure was applied to each of the three idealized nesting models representing both AS4/3501-6 and IM7/8551-7A materials. The maximum values for each stress component and their locations along the undulation were obtained from examining contour and path plots of the finite element results. Strength data for the AS4/3501-6 and IM7/8551-7A materials were obtained from references [5,6] and are presented in Table 4. The maximum stress theory is based on comparing values of five individual components of stress to the five corresponding material strength allowables. These strengths are the longitudinal tensile strength (X_T), transverse tensile strength (Y_T), shear strength (S), longitudinal compressive strength (X_C), and transverse compressive strength (Y_C). If any of the stresses exceed their corresponding strength allowable, failure is predicted. The inequalities that must be satisfied to avoid failure are:

$$\sigma_1 < X_T \quad (6)$$
$$\sigma_2 < Y_T \quad (7)$$
$$\tau_{12} < S. \quad (8)$$

If the normal stresses are compressive, then the compressive allowables are substituted into the theory as

$$|\sigma_1| < |X_C| \tag{9}$$
$$|\sigma_2| < |Y_C|. \tag{10}$$

This failure theory does not consider any interactive terms relating combinations of stresses to a predicted mode of failure. Failure predicted from equations (6) and (9) represents a tensile or compressive warp fiber failure. Equations (7) and (10) consider a transverse failure by either separating or crushing the warp and fill tows. Finally, equation (8) represents an interlaminar shear failure in either the warp tows, matrix material, or the interface between the two. Transverse isotropy was applied to the strength properties, therefore

$$Z_C = Y_C \tag{11}$$
$$Z_T = Y_T \tag{12}$$
$$S_{13} = S_{12}. \tag{13}$$

The interlaminar shear strength, S_{23}, was assumed to be equal to the value of the in-plane shear strength, S_{12} in this analysis. Stress components defined along paths on the upper, middle and lower surfaces of the warp tow located in the center of the model were analyzed. The longitudinal and transverse normal stresses were found to be slightly higher along the upper surface of the warp tow while the interlaminar shear stresses appeared highest along the tow centerline. Maximums for all of the stress components were located in the region of the warp tow undulation.

Compression strengths were predicted for the three idealized nesting cases of each material. A linear elastic analysis was used to extrapolate the results of the finite element analysis to failure based on the maximum stress failure theory. Table 5 presents the predicted strength values for each of the idealized nesting cases and materials. For all of the cases considered, failure was predicted to occur as a result of longitudinal (warp) fiber compression failures.

Analysis of the AS4/3501-6 material predicted the split-span nesting case to have the highest compression strength of the three idealized nesting cases with a value of 100.0 ksi (689.5 MPa). The stacked and diagonal cases revealed slightly lower predicted compression strengths with values of 96.7 (666.7 MPa) and 94.2 ksi (649.5 MPa) respectively. A reduction in compression strength of 3.3 and 5.8 percent was identified for the stacked and diagonal nesting cases respectively when compared to the split-span nesting case. Although all of the failures predicted by the finite element models were longitudinal fiber compression failures, varying levels of the other stress components were identified. Figure 18 presents the non-dimensionalized peak values of the three stress components at the failure load. Each stress component, evaluated at the failure load, is shown non-dimensionalized by dividing by its corresponding strength allowable. The peak values identify the stress levels of each component at the failure load. Since the maximum stress failure theory does not consider interactive stress terms in its failure predictions, the magnitudes of the other stress components need to be addressed individually as well.

For the AS4/3501-6 material, the transverse normal stress (σ_2) was the next largest component in all of the idealized nesting cases. The diagonal case revealed a maximum transverse stress that was 80.0 percent of the corresponding strength when longitudinal compression failure was predicted. This high transverse stress is particularly significant when considering that the transverse strength prediction for a 6K tow was based on strength data from prepreg tape. Due to the high transverse stress identified in this nesting case, it is conceivable that failure may be due to an interaction between the longitudinal and transverse stresses. The transverse stress levels in the split-span and stacked idealized nesting cases were 69.0 and 60 percent, respectively. Although these stress levels appear to be moderately high, it is less likely that they are major contributors to failure. The shear stress components in all three of the idealized nesting cases were below 50 percent of the shear strength at the predicted longitudinal compression failure.

Analysis of the IM7/8551-7A material predicted the split-span nesting case to have the highest compression strength, similar to the predictions for AS4/3501-6 material. Compression strengths of 100.3 ksi (691.6 MPa), 97.5 ksi (672.3 MPa) and 95.9 ksi (661.2 MPa) were predicted for the split-span, stacked and diagonal nesting cases respectively. The reduction in strengths for the stacked and diagonal nesting cases are 3.6 and 6.1 percent when comparing them to the split-span nesting case. Although all of the failures predicted by the finite element models were longitudinal fiber compression failures, varying levels of the other stress components were predicted. Figure 19 presents the non-dimensionalized stress components evaluated at the predicted failure load. Each stress component was non-dimensionalized by dividing by its corresponding strength allowable. The shear stress component was the next largest stress for the stacked and split-span nesting cases. The stacked case predicted a shear stress level of 89 percent at the failure strength. Due to this high stress level, it is conceivable that a lower strength may result from the interaction between the longitudinal fiber compression stress and shear stress for this particular nesting case. Shear stress levels of 70.0 and 41.6 percent were predicted in the split-span and diagonal nesting cases respectively. The transverse stress components in all three of the idealized nesting cases were below a 52 percent stress level at the predicted failure strength.

Similar strength trends were predicted for both the AS4/3501-6 and IM7/8551-7A materials. In each case, the split-span nesting case was predicted to have the highest compression strength followed by the stacked and diagonal cases, respectively. This trend was the same as the one defined by the static compression strength data discussed previously. Figures 20 and 21 compare the predicted and experimental compression strengths of each nesting case for the AS4/3501-6 and IM7/8551-7A materials, respectively. For both materials, the finite element analysis overpredicted the compression strengths of each nesting case.

Several possible explanations exist for these overpredictions. First, the use of a two-dimensional model oversimplifies the true three-dimensional geometries of these materials. The models defined by this investigation only considered material variations in the global X-Y plane. Conventional five harness satin weave materials possess undulations in both the warp and fill fiber tows. The out-of-plane fill fiber tow undulations were not considered in the analysis. The use of a three-dimensional model may predict failure to occur at lower applied stress levels and in other areas than in this investigation.

A second possible explanation involves the use of prepreg tape strength properties in these failure predictions. Prepreg tape strength properties were used for both the AS4/3501-6 and IM7/8551-7A materials because strength data for fiber tows was unavailable. The longitudinal, transverse and shear strengths of fiber tows could be less than the strengths of the prepreg tape material used in the analysis. Under these conditions, an overprediction of the compression strengths would occur.

Finally, the use of a non-interactive failure theory may have contributed to the overprediction of compression strengths. Although longitudinal compression failure was predicted for all cases, significant magnitudes of transverse stress and shear stress were present in several cases as previously discussed. A failure theory that accounts for interactions of stress components would produce somewhat lower predicted compression strengths.

CONCLUSIONS

The effects of idealized nesting on the compressive performance of five harness satin woven textile composite materials were investigated. Three idealized nesting cases were defined: split-span, stacked and diagonal. Each of the idealized nesting cases were fabricated from AS4/3501-6 and IM7/8551-7A carbon/epoxy material and tested in compression. Randomly nested specimens, considered the control case, were fabricated from both materials and tested to failure for comparison. Compressive strength reductions were produced in all the idealized nesting cases, the reductions increasing in magnitude from the split-span to the stacked to the diagonal nesting case. Stiffness values were not significantly affected by any of the idealized nesting cases. Ultimate strains followed the same trends as compressive strengths. Two-dimensional finite element analyses were performed to verify the strength reduction trends and to identify possible modes of failure associated with each idealized nesting case. Although the predicted strength reduction trends for the idealized nesting cases were consistent with test results, the magnitudes of compressive strengths were overpredicted. These overpredictions may have been the result of the 2-D model, the strength properties, or the non-interacting failure criteria used in the analysis.

REFERENCES

1. Jortner, J., "Fabric Nesting and Some Effects on Constitutive Behavior of Plain -Weave Cloth-Reinforced Laminates," Proceedings of the Sixth Japan-U.S. Conference on Composite Materials, 1992, pp. 464-473.

2. Naik, N.K., Shembekar, P.S., "Elastic Behavior of Woven Fabric Composites: II-Laminate Analysis," Journal of Composite Materials, Vol. 26, No. 15, 1992, pp. 2227-2245.

3. ASTM Standard D 3410-87, "Compressive Properties of Unidirectional of Crossply Fiber-Resin Composites," American Society for Testing and Materials, Philadelphia, PA, 1987.

4. Whitcomb, J.D., "Failure Analysis of 2D and 3D Woven Composites," NASA Advanced Technology Mechanics of Composites Work Group Quarterly Report, NASA Langley Research Center, October-December, 1992, pp. 80-85.

5. Nelson, R. H., "AS4/3501-6 Design Allowables," Hercules Incorporated Bacchus Works, Magna, UT, September, 1984.

6. Hercules Aerospace Products, "Magnamite 8551-7A Tough Resin: Graphite Prepreg Tape and Fabric Module", Bacchus Works, Magna, UT, 1985.

7. Tsai, S.W., Composites Design, 3rd Ed, Think Composites, 3303 Locust Camp Rd (Box 581), Dayton, OH 45419, 1987.

Table 1. Static Compression Results For AS4/3501-6

Nesting Case	Compression Strength ksi (MPa)	Stiffness Msi (GPa)	Ultimate Strain (%ε)
Random	116.5 (803.3)	9.98 (68.81)	1.25
	115.5 (796.4)	10.11 (69.71)	1.31
	115.6 (797.1)	10.23 (70.54)	1.17
	105.9 (730.2)	10.22 (70.47)	1.02
	116.6 (804.0)	10.08 (69.50)	1.33
	114.0 (786.2)	10.12 (69.80)	1.22
Split-Span	89.9 (619.9)	10.05 (69.29)	0.98
	100.1 (690.2)	10.11 (69.71)	1.09
	113.0 (779.1)	10.23 (70.54)	1.23
	71.3 (491.6)	10.55 (72.74)	0.70
	62.0 (427.5)	10.41 (71.78)	0.58
	64.4 (444.0)	11.04 (76.12)	0.55
	83.5 (575.4)	10.40 (71.71)	0.86
Stacked	95.4 (657.8)	10.26 (70.74)	1.02
	108.3 (746.7)	10.09 (69.57)	1.19
	85.7 (590.9)	9.94 (68.54)	0.94
	71.2 (490.9)	9.61 (66.26)	0.63
	69.3 (477.8)	9.63 (66.40)	0.63
	72.6 (500.6)	10.18 (70.19)	0.73
	67.0 (462.0)	10.24 (70.60)	0.68
	81.4 (561.0)	9.99 (68.90)	0.83
Diagonal	67.7 (466.8)	10.53 (72.60)	0.62
	75.7 (522.0)	9.88 (68.12)	0.81
	62.6 (431.6)	9.93 (68.48)	0.61
	61.7 (425.4)	9.59 (66.12)	0.69
	78.2 (539.2)	9.52 (65.64)	0.90
	68.8 (474.4)	10.05 (69.29)	0.72
	69.1 (476.6)	9.92 (68.38)	0.73

Table 2. Static Compression Results For IM7/8551-7A

Nesting Case	Compression Strength ksi (MPa)	Stiffness Msi (GPa)	Ultimate Strain (%ε)
Random	86.6 (597.1)	10.60 (73.09)	0.83
	87.9 (606.1)	10.71 (73.85)	0.86
	91.2 (628.8)	10.83 (74.67)	0.89
	85.2 (587.5)	----	----
	80.2 (553.0)	10.67 (73.57)	0.76
	90.4 (623.3)	10.97 (75.64)	0.86
	86.9 (599.2)	10.76 (74.19)	0.84
Split-Span	75.6 (521.3)	10.37 (71.50)	0.74
	72.0 (496.4)[b]	11.32 (78.05)[b]	----
	75.4 (519.9)	10.82 (74.60)	0.71
	75.8 (522.6)	11.05 (76.19)	0.69
	84.4 (581.9)	10.68 (73.64)	0.84
	85.0 (586.1)	10.83 (74.67)	0.81
	80.2 (553.1)	10.84 (74.74)	0.75
Stacked	61.1 (421.3)[c]	10.84 (74.74)[c]	0.57[c]
	64.3 (443.3)[c]	10.82 (74.60)[c]	0.61[c]
	76.4 (526.8)	10.47 (72.19)	0.65
	73.7 (508.2)	10.26 (70.74)	0.72
	76.9 (530.2)	10.68 (73.64)	0.75
	75.3 (519.2)	10.84 (74.74)	0.70
	77.4 (533.7)	10.82 (74.60)	0.72
Diagonal	71.7 (494.4)	10.89 (75.09)	0.64
	74.7 (513.0)	10.72 (73.91)	0.71
	76.7 (528.8)	10.80 (74.47)	0.76
	73.2 (504.7)	10.85 (74.81)	0.68
	77.4 (533.7)	10.76 (74.19)	0.73
	75.8 (522.6)	10.80 (74.45)	0.70

[b] Grip failure.

[c] Not used in any averages due to poor quality of the specimen shown by C-scan results

---- Data not available due to strain gage failure

Table 3. AS4/3501-6 and IM7/8551-7A Material Property Data

Properties	AS4/3501-6		IM7/8551-7A	
	Warp and Fill Tows	Epoxy Regions	Warp and Fill Tows	Epoxy Regions
E_1 (Msi)	18.3	0.52	22.2	0.52
E_2 (Msi)	1.2	-----	1.3	-----
E_3 (Msi)	1.2	-----	1.3	-----
G_{12} (Msi)	0.51	0.19	0.73	0.19
G_{23} (Msi)	0.42	-----	0.51	-----
G_{13} (Msi)	0.51	-----	0.73	-----
υ_{12}	0.30	0.35	0.30	0.35
υ_{23}	0.42	-----	0.42	-----
υ_{13}	0.30	-----	0.30	-----

Table 4. Ultimate Strengths For AS4/3501-6 and IM7/8551-7A Tape Material

Property	AS4/3501-6 Ultimate Strength ksi (MPa)	IM7/8551-7A Ultimate Strength ksi (MPa)
Longitudinal Tensile Strength, X_T	278.2 (1918.2)	323.0 (2227.1)
Longitudinal Compressive Strength, X_C	201.5 (1389.3)	220.0 (1516.9)
Transverse Tensile Strength, Y_T	5.65 (38.96)	9.05 (62.40)
Transverse Compressive Strength, Y_C	16.95 (116.87)	17.00 (117.22)
In-plane-Shear Stress, S	15.70 (108.25)	12.00 (82.74)

Table 5. Predicted Compression Strengths For AS4/3501-6 and IM7/8551-7A Materials

Nesting Case	AS4/3501-6 Predicted Compression Strengths ksi (MPa)	IM7/8551-7A Predicted Compression Strengths ksi (Mpa)
Split-Span	100.0 (689.5)	100.3 (691.6)
Stacked	96.7 (666.7)	97.5 (672.3)
Diagonal	94.2 (649.5)	95.9 (661.2)

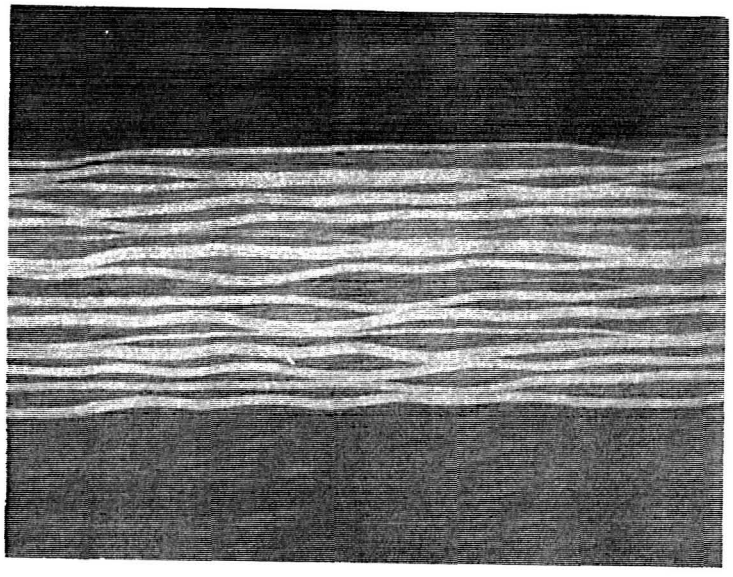

Figure 1. Randomly scattered warp tow waves in a five harness satin weave laminate.

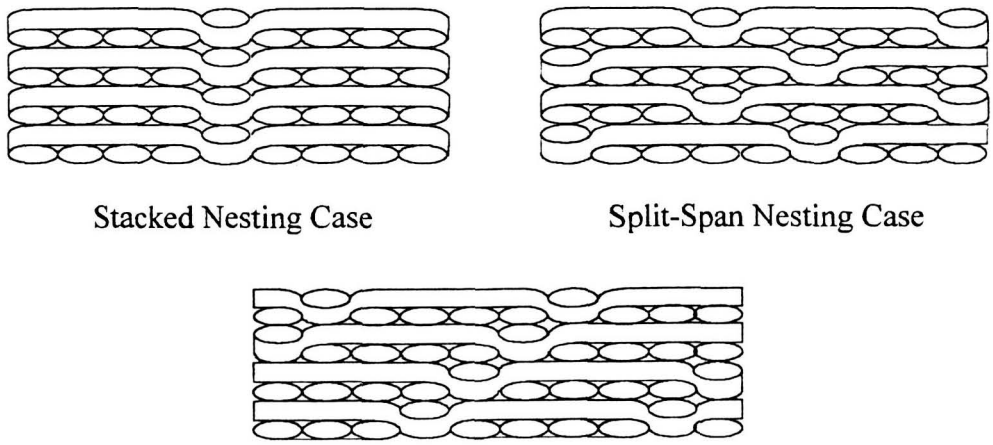

Figure 2. Stacked, split-span, and diagonal idealized nesting cases.

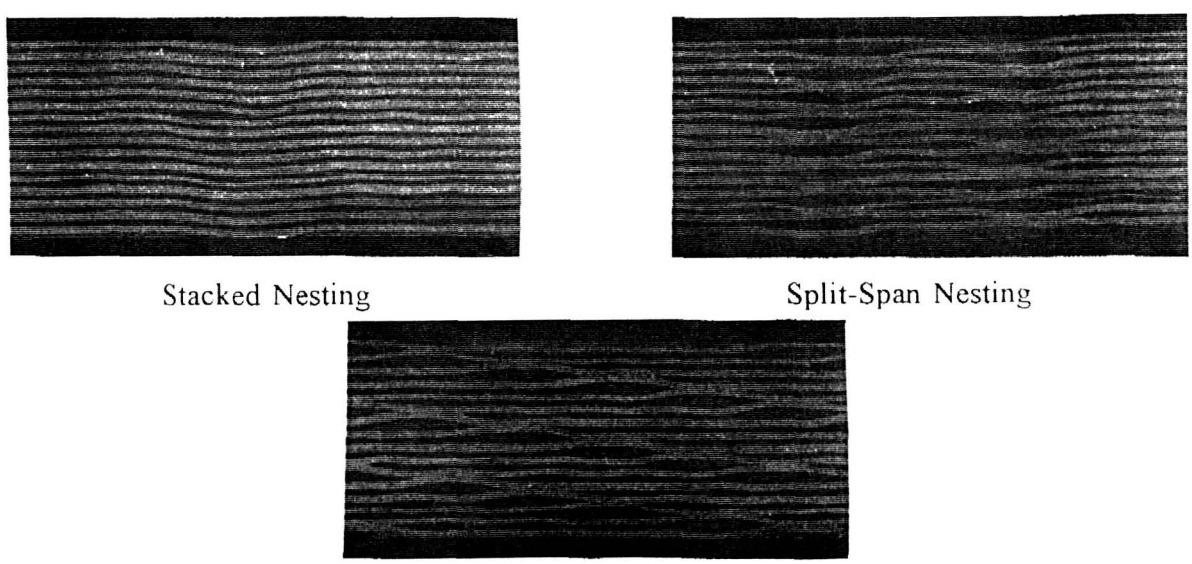

Figure 3. Idealized nesting cases (IM7/8551-7A material).

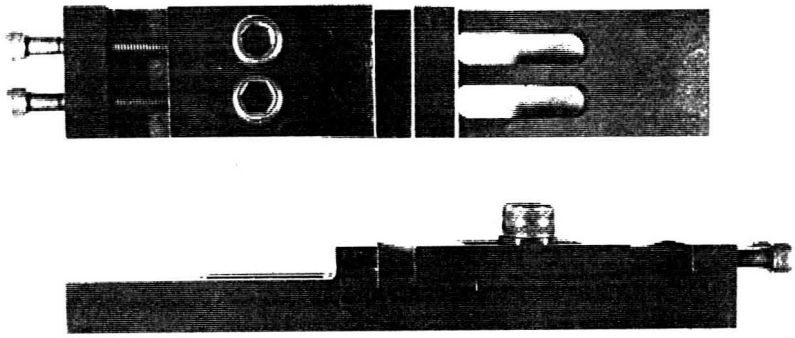

Figure 4. NASA short block test fixture.

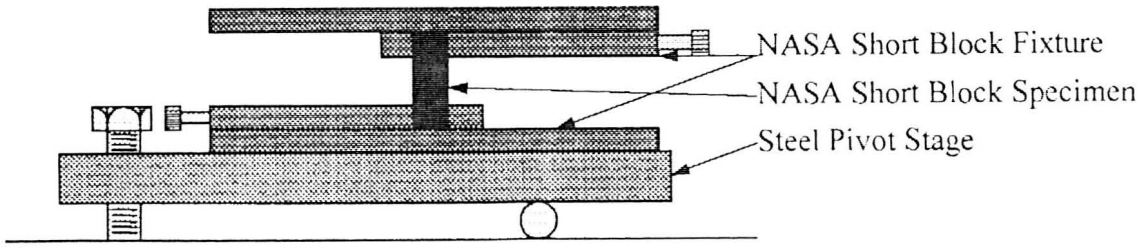

Figure 5. Compression testing pivot stage.

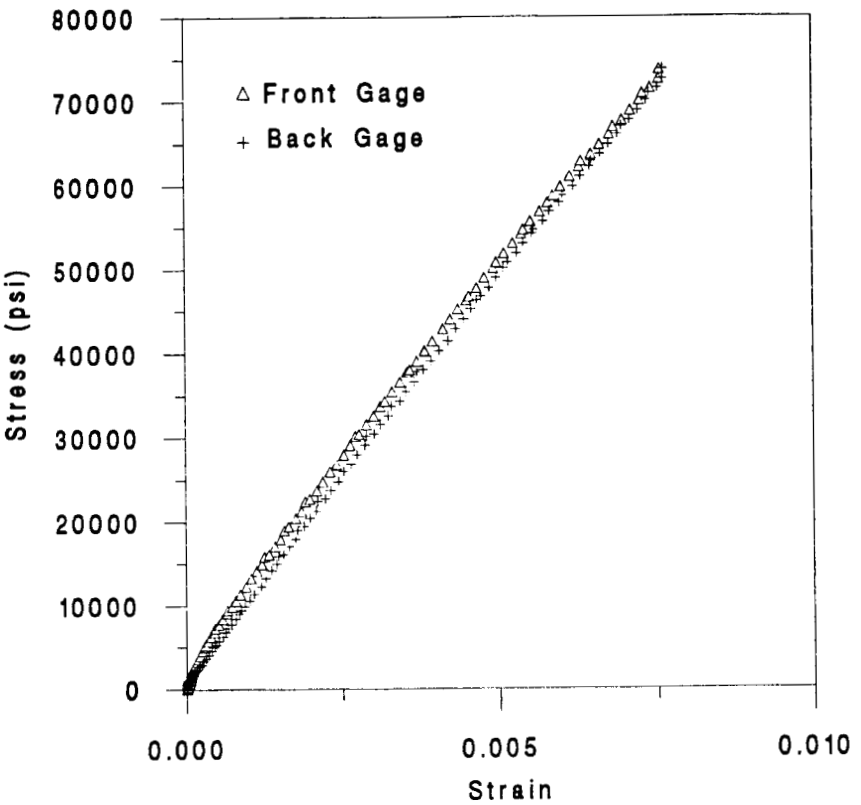

Figure 6. Typical stress versus strain curve obtained from NASA short block compression testing.

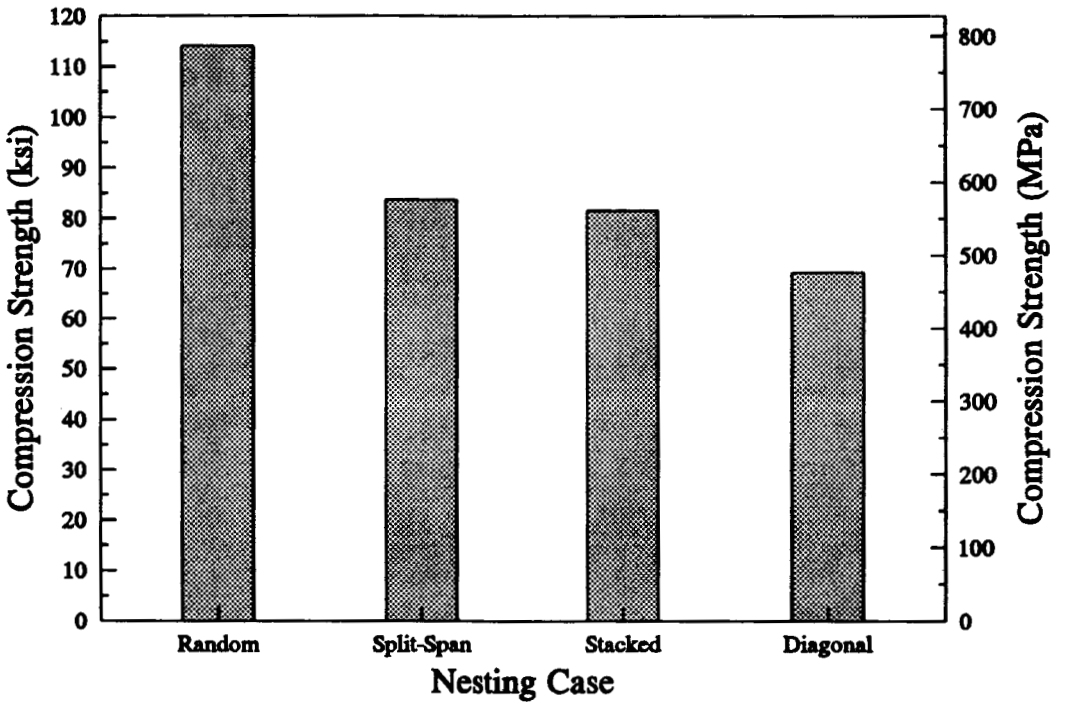

Figure 7. AS4/3501-6 average compression strength results for each nesting case

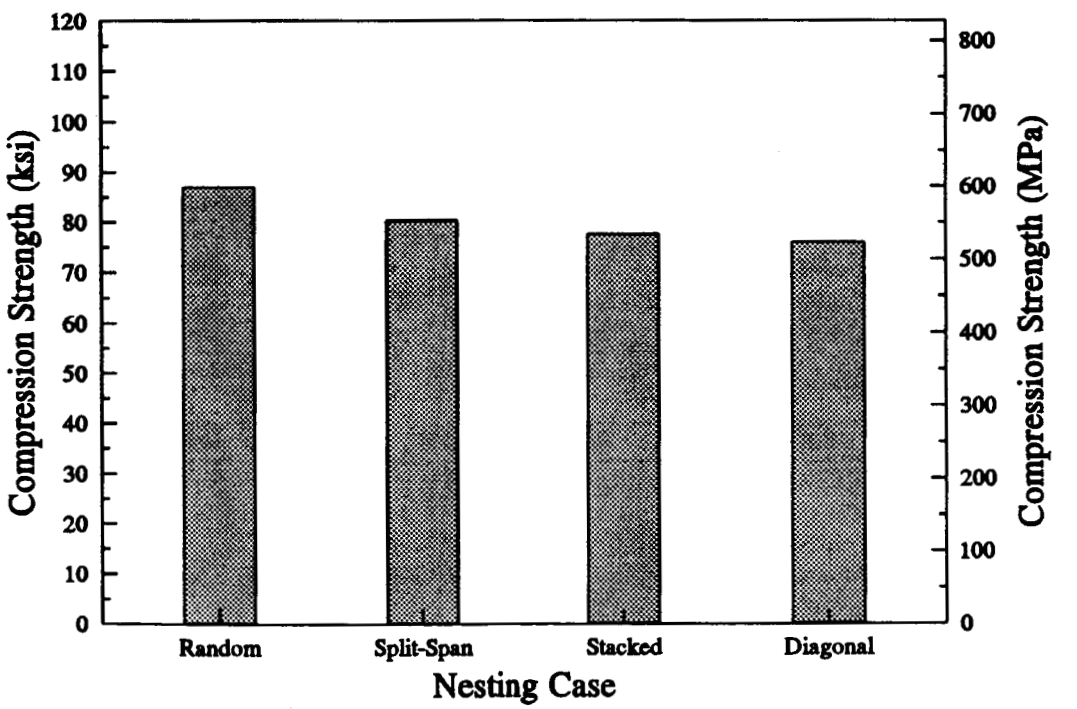

Figure 8. IM7/8551-7A average compression strength results for each nesting case.

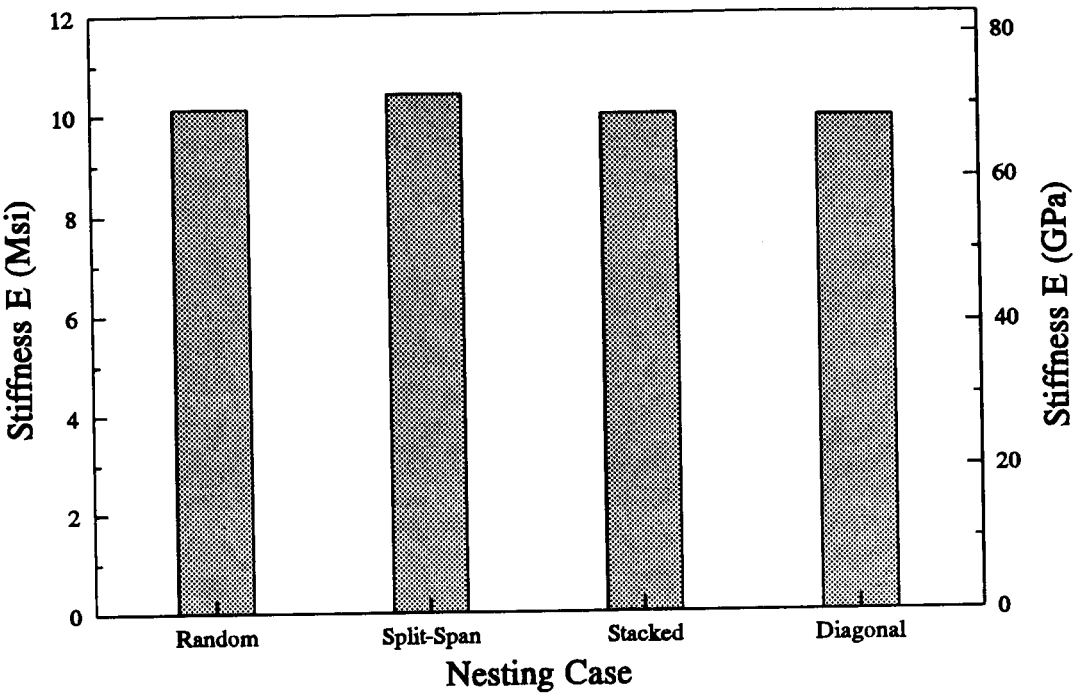

Figure 9. AS4/3501-6 average stiffness results for each nesting case.

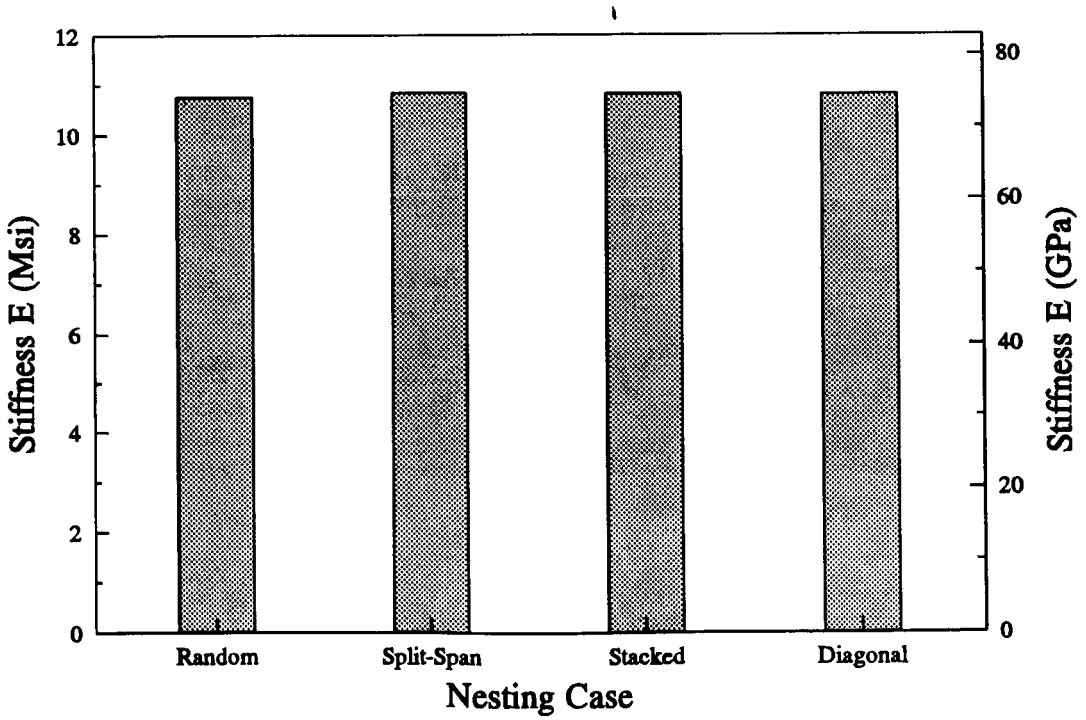

Figure 10. IM7/8551-7A average stiffness results for each nesting case.

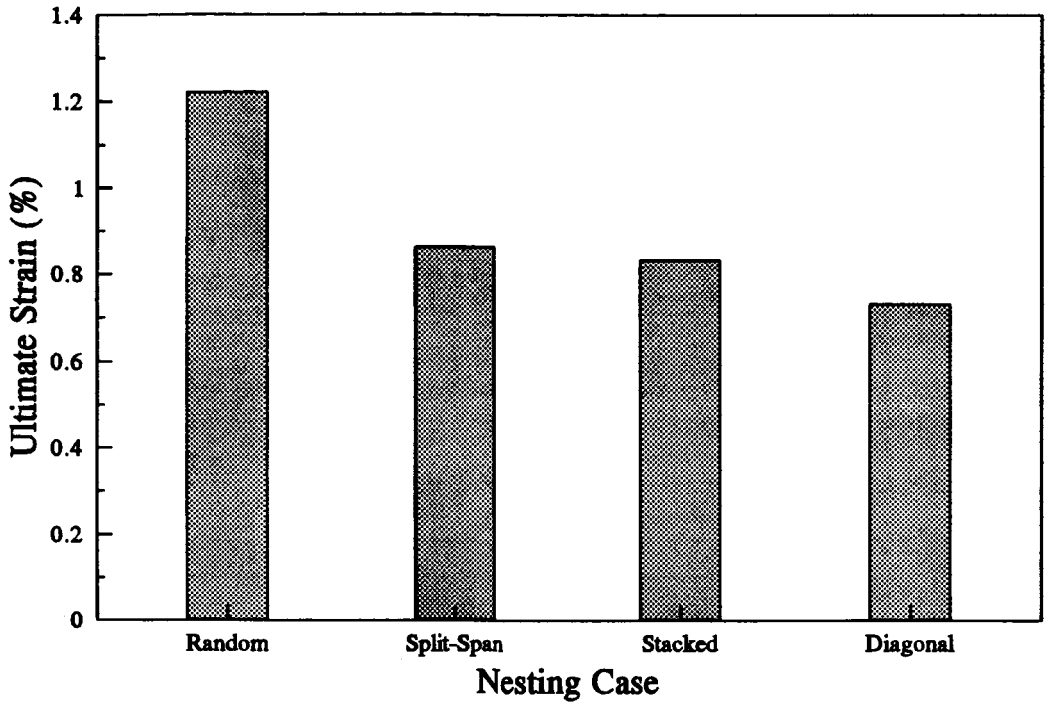

Figure 11. AS4/3501-6 average ultimate strain results for each nesting case.

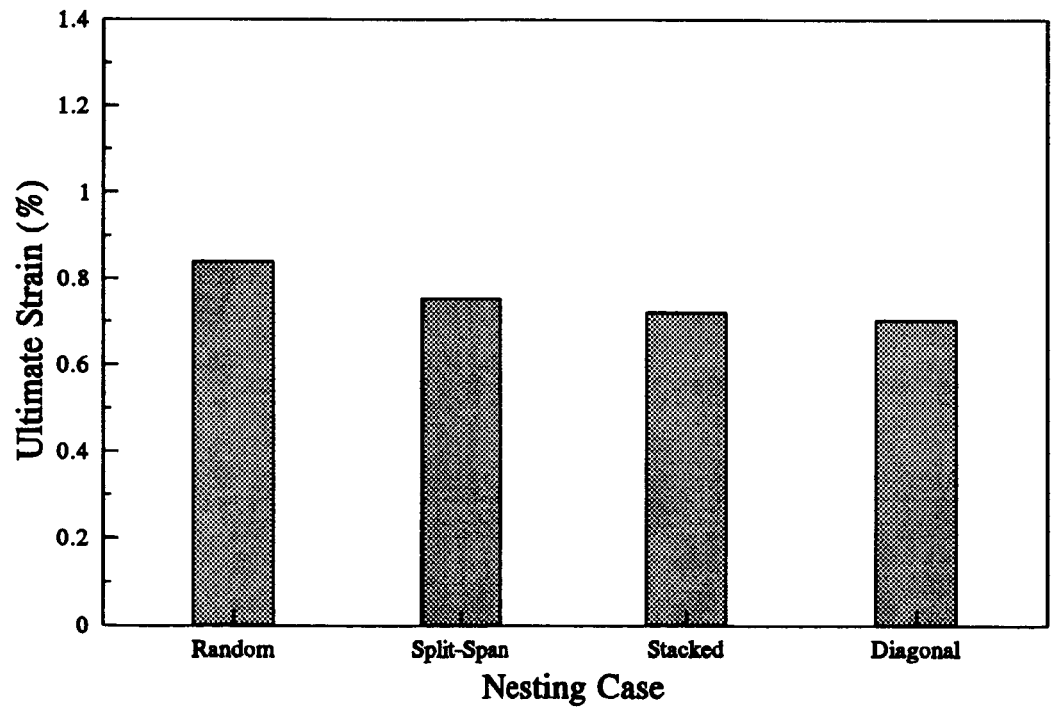

Figure 12. IM7/8551-7A average ultimate strain results for each nesting case.

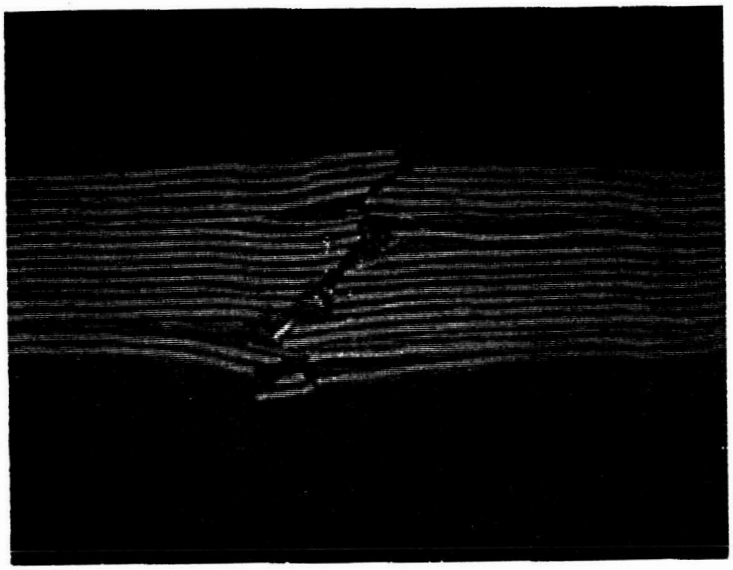

Figure 13. Straight shear failure, stacked nesting case.

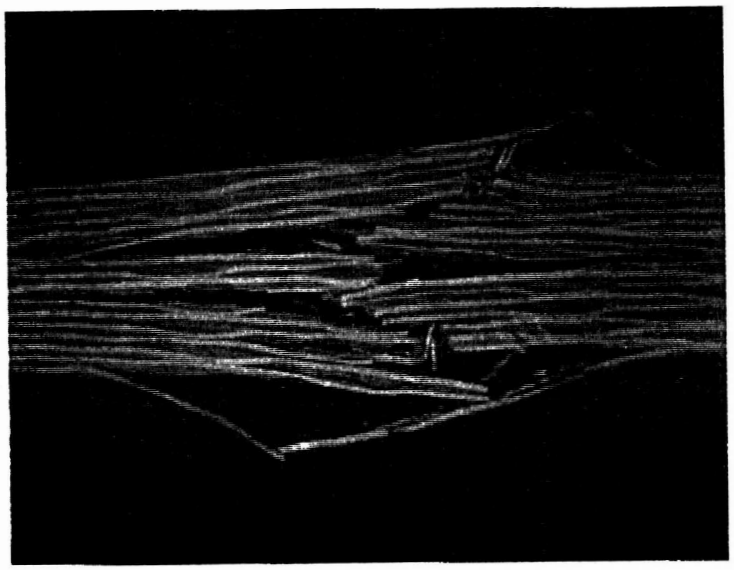

Figure 14. Wedge shear failure, split-span nesting case.

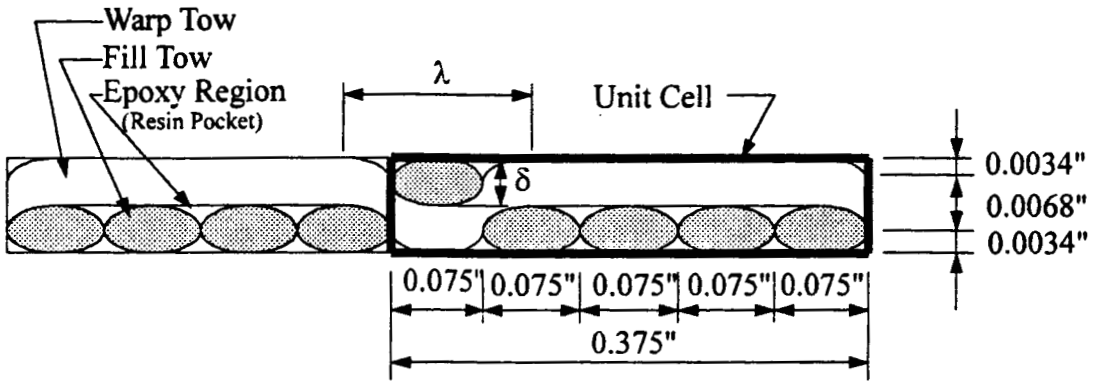

Figure 15. Two-dimensional unit cell of a five harness satin weave.

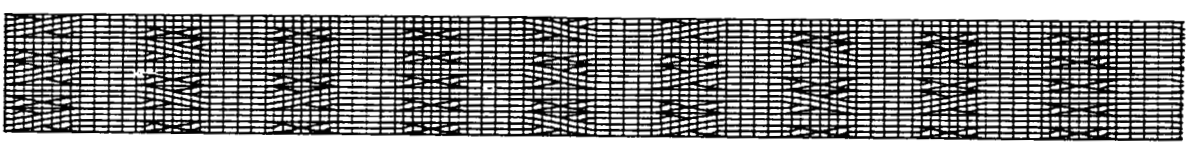

Split-Span Nesting Mesh

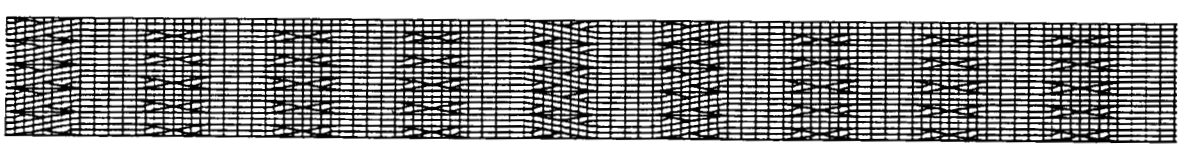

Stacked Nesting Mesh

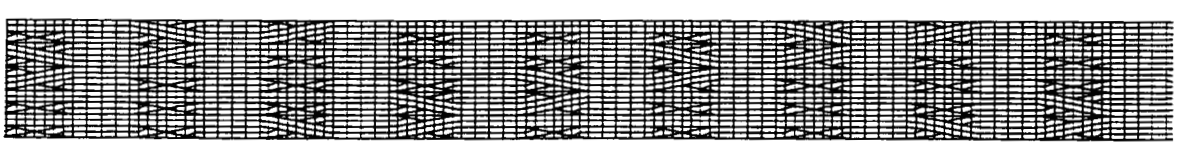

Diagonal Nesting Mesh

Figure 16. Finite element meshes for the split-span, stacked, and diagonal nesting cases.

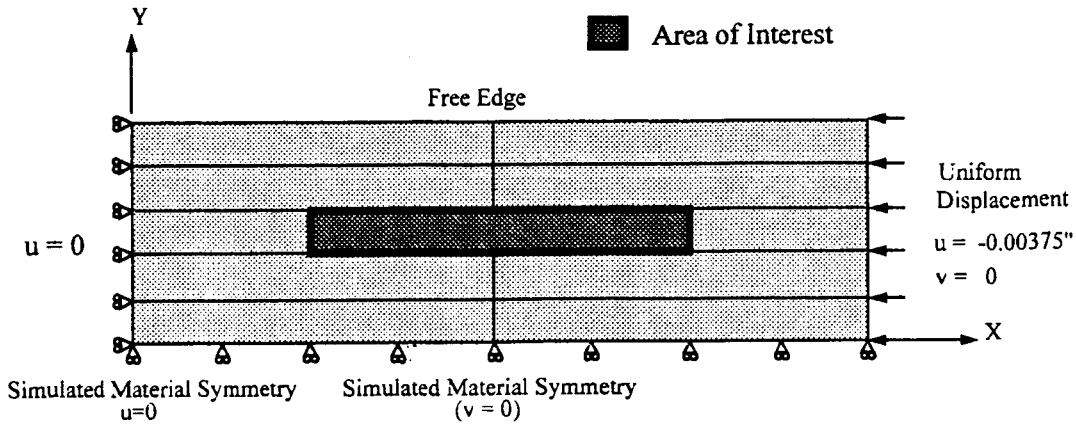

Figure 17. Boundary conditions used for finite element analysis.

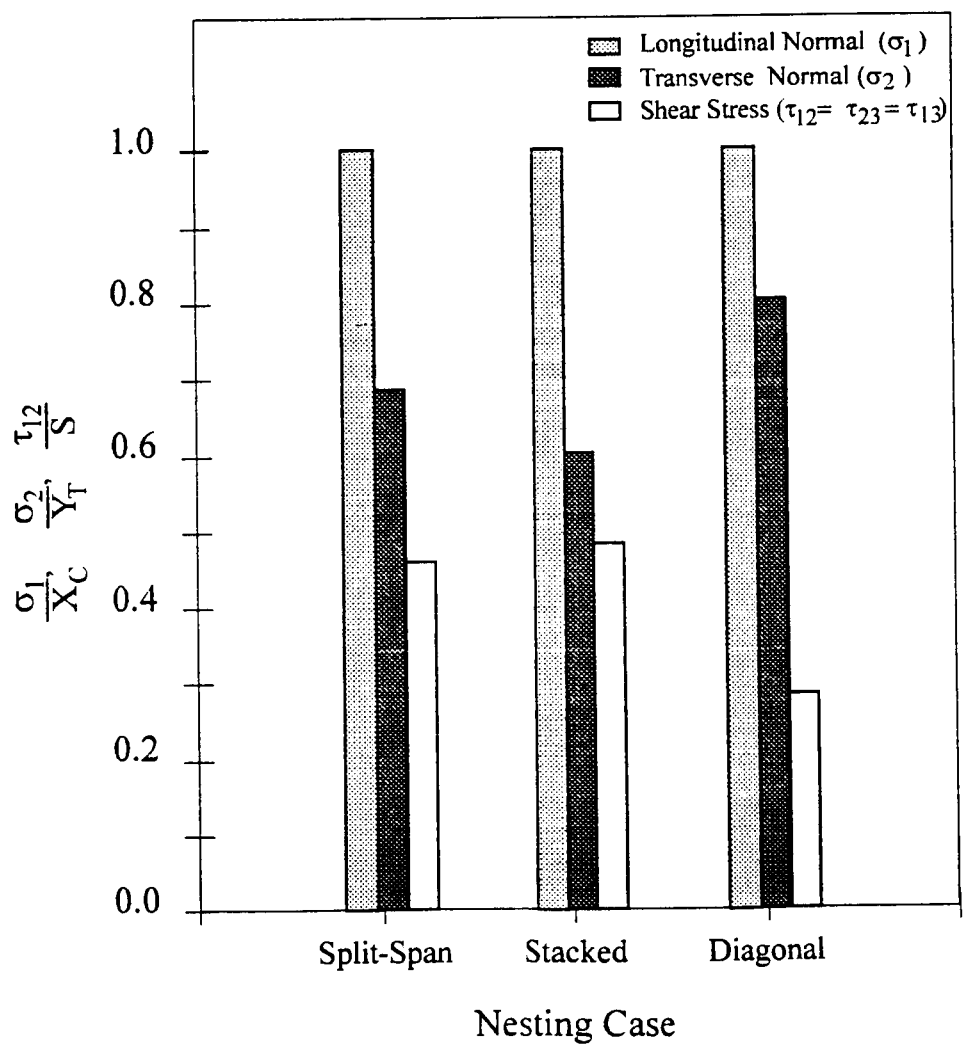

Figure 18. Peak values of stress components for A4/3501-6.

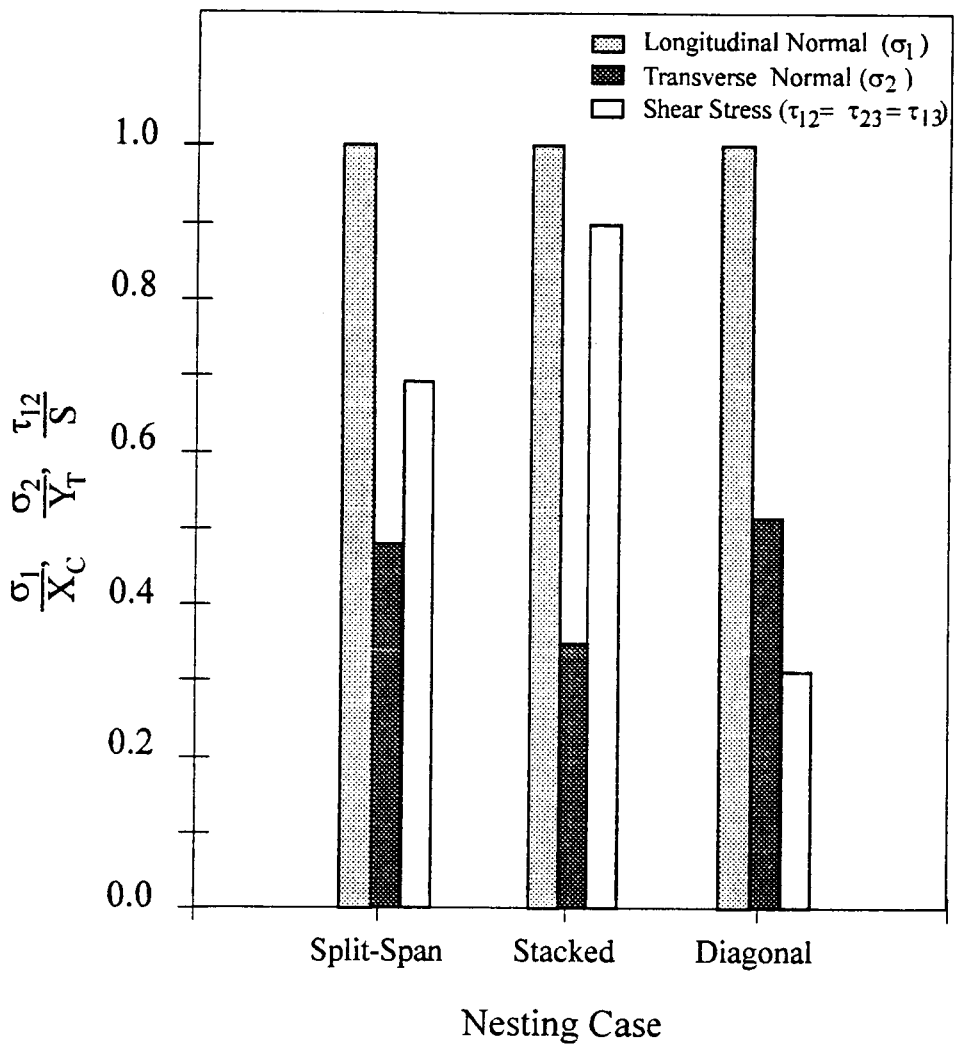

Figure 19. Peak values of stress components for IM7/8551-7A.

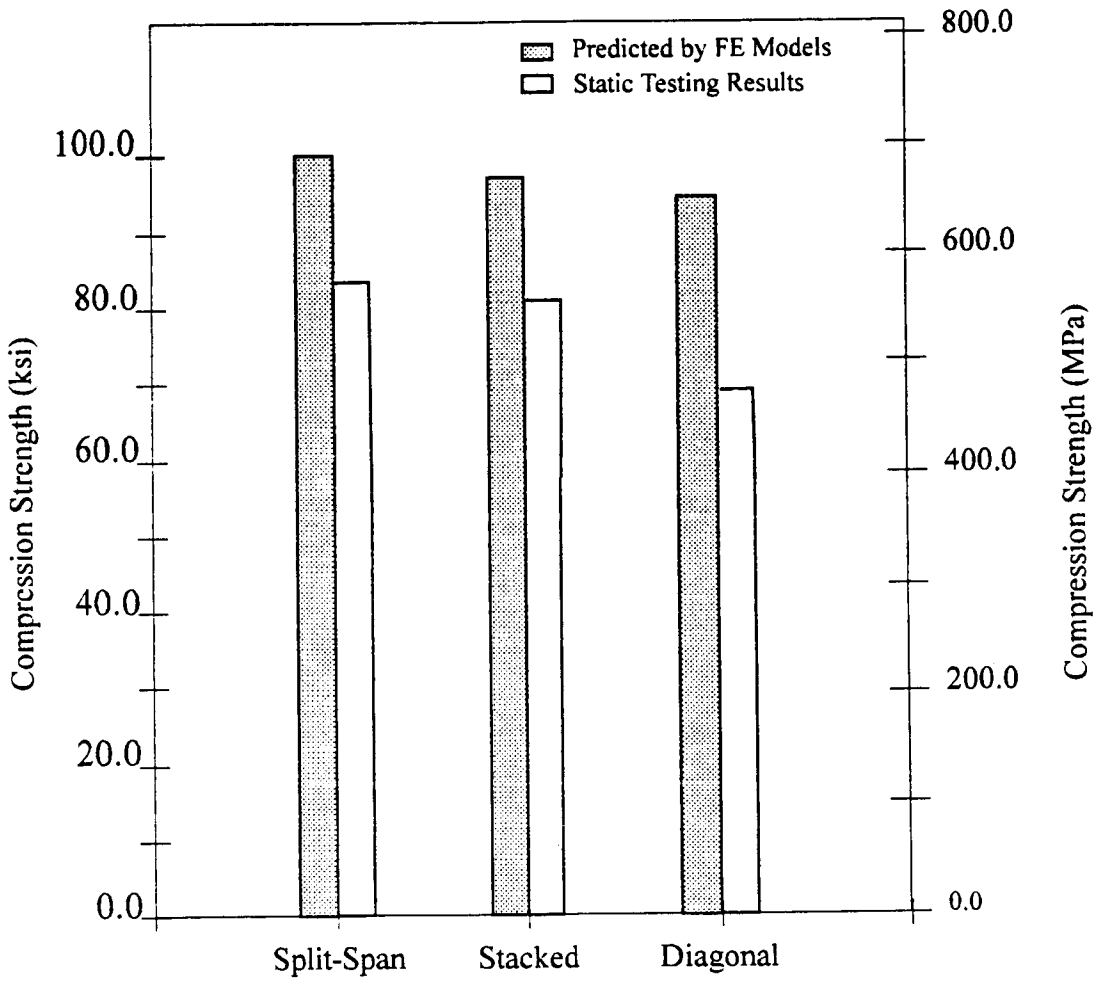

Figure 20. AS4/3501-6 compression strength comparison.

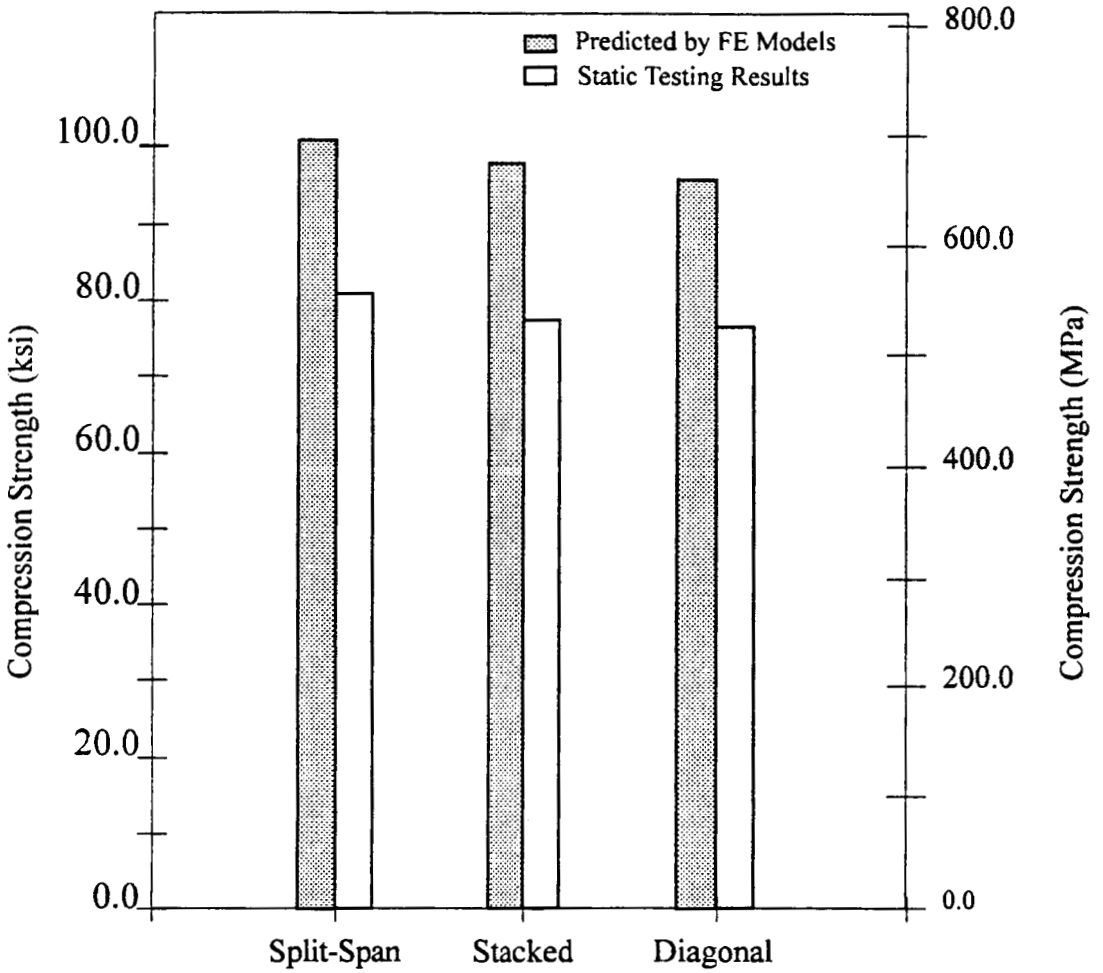

Figure 21. IM7/8551-7A compression strength comparison.

CHARACTERIZATION OF TWO-DIMENSIONALLY BRAIDED COMPOSITES SUBJECT TO STATIC AND FATIGUE LOADING

Scott T. Burr * and Don H. Morris **
Dept. of Engineering Science and Mechanics
Virginia Polytechnic Institute and State University
Blacksburg, VA

SUMMARY

This paper presents a characterization of damage processes in four different two-dimensionally braided architectures consisting of graphite fibers in an epoxy matrix, subjected to both static and fatigue loading. Both notched and unnotched specimens were tested from each architecture. Damage mechanisms in static compression testing were found to range from matrix cracking in an architecture controlled by shearing characteristics of the matrix to axial fiber bundle kinking and splitting in architectures controlled by unidirectional fiber bundles. In both static tension and tension-tension fatigue testing, it was found that all architectures sustained the same basic damage types and progression sequences. The first types of damage to occur were splits in the braider bundles and cracks in the resin rich areas. Once a sufficient density of this type of damage had occurred, the axial bundles began to disbond from the surrounding constituents, and continued to do so until ultimate failure. One architecture sustained an additional mode of failure, which involved splitting of the axial bundles along their length. Varied degrees of notch sensitivity were found among the different architectures. In one architecture, this was attributed to differences found in the stacking of the individual plys of the braided architecture. As the density of axial bundles adjacent to the notch increased, the rate of stiffness loss increased and the life decreased.

INTRODUCTION

Braided composite materials have experienced a renewed interest due to the ability of manufacturer's to braid near-net-shape preforms [1-8]. While providing the composites manufacturer more flexibility, net shape parts can also reduce both manufacturing cost and time. Several researchers have studied the post-impact properties[9-12]. Braided composites have been found to have a significantly greater post-impact property retention as compared to laminated composites. Characterizations of stiffness and strength of braided composites subject to both static and fatigue loading have also been completed by several researchers [13-25]. However, studies of the damage processes that occur within an initially undamaged material are limited. This paper presents a characterization of damage processes in four

Work funded by the NASA Langley Research Center under grant number NAG-1-343.
Senior Graduate Research Assistant * and Professor **

different two-dimensionally braided architectures consisting of graphite fibers in an epoxy matrix, subjected to both static and fatigue loading. Stiffness loss monitoring, which has been proven to be an effective experimental tool in damage mechanism study by several researchers [26-33], is presented along with damage types and sequences.

MATERIAL SYSTEMS

Four different two-dimensionally braided architectures were manufactured using an identical braiding process. This process is characterized by axial fiber bundles which run along straight lines as shown in Figure 1. The braider fiber bundles are oriented at a specified angle with respect to the axial fiber bundles, and run over and under consecutive axial fiber bundles. The braider fiber bundles run over two and under two braider fiber bundles oriented at opposite angles to each other. By varying the fiber bundle size and braid angle, four different architectures were manufactured. Table 1 lists the specifications of each of the architectures in this study. Two braid angles were used, which were 45° and 70°. Braider fiber bundles ranged in size from 6K to 15K, while axial fiber bundles ranged from 6K to 75K. Percentage of total areal weight of the preform for axial fibers ranged from 12% to 46%.

Two sets of notation will be used to describe the individual material systems. The first is a shorthand notation consisting of three letters. The second is a longhand notation which describes in detail the construction of the braid. Figure 2 shows the longhand notation for an architecture. The first number inside the brackets designates the angle for the axial fiber bundles with respect to the longitudinal axis, which in this study is always zero. Its subscript designates the size of the axial fiber bundle in thousands of fibers. The second number in the brackets designates the angles of the braider fiber bundles with respect to the longitudinal axis. Its subscript designates the size of the braider fiber bundle in thousands of fibers. The final subscript outside the brackets designates the percent of the total areal weight of the preform occupied by the axial fiber bundles. The corresponding shorthand and longhand notations are listed in Table 1.

STATIC TENSION TESTING

Experimental Program

The tension testing program consisted of two groups of straight sided test coupons with a gage length of 10.2 cm (4 in.) for each architecture. The gage width was 2.54 cm (1.0 in.) for all except the LLL architecture which had a gage width of 3.81 cm (1.5 in.) due to its larger unit cell width. The first group was tested to failure to determine material properties and general stress-strain response. Specimens in the second group were tested to specific load levels, then sectioned and studied to determine damage types, initiation levels, and progression sequences. The edges of the first group of specimens were monitored

during the test with a stereo microscope, while the second group was monitored in-situ with x-ray radiography at successive points in the loading sequence. Strain was monitored using 12.7 mm by 12.7 mm (0.5 in. by 0.5 in.) strain gages. All tests were run under stroke control at a rate of 0.64 mm/min (0.025 in/min).

Conclusions

Representative stress-strain plots are shown in Figure 3, with material properties listed in Table 2. Two basic stress-strain responses were found to occur. The first response was very nonlinear, characteristic of the LSS architecture which contained only 12% axial fibers. The second response was very linear, characteristic of the remaining three architectures containing 46% axial fibers. The main damage types and sequences, however, were consistent for all architectures. Splitting in the braider bundles was found to be the initial damage mode. The axial bundles then began a process of simultaneously disbonding along their outer boundaries.This sequence is shown in Figure 4. The SLL architecture also contained longitudinal splits in the axial bundles which extended along the gage length of the specimen during the loading sequence. The final failure mode in each architecture was rupture of the axial fiber bundles.

STATIC COMPRESSION TESTING

Experimental Program

The compression testing program consisted of two groups of straight sided coupons tabbed with a 1.6 mm (0.0625 in.) thick glass fiber composite. The gage length of each specimen was 12.7 mm (0.5 in.). The gage width was 2.54 cm (1.0 in.) for all except the LLL architecture was had a gage width of 3.81 cm (1.5 in.) due to its larger unit cell width. The first group was tested to failure to determine material properties and general stress-strain response. Specimens in the second group were tested to load levels as close to ultimate failure as possible, then sectioned and studied to determine damage types and failure mechanisms. The edges of all specimens were monitored during the test with a stereo microscope. Strain was monitored on the front and back faces of the specimens using 6.35 mm by 6.35 mm (0.25 in. by 0.25 in.) strain gages. All tests were run under stroke control at a rate of 0.25 mm/min (0.01 in/min).

Conclusions

Representative stress-strain plots are shown in Figure 3, with material properties listed in Table 3. As in the tension testing, two basic stress-strain responses were found to occur. The LSS architecture was controlled by the shearing characteristics of the matrix. This was indicated by its extremely nonlinear

stress-strain curve, pre-failure matrix cracking, and very high strain to failure. Figure 5 shows a representative micrograph containing pre-ultimate failure matrix cracking in the LSS architecture. Audible popping noises could be heard very early in the test, continuing up to ultimate failure. The remaining three axially dominated architectures were controlled by kinking and subsequent splitting of the axial fiber bundles. Figure 6 shows a kink band formed prior to ultimate failure in the SLL architecture.The axial fiber bundles split somewhere near the center of the bundle after the kink band had formed, as shown in a post failure micrograph of Figure 7.

TENSION-TENSION FATIGUE TESTING

Experimental Procedure

All tests were completed on a servo-hydraulic test frame at a rate of 5 Hz, and a minimum/maximum stress ratio of 0.1. Tests were run under load control using a haversine input signal. Specimens consisted of straight sided test coupons with a gage length of 10.2 cm (4 in.) for each architecture. The gage width was 2.54 cm (1.0 in.) for all except the LLL architecture which had a gage width of 3.81 cm (1.5 in.) due to its larger unit cell width. Strain was monitored with a 25.4 mm (1.0 in.) extensometer mounted on the face of the specimen. The feet of the extensometer were placed on grooved aluminium pads which were 6.35 mm wide by 3.2 mm tall (0.25 in. by 0.125 in.). The aluminium pads were adhered to the specimen using silicone glue. Rubber bands were used to hold the extensometer in place.

Strain and load signals were monitored by a personal computer equipped with an analog to digital signal board and a digital memory allocation (DMA) board. These boards work in tandem to allow the data acquisition system to continuously monitor the load and strain signals by simultaneously reading and writing the data to a buffer in the RAM of the computer. The personal computer is then instructed by the software to read the data from its memory and performs analyses on the measured signals. The software developed for the present paper retrieves 400 load and strain data points from each test cycle . From this data, dynamic tangent modulus, secant modulus and energy loss values are calculated for each individual cycle. If a preset number of cycles has occurred since the last save, or if one or more of the calculated values has exceeded a predetermined value, the information is written to both a file and a corresponding real time graph on the screen of the computer. This process provides the capability of analyzing each cycle the specimen undergoes, and calculating and displaying in real time the parameters of interest from the individual cycle.

Four specimens from each architecture were tested to failure at different stress levels to determine a rough S-N response. From this data, two stress levels which would produce a life of approximately 25,000 cycles and 90,000 cycles were determined. This corresponds to a test duration of approximately 1.3 hours and 5 hours respectively. Six specimens from each architecture were then tested at the lower stress level, and six were tested at the higher stress level. Of the six specimens, three were notched and three were

unnotched.The notched specimens all contained holes of diameter d= 0.25 w , and were tested at equivalent net-section stress levels. This provided an indication of how each architecture responded to a stress concentration. Each group of three specimens at each loading condition was tested to specific levels defined by either a predetermined stiffness loss or cycle number, all of which were less than ultimate failure. The specimens were then x-rayed, sectioned and polished to determine damage types, initiation levels, and progression sequences.

Experimental Results

Unnotched Specimens

$[0_{6K}/\pm45_{15K}]_{12\%\ axial}$ (LSS) Architecture. Two characteristic normalized dynamic tangent modulus versus cycle number curves for the LSS architecture are shown in Figure 8. Dynamic tangent modulus values were normalized by the initial dynamic tangent modulus of the test. It was generally found that as the peak stress level was increased, the rate of stiffness loss increased, while the life of the specimen decreased. Specimens from this architecture which were tested to failure displayed a characteristic stiffness loss at failure between 25% and 30%. A typical energy loss graph is shown in Figure 9. Energy loss values on the first cycle of the test were typically three times greater than subsequent cycles. This is attributed to the large amount of cracking in the resin rich pockets and splitting in the braider bundles, a large portion of which takes place on the first loading cycle. As the test progressed, large damage events which produced audible noise showed up as spikes in the energy loss graph. These events caused a momentary fluctuation in the extensometer large enough to produce large spikes. By monitoring the edge of the specimen with a stereo microscope during the test, correlations were made. Cracks in the braider bundles and resin rich areas produced audible noises and energy loss events ranging from 5%-35%, as compared to disbonds and ruptures in the axial bundles which produced energy loss events of greater than 75%. Many times the larger events yielded cycle information out of range of the measurement. Thus, any event which caused an energy loss fluctuation out of range was scaled to 50%. Large scale energy events were produced throughout the test, with the highest density of large events occurring just prior to ultimate failure.

A characteristic micrograph of a damaged specimen is shown in Figure 10. Cracks are seen oriented vertically through the resin rich areas in the center of the micrograph, and also through braider bundles in the upper left corner of the micrograph. An axial bundle spans the micrograph horizontally, and is oriented in the loading direction. The dark lines bordering the axial bundle are regions where the bundle has disbonded from its surrounding constituents. It was determined from sectioning specimens at different points in their respective lives that the first types of damage to occur are splits in the braider bundles and the cracks in the resin rich areas. Once a sufficient density of this type of damage has occurred, the axial bundles begin to disbond from the surrounding constituents, and continue to do so until ultimate failure. The exact density of damage in the matrix and braider bundles which occurs before axial bundle disbonding begins could not be determined with the limited number of specimens available.

$[0_{36K}/\pm45_{15K}]_{46\%\ axial}$ (LLS) Architecture. Two characteristic normalized dynamic tangent modulus versus cycle number curves for the LLS architecture are shown in Figure 11. As with the LSS architecture, it was generally found that as the peak stress level was increased, the rate of stiffness loss increased, while the life of the specimen decreased. Specimens from this architecture which were tested to failure displayed a characteristic stiffness loss at failure between 20% and 25%. The stiffness losses occurred in large, sporadic decreases, unlike the smooth response from the LSS architecture. Large scale damage events like those discussed in the LSS architecture also occurred throughout the life of the specimen, but were more often accompanied by a large a decrease in stiffness. These large scale events were found in the highest densities just prior to ultimate failure.

Regardless of the differences in stiffness loss behavior, the types and order of occurrence of damage mechanisms were consistent with that found for the LSS architecture.

$[0_{30K}/\pm70_{6K}]_{46\%\ axial}$ (SLL) Architecture. Two characteristic normalized dynamic tangent modulus versus cycle number curves for the SLL architecture are shown in Figure 12. It was again generally found that as the peak stress level was increased, the rate of stiffness loss increased, while the life of the specimen decreased. Specimens from this architecture which were tested to ultimate failure displayed a characteristic stiffness loss just prior to ultimate failure between 5% and 10%. The stiffness loss response was relatively smooth until just before ultimate failure, where it dropped to levels between 25% and 30% in a very catastrophic manner.

The types and order of occurrence of damage mechanisms were again consistent with that found for the LSS architecture. The SLL architecture, however, contained an additional mode of failure. As well as the axial bundles disbonding from the surrounding constituents, they also split along their length. Many of these longitudinal splits were found to exist in the untested material, and propagated into regions were they did not exist as the loading sequence progressed. It should be noted that when the individual layers were nested instead of stacked as shown in Figure 13, the axial bundles contained a split which ran directly through their centers, and occurred as long as the layers were nested. When the layers were in positions where they were more stacked in nature, the splits did not exist.

$[0_{75K}/\pm70_{15K}]_{46\%\ axial}$ (LLL) Architecture. Due to the large nature of the LLL architecture, strain measurement techniques used on the previous three architectures did not accurately measure the strain response. This is because the width of the axial bundles was approximately the same as that of the aluminium tabs the extensometer was mounted on. Once the damage sequence of axial bundle disbonding began to occur under the aluminium tabs, the strain readings began to decrease. This is because the braider bundles on the exterior of the specimen, upon which the extensometer is mounted, have already split. Once the axial bundle disbonds from them, they no longer transmit the same level of strain. This produces an apparent stress-strain response which stiffens as the damage density increases, which is erroneous. This problem is currently being solved, however, this paper will not contain any fatigue data on the LLL architecture.

Notched Specimens

$[0_{6K}/\pm45_{15K}]_{12\%\ axial}$ (LSS) Architecture. The response of the LSS architecture to the notch varied from completely insensitive to critically sensitive. A characteristic x-ray radiograph of a notched specimen from the LSS architecture which has under gone a 25% stiffness reduction is shown in Figure 14. The response of three LSS specimens subjected to the same peak stress is shown in Figure 15. Associated with each individual curve is a diagram which shows the location of the axial bundles with respect to the hole. The axial bundles are shown as ellipses, and are oriented in a plane protruding outward perpendicular from the page. The three vertical lines represent the center and edges of the notch. The uppermost curve represents the response of a specimen with a random distribution of axial bundles. The stiffness loss versus cycle curve of this specimen was comparable with that of an unnotched specimen, showing no apparent notch sensitivity. The middle curve was the response of a specimen with four of the five layers oriented such that the axial bundles were adjacent to the edges of the hole, while the last response is from a specimen with axial bundles from all five layers adjacent to the hole. As can be seen in the graph, as the density of axial bundles increases around the hole, the rate of stiffness loss is significantly increased, and life is decreased. This is consistent with data found from three notched coupons tested at a lower stress level, which again showed that as the density of axial bundles adjacent to the hole increased, the rate of stiffness loss increased while life decreased.

The types and order of occurrence of damage mechanisms were consistent with that found for the unnotched specimens. The main difference was that the damage was concentrated to the region immediately around the notch instead of evenly distributed throughout the specimen. Energy loss information also differed in that none of the large scale energy loss events characteristic of the unnotched specimen response were detected in any of the notched specimens.

$[0_{36K}/\pm45_{15K}]_{46\%\ axial}$ (LLS) Architecture. The response of the LLS architecture to a notch varied from sensitive to critically sensitive. A characteristic x-ray radiograph of a notched specimen from the LLS architecture which has under gone a 25% stiffness reduction is shown in Figure 14. Stiffness versus cycle number information is shown in Figure 16 for three notched LLS specimens subject to the same peak stress level. The response varied much like that found in the LSS architecture. The correlation between axial bundle placement and rate of stiffness loss could not, however, be made. Because the axial bundles are approximately six times larger than for the LSS architecture, the chances of the notch being surrounded by axial bundles are much greater. Sectioning of the notched region in specimens from the LLS architecture showed very similar nesting patterns and axial bundle placements with respect to the notch. No noticeable differences were found between comparable specimens.

Damage types and progressions were consistent with those found in all previous tests, with the exception of the damage concentrated in the region of the notch. Matrix cracking and braider bundle splitting occurred first, with axial bundle disbonding following. The axial bundles located immediately adjacent the notch also sustained splits along their longitudinal axis, usually one to two notch diameters in length as can be seen in Figure 14.

$[0_{30K}/\pm 70_{6K}]_{46\%\ axial}$ (SLL) Architecture. The SLL architecture was found to be critically sensitive to the notch. A characteristic x-ray radiograph of a notched specimen from the SLL architecture which has under gone a 20% stiffness reduction is shown in Figure 14. The response from three specimens subjected to the same peak stress level is shown in Figure 17. Because of the extreme sensitivity of this architecture to the notch, equivalent net section stress levels (unnotched gross section stress equals notched net section stress) for the predetermined high stress level could not be attained. Instead, the peak stress level was reduced to a level below the predetermined low stress level. The response at the reduced stress level still showed an extreme sensitivity to the notch.

Damage types and progressions were consistent with those found for the other architectures. However, some of the axial bundles in the SLL architecture contained longitudinal splits as a result of the manufacturing process. The damage was again concentrated around the notch, however, the entire gage section contained a significant density of splits in both the axial and braider bundles.

Conclusions

All architectures sustained the same basic damage types and progression sequences. It was determined from sectioning specimens at different points in their respective lives that the first types of damage to occur were splits in the braider bundles and the cracks in the resin rich areas. Once a sufficient density of this type of damage had occurred, the axial bundles began to disbond from the surrounding constituents, and continued to do so until ultimate failure. The exact density of damage in the matrix and braider bundles which occurred before axial bundle disbonding could not be determined with the limited number of specimens available. The SLL architecture sustained an additional mode of failure, which involved splitting of the axial bundles along their length. Many of these splits were present in the architecture prior to testing, however, they were found to grow when subjected to fatigue loading.

The LSS architecture was found to have a varied response to a notch. Behavior ranged from complete notch insensitivity to critical notch sensitivity. This was attributed to differences found in the stacking of the individual plys of the braided architecture. As the density of axial bundles adjacent to the notch increased, the rate of stiffness loss increased and the life decreased. The LLS architecture also was found to have a varied notch sensitivity, however, no differences were found in the architecture which could have attributed to this type of behavior. The SLL architecture was found to be extremely notch sensitive, so much so that equivalent net section stress levels undergone by the unnotched specimens could not be attained. Data from the LLL architecture was not presented due to problems in strain measurement caused by the large size of the architecture. This architecture will be tested once an accurate strain measurement technique has been developed.

REFERENCES

1. Ko, F. K.: 3-D Fabrics for Composites, Textile Structural Composites, Elsevier Science Publishers, Ed. T. W. Chou and F. K. Ko, 1989, pp. 129-171.

2. Ko, F. K., Pastore, C. M., Head, A. A.: Structural Geometry of Braids - Chapter 4, Handbook of Industrial Braiding, Atkins & Pearce, pp. 4-1 - 4-14.

3. Temple, S.: Large Scale Manufacture of Three-Dimensional Woven Preforms, *IMechE*, 1986, pp. 133-140.

4. Florentine, R. A.: Magnaweave Process - From Fundamentals to Applications, *Textile Research Journal*, October 1983, pp. 620-623.

5. Klein, A. J.: Braids and Knits: Reinforcement in Multidirections, *Advanced Composites*, September/October, 1987, pp. 36-48.

6. Zawislak, S. P., Maiden, J. R.: Advanced Weaving Concepts for Complex Structural Preforms, *FiberTex 1988*, pp. 91-111.

7. Suarez, J. and Mahon, J.: Consolidation of Graphite/Thermoplastic Textile Preforms for Primary Aircraft Structure, *The First NASA Advanced Composites Technology Conference, Part 1*, January, 1991, pp. 293-338.

8. Brandt, J., Drechsler, K., and Richter, H.: The Application of 2-D and 3-D Woven Thermoplastic Fiber Preforms for Aerospace Components, *36th International SAMPE Symposium*, April 15-18, 1991.

9. Ko, F., Hartman, D.: Impact Behavior of 2-D and 3-D Glass/Epoxy Composites, 31st International SAMPE Symposium, April 7-10, 1986, pp. 1272-1293.

10. Simonds, R. A., Stinchcomb, W., and Jones, R. M.: Mechanical Behavior of Braided Composite Materials, *Composite Materials: Testing and Design (Eighth Conference), ASTM STP 972*, J. D. Whitcomb, Ed., American Society for Testing and Materials, Philadelphia, 1988, pp. 438-453.

11. Li, W., Hammad, M., Reid, R. and El-Shiekh, A.: The Effect of Unit Cell Size on Impact Tolerance of 3-D Braided Graphite/Epoxy Composites, *ICCM-7*, Beijing, China, Aug. 1-4, 1989.

12. Wei, L., Hammad, M., El-Shiekh, A.: Effect of Braiding Process on the Damage Tolerance of 3-D Braided Graphite/Epoxy Composites, 34th International SAMPE Symposium, May 8-11, 1989, pp. 2109-2117.

13. Shimokawa, T. & Hamaguchi, Y.: Distributions of Fatigue Life and Fatigue Strength in Notched Specimens of Carbon Eight-Harness-Satin Laminate, *Journal of Soc. Mater. Sci., Jpn.*, Vol. 32, 1983, pp. 1050-1056.

14. Gause, L. W., Alper, J. M., and Dalrymple, R. H.: Fatigue Properties of Multidirectional Braided Composites, *Report No. NADC-85022-60*, February 1985.

15. Fujii, T., Fukuda, T., and Osaka, K.: Modeling and Simulation of Low-Cycle Fatigue Behavior of Glass-Mat Composite Laminates, *Fifth International Conference on Composite Materials, ICCM-V*, San Diego, CA, July 1985, pp. 141-152.

16. Crane, R.M., Camponeschi, E.T. Jr.: Experimental and Analytical Characterization of Multidimensionally Braided Graphite/Epoxy Composites, *Experimental Mechanics*, September 1986, pp. 259-266.

17. Macander, A. B., Crane, R. M., and Camponeschi, E. T., Jr.: Fabrication and Mechanical Properties of Multidimensionally (X-D) Braided Composite Materials, *Composite Materials: Testing and Design (Seventh Conference)*, ASTM STP 893, 1986, pp. 422-443.

18. Schulte, K., Reese, E., and Chou, T. W.: Fatigue Behaviour and Damage Development in Woven Fabric and Hybrid Fabric Composites, *Sixth International Conference on Composite Materials, ICCM 6*, Vol. 4, July 1987, pp. 4.89-4.99.

19. Gause, L. W. and Alper, J. M.: Structural Properties of Braided Graphite/Epoxy Composites, *Journal of Composites Technology and Research*, JCTRER, Vol. 9, No. 4, Winter 1987, pp. 141-150.

20. Liao, D., Tan, T.M., Ko, F.K.: Compressive Behavior of 3-D Braided Composites Part I. Experimental Observations, 36th International SAMPE Symposium, April 15-18, 1991, pp. 129-140.

21. Hirokawa, T., Yasuda, J., and Iwasaki, Y.: The Characteristics of 3-D Orthogonal Woven Fabric Reinforced Composites, *36th International SAMPE Symposium*, April 15-18, 1991, pp. 151-160.

22. Chou, S., Chen, H., and Lai, C.: The Fatigue Properties of Weft-Knit Fabric Reinforced Epoxy Resin Composites, *Composites Science and Technology*, Vol. 45, 1992, pp. 283-291.

23. Masters, J. E., Foye, R. L., Pastore, C. M., Gowayed, Y. M.: Mechanical Properties of Triaxially Braided Composites: Experimental and Analytical Results, *Journal of Composites Technology and Research*, JCTRER, Vol. 15, No. 2, Summer 1993, pp. 112-122.

24. Naik, R. A., Ifju, P. G., and Masters, J. E.: Effect of Fiber Architecture Parameters on Deformation Fields and Elastic Moduli of 2-D Braided Composites, *Journal of Composite Materials*, Vol. 28, No. 7, 1994, pp. 656-681.

25. Cox, B. N., Carter, W. C., Dadkhah, M. S., and Morris, W. L.: Micromechanics of Fatigue in Woven and Stitched Composites, *NASA Contractor Report 4626*, September 1994.

26. O'Brien, T. K. and Reifsnider, K. L.: Fatigue Damage: Stiffness/Strength Comparisons for Composite Materials, *Journal of Testing and Evaluation*, Vol. 5, No. 5, Sept. 1977, pp. 384-393.
27. O'Brien, T.K.: Stiffness Change as a Nondestructive Damage Measurement, Mechanics of Nondestructive Testing, W.W. Stinchcom, ed., Plenum Press, New York, 1980, pp. 101-121.

28. Highsmith, A.L. & Reifsnider, K.L.: Stiffness Reduction Mechanics in Composite Laminates, ASTM STP 775 (1982) pp. 103-117.

29. Camponeschi, E.T. & Stinchcomb, W.W.: Stiffness Reduction as an Indicator of Damage in Graphite/Epoxy Laminates, ASTM STP 787 (1982) pp. 225-246.

30. Ogin, S.L., Smith, P.A., & Beaumont, P.W.R.: Matrix Cracking and Stiffness Reduction During the Fatigue of a (90/0)s GFRP Laminate, *Comp. Sci. Technol.*, **24** (1985) pp. 23-31.

31. Schulte, K., Novack, H., Trautmann, H.F., & Baron, Ch.: Estimation of the Durability of Composite Materials by Means of Stiffness Reduction Under Variable Loading Conditions, *1st European Conference on Composite Materials* (ECCMI), Bordeaux, Sept. 1985.

32. O'Brien, T.K., & Reifsnider, K.L.: Fatigue Damage Evaluation Through Stiffness Measurements in Boron-Epoxy Laminates, *Journal of Composite Materials*, Vol. 15, Jan. 1985, p. 55.

33. Wavers, M., Verpoest, I., Aernoudt, E., De Meester, P.: Fatigue Damage Development in Carbon Fiber Reinforced Epoxy Composites: Correlation Between the Stiffness Degradation and the Growth of Different Damage Types, *Sixth International Conference on Composite Materials, ICCM 6*, Vol. 4, July 1987, pp. 4.114-4.128.

Table 1: 2-D Braid Architecture Parameters

Architecture		Axial Fiber Bundle Size	Braider Fiber Bundle Size	No. of Layers of Braid	Braid Angle	Unit Cell Size (mm)
Shorthand	Longhand					
LSS	$[0_{6K}/\pm45_{15K}]_{12\% \text{ axial}}$	6K	15K	5	45°	11.7 x 6.1
LLS	$[0_{36K}/\pm45_{15K}]_{46\% \text{ axial}}$	36K	15K	3	45°	10.7 x 4.6
SLL	$[0_{30K}/\pm70_{6K}]_{46\% \text{ axial}}$	30K	6K	4	70°	12.2 x 2.5
LLL	$[0_{75K}/\pm70_{15K}]_{46\% \text{ axial}}$	75K	15K	3	70°	22.4 x 4.1

Table 2: 2-D Braid Tensile Properties

Architecture		Elastic Modulus (GPa)	Ultimate Stremgth (MPa)	Ultimate Strain (%)
Shorthand	Longhand			
LSS	$[0_{6K}/\pm45_{15K}]_{12\% \text{ axial}}$	35.7 ± 1.0	370.0 ± 2.1	1.24 ± 0.05
LLS	$[0_{36K}/\pm45_{15K}]_{46\% \text{ axial}}$	74.5 ± 9.6	644.5 ± 82.7	0.91 ± 0.24
SLL	$[0_{30K}/\pm70_{6K}]_{46\% \text{ axial}}$	67.0 ± 3.9	843.5 ± 33.2	1.33 ± 0.10
LLL	$[0_{75K}/\pm70_{15K}]_{46\% \text{ axial}}$	60.5 ± 3.2	487.1 ± 16.1	0.93 ± 0.18

Table 3: 2-D Braid Compression Properties

Architecture		Elastic Modulus (GPa)	Ultimate Stremgth (MPa)	Ultimate Strain (%)
Shorthand	Longhand			
LSS	$[0_{6K}/\pm45_{15K}]_{12\% \text{ axial}}$	32.4 ± 1.0	352.8 ± 37.1	1.56 ± 0.22
LLS	$[0_{36K}/\pm45_{15K}]_{46\% \text{ axial}}$	69.6 ± 1.8	620.6 ± 16.6	1.03 ± 0.04
SLL	$[0_{30K}/\pm70_{6K}]_{46\% \text{ axial}}$	62.1 ± 0.3	502.6 ± 43.2	0.86 ± 0.08
LLL	$[0_{75K}/\pm70_{15K}]_{46\% \text{ axial}}$	63.4 ± 2.1	438.5 ± 51.7	0.77 ± 0.14

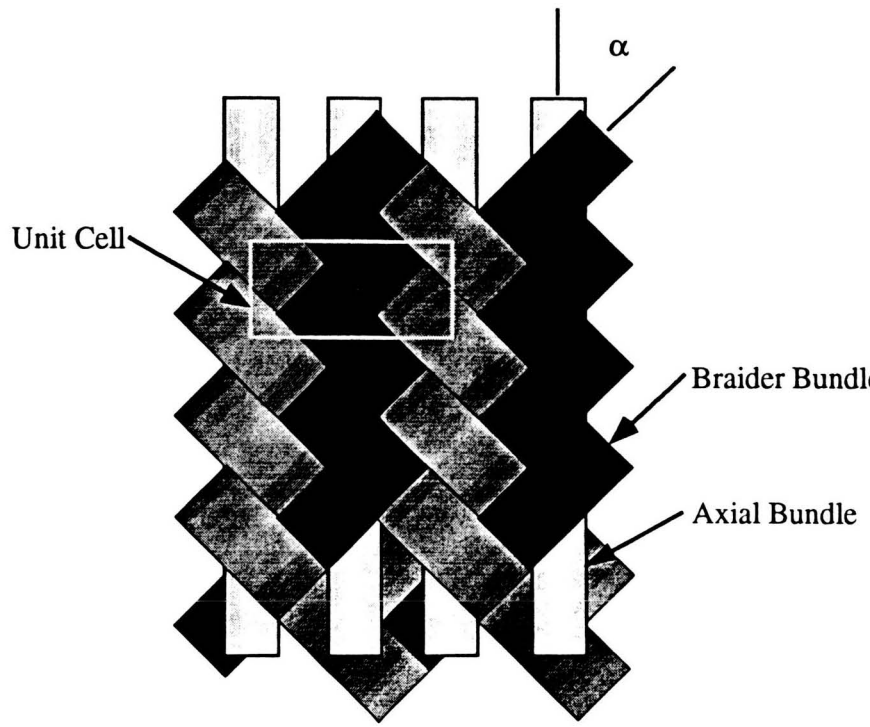

Figure 1 - Two-Dimensional Braid Schematic

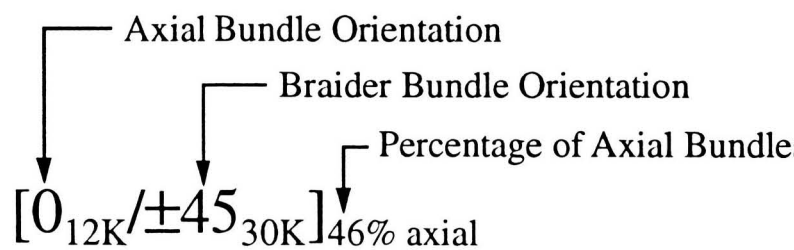

Figure 2 - Longhand Nomenclature for 2-D Braids

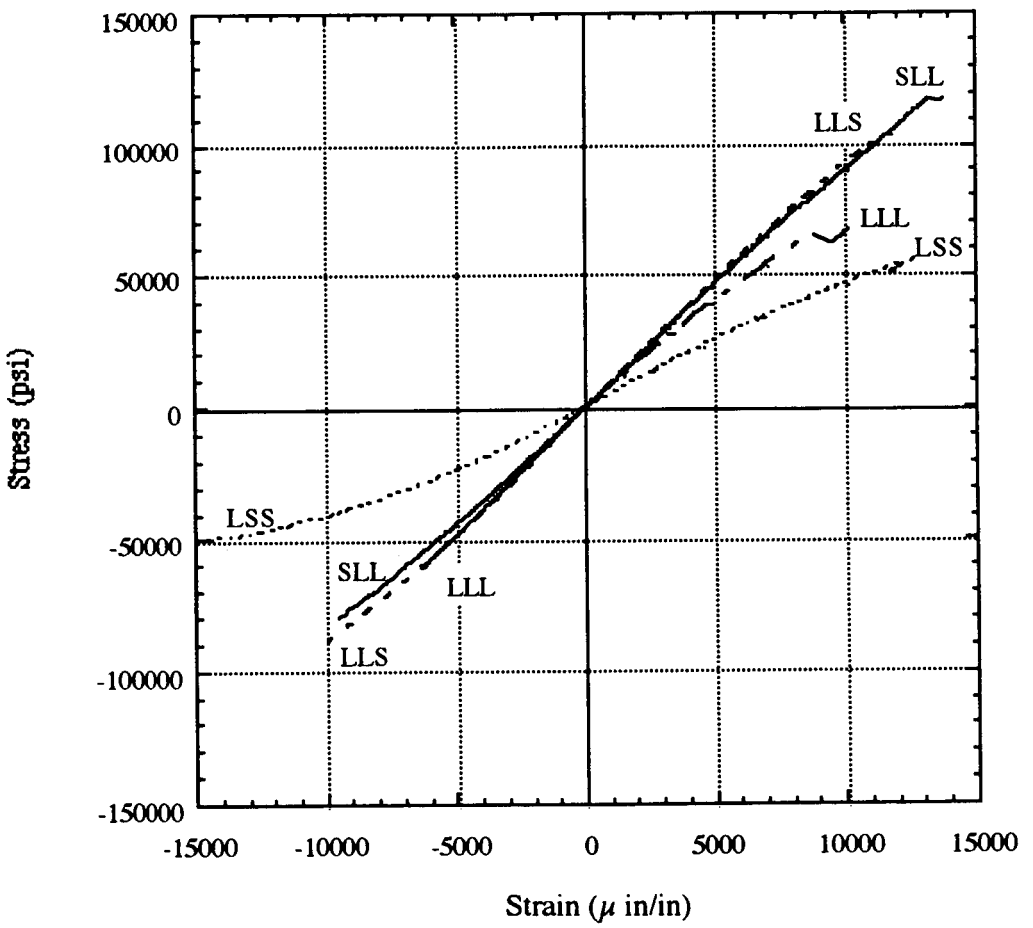

Figure 3 - Representative Stress-Strain Responses from Four Braided Composite Architectures

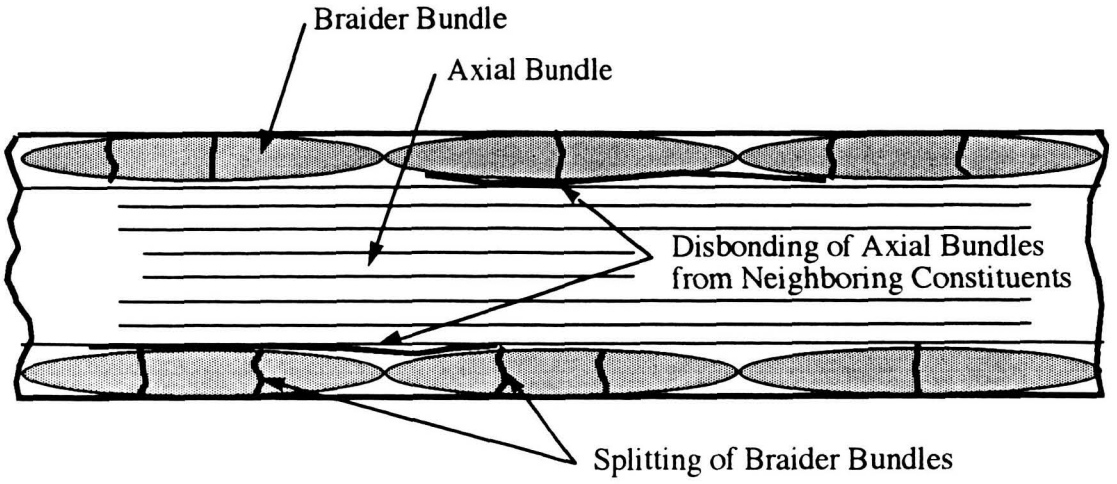

Figure 4 - Damage Mechanisms in Braided Architectures as a Result of Tensile Loading

Figure 5 - Matrix Cracking in the LSS Architecture as a Result of Compression Loading

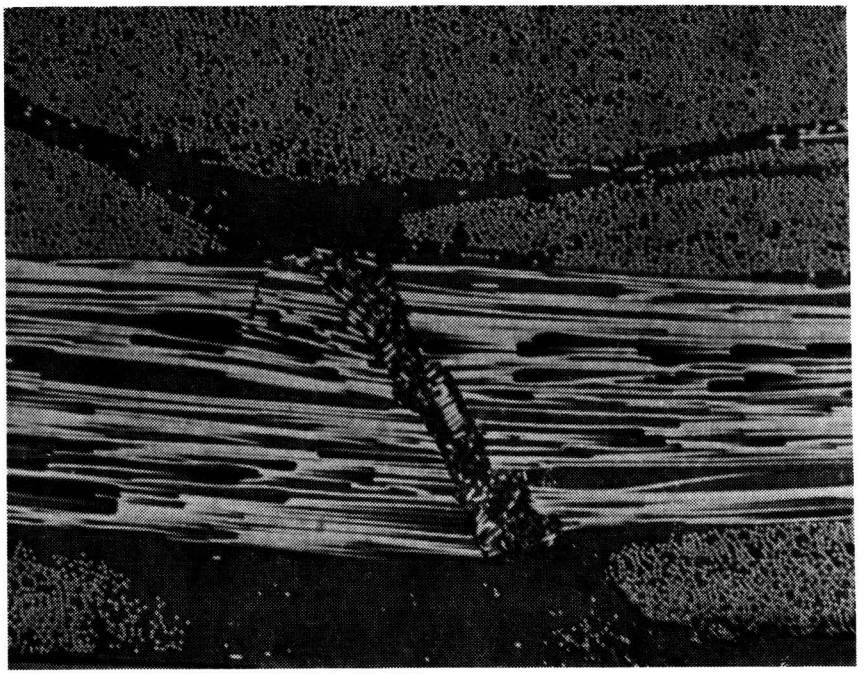

Figure 6 - Kink Band Formation in Axial Fiber Bundle Prior to Ultimate Failure

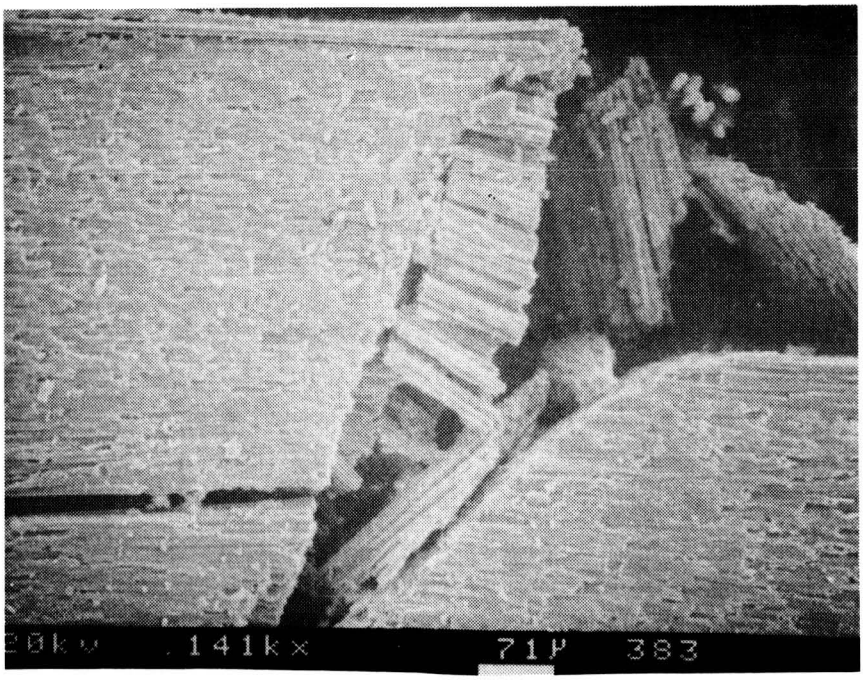

Figure 7 - Post Ultimate Failure Splitting and Remaining Kink Band Particles in an Axial Fiber Bundle

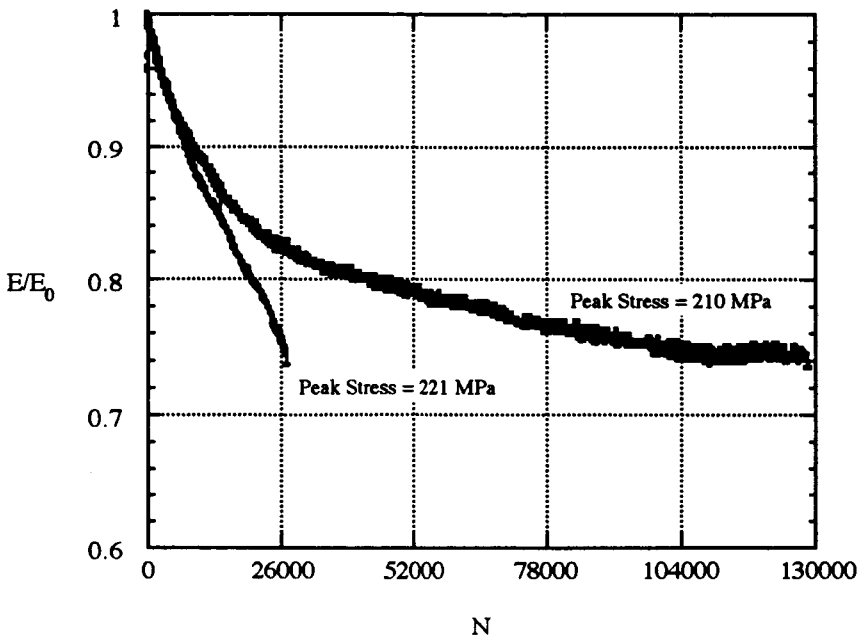

Figure 8 - Characteristic Normalized Dynamic Tangent Modulus vs. Cycle Number for the LSS Architecture

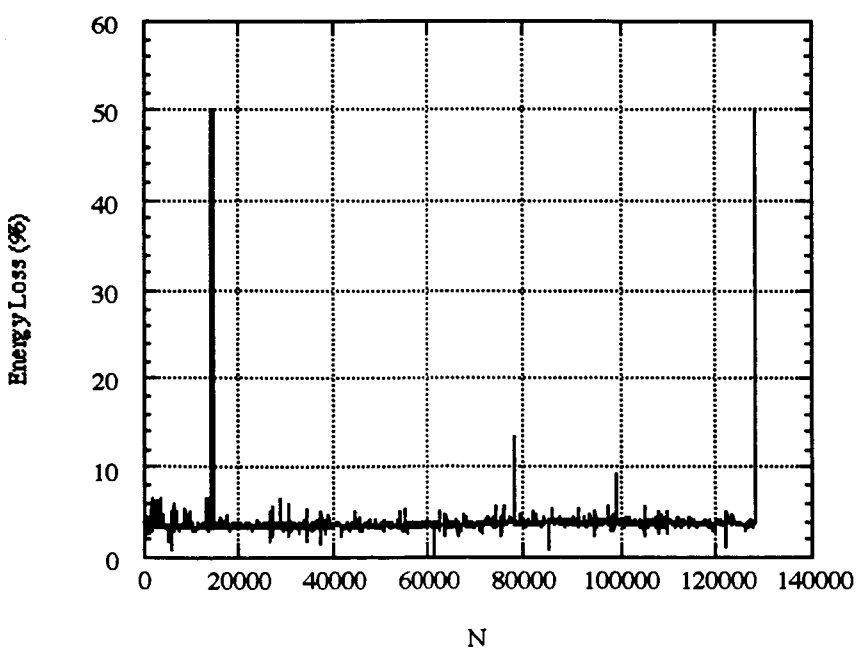

Figure 9 - Typical Energy Loss vs. Cycle Number Response

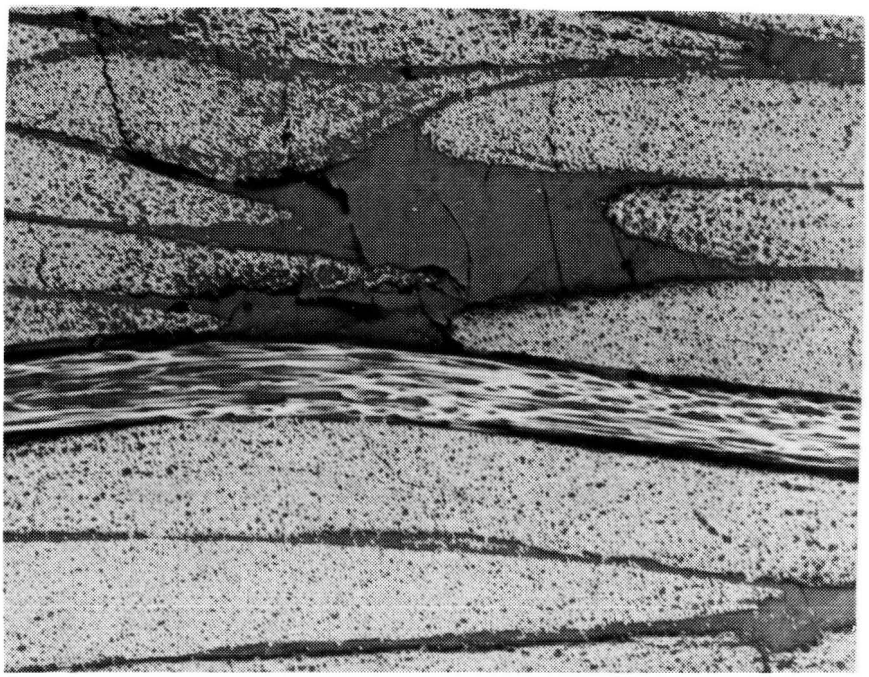

Figure 10 - Micrograph of Typical Damage Mechanisms in Tension-Tension Fatigue

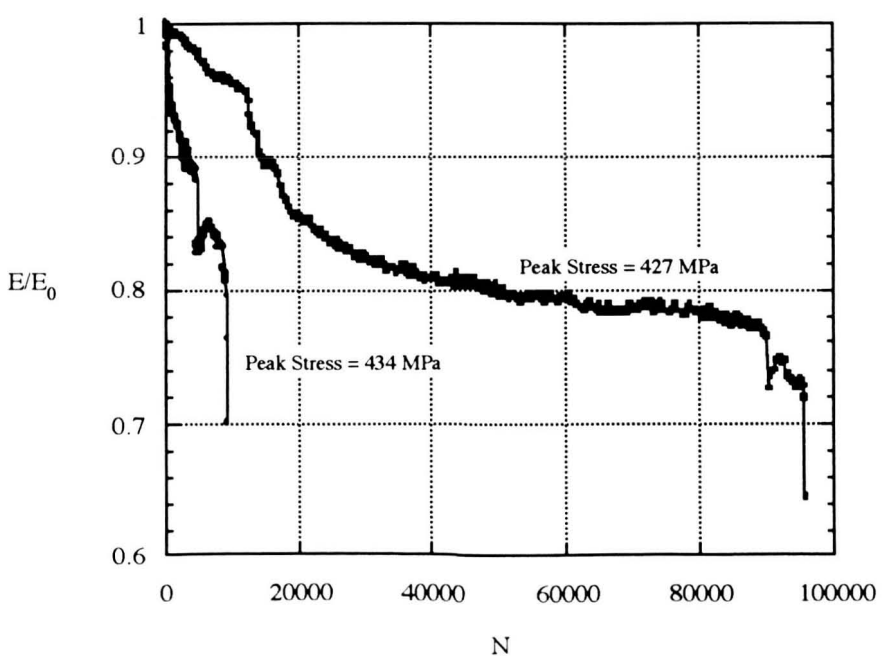

Figure 11 - Characteristic Normalized Dynamic Tangent Modulus vs. Cycle Number for the LLS Architecture

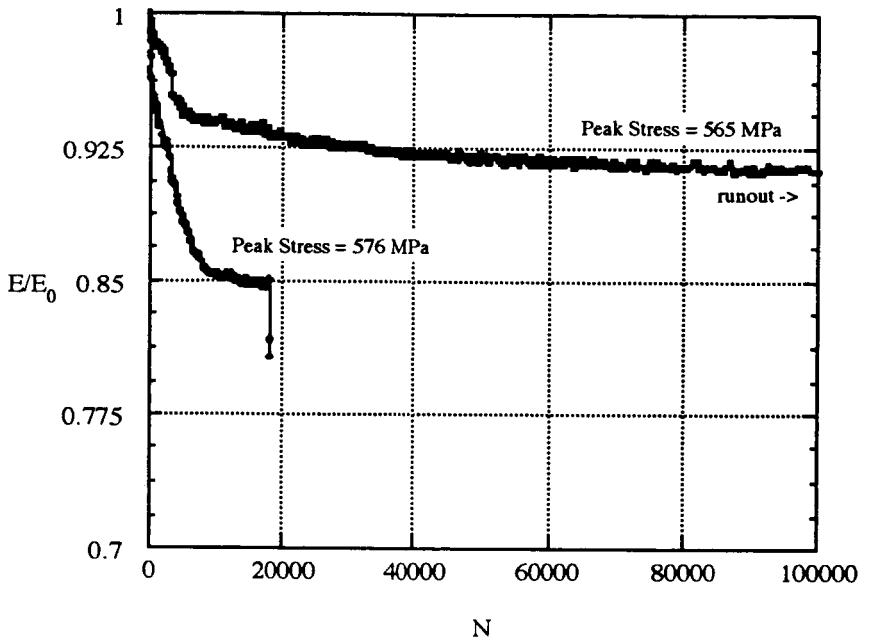

Figure 12 - Characteristic Normalized Dynamic Tangent Modulus vs. Cycle Number for the SLL Architecture

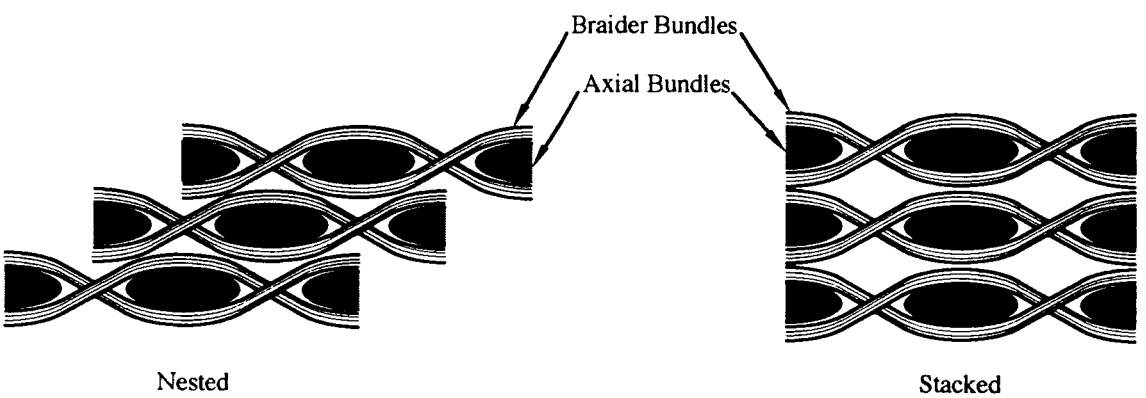

Figure 13 - Nested vs. Stacked Positions of Individual Braided Layers

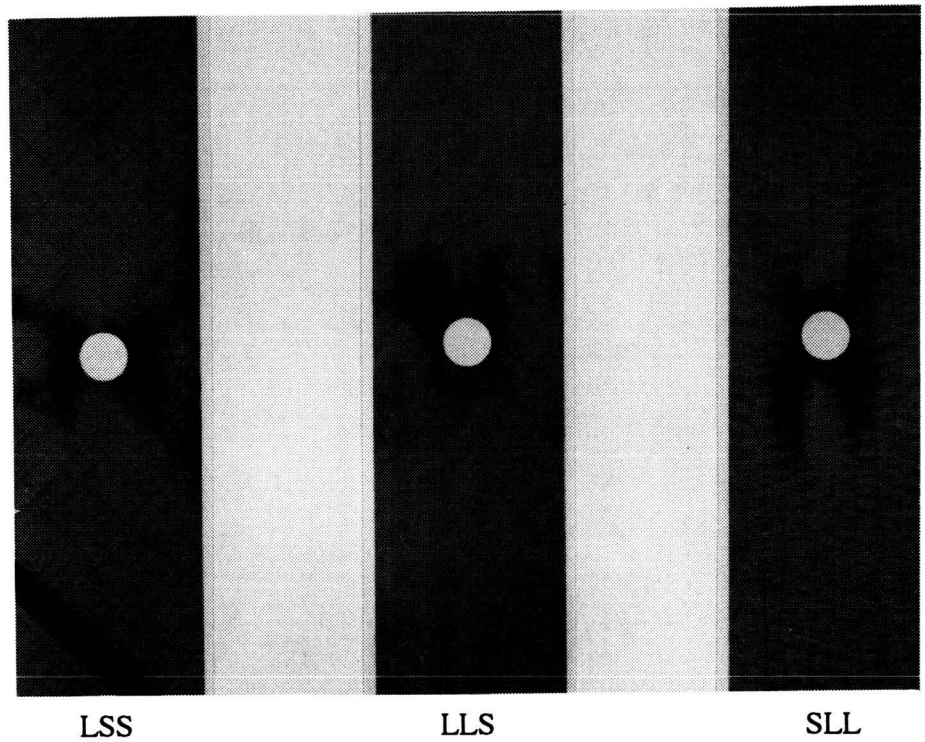

Figure 14 - X-Ray Images of Notched 2-D BraidedSpecimens
(stiffness reduction > 20%)

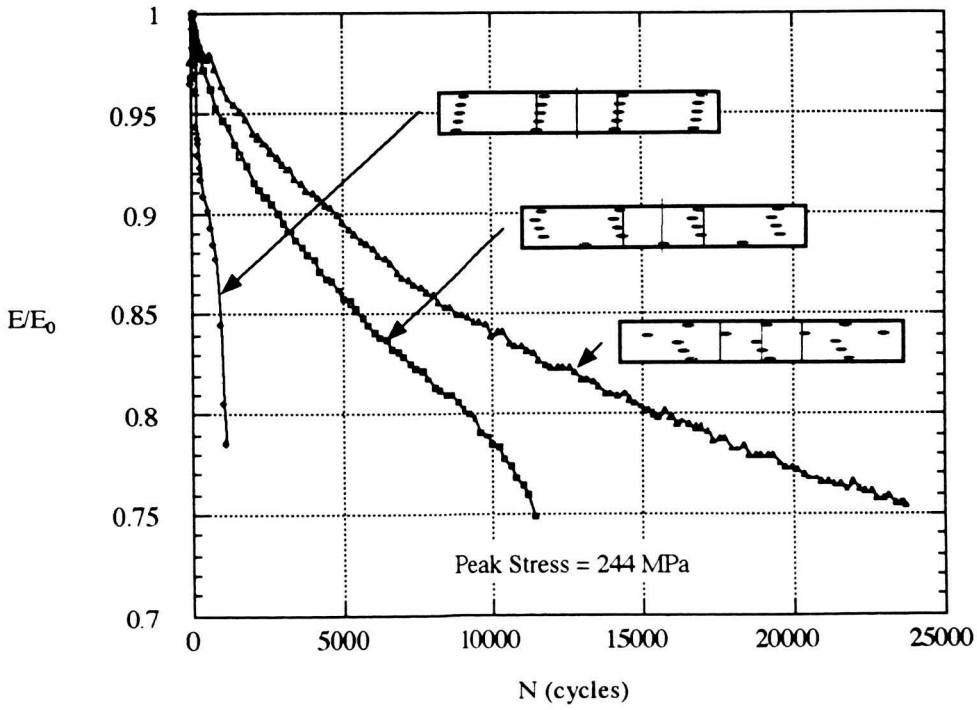

Figure 15 - Dynamic Tangent Modulus vs. Cycle Number for Three Identical Notched LSS Specimens Subjected to the same Peak Stress Level

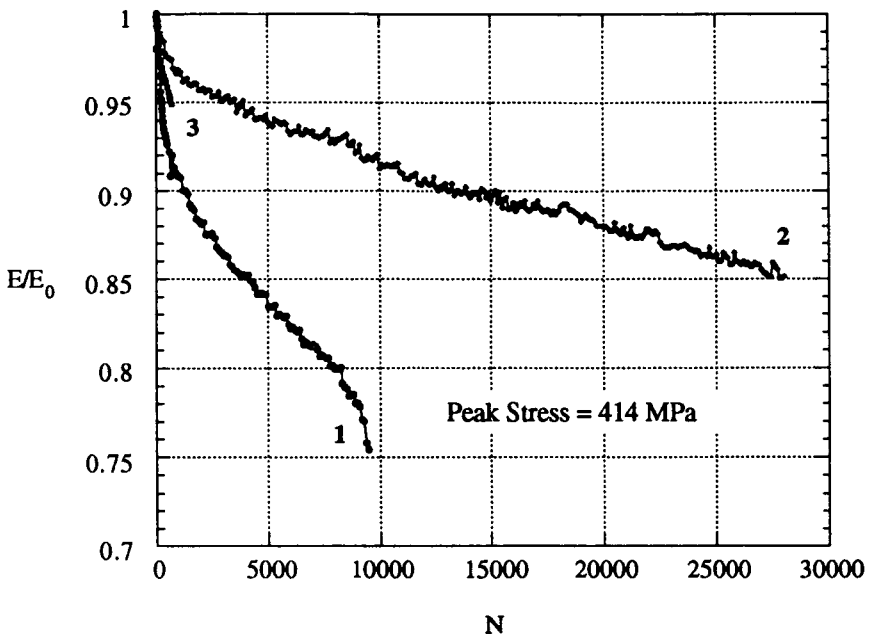

Figure 16 - Dynamic Tangent Modulus vs. Cycle Number for Three Identical Notched LLS Specimens Subjected to the same Peak Stress Level

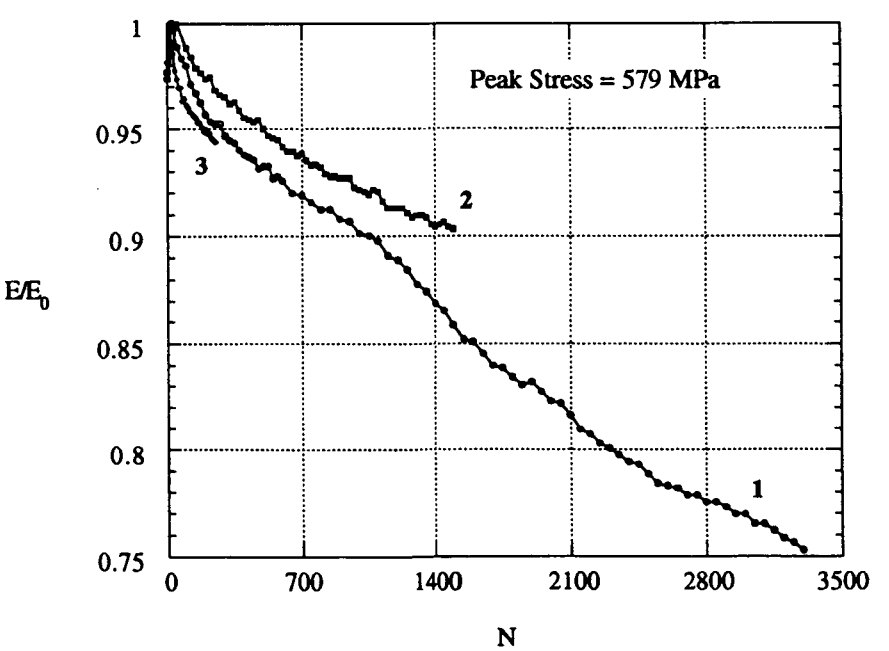

Figure 17 - Dynamic Tangent Modulus vs. Cycle Number for Three Identical Notched SLL Specimens Subjected to the same Peak Stress Level

MODELING THE PROPERTIES OF 3D WOVEN COMPOSITES

Brian N. Cox
Rockwell International Science Center
Thousand Oaks, CA

ABSTRACT

An extensive study has been completed of the internal geometry, the mechanisms of failure, and the micromechanics of local failure events in graphite/epoxy composites with three dimensional (3D) woven reinforcement. This work has led to the development of models for predicting elastic constants, strength, notch sensitivity, and fatigue life. A summary is presented here.

INTRODUCTION

The results and models summarized here are the outcome of several years work funded under NASA Langley's Advanced Composite Technology program. The subject materials of most of the experiments conducted were graphite/epoxy composites with woven 3D interlock reinforcement. The manufacture and structure of these composites are described in Refs. [1-3].

In the course of the research, guidelines were developed primarily for modeling 3D woven composites. However, many of the underlying concepts are more widely applicable to textiles in general, including 2D and 3D braids and weaves and stitched/woven or stitched/knitted materials.

The simplest model was always sought for predicting any given property that is physically correct and has the fewest unknown parameters. Specifying the degree of modeling sophistication necessary in different applications was one of the primary accomplishments.

ELASTIC REGIME

Flat or curved panels

The macroscopic elastic constants of flat or curved panels can be predicted by the simplest of all models, viz. orientation averaging calculations based on isostrain or isostress conditions. Here, "macroscopic" signifies gauge lengths at least several times any scale of the underlying fabric architecture. For most current textile composites, this means $\gtrsim$ 10 mm. A computer code called the Modified Laminate Model was developed to apply orientation averaging to the geometry of 3D interlock weaves [4]. The code includes an input parameter for waviness in nominally straight tows. Simple, analytic estimates were also provided for the extent to which waviness knocks down tow stiffness and the concomitant effects on composite elastic constants.

Analyzing Structures

Many vital potential applications of textiles involve geometrically complex structural parts, e.g. woven or braided beams, ribs, and window belts; and integrally woven or stitched skin/stiffener assemblies. To design such internally complex structures and predict their reliability, the arrangement of tows must be modeled explicitly. When

triaxial stress states exist, the isostrain or isostress assumptions of orientation averaging are likely to fail. At the same time, a very efficient formulation is necessary to deal with significant volumes of material, i.e., one with the fewest degrees of freedom permitted by the physics of the problem. A new model called the Binary Model was formulated for such applications [5].

Calibration tests using flat panels of 3D weaves indicate that for calculations in the elastic regime, stiffness parameters in the Binary Model can be specified a priori in terms of fiber and resin properties [6]. The Binary Model is now being adapted to model 3D braided engine mounting structures in ARPA's Affordable Composite Technology program[1]; to model stitched structures in aircraft wings; and to model brittle fracture and creep rupture in ceramic and intermetallic matrix composites.[2]

Effects of Irregular Geometry

Tows in textile composites are inevitably irregular [4]. The Binary Model allows Monte Carlo simulations of the effects of irregularity by permitting random initial tow offsets. Theoretical studies using the Binary Model have shown that stress variations in primary load bearing tows *due to their own waviness* are commonly much greater than those caused by local configurations of the ideal tow architecture [6]. It is inferred that detailed analysis of local stress distributions based on finite element simulations using highly refined grids to represent *geometrically ideal* unit cells are of questionable value in predicting strength. Insofar as such calculations are right, i.e., in their predictions of average stresses that are not sensitive to details of the unit cell, they could be replaced by simpler models.

MODELING UNNOTCHED STRENGTH

Compression

Extensive and detailed experimental analyses show that textile composites fail in monotonic compression by kink band formation when the external load is approximately aligned with one set of tows [3]. Kink band formation follows Argon's law: the critical stress is the ratio of the critical shear stress for large shear strains in the tow divided by the local tow misalignment angle [7]. The keys to predicting compressive strength are therefore 1) to measure the distribution of misalignment angles and 2) to predict the axial stress in a tow for a given external load.

The local axial stress can be computed by either the Modified Laminate Model of Ref. [4] or the Binary Model [5,6], depending on whether the part or reinforcement geometry implies important triaxial stress distributions (e.g., on whether the part is a nearly laminar skin or a complex shape). The misalignment *cannot* be predicted. It must be measured. *Its control in manufacture will always be a critical issue for textile composites.*

Tension

For aligned loads, tensile failure occurs by tow rupture. Tensile failure strains or the stresses in aligned fibers at peak load are fairly consistent over different composites of

---

[1] Work in collaboration with UC Santa Barbara in a Pratt and Whitney program.

[2] Joint work between Rockwell and UC Santa Barbara (in their ARPA URI) on the design of advanced, high temperature engine materials.

the fiber and resin within the same textile class. However, strengths are generally substantially reduced from those that might be expected from data for unidirectional tape laminates [3,7]. Textile processing is apparently injurious to fiber tows; and nonuniform load distribution due to random tow waviness promotes early failure in relatively straight tows [6]. Strength predictions should be based on calculations of tow stresses, e.g. via the Modified Laminate Model or the Binary Model, coupled with experimental tensile test data to calibrate tow strength and waviness effects.

MODELING FATIGUE

Compression

Compression-compression cyclic loading results in tow failure by kink band formation. A new rule for fatigue damage accumulation has been postulated, extending Argon's law by introducing a degradation rate for the critical shear flow stress [9]. A procedure has also been established for deducing unknown fatigue parameters from load-life data [9]. Given this calibration, fatigue life can be predicted for general tow arrangements by computing the local axial tow stress via the Modified Laminate Model or the Binary Model, as applicable; and combining this with distributions of measured misalignment angles. From these data, the expected number of kink bands in a critical structure after N cycles can be predicted. The critical number of kink bands for failure of the part should be determined by calibrating experiments.

Tension-Compression Fatigue

Experiments of 3D interlock weaves show that most fatigue damage occurs on the compressive load cycle [10]. Empirical laws for the moderate but significant effects of the tensile load cycle await more test data.

MODELING NOTCHED STRENGTH

Predictions of ultimate strength when a notch exists should be based on a cohesive zone model. Damage emanates from any stress concentrator as a band of ruptured tows and other nonlinear effects. The critical material property for the cohesive zone model is the relation p(u) between the tractions across the band and the displacement discontinuity it introduces. If p(u) is known, then damage propagation, strength, fracture toughness, and specimen size and shape effects can be computed by now standard methods for solving line spring, bridged crack models by integral equation formulations (e.g. [11]) or using finite element methods. There are two viable approaches to determining the material property p(u). It can be measured directly via tensile tests, as in Ref. [8]; or it can be deduced from crack growth and/or notch sensitivity data for some set of standard specimens. In the latter method, p(u) could conveniently be expressed in parametric form. Key parameters are p_{max}, the maximum value of p, which determines unnotched strength; $W_f = 2\int pdu$, the work of fracture for a cohesive zone in the steady state or small scale bridging limit (e.g. [12-15]); and u_c, the critical opening displacement at which p vanishes. Other details of the shape of p(u) may prove to be of minor significance.

Reference [8] warns of considerable variance in measurements of p(u) for different specimens cut from the same composite panel. Randomness in p(u) will be reflected in randomness in notched strength. A viable approach would be to establish distributions for parameters such as W_f, p_{max}, and u_c; and then compute distributions for notched strength.

SUMMARY

Graphite/epoxy composites with woven 3D reinforcement possess remarkable properties. In stiffness and strength, they are not greatly inferior to 0°/90° tape laminates with comparable proportions of fibers in the 0° and 90° directions. They have excellent delamination resistance, provided the through-thickness reinforcement is not severely crimped during processing [3]. Fatigue damage accumulates mainly in the compressive load cycle and reduces allowable loads by only ~ 20% over 10^6 cycles [9,10]. Above all, their work of fracture and notch insensitivity are an order of magnitude higher than for tape laminates; and in fact far higher than for any other class of engineering materials [3,8]. To allow the exploitation of these excellent properties, design models have now been formulated for stiffness, strength, fatigue life, and notch sensitivity.

ACKNOWLEDGMENTS

Work funded by NASA Langley Research Center under the Advanced Composites Technology Program; contract numbers NAS1-18840 and NAS1-19243; contract monitor Dr. C.C. Poe.

1. B.N. Cox, M.S. Dadkhah, R.V. Inman, W.L. Morris and J. Zupon, "Mechanisms of Compressive Failure in 3D Composites," *Acta Metall. Mater.*, 40 3285–98 (1992).

2. A. Falcone, H. Dursch, K. Nelson, and W. Avery, "Resin Transfer Molding of Textile Composites," NASA Contractor Report CR 191505, July, 1993.

3. B.N. Cox, M.S. Dadkhah, W.L. Morris and J.G. Flintoff, "Failure Mechanisms of 3D Woven Composites in Tension, Compression, and Bending," *Acta Metall. Mater.*, 42 3967-84 (1994).

4. B.N. Cox and M.S. Dadkhah, "The Macroscopic Elasticity of 3D Woven Composites," *J. Mater. Sci.*, in press.

5. B.N. Cox, W.C. Carter, and N.A. Fleck, "A Binary Model of Textile Composites. I Formulation," *Acta Metall. Mater.*, 42 3463-79 (1994).

6. J. Xu, B.N. Cox, M.A. McGlockton, and W.C. Carter, "A Binary Model of Textile Composites: II The Elastic Regime," *Acta Metall. Mater.*, in press.

7. A.S. Argon, *Fracture of Composites, Treatise of Materials Science and Technology,* Vol. 1, Academic Press. New York (1972).

8. B.N. Cox, M.S. Dadkhah, and W.L. Morris, "On the Tensile Failure of Some 3D Woven Composites," submitted to *J. Mater. Sci.*

9. M.S. Dadkhah, B.N. Cox, and W.L. Morris, "Compression-Compression Fatigue of 3D Woven Composites," *Acta Metall. Mater.*, in press.

10. "Failure Models for Textile Composites," Final Report on NASA Contract No. NAS1-19243, Rockwell Science Center, January, 1994.

11. B.N. Cox and D.B. Marshall, "Stable and Unstable Solutions for Bridged Cracks in Various Specimens," *Acta Metall. Mater.* 39, 579-89 (1991).

12. B. Budiansky, J.W. Hutchinson, and A.G. Evans, "Matrix Fracture in Fiber-Reinforced Ceramics," *J. Mech. Phys. Solids* 34, 167 (1986).

13. L.R.F. Rose, "Crack Reinforcement by Distributed Springs," *J. Mech. Phys. Solids* 34, 383 (1987).

14. G. Bao and Z. Suo, "Remarks on Crack Bridging Concepts," *Appl. Mech. Review* 45 (1992) 355-66.

15. B.N. Cox and D.B. Marshall, "Concepts for Bridged Cracks in Fracture and Fatigue," *Acta Metall. Mater.*, 42 (1994) 341-63.

EVALUATION OF BRAIDED STIFFENER CONCEPTS FOR TRANSPORT AIRCRAFT WING STRUCTURE APPLICATIONS

Jerry W. Deaton and H. Benson Dexter
NASA Langley Research Center
Hampton, Virginia 23681-0001

Alan Markus and Kim Rohwer
McDonnell Douglas Aerospace
Long Beach, California 90846-0001

INTRODUCTION

Braided composite materials have potential for application in aircraft structures. Stiffeners, wing spars, floor beams, and fuselage frames are examples where braided composites could find application if cost effective processing and damage requirements are met. Braiding is an automated process for obtaining near-net shape preforms for fabrication of components for structural applications. Previous test results on braided composite materials obtained at NASA Langley indicate that damage tolerance requirements can be met for some applications. In addition, the braiding industry is taking steps to increase the material through-put to be more competitive with other preform fabrication processes.

Data are presented on the compressive behavior of three braided stiffener preform fabric constructions as determined from individual stiffener crippling test and three stiffener wide panel tests. Stiffener and panel fabrication are described and compression data presented for specimens tested with and without impact damage. In addition, data are also presented on the compressive behavior of the stitched stiffener preform construction currently being used by McDonnell Douglas Aerospace in the NASA ACT wing development program.

OBJECTIVE AND APPROACH

Figure 1 outlines the objective and approach used to characterize the braided stiffener concepts for application to transport aircraft wing structure reported herein. Two braided T-stiffener architectures were selected for evaluation; a braided/woven configuration of [±45°/0°] and a 100% braid configuration of [±53°/0°]. These architectures were selected as they compare closely with the stitched Saerbeck warp knit material configuration currently being evaluated by McDonnell Douglas Aerospace in their stitched wing concept under the NASA Advanced Composites Technology Program. The materials selected, preform and panel fabrication, and compression property characterizations are discussed in more detail.

OBJECTIVE AND APPROACH

Objective:

Assess potential of braided stiffeners for stitched/resin transfer molded aircraft wing structures

Approach:

- **Braided stiffener selection**
  - **Architectures**
  - **Fiber**
  - **Resin**
- **Fabrication of panels**
- **Evaluation of panel compression properties**

Figure 1. Objective and approach.

COST COMPARISON OF BRAIDED VS STITCHED SAERBECK STIFFENERS

The impetus for this study is the potential cost saving by going to the braided stiffener concept compared to the stitched Saerbeck warp knit material as shown in figure 2. The figure indicates a cost savings of about 15 percent for straight braided stiffeners can be obtained if this concept can meet the design requirements. The data shown assumes a production run but no capital equipment for producing either type of stiffeners. Curved braided stiffeners will cost more than straight braided stiffeners but they can be braided to fit wing curvature whereas the stitched Saerbeck warp knit material concept may not conform to wing curvature without buckling. The remainder of this paper will address the materials, preform and panel fabrication, and compression properties of braided stiffener panels.

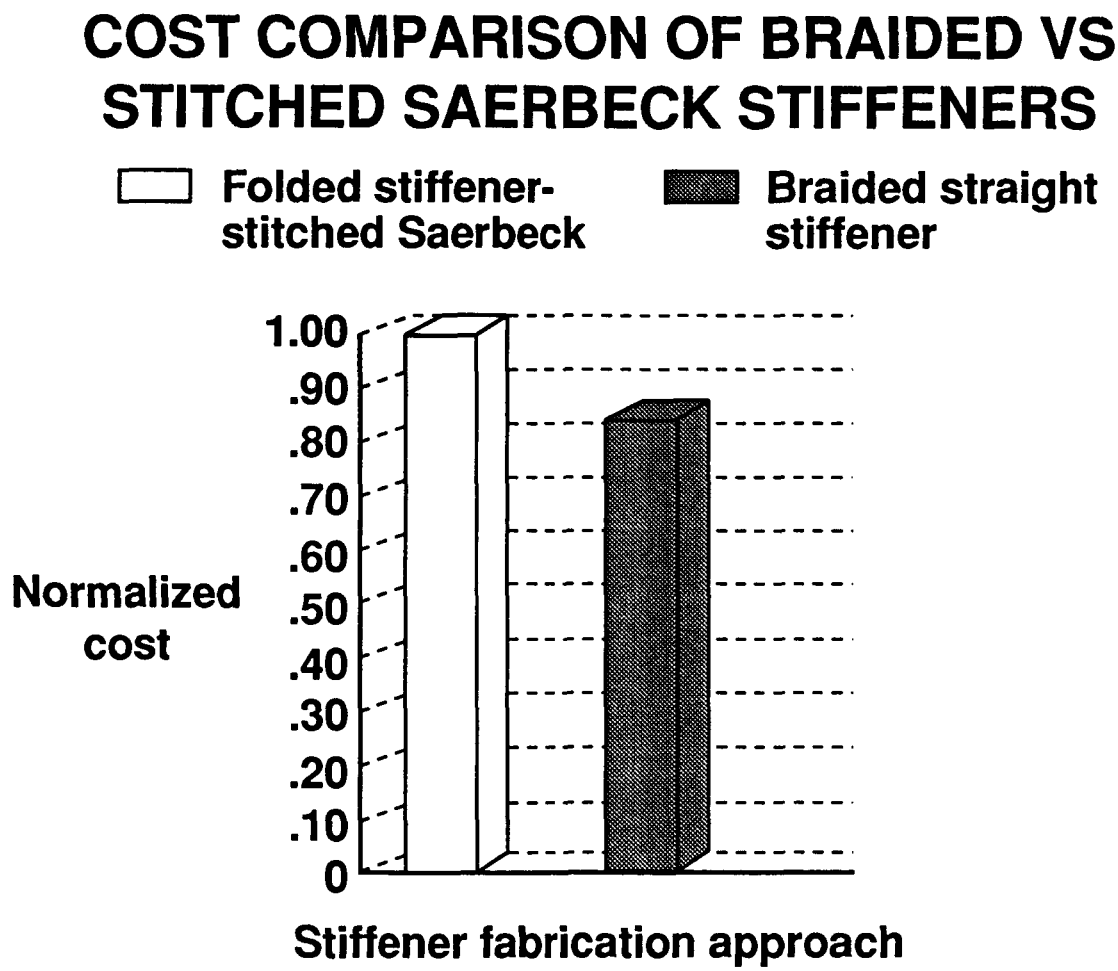

Figure 2. Cost comparison of braided vs stitched Saerbeck stiffeners.

Figure 3 shows the desired cross section of the braided T-stiffeners after resin film infusion (RFI) processing into panels. The dimensions shown are nominal values for processed stitched Saerbeck warp knit stiffeners which the braided stiffeners could replace. Braided stiffeners of these dimensions would allow use of existing tooling for processing into compression panels for property evaluation.

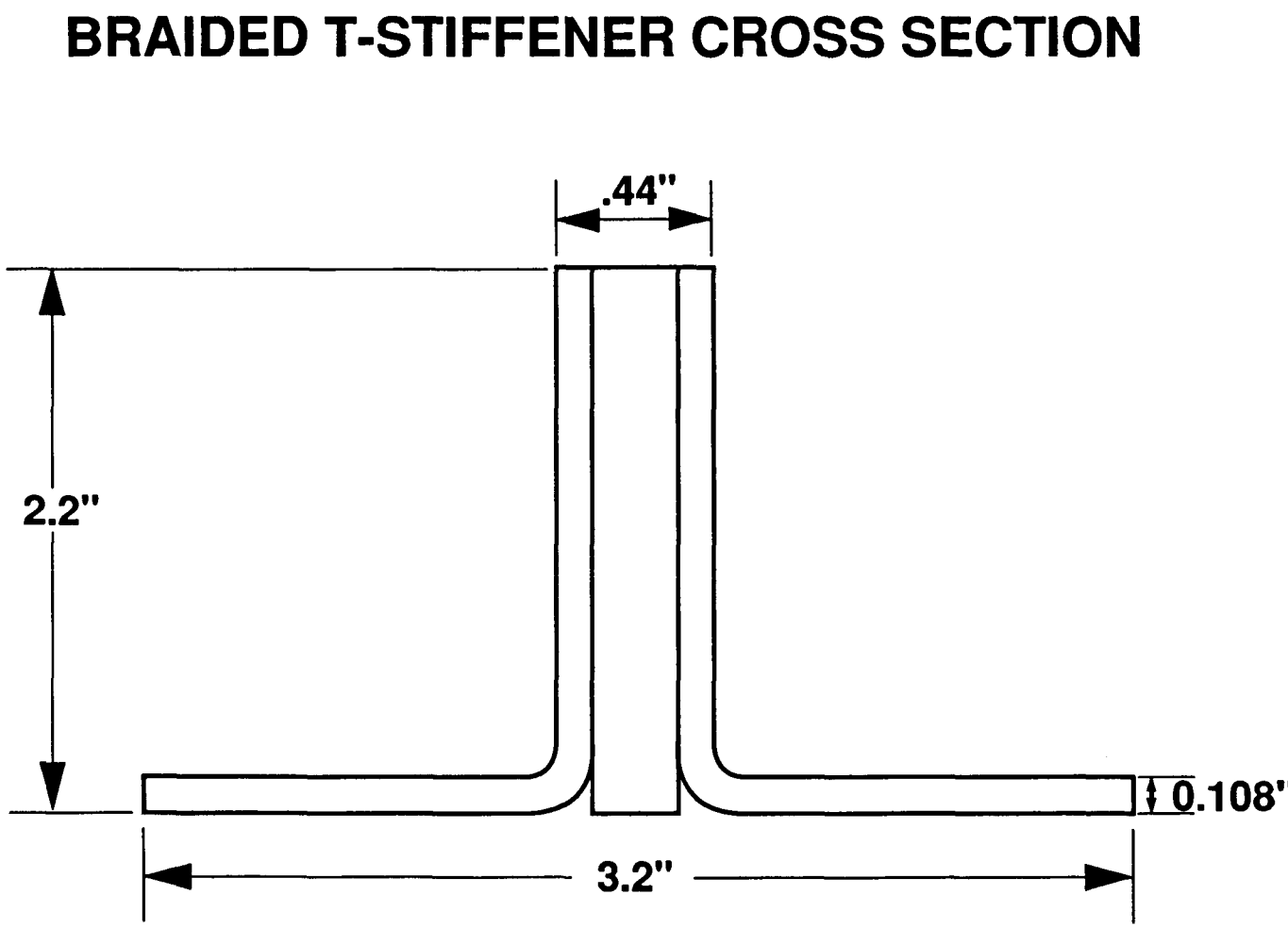

Figure 3. Braided T-stiffener cross section.

BRAIDED T-STIFFENER PREFORM ARCHITECTURES

Two different architectures are shown in figure 4 employing braids to produce stiffeners equivalent to the stitched Saerbeck warp knit stiffener concept currently being proposed as baseline under the NASA ACT wing development program with McDonnell Douglas Aerospace. The braided/woven configuration shown on the left consists of triaxially braided tubes and woven fabric which are stitched together in the blade area of the T-stiffener. The triaxially braided tubes were fabricated from AS4 6K graphite fiber in the ±45° direction and either AS4 12K or IM7 12K/2E graphite fiber in the 0° direction. The AS4 axial fiber is used in stiffeners for the compression cover of the wing whereas the IM7 fiber is used in stiffeners for the tension cover. The plain weave fabric was woven with AS4 6K graphite fiber and had the same yarn count in the warp and fill directions. The tubes were braided on mandrels whose circumferences equaled the height of the blade plus the flange, for tube #1, and the height of the blade, for tube #2. Similarly, the fabrics were woven to widths equal to the height of the stiffener blade plus the flange width and a width equal to the blade height. Thus, there are no lose fibers in this configuration, except at the cut ends of the stiffeners where the fill yarns of the woven fabrics may unravel. However, since the woven fabric is sandwiched between the braided components and the blade of the T-stiffener is stitched, unraveling should not be a problem. The configuration shown on the right consists of just braided tubes which were braided on mandrels similar to that just described for the braided/woven configuration. These triaxially braided tubes were fabricated from AS4 6K graphite fiber in the ±53° direction and either AS4 18K or IM7 12K/3E graphite fiber in the 0° direction. Again, the AS4 fiber is used in stiffeners for the compression cover of the wing and the IM7 fiber is used in stiffeners for the tension cover. Both of these configurations were evaluated in combination with the stitched Saerbeck warp knit skin material.

BRAIDED T-STIFFENER PREFORM ARCHITECTURES

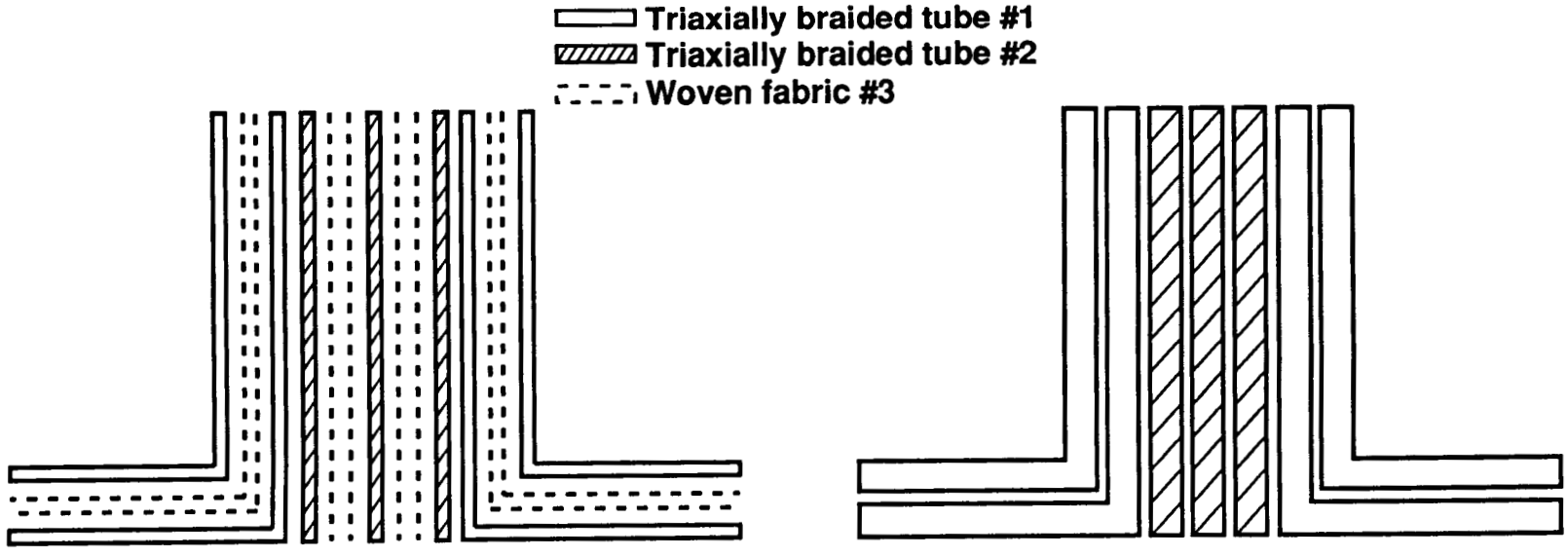

Braided/woven

- Bias fiber - AS4 6K
- Axial fiber - AS4 12K
  - IM7 12K/2E
- Braid angle ±45°/0°
- Fabric - AS4 6K, 10.5/in. warp and fill

100% braided

- Bias fiber - AS4 6K
- Axial fiber - AS4 18K
  - IM7 12K/3E
- Braid angle ±53°/0°

Figure 4. Braided T-stiffener preform architectures.

SCHEMATIC OF SAERBECK/LIBA MULTIAXIAL WARP KNITTING MACHINE

Saerbeck produces multiaxial warp knit fabrics on a machine developed by Liba, a German-owned company. Figure 5 shows a schematic of the machine which can produce fabric with up to 8 plies, each of which can be oriented 0° or ±30° through 90°. Fabrics can be produced up to 100 inches wide at 50 lineal yards per hour. Yarn carriers with multiple tows traverse the width of the fabric and place tows around pins that are attached to a moving belt. The tow size and the number of tows per inch determine the ply areal weight. Different tow sizes can be used in each direction if desired. Figure 5 illustrates 90° and ±45° tows being laid down by the yarn carriers moving along fixed guides. The 0° tows are laid down off a beam just prior to the knitting head, which can use either a chain of tricot stitch to knit these 4 plies into a stack. This type of machine was used to produce 7-ply material (+45°, -45°, 0°, 90°) for fabricating stitched tension and compression skins to attach the braided stiffeners to assess their CAI performance. Tow sizes and knitting parameters were varied to obtain nominal percentages of fibers in the 0°, ±45°, and 90° directions of 44/44/12, respectively. The 0° direction contains 12K fiber tows. The ±45° directions each contain 6K fiber tows and the 90° direction contains 3K fiber tows. The compression skin material uses all AS4 graphite fiber and the tension skin material uses AS4 fibers in the ±45° and 90° directions and IM7 fiber is the 0° direction.

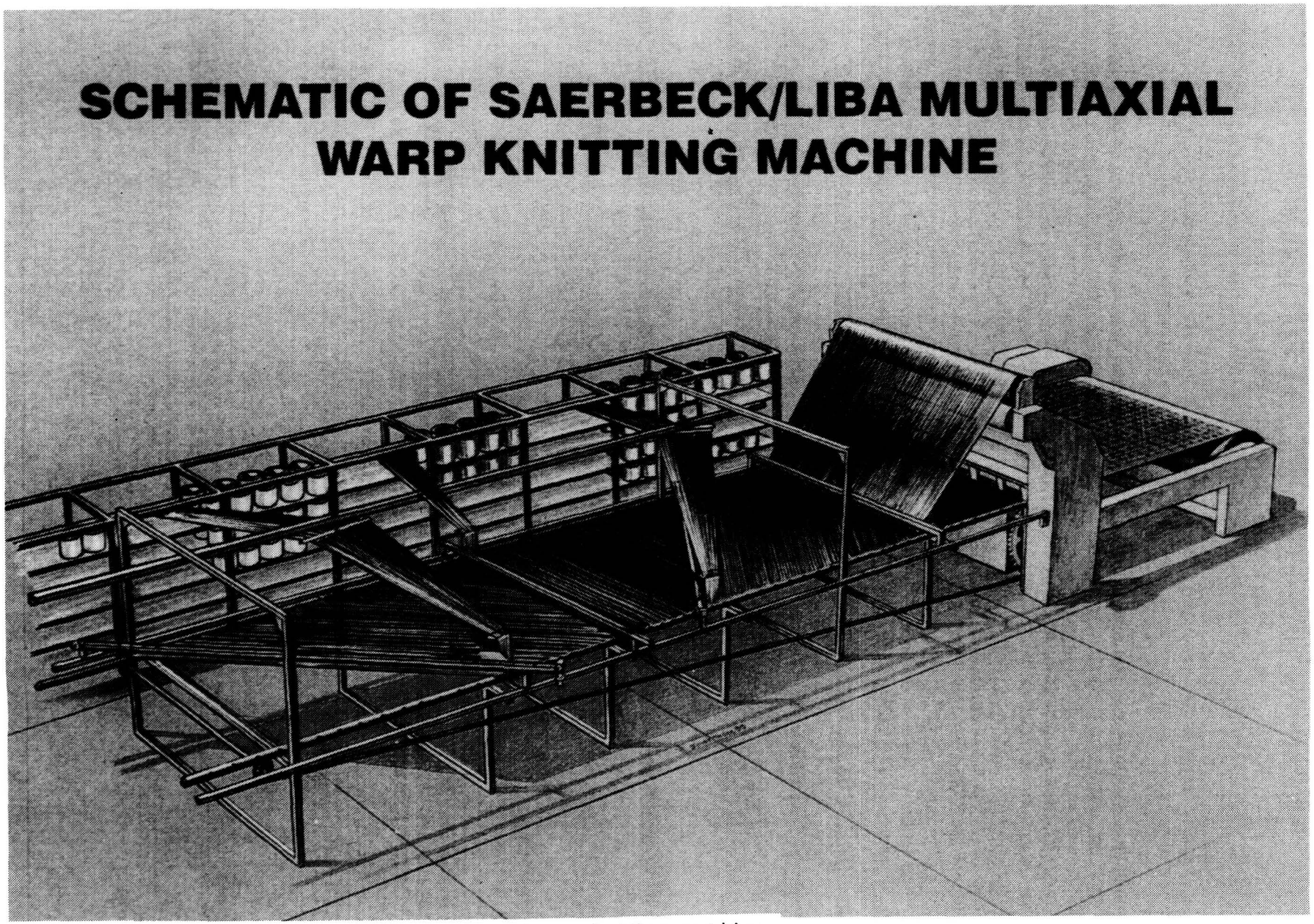

Figure 5. Schematic of Saerbeck/Liba multiaxial warp knitting machine.

COMPUTER CONTROLLED SINGLE-NEEDLE STITCHING MACHINE

Figure 6 shows the computer controlled single-needle stitching machine installed in the Advanced Composites Section, Fabrication Division, NASA- Langley. The machine is capable of stitching dry high-performance textile materials over an area of 4 ft by 6 ft and thicknesses greater than 1.5 inches. The machine uses a lock stitch and can be programmed to stitch in any direction (including curves) within the 4 ft by 6 ft area. Stitch pitch can be varied from 4 to 14 per inch and stitching speed can be varied from 40 to 200 stitches per minute. Both stitch pitch and stitching speed can be changed within a stitching program by a key stroke on the control keyboard. The machine is capable of stitching with a wide variety of needle and bobbin threads, such as, polyester, nylon Kevlar, and carbon. Also, different thread sizes can be used in combination for the needle and bobbin. The machine was used to stitch the tension and compression skins and the attachment of the braided stiffeners to produce 3-stiffener wide preforms for this investigation.

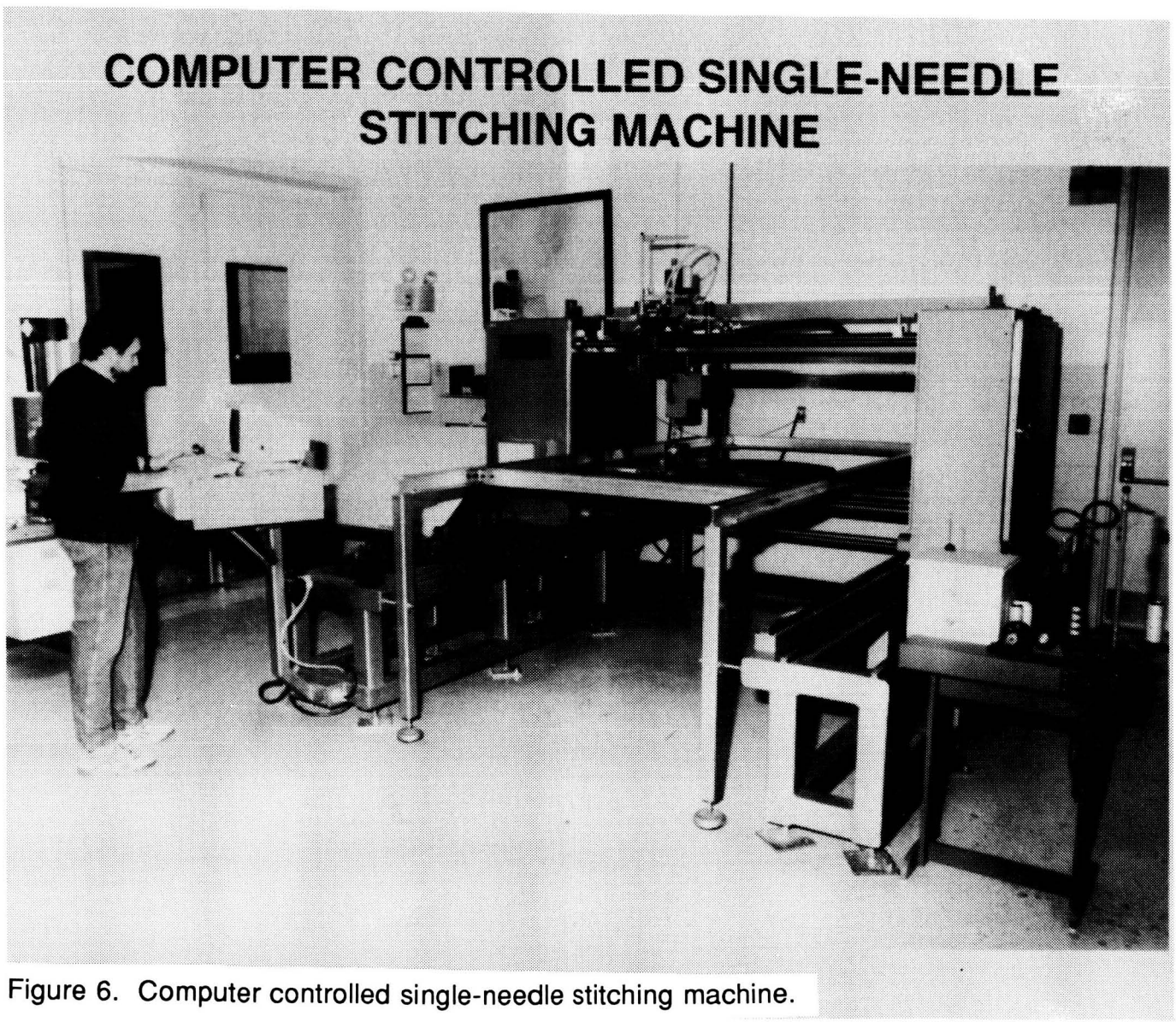

Figure 6. Computer controlled single-needle stitching machine.

STITCHED MULTIAXIAL WARP KNITTED TENSION SKIN

A completed stitched tension skin is shown in figure 7. The skin consists of 6 stacks of the 7-layer Saerbeck material with the IM7 fiber in the 0° direction previously described stitched together using a stitch pitch of 8 and a row spacing of 0.5 inch. The stitch area was 2 ft wide and 4 ft long. The needle thread was 1600 denier Kevlar (400/1x4) with a low-melt nylon coating and the bobbin thread was 400 denier Kevlar (200/1x2).

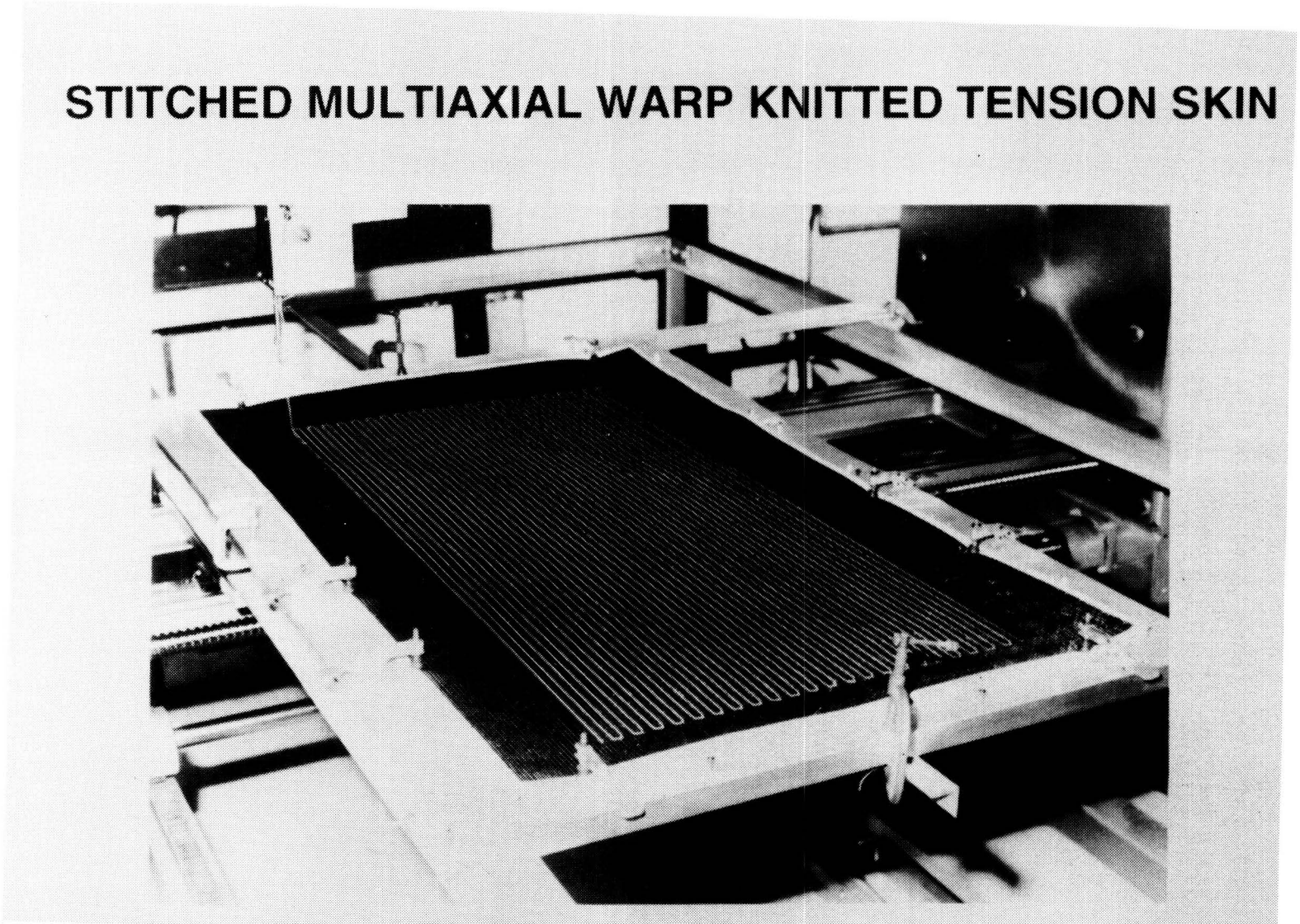

Figure 7. Stitched multiaxial warp knitted tension skin.

STITCHED MULTIAXIAL WARP KNITTED COMPRESSION SKIN

Figure 8 shows a completed stitched compression skin. It consists of 6 stacks of the 7-layer all AS4 Saerbeck warp knit material. The stitching parameters were; stitch pitch of 8, and a row spacing of 0.2 inch. The needle and bobbin threads are the same size as used for the tension skin, 1600 denier for the needle thread and 400 denier for the bobbin thread. The overall stitch area was also 2 ft by 4 ft, however, the skin is not stitched in the area where the stiffener flanges are to be stitched to the skin. Also shown in figure 8 is a 4 foot length of braided T-stiffener along with the stiffener locating tool which aids in stitching the stiffener to the skin.

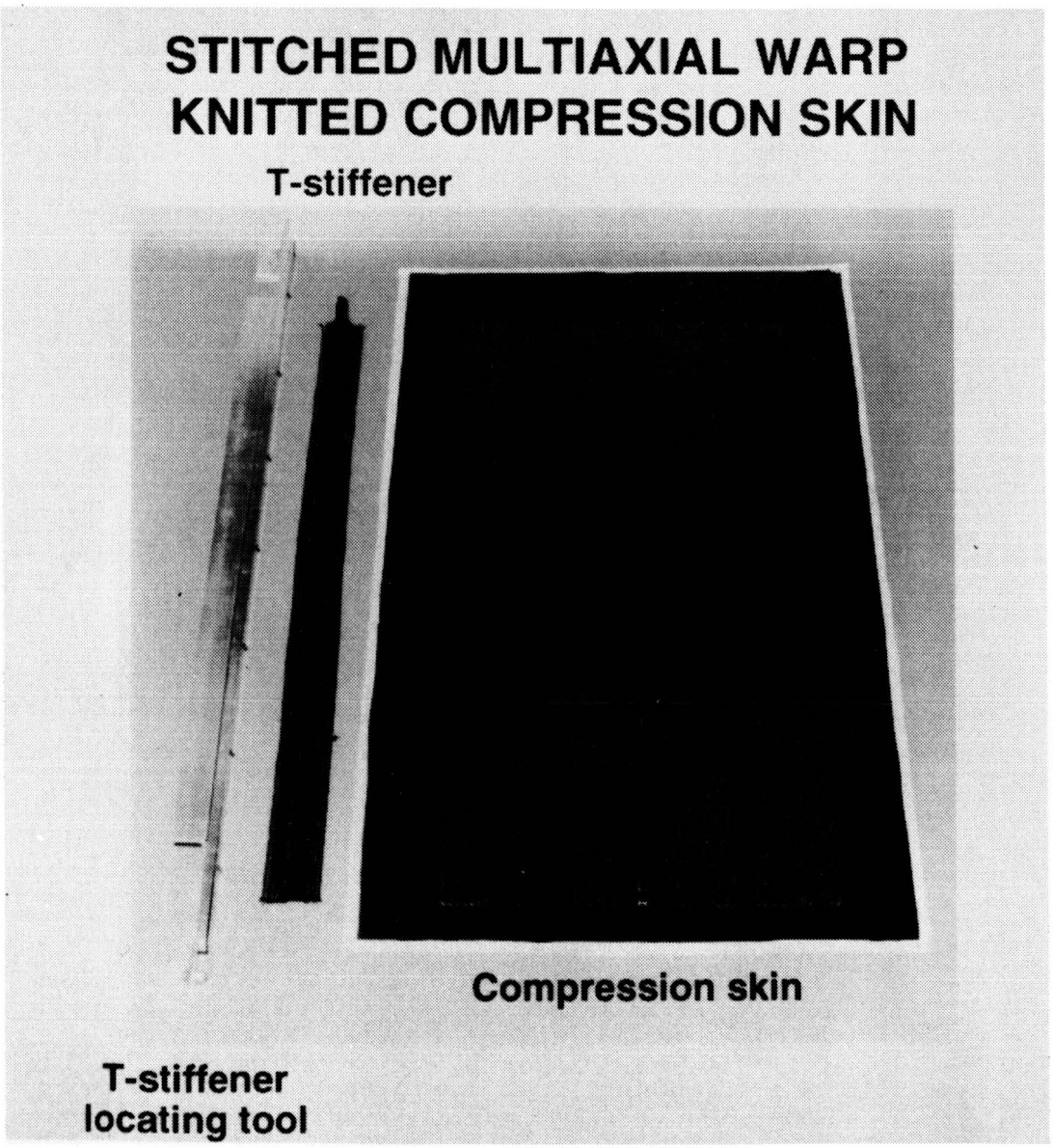

Figure 8. Stitched multiaxial warp knitted compression skin.

STITCHED MULTIAXIAL WARP KNITTED PREFORMS WITH BRAIDED/WOVEN STIFFENERS

Completed compression and tension skin preforms with stiffeners attached are shown in figure 9. The overall sizes are the same and both preforms have a 7-inch stiffener spacing. The basic differences in the two preforms is the stitching parameters used to assemble the skins and the use of the IM7 graphite fiber in the 0° direction of both the skin material and stiffener in the tension preform. The blade of the stiffener was inserted into the T-stiffener locating tool shown in figure 8 and placed over locating pins at each end of the stitching frame and one flange was stitched to the skin using the same stitching parameters for fabricating the compression skin preform. After one stiffener flange was stitched to the skin, the tool was removed and turned, end for end, and placed over the stiffener blade and the other flange was stitched to the skin.

Figure 9. Stitched multiaxial warp knitted preforms with braided/woven stiffeners.

TOOLING FOR RESIN INFUSION OF SAERBECK SKIN/BRAIDED 3-STIFFENER PREFORM

McDonnell Douglas Aerospace uses the tooling method shown in figure 10 to mold 3-stiffener panels in an autoclave using Hercules 3501-6 resin. This approach uses hard mandrels to support the stiffener blades. Air and resin vent holes are at the top of each stiffener. The edges of the assembly are sealed with tape to prevent resin leakage while the preform debulks and resin flows. The accurately located stiffeners in conjunction with the aluminum mandrels and silicone pressure pads give uniform compaction and the desired dimensions upon cure. As with flat panels, the resin film infusion (RFI) flow path is through the thickness of the skin. However, the flow becomes two-dimensional at the base of the stiffeners, then becomes in-plane with respect to the fibers in the stiffener blade. Research conducted by Virginia Polytechnic Institute and the College of William and Mary using a computer model and dielectric sensors arrived at an autoclave cure cycle that resulted in full infusion for panels fabricated for this investigation, as determined from ultrasonic C-scans. Panel sizes were 24 inches long and 22 inches wide for the RFI processing. Four panels of this size for each braided stiffener architecture were processed by McDonnell Douglas Aerospace for this joint program with NASA-Langley.

TOOLING FOR RESIN INFUSION OF SAERBECK SKIN/ BRAIDED 3-STIFFENER PREFORM

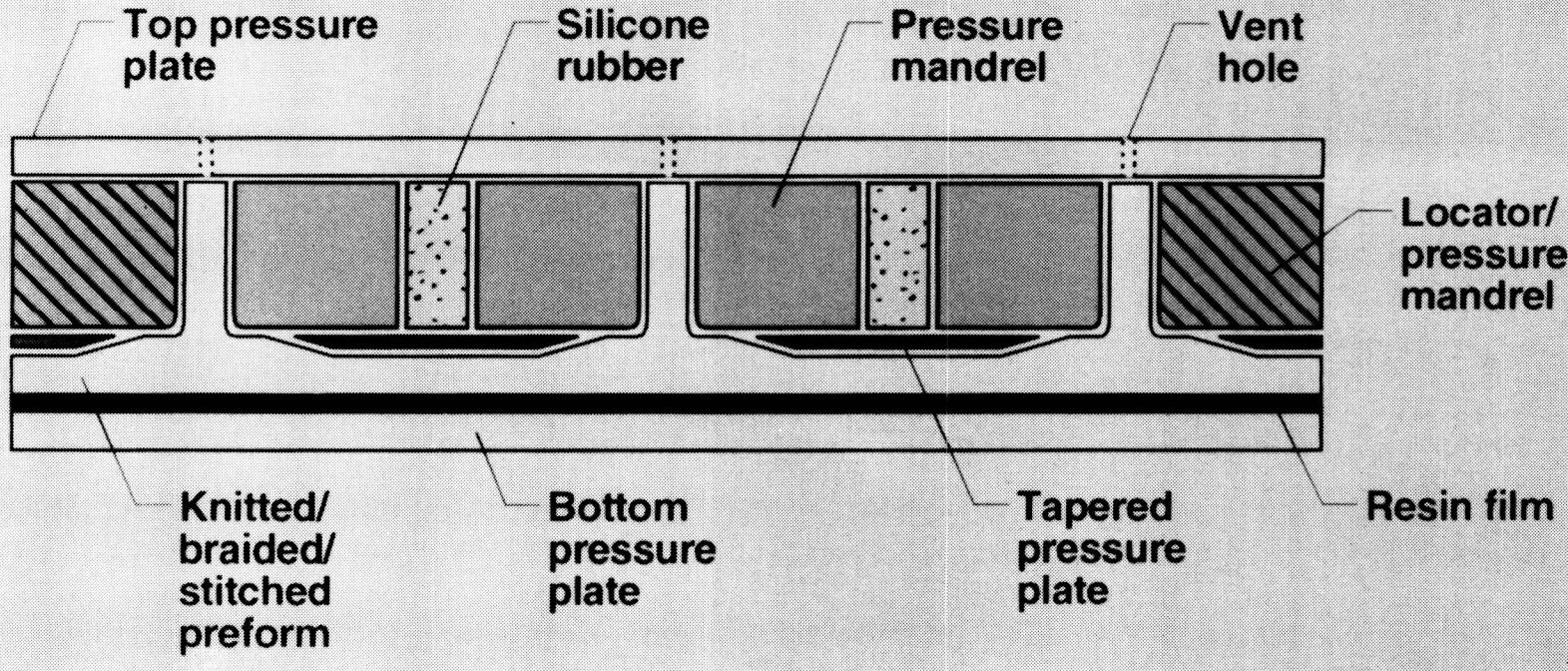

Figure 10. Tooling for resin film infusion of Saerbeck skin/braided 3-stiffener preform.

IMPACTING OF 3-BRAIDED STIFFENER PANELS

Figure 11 illustrates how the 3-stiffener panels were supported for the impact event. Panels were supported by hardwood blocks at each end and C-clamped at each stiffener location. A drop weight impactor having a diameter of one inch was used to apply a 100 ft-lb impact on the skin side mid-bay between two stiffeners or at the flange edge of the center stiffener as illustrated on the sketch. After the panels were impacted C-scans were used to determine the amount of damage. One 3-stiffener panel from each group of four was designated for single-stiffener crippling tests. This panel was also impacted but at different locations. The panel was impacted (100 ft-lb) on the skin side directly behind the center stiffener at the quarter-length from each end. One of the other stiffeners also received a 20 ft-lb impact at the quarter-length from each end on the side-of-blade. All 3-stiffener panels were returned to Langley for trimming, machining, measurements, end potting, instrumentation, and testing.

IMPACTING OF 3-BRAIDED STIFFENER PANELS

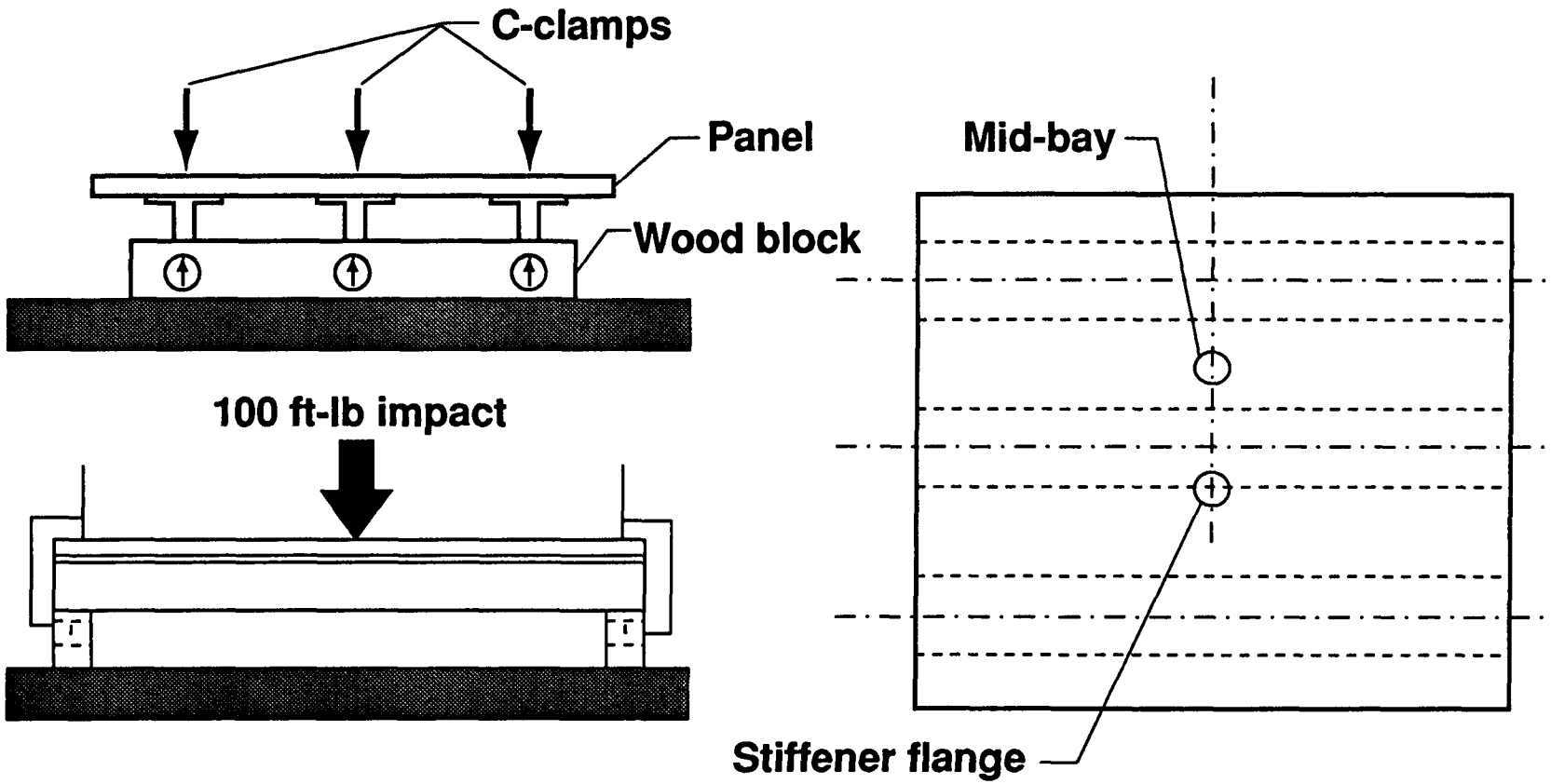

Figure 11. Impacting of 3-braided stiffener panels.

DESCRIPTION OF 3-BRAIDED STIFFENER COMPRESSION PANELS

The 3-braided stiffener compression panels were measured as indicated in figure 12 after the panels were trimmed to a width of 21.0 inches and a length of 22.0 inches. Five thickness measurements, stiffener flange width, and stiffener height were obtained, along the length, for each panel segment or stiffener and the average values are given in the figure. The skin and stiffener concept being evaluated and the associated panel number are also indicated in the figure along with the calculated cross-sectional area. In addition to the braided stiffener panels listed in figure 12, dimensions for a stitched skin and stitched stiffener panel (S7) are also shown. This panel was obtained from the trimmed ends of a large compression repair panel which was one of the test components from the McDonnell Douglas Aerospace ACT wing development program. After all measurements were obtained each panel end was potted and machined flat, square and parallel for uniform load introduction. Back-to-back strain gages were installed on the single-stiffener crippling and 3-braided stiffener compression panels. For the single-stiffener crippling panels, a minimum of six strain gages were mounted at the mid-length on the skin and side-of-blade of the stiffener. Back-to-back strain gages were also mounted at the mid-length for the 3-braided stiffener compression panels, on the top of each stiffener and on the skin between each stiffener. Strain gages for impacted panels were also mounted approximately 1-inch above and below and on both sides of the impact site.

DESCRIPTION OF 3-BRAIDED STIFFENER COMPRESSION PANELS

Figure 12. Description of 3-braided stiffener compression panels.

Typical Stiffener

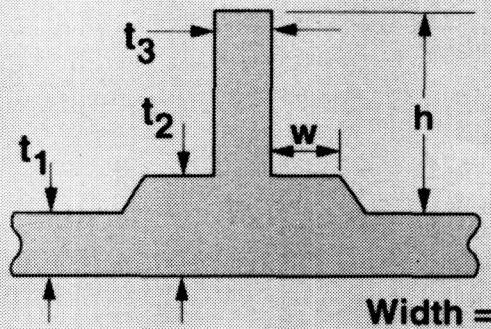

Width = 21.0 in.
Length = 22.0 in.
Stiffener spacing = 7.0 in.

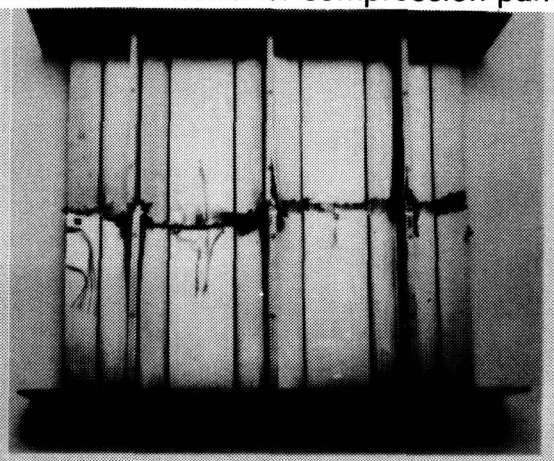

(a) Panel numbers 1 through 8.

Nominal Dimensions

Panel No.	Skin	Stiffener	t_1, in.	t_2, in.	t_3, in.	w, in.	h, in.	Cross-sectional area, $in.^2$
1	Saerbeck	Braided/woven	0.359	0.464	0.427	1.58	2.14	11.52
2	AS4 fiber	AS4 fiber	0.346	0.450	0.429	1.51	2.14	11.11
3*	(44% 0°, 44%	(±45/0°)	0.340	0.444	0.427	1.51	2.14	—
4	±45°, 12% 90°)		0.336	0.440	0.424	1.58	2.14	10.90
5	Saerbeck	100% Braided	0.340	0.448	0.422	1.51	2.14	10.99
6	AS4/IM7 fiber	AS4 fiber	0.335	0.443	0.422	1.51	2.13	10.87
7	(44% 0°, 44%	(±53/0°)	0.332	0.436	0.424	1.50	2.14	10.85
8*	±45°, 12% 90°)		0.323	0.427	0.423	1.50	2.14	—

*Single stiffener specimens machined from panel after impacting

DESCRIPTION OF 3-BRAIDED STIFFENER COMPRESSION PANELS

Typical Stiffener

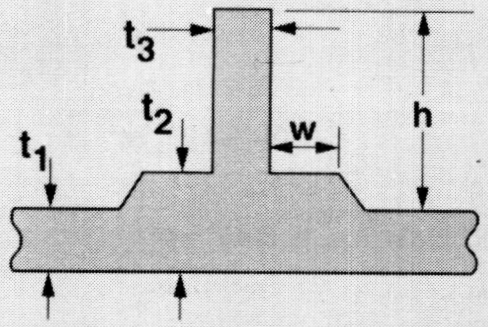

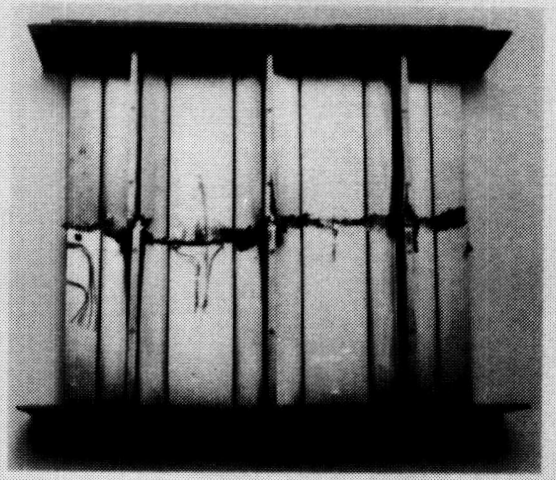

Width = 21.0 in.
Length = 22.0 in.
Stiffener spacing = 7.0 in.

*Width = 15.0 in.
Length = 9.9 in.
Stiffener spacing = 8.0 in.

Nominal Dimensions

Panel No.	Skin	Stiffener	t_1, in.	t_2, in.	t_3, in.	w, in.	h, in.	Cross-sectional area, $in.^2$
1c	Saerbeck	Braided/woven	0.344	0.449	0.425	1.50	2.14	11.01
2c	AS4/IM7 fiber	AS4/IM7 fiber	0.350	0.455	0.427	1.50	2.14	11.17
3c	(44% 0°, 44% ±45°, 12% 90°)	(±45/0°)	0.346	0.451	0.427	1.50	2.14	11.09
S7*	Stitched Saerbeck AS4 fiber (44% 0°, 44% ±45°,12% 90°)	Stitched Saerbeck AS4 fiber (44% 0°, 44% ±45°,12% 90°)	0.341	0.554	0.438	1.15	2.09	8.14

Figure 12. Concluded.

(b) Panel numbers 1c through 3c and S7.

STRESS-STRAIN RESPONSE OF SINGLE-BRAIDED STIFFENERPANELS

Figure 13 shows the stress-strain response of the single braided stiffener panels which were machined from panels RFI processed as 3-stiffener panels. The data shown are for specimens tested in compression without impact damage. The first digit of the panel number shown above the stress-strain plots refers to the 3-stiffener panel given in figure 12 from which the single-stiffener crippling specimen was obtained and the second digit is the specimen number for record keeping. The data are the average of all six strain gage readings since the output of all six gages were virtually identical up until just prior to failure. The data indicate that the 100% braided AS4 stiffener stitched to the Saerbeck warp knit material with the IM7 graphite fiber in the 0° direction has about 7% higher compression strength compared to the braided/woven all AS4 stiffener stitched to the all AS4 Saerbeck warp knit material. However, the stitched Saerbeck stiffener and Saerbeck skin concept has about 25% higher compression strength than the best braided stiffener concept. The 0° and ±45° direction tows in the stitched Saerbeck stiffener are straighter than the 0° and bias tows in the braided stiffener concepts and can better support compression loads.

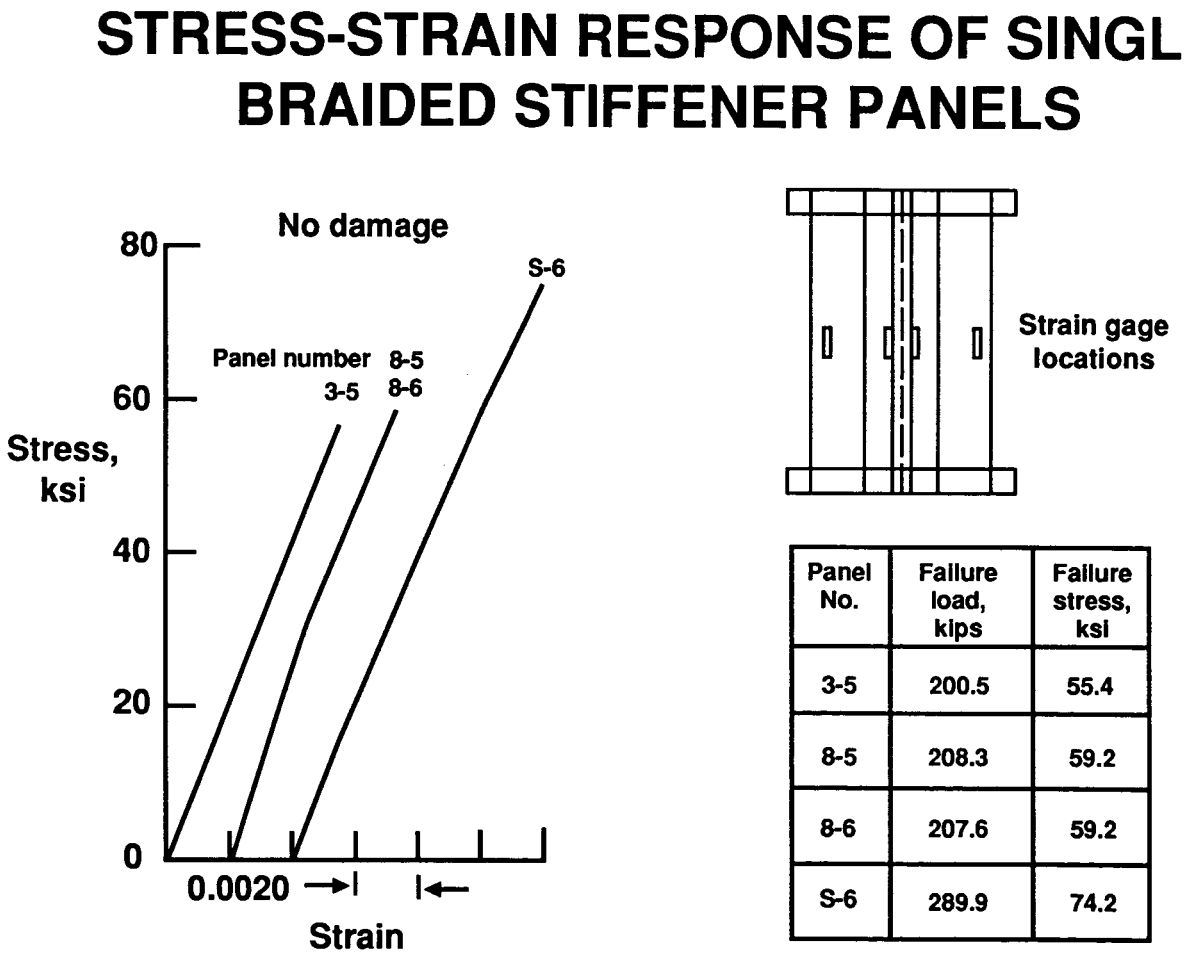

Panel No.	Failure load, kips	Failure stress, ksi
3-5	200.5	55.4
8-5	208.3	59.2
8-6	207.6	59.2
S-6	289.9	74.2

Figure 13. Stress-strain response of single-braided stiffener panels.

STRESS-STRAIN RESPONSE OF SINGLE BRAIDED STIFFENER PANELS IMPACTED AT MID-STRINGER

Data are shown in figure 14 for the six single-stiffener crippling specimens which were impacted on the skin side directly beneath the blade of the stiffener as indicated on the figure. Again, the first digit of the panel number relates to the panel number given in figure 12 from which the single-stiffener specimens were obtained. The data shown are the average from all six strain gages and is representative for both specimens evaluated. Both braided stiffener concepts (panels 3 and 8) had about the same compression after impact (CAI) strength as the specimens tested which were not impacted (see figure 13). The stitched stiffener concept also did not show any loss in compression strength due to the 100 ft-lb impact and, again, had about 25% higher compression strength than the two braided stiffener concepts.

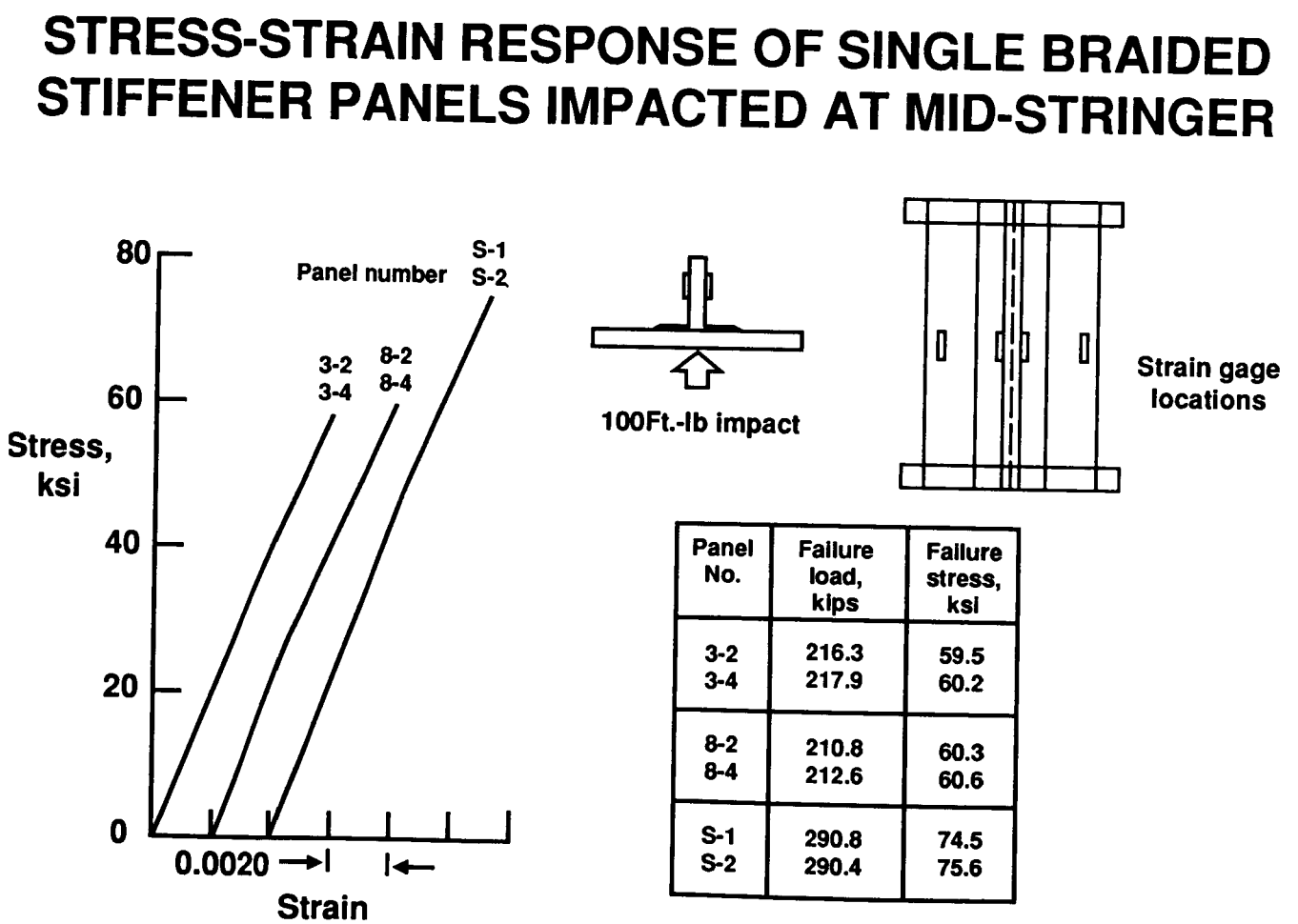

Figure 14. Stress-strain response of single-braided stiffener panels impacted at mid-stringer.

STRESS-STRAIN RESPONSE OF SINGLE BRAIDED STIFFENER PANELS IMPACTED ON SIDE OF STRINGER

Figure 15 shows the results for the single-stiffener specimens which were impacted on the side-of-blade as indicated on the figure. The data shown are the average from all strain gages and is representative for each specimen. The data shown indicate that the AS4 braided/woven stiffener and the 100% braided AS4 stiffener concepts had about the same compression after blade impact strength which is the about the same as for the specimens which were not impacted (see figure 13). The stitched Saerbeck stiffener concept specimen has more than 25% higher compression strength after side of blade impact than the two braided stiffener concepts evaluated under this condition.

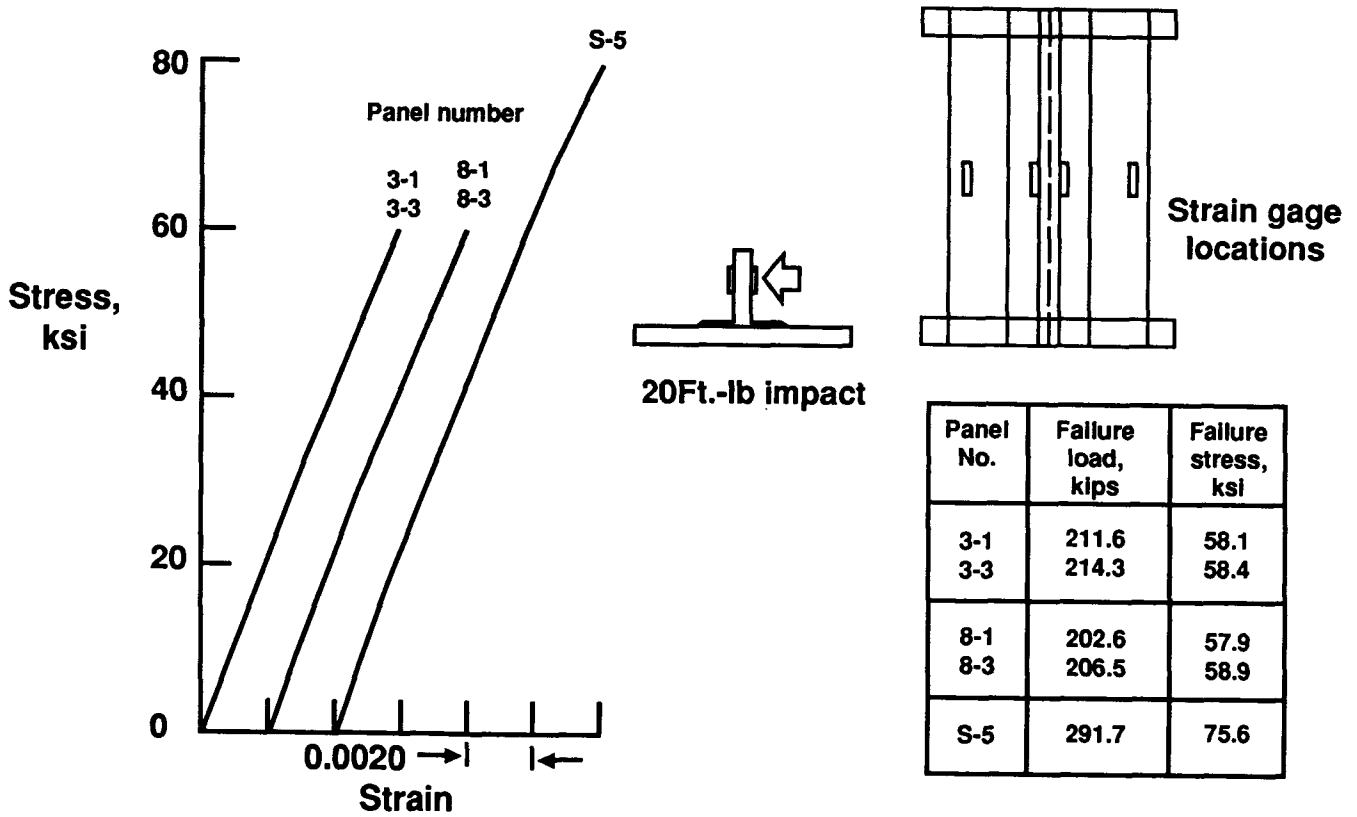

Panel No.	Failure load, kips	Failure stress, ksi
3-1 3-3	211.6 214.3	58.1 58.4
8-1 8-3	202.6 206.5	57.9 58.9
S-5	291.7	75.6

Figure 15. Stress-strain response of single-braided stiffener panels impacted on side of stringer.

SINGLE BRAIDED STIFFENER WING PANEL COMPRESSION FAILURE

Failure photographs for the AS4 braided/woven stiffener stitched to the AS4 Saerbeck warp knit wing lay-up material which was impacted (100 ft-lb) on the skin side are shown in figure 16. The type of failure shown is typical for all single-stiffener specimens tested, all failed at about the quarter-length away from the impact site. Note that there is no separation of skin and stiffener indicated which is also typical for all single-stiffener specimens tested in this investigation.

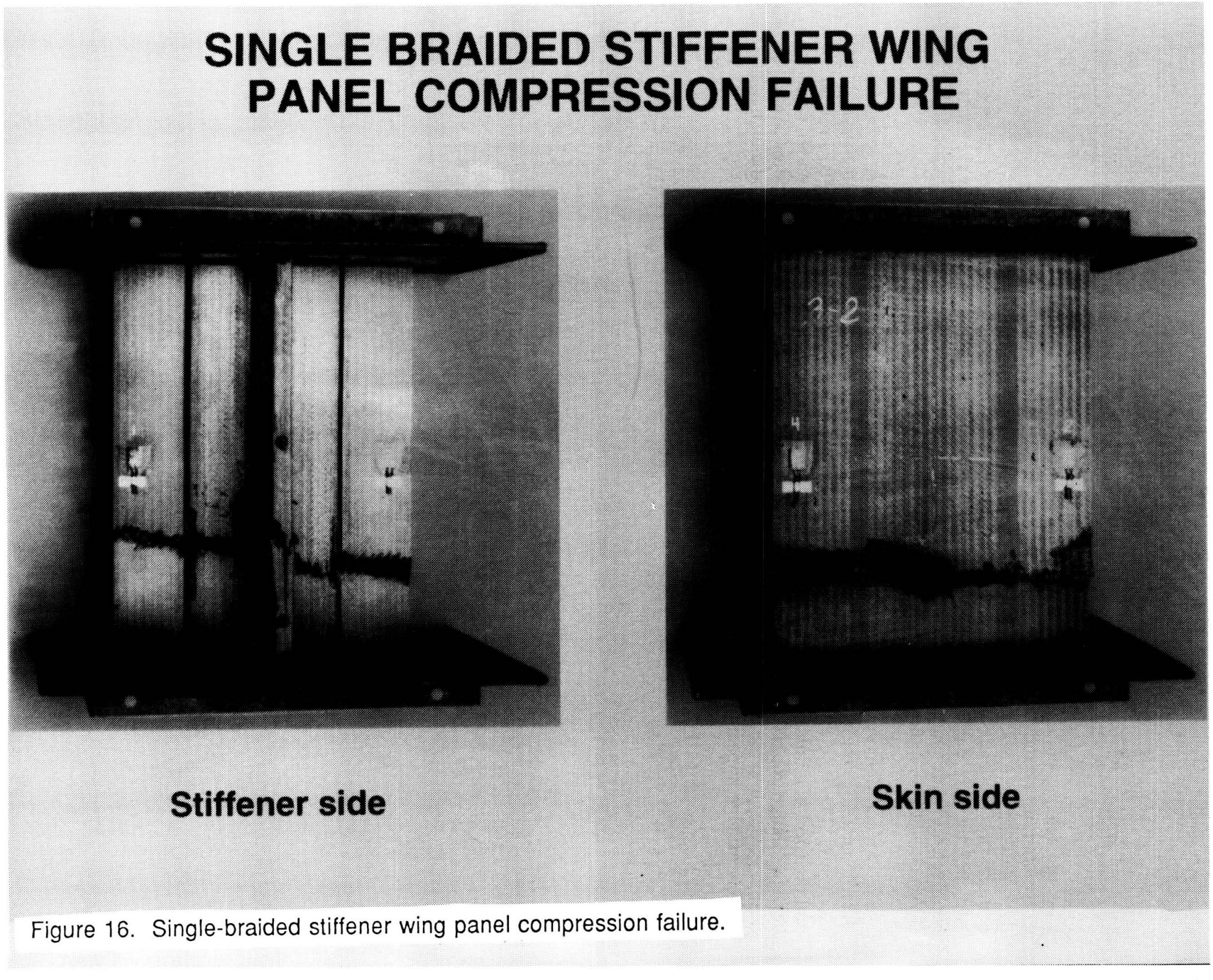

Figure 16. Single-braided stiffener wing panel compression failure.

COMPRESSION STRENGTH OF SINGLE STRINGER STIFFENED PANELS FOR DOUGLAS WING

Figure 17 summarizes the single-stiffener compression results presented in figures 13-15. The open bars represent the average failure stress of the single-stiffener specimens tested without impact damage and the hatched bars represent the average failure stress of the specimens which were impacted as indicated by the key at the top of the figure. The skin and stiffener configurations are indicated along the abscissa, beneath the respective data bars. It is clear that the braided/woven stiffener and the 100% braided stiffener concepts have about the same compression properties which is about 25% less than the stitched Saerbeck stiffener concept. Although the two braided stiffener concepts were out performed in compression by the stitched Saerbeck stiffener concept their average failure stress is still about 50% greater than the 40 ksi (CAI) design goal indicated on the figure by the dashed line.

An additional stitched Saerbeck stiffener was used to obtain data on the effect of a 100 ft-lb stiffener flange impact and the results are indicated by the cross-hatched bar on the far right of the figure. The failure stress of this specimen was only about 67% of the undamaged strength and the specimen failed through the impact site. A similar reduction in strength applied to a stiffener flange impact for the two braided stiffener concepts would fall just under the CAI design goal. However, data obtained from the 3-stiffener panels to be presented indicate that a stiffener flange impact is not the critical impact location.

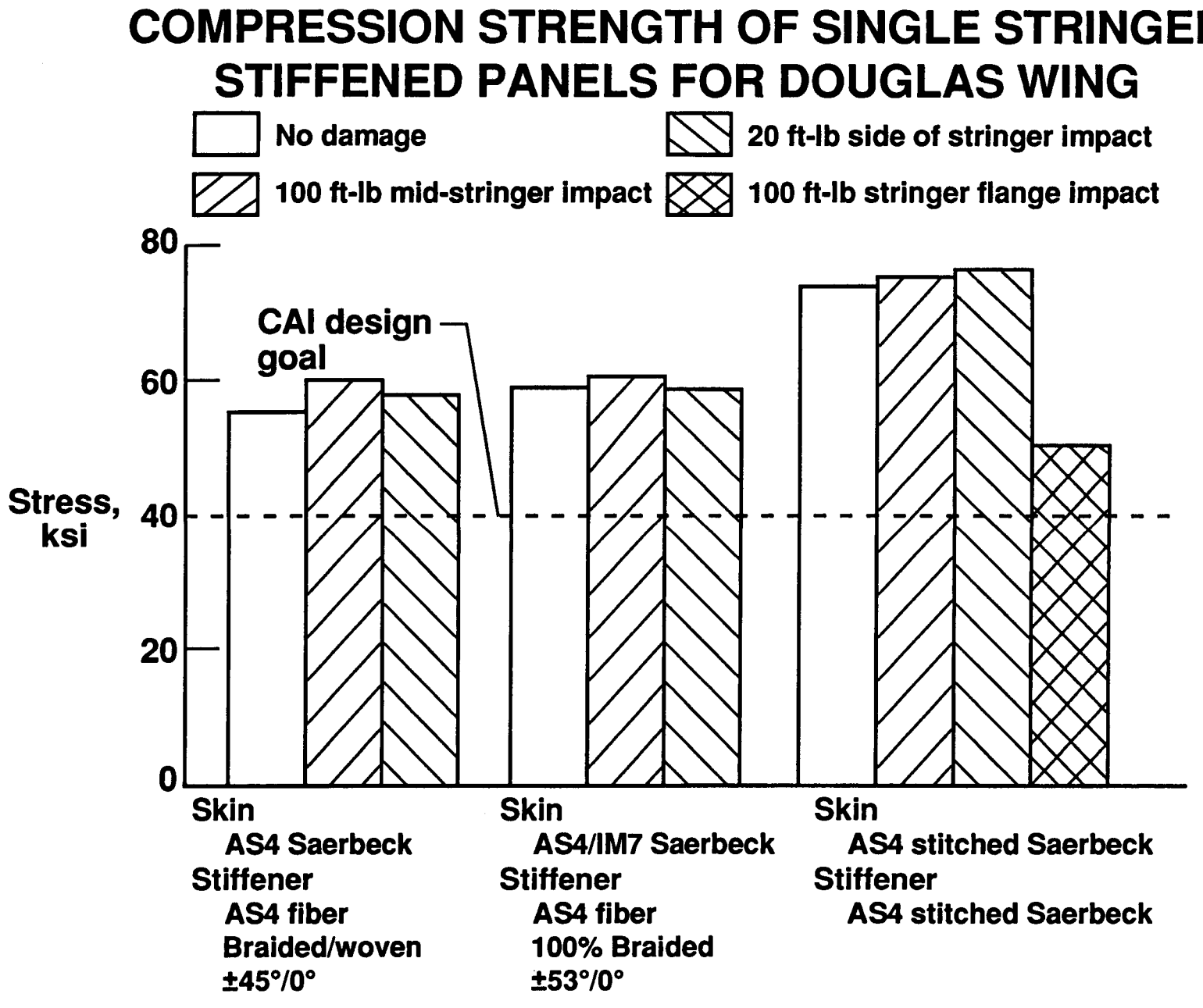

Figure 17. Compression strength of single stringer stiffened panels for Douglas wing.

The stress-strain response of the 3-braided stiffener panels tested in compression without impact damage is shown in figure 18. The panel number shown at the top of the stress-strain curves refer to the panel number given in figure 12 which identifies the fabrication of the panel for which stress-strain data are presented. The data shown are the average of the mid-bay back-to-back strain gage output. Results indicate that the braided/woven stiffener with the IM7 tows in the 0° direction stitched to the Saerbeck warp knit wing lay-up material also with the IM7 tows in the 0° direction (panel 2C) gives the best compression strength, about 9% greater than the braided/woven stiffener and skin fabricated from all AS4 materials (panel 4) but only about 4% greater than the panel with the same skin configuration but with the 100% braided stiffener using all AS4 fiber (panel 6). The maximum displacement values given in the figure were obtained from a linear variable differential transformer which measured end shorting of the test specimens. Global panel strain, defined as the measured end shorting at failure divided by the specimen length, was about the same for all three panel configurations evaluated.

STRESS-STRAIN RESPONSE OF 3-BRAIDED STIFFENER PANELS

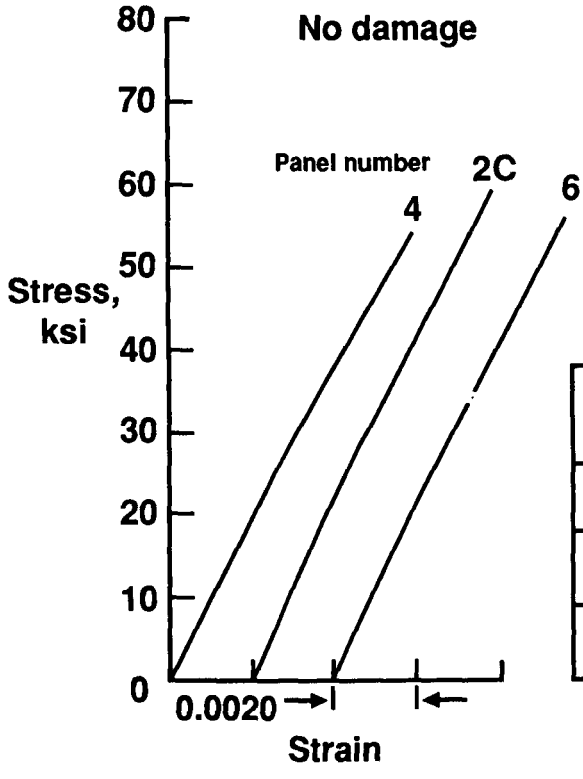

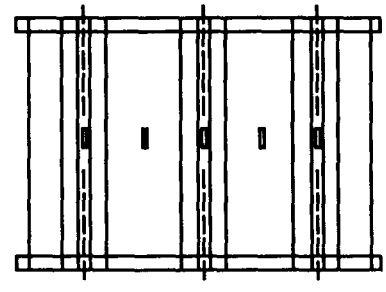

Strain gage locations

Panel No.	Failure load, kips	Failure stress, ksi	Maximum displacement, in.	Global* panel strain	Max. strain gage reading
4	590.9	54.2	0.152	0.0069	0.0061
2C	622.1	59.3	0.161	0.0073	0.0062
6	615.8	57.0	0.143	0.0065	0.0060

* Global panel strain = max. displacement/length

Figure 18. Stress-strain response of 3-braided stiffener panels.

STRESS-STRAIN RESPONSE OF 3-BRAIDED STIFFENER PANELS IMPACTED AT STIFFENER FLANGE

Figure 19 shows the stress-strain response for the 3-stiffener panels impacted on the skin side back of the center stiffener flange previously described. Again, the panel number shown at the top of the stress-strain plots refer to the panel numbers given in figure 12 which identifies the panel fabrication configuration. Again, the data are the average of the mid-bay back-to-back strain gages located adjacent to the impact site. The braided/woven stiffeners with the IM7 tows in the 0° direction stitched to the Saerbeck warp knit wing lay-up material with IM7 tows in the 0° direction (panel 3C) gives the best CAI strength, 13% greater than the all AS4 braided/woven stiffeners stitched to the all AS4 Saerbeck wing lay-up material (panel 2) and about 5% greater than panel 5 which had the all AS4 100% braided stiffeners stitched to the Saerbeck skin material with the IM7 tows in the 0° direction. The global panel strains for the three panels are similar, slightly less than those of the panels tested without impact damage (see figure 18).

STRESS-STRAIN RESPONSE OF 3-BRAIDED STIFFENER PANELS IMPACTED AT STIFFENER FLANGE

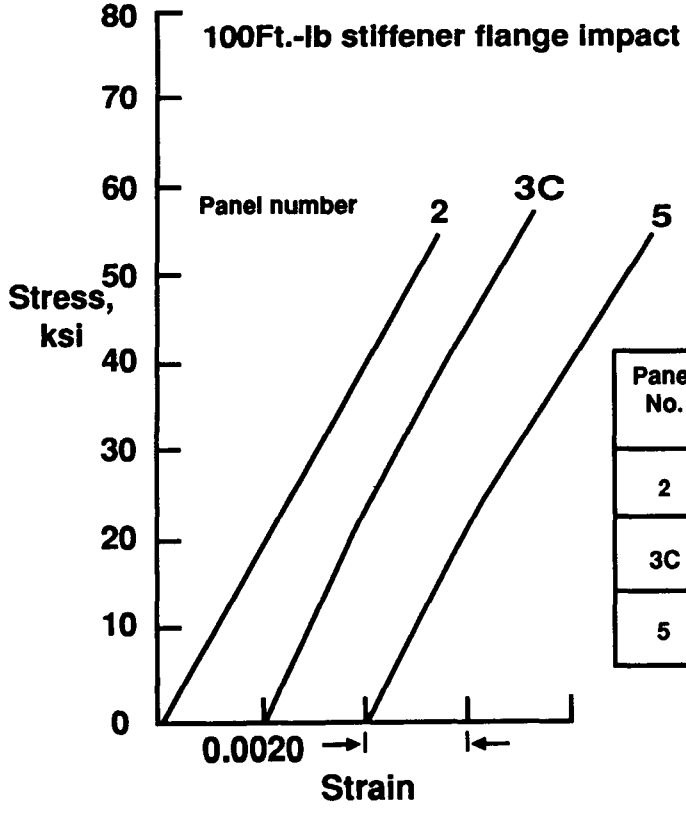

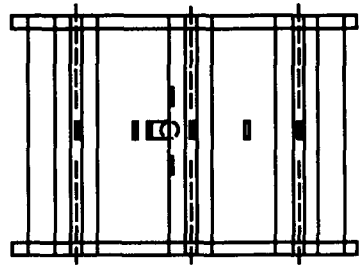

Strain gage locations

Panel No.	Failure load, kips	Failure stress, ksi	Maximum displacement, in.	Global* panel strain	Max. strain gage reading
2	579.3	52.2	0.142	0.0064	0.0067
3C	656.0	59.2	0.151	0.0068	0.0063
5	619.1	56.5	0.143	0.0065	0.0069

* Global panel strain = max. displacement/length

Figure 19. Stress-strain response of 3-braided stiffener panels impacted at stiffener flange.

STRESS-STRAIN RESPONSE OF 3-BRAIDED STIFFENER PANELS IMPACTED AT MID-BAY

Data are shown in figure 20 for the 3-stiffener panels subjected to a mid-bay impact of 100 ft-lb on the skin side. The data are the average of the back-to-back strain gages located in the bay adjacent to the impact location. The all AS4 braided/woven stiffener stitched to the all AS4 Saerbeck wing lay-up material, panel 1 had the best CAI strength, about 7% higher than panel 1C and about 14% higher than panel 7. Note also the differences in the global panel strains. Also shown in figure 20 are the stress-strain results for the short stitched Saerbeck stiffener stitched on to the stitched Saerbeck warp knit wing lay-up material. This panel only had two stiffeners which were 8-inches apart. The CAI strength of this panel was about 12% higher than the CAI strength of the best braided stiffener specimen.

STRESS-STRAIN RESPONSE OF 3-BRAIDED STIFFENER PANELS IMPACTED AT MID-BAY

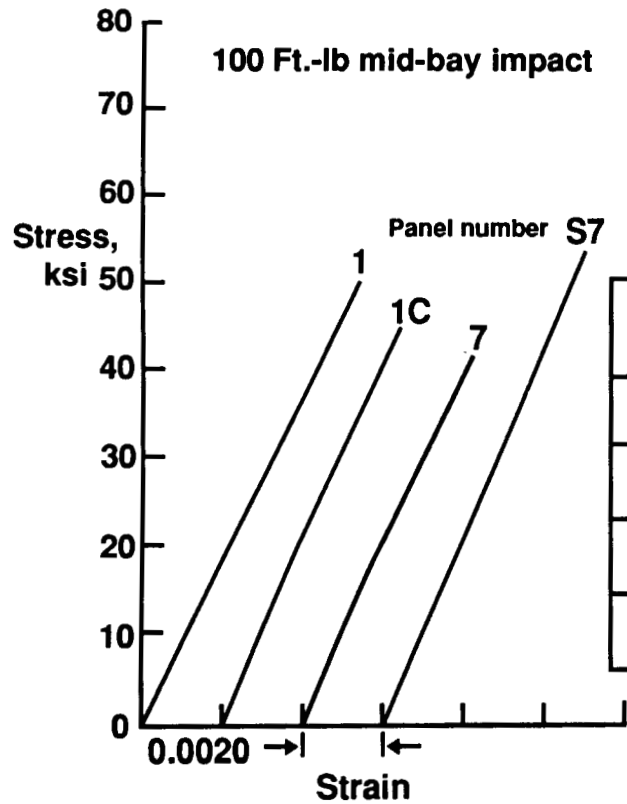

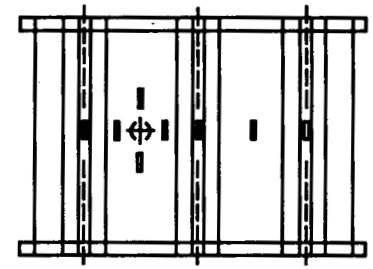

Strain gage locations

Panel No.	Failure load, kips	Failure stress, ksi	Maximum displacement, in.	Global* panel strain	Max. strain gage reading
1	561.6	48.8	0.142	0.0064	0.0083
1C	503.3	45.7	0.115	0.0052	0.0065
7	460.9	42.9	0.106	0.0048	0.0056
S7	446.7	54.9	0.070	0.0071	0.0060

* Global panel strain = max. displacement/length

Figure 20. Stress-strain response of 3-braided stiffener panels impacted at mid-bay.

3-BRAIDED STIFFENER WING PANEL COMPRESSION FAILURE

Figure 21 shows failure photographs of the 3-stiffener panel fabricated from all AS4 braided/woven stiffeners stitched to the all AS4 Saerbeck warp knit wing lay-up skin material which was impacted mid-bay at 100 ft-lb. As with the single-stiffener failures there was no skin stiffener separation for any of the 3-stiffener compression panels tested in this investigation. The failure shown is typical for all panels tested, although the panels tested without impact damage failed nearer the end of the panel.

3-BRAIDED STIFFENER WING PANEL COMPRESSION FAILURE

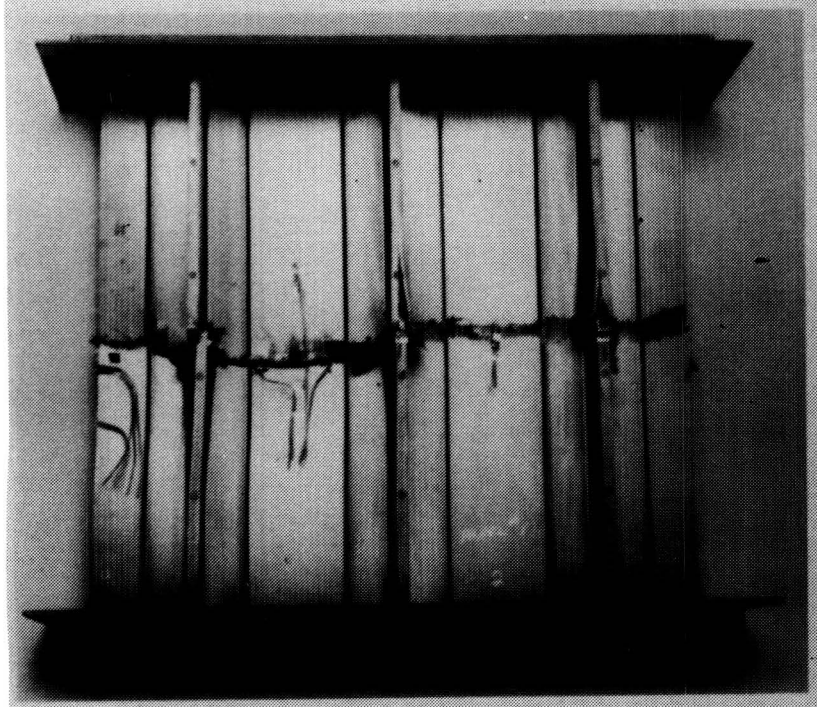

Stiffener side

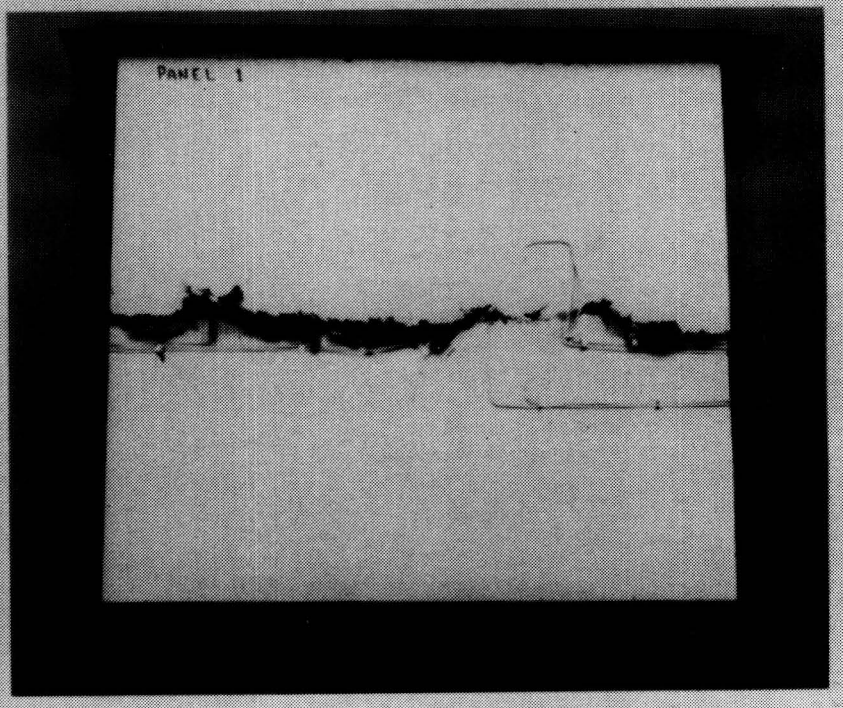

Skin side

Figure 21. 3-braided stiffener wing panel compression failure.

COMPRESSION STRENGTH OF 3-STRINGER STIFFENED PANELS FOR DOUGLAS WING

A summary of the 3-stiffener compression results presented in figures 18-20 are shown in figure 22. The open bars represent the failure stress of the 3-stiffener specimens tested without impact damage and the hatched bars represent the failure stress of the specimens which were impacted as indicated by the key at the top of the figure. The skin and stiffener configurations investigated are indicated along the abscissa. The braided/woven stiffener and skin material which had the IM7 tows in the 0° direction has the highest undamaged compression strength and the highest compression strength after a 100 ft-lb stiffener flange impact. However, the braided/woven stiffener and skin material which used all AS4 Tows had the highest compression strength of the 3-stringer panels subjected to a 100 ft-lb mid-bay impact. Also shown on the figure for comparison are the results of the 2-stringer panel tested during this investigation and the compression strength of a 3-stringer panel (ref. 1) which was fabricated using the stitched Saerbeck stiffener and stitched Saerbeck skin. Note that the compression strength of all 3-stiffener panels are not affected by the 100 ft-lb stiffener flange impact and the 100 ft-lb mid-bay impact is critical. All 3-stiffener panels employing braids in the stiffeners exceeded the CAI design goal of 40 ksi indicated on the figure by the dashed line.

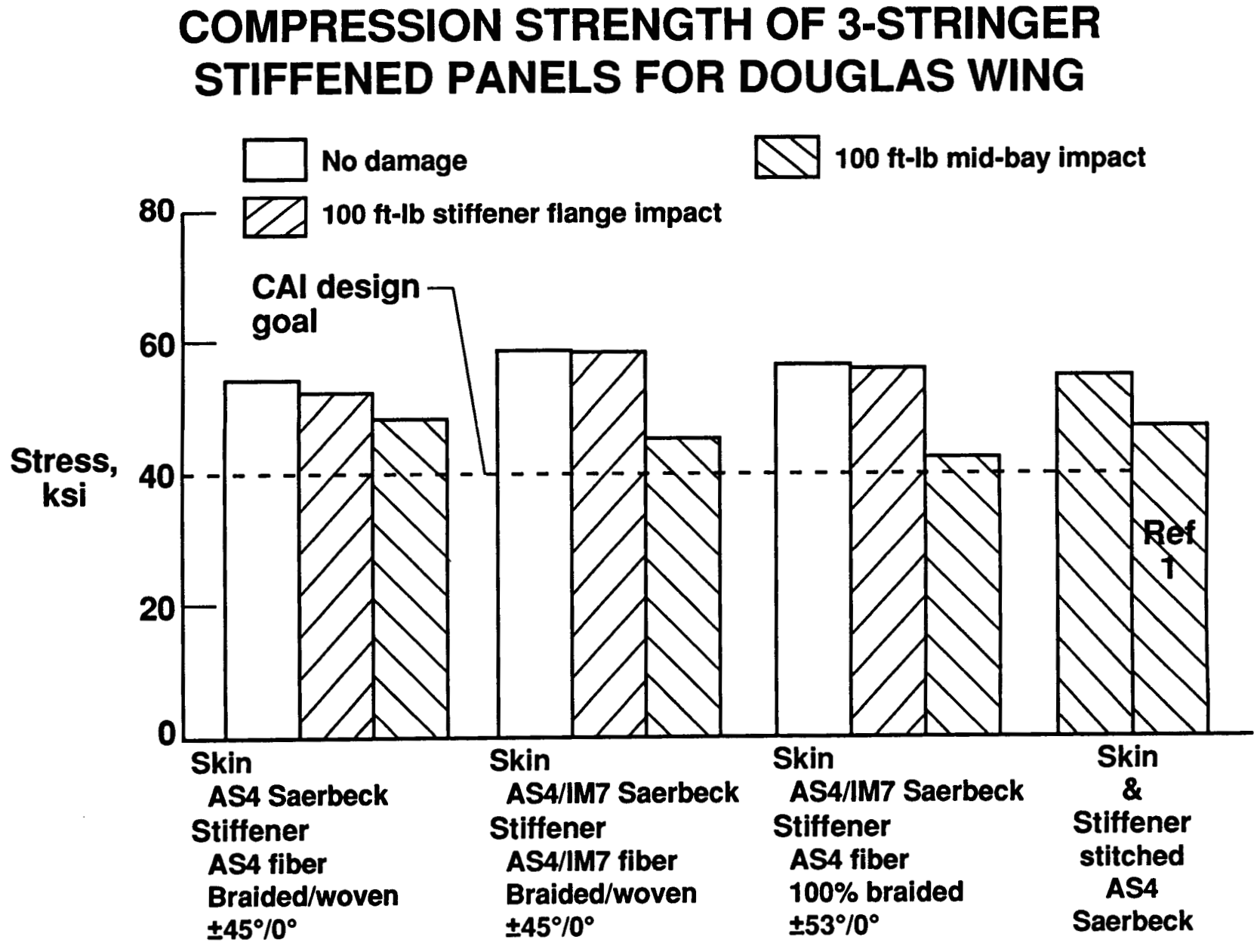

Figure 22. Compression strength of 3-stringer stiffened panels for Douglas wing.

CONCLUDING REMARKS

Three different braided stiffener and stitched skin configurations resin film infused with 3501-6 resin have been evaluated to assess their potential for application to aircraft wing structure. The three concepts evaluated include: 1) all AS4 braided/woven stiffener (±45°/0°) stitched to all AS4 Saerbeck warp knit material with a wing lay-up (44% 0°, 44% ±45°, 12% 90°) ; 2) all AS4 100% braided stiffener (±53°/0°) stitched to AS4/IM7 Saerbeck warp knit wing lay-up (44% 0°, 44% ±45°, 12% 90°), IM7 tows in the 0° direction and AS4 tows in the ±45° and 90° directions; and 3) AS4/IM7 braided/woven stiffener (±45°/0°), AS4 tows in the ±45° direction and IM7 tows in the 0° direction, stitched to AS4/IM7 Saerbeck wing lay-up material as in (2). Single-stiffener and 3-stiffener wide panels were tested in compression with and without impact damage. The results of this investigation support the following observations.

1. All braided/woven and 100% braided stiffened panels exceeded the compression-after impact design goal of 40 ksi

2. CAI strength of single- stiffener specimens not affected by 100 ft-lb mid-stringer or 20 ft-lb side of stringer impacts

3. CAI strengths of 3-braided stiffener panels indicate that 100 ft-lb mid-bay impact is most critical

4. Preliminary cost studies indicate braided stiffener concepts are about 15% less than currently used stitched Saerbeck stiffeners

5. Based on CAI performance and cost estimates the braided stiffener concept is a viable alternative to the stitched Saerbeck stiffener concept

REFERENCES

1. Dexter, H. Benson, Palmer, Raymond J., and Hasko, Gregory, H,: Mechanical Properties and Damage Tolerance of Multiaxial Warp Knit Structural Elements, Fourth NASA/DoD Advanced Composites Technology Conference, Salt Lake City, Utah, June 7-11, 1993, NASA CP- 3229, Part 2, pp 579-604.

COMPARISON OF THE COMPRESSIVE STRENGTHS FOR STITCHED AND TOUGHENED COMPOSITE SYSTEMS

James R. Reeder
Mechanics of Materials Branch
NASA Langley Research Center
Hampton, VA

ABSTRACT

The compression strength of a stitched and a toughened matrix graphite/epoxy composite was determined and compared to a baseline unstitched untoughened composite. Two different layups with a variety of test lengths were tested under both ambient and hot/wet conditions. No significant difference in strength was seen for the different materials when the gage lengths of the specimens were long enough to lead to a buckling failure. For shorter specimens, a 30% reduction in strength from the baseline was seen due to stitching for both a 48-ply quasi-isotropic and a $(0/45/0/-45/90/-45/0/45/0)_S$ laminate. Analysis of the results suggested that the decrease in strength was due to increased fiber misalignment due to the stitches. An observed increasing strength with decreasing gage length, which was seen for all materials, was explained with a size effect model. The model assumed a random distribution of flaws (misaligned fibers). The toughened material showed a small increase in strength over the baseline material for both laminates presumably due to the compensating effects of a more compliant matrix and straighter fibers in the toughened material. The hot/wet strength of the stitched and baseline material fell 30% below their ambient strengths for shorter, non-buckling specimen, while the strength of the toughened matrix material only fell 20%. Video images of the failing specimen were recorded and showed local failures prior to global collapse of the specimen. These images support the theory of a random distribution of flaws controlling composite failure. Failed specimen appearance however, seems to be a misleading indication of the cause of failure.

INTRODUCTION

Composite materials are now being considered more often for primary structures. As composite structures compete with metal structures there is pressure to make composites faster, cheaper, and stronger. The in-plane properties compare very well with metals. However, low out-of-plane properties of composite materials have lead to delamination problems and low damage resistance. Two methods can be used to improve these thickness-direction properties: the matrix can be toughened; or through-the-thickness fiber arrangements can be employed. Tougher matrix systems have shown dramatic improvements in damage resistance [1] as has through-thickness stitching [2]. Of course, changing the matrix properties or introducing stitches to a laminate will affect the in-plane properties, and aircraft structures are primarily sized by in-plane properties. The objective of this work was to determine the influence of stitching versus a toughened matrix on the in-plane compression strength of composite materials.

First, the compression failure of an unstitched material made of AS4/3501-6 was studied to provide a baseline. This material was then compared to both a stitched composite made of the same fiber and matrix and to an unstitched composite made of the same fiber but with a tough matrix (8551-7 epoxy). Analyses were developed to model the compression strength of the baseline material. These models were then used to explain the differences observed in compression strength between the baseline and both the stitched and the toughened matrix materials.

Several factors which can affect the compression response of a laminate were investigated. First, because laminate compression strength is a complex combination of material and structural response, tests over a wide range of unsupported specimen gage lengths were conducted. Second, since composite laminates are tailored to different applications, laminates which differed in stacking sequence and thickness were tested. Compression results of a moderately thick common quasi-isotropic laminate were studied and then compared to a thinner $(0/45/0/-45/90/-45/0/45/0)_S$ laminate, which was stronger and stiffer in the 0° direction. The final factor studied was the effect of environment. Initially all the laminates were tested at room temperature and under ambient moisture conditions. Tests were then run at $180^\circ F$ on specimens which had been subjected to a prolonged water soak. Such hot/wet properties are often used in design because they represent one of the more critical environments that a normal aircraft structure might be expected to endure.

SYMBOLS LIST

A	cross-sectional area of specimen, in^2
C	end constraint coefficient
E	laminate longitudinal modulus, Msi
G	laminate through-thickness shear modulus, Msi
G_m	matrix tangent shear modulus, Msi
I	bending moment of inertia, in^4
L	specimen gage length, in
m	Weibull slope parameter
t	specimen thickness, in
V_f	fiber volume fraction
V_m	matrix volume fraction
w	specimen width, in
α	initial fiber misalignment, rad.
β	rotational spring stiffness, in-lb/rad
γ	composite shear strain
γ_m	matrix shear strain
σ	laminate strength, ksi
σ^0	strength in 0° ply, ksi
$\sigma_{0.5}$	reference laminate strength at 0.5 in. gage length, ksi
$\sigma^0_{0.5}$	0° ply strength at reference 0.5 in. gage length, ksi
τ_m	shear stress in matrix, ksi

MATERIAL

Traditionally, composite material has been manufactured by stacking together layers of prepreg tape material. Prepreg tape is a combination of unidirectional fibers and partially cured matrix. These layers are then consolidated by heating them under pressure to form a laminate. Unfortunately, when these layers of prepreg are stitched, some fibers are broken because they are held in place by the partially cured matrix. These broken fibers significantly reduce the in-plane properties of the composite [3]. To solve this problem, stitched laminates have more recently been made from uniweave fabric. The uniweave fabric material does not contain the partially cured matrix, so fibers are able to move out of the way of the needle and thus fewer fibers are broken [3]. In the uniweave layer, a small percentage of thin compliant glass fibers are woven transverse to the aligned fibers to hold the layer together so it can be handled. Once a stack of uniweave layers has been stitched, it is put into a mold and low viscosity resin is heated and forced to infiltrate the laminate. This process is called resin transfer molding (RTM). The mold is then heated to cure the matrix.

The baseline material in this study was an uniweave laminate without stitching. The base line laminates were manufactured with the RTM process used for the stitched laminates. The uniweave material was made of AS4 fibers in the primary direction. The weaving fibers were glass and only accounted for 1% of the fabric weight. The matrix was 3501-6 epoxy which is a common low-toughness composite matrix. The stitched laminates consisted of uniweave plies stitched with a 1250 yd/lb glass yarn. The laminates were stitched in the load carrying direction with eight rows of stitches per inch. Within a row, a stitch was made every 1/8 of an inch using a modified lock stitch. This stitch placed the stitch knot on the back surface of the laminate where it would have less of an effect on the fibers in the laminate [2]. The toughened matrix material was a conventional prepreg tape. The prepreg tape contained the same AS4 fibers as in the baseline and stitched materials, but had a toughened 8551-7 epoxy matrix. These laminates were manufactured in an autoclave curing process.

Two laminates of each material were tested. The first was a 48-ply quasi-isotropic laminate with a $(45/0/-45/90)_{6S}$ layup which was intended to represent an aircraft frame structure. The laminate thickness, t, was approximately 0.25 inches. The other laminate was a 0.1 in. thick 18-ply $(0/45/0/-45/90/-45/0/45/0)_S$ laminate. This laminate was stiffer and stronger than the quasi-isotropic laminate because of the larger proportion of 0° plies and represented a wing skin.

TESTS SPECIMEN AND PROCEDURE

The compression tests in this study were conducted using a NASA linear-bearing fixture [4] as shown in Figure 1. This fixture has four rods mounted with linear bearings to keep the grips aligned. The test specimen extended 2.25 in. into each grip, load was introduced primarily through end loading. The face grips primarily provided lateral restraint. They also reduced the tendency for the specimen to fail at the ends by introducing some of the load through shear thereby reducing the end loads. Soft plastic shims were placed between the grips and the specimen so that the grip faces did not bite into the test specimen and so that the stress concentration at the grip line was reduced. This loading configuration did not require the use of bonded tabs. Bonded tabs, which are required for many other compression tests [5], have been shown to cause a significant stress concentration at the end of the gage section [6, 7] as well as requiring an additional manufacturing step. This fixture was modified slightly from that described in Reference 4, to allow laminates of different thicknesses to be tested. The back grip plate was made adjustable so that the centerline of the test specimen could be aligned with the centerline of the load frame.

All test specimens had a 1 in. width, w, but ranged in length between 4.69 and 14.5 inches. These specimens had unsupported gage lengths, L, of 0.19, 0.5, 1.0, 2.0, 3.5, 5.5, and 10.0 inches. Only the thicker quasi-isotropic laminates were tested with the 5.5 and 10 inch gage lengths. Strain gages were applied to many of the specimens to check specimen alignment, to confirm Euler buckling, to measure longitudinal modulus and Poisson's ratio, and to determine strain at failure. The specimens with 1.0, 2.0, 3.5, or 5.5 in. gage lengths were strain gaged front and back with 1/4 in. strain gages in both the longitudinal and transverse directions. Because of their small gage length, specimens with the 0.5 in. gage length were strain gaged front and back with 3/16 in. strain gages in the longitudinal direction only. The 0.19 in. gage length specimens were too small for strain gage measurements.

As mentioned, compression tests were first run under ambient conditions. The laboratory temperature was 77°F. All ambient specimens contained a nominal amount of moisture since they had been stored under normal atmospheric conditions for a prolonged period.

The hot/wet specimens were soaked in water at 160°F for 45 days and then tested at 180°F. These hot/wet test parameters are similar to those used for general material evaluations [8]. In order to determine the amount of moisture absorbed by the specimen, they were weighed after being dried and again after being soaked. The specimens were stored in water until they were tested. For strain gauging, the specimens were removed from the water for approximately 6 hours while the strain gages were bonded. M-Bond GA-2@ [9] room-temperature-cure epoxy adhesive was used because it provided adequate adhesion under this hot/wet environment. After bonding, the specimens were returned to water for 1 to 2 days before being tested.

To perform elevated temperature tests, an oven was placed around the linear-bearing fixture and heated to 180°F. Prior to testing, each specimen was put in a small water bath which was then placed in the oven. When the water temperature reached 180°F, the specimen was removed from the bath and the excess surface moisture was dried. If the specimen was strain gaged, the specimen was allowed to sit in the oven without being gripped for several minutes until the specimen temperature and strains stabilized so that the gages could be zeroed. The specimen was then placed in the grips and loaded to failure. The specimen was placed in the grips as quickly as possible to minimize drying. The elapsed time between removing the specimen from the 180°F water bath and actually testing was usually less than 30 minutes.

All compression tests were conducted in displacement control. The initial displacement rate was 0.02 in/min but the rate was slowed to 0.01 in/min near failure to better capture the failure mechanisms. The load and crosshead displacement as well as strain readings were recorded every 0.5 seconds. To determine longitudinal modulus, the front and back strain gage readings were averaged and plotted versus load. The modulus was calculated from the slope of a least squares regression line which was fit to the points which fell between 1000 and 3000 με. The Poisson's ratio was determined by plotting the averaged front and back transverse strain versus the average longitudinal strain. Poisson's ratio was taken as slope of the regression line fit to the points with average longitudinal strains between 1000 and 3000 με. The front to back longitudinal strain differed by less than 200 με when the average longitudinal strain was 3000 με, indicating that the specimen was well aligned. At least three repetitions of each strength test were performed.

During several of the ambient tests, the machined edge of the specimen was viewed with a high speed video system which recorded 1000 frames per sec. The hot/wet tests were not recorded on video because the oven blocked the edge view of the specimen.

BASELINE MATERIAL AND MODELS DEVELOPMENT

The compression strength of the baseline unstitched uniweave quasi-isotropic laminate is shown in Figure 2. The strength of this material varies widely over the gage lengths tested. This is not surprising since the longer specimens were quite long compared to their thickness and, therefore, buckled. Once the gage length was small enough to prevent buckling one might expect to find some constant "material compression strength" [10]. Instead the compression strength was found to continue to increase as the gage length was reduced. Buckling theory was used to model the longer gage length specimen. The strength in the short gage length region was modeled with a size effect model which will be described later.

The Euler buckling strength a beam with fixed ends is given by

$$\sigma = \frac{4\pi^2 EI}{A2L^2} \tag{1}$$

where I is the bending moment of inertia ($I=w\,t^3/12$), A is the cross-sectional area ($A=w\,t$) and E is the laminate longitudinal modulus. This equation also assumes a homogeneous material. For the laminates in this study which contain dispersed 0, $\pm$45, and 90 degree layers, this assumption should be acceptable. This model used a value of E of 7.18 Msi and an average thickness of 0.255 inches which were measured for these laminates. As can be seen form Figure 2 this model does a poor job of modeling the compression response of the test specimen. Two reasons for this are that it neglects the effect of shear deformation and that it assumes perfectly fixed end conditions. Shear deformation is generally more significant for graphite/epoxy composite beams than for metal beams because the shear modulus is smaller compared to the longitudinal modulus for the composites. Even though a specimen was firmly clamped in each grip, the end condition is not perfectly clamped. The material which was held in the grip was constrained from lateral movement but could deform longitudinally. A gradient in longitudinal deformation across the thickness of the specimen would result in a rotation of the specimen cross section at the grip [11].

Equation 2 [12] accounts for shear deformation and compliance of the end condition.

$$\sigma = \frac{C\pi^2 EI}{A2L^2}\left(\frac{1}{1+1.2\dfrac{C\pi^2 EI}{A2L^2 G}}\right) \tag{2}$$

G is the through-the-thickness shear stiffness of the material. The end constraint coefficient, C, for a column which is constrained from lateral movement at the ends and where rotation is resisted by rotational springs is approximated in Reference [13] as

$$C = \frac{\left(EI/\beta L + .4\right)^2}{\left(EI/\beta L + .2\right)^2} \tag{3}$$

where β is the rotational spring stiffness.

This buckling model is plotted in Figure 2 and agrees well with the strength data at longer gage lengths. The value of G used in the model was 0.691 Msi which was calculated using laminate property transformations described in Reference 14 and the lamina properties given in Table 1. The rotational spring stiffness, β, was chosen to be 16,000 in-lb/rad which produced a good fit to the data. The model does a good job of modeling strength for gage lengths between 3.5 and 10.0 inches.

Figure 3 contains load-displacement curves from representative tests with gage lengths from 0.5 to 5.5 in. Diverging strain values from the front and back gages as seen for the 3.5 and 5.5 in. specimens indicate buckling. This buckling failure mode can also be seen in photographs taken during testing as shown in Figure 4. The 3.5 in specimen can be seen to have buckled out of plane in the photograph taken 0.001 before failure. After failure, the specimen contains many delaminated ply groups and therefore appears to have failed in a brooming failure mode [15]. The curves in Figure 3 indicate that at gage lengths below 3.5 in. buckling no longer controls failure so a different model should be used.

The strength model used for the small gage length region assumed the strength of the specimen was governed by flaws that were randomly spread throughout the material. The severity of the flaws was assumed to obey a Weibull distribution [16]. Since the flaws were randomly distributed, a larger specimen should on average contain a more severe flaw than a smaller specimen and therefore have a lower strength. The model that describes this size effect [17] is given by

$$\sigma = \sigma_{0.5}\left(0.5/L\right)^{1/m} \tag{4}$$

where σ is the strength at a gage length L, $\sigma_{0.5}$ is a reference strength taken as the strength at a gage length of 0.5 inches, and m characterizes the spread of the Weibull distribution of flaws. This size effect model is also shown in Figure 2 and shows good correlation to the measured strength data for specimens with gage lengths less than 3.5 inches. The reference strength value and the Weibull spread were determined to be 99.6 ksi and 10.4, respectively, by a least squares regression analysis. The measured compression strengths for this material are of the same magnitude as reported by others for similar materials [5,18].

The increase in strength with decreasing gage length as seen in the small gage length region in Figure 2 was not seen in data presented by others [18] and may be evident here because of a more uniform stress field in the gage section. A stress concentration like that caused by bonded tabs would disguise this effect because the amount of material in the elevated stress region would remain the same as the gage length changed. When efforts have been made to reduce the stress concentration at the end of the gage section, nonuniform strength has been observed [19,20]. Figure 5 shows a photograph of the edge of a 0.5 inch gage length specimen failing. The dark spot that appeared on the edge of the specimen 4 seconds before failure was the initial failure caused by a flaw. The spot is formed when fibers in a 0° ply at the edge of the specimen, buckle outward from the edge so that they no longer reflect the incident light. After final failure, the specimen appeared very similar to the 3.5 in gage length specimen (Figure 4) which failed due to global buckling. Therefore, the appearance of a failed compression specimen does not always indicate the controlling failure mechanism. The size effect model represents the data adequately for the small gage lengths and therefore, supports the theory that the flaw distribution in the laminate governs compressive strength. This model, however, does not provide information about the form of the flaw. Therefore, no insight is gained as to how strength might be improved or how the strength will be affected by other parameters such as environment.

Wisnom [21] has proposed a model for compression strength of a 0° ply, σ^0, based on the collapse of misaligned 0° fibers. This model is represented by the equation

$$\sigma^0 = \frac{G_m \gamma}{V_m(\gamma + \alpha)} \tag{5}$$

where G_m is the secant shear modulus of the matrix material, α is the initial fiber misalignment, and γ is the composite shear strain which produces additional fiber misalignment. V_m is the matrix volume fraction, which is assumed to be the complement of the fiber volume fraction or $(1-V_f)$. This is a nonlinear equation since both G_m and γ are functions of the compressive stress. The equation assumes that at some critical stress a small amount of additional loading will reduce the matrix secant modulus so that the additional stress cannot be supported, and the composite therefore collapses.

The application of the fiber collapse model requires a shear stress-strain curve for the neat resin. The shear response of the 3501-6 matrix [22] is shown in Figure 6 under both room temperature/dry and hot/wet conditions. The hot/wet results originally presented in Reference 22 were at 200°F. These results were transformed to 180°F using a Richard-Blacklock interpolation [23]. The shear response of the toughened 8551-7 resin [24] is also presented in this figure. A polynomial least squares regression line was fit to each set of data and expressions for the secant moduli, G_m, were calculated. The critical stress can be found numerically by incrementing the matrix shear strain γ_m. The corresponding G_m and composite shear strain ($\gamma = \gamma_m V_m$) were then found and substituted into Equation 5. As the matrix shear strain is increased, the stress required to produce the strain will increase to a point and then fall off due to decreasing matrix modulus and increasing fiber misalignment. The peak stress is the predicted strength of the 0° ply. The predicted 0° ply strengths, σ^0, for 3501-6 and 8551-7 composites were calculated for a variety of initial misalignments as shown in Figure 7.

The fiber collapse model can be used in combination with the size effect model by assuming that the critical flaws in the composite are regions where the fibers are not aligned well with the loading axis. At smaller gage lengths there is less material in the gage section so the chance of having as large a fiber misalignment present would be less and the average strength would be higher. The reference laminate strength, $\sigma_{0.5}$, for this 3501-6 quasi-isotropic laminate was calculated from the test data to be 99.6 ksi, as reported earlier. The stress in the 0° ply was calculated using laminate theory to be 2.46 times the average stress. The lamina properties used in this analysis are presented in Table 1. Therefore, the reference strength of 0° ply, $\sigma^0_{0.5}$. is 245 ksi. This reference strength corresponds to a fiber misalignment of 1.5° as indicated by the RT/DRY 3501-6 curve in Figure 7. This fiber misalignment is comparable to reported measurements of fiber misalignment between 0.7° and 2° [25]. Although the moisture content in the specimens which were tested under ambient conditions was measurable (see Table 2), it was considerably less than the saturated specimens and was considered insignificant allowing the comparison to the RT/DRY fiber collapse results. This combination of the fiber collapse and size effect models will be used to analyze the compression strengths of the different materials subjected to different environmental conditions.

COMPARISON OF STITCHED AND TOUGHENED MATRIX COMPOSITES

The compression strength is plotted in Figure 8 versus gage length for the baseline, stitched and toughened matrix materials. The thickness of these laminate are somewhat different (see Table 2) which affects their compression strength. Strength is believed to provide the best parameter of comparison because it is directly related to how much structural weight will be needed to support a given load since the densities of the materials are basically the same. The differences in thickness among the different materials , which also affects E and V_f, is a characteristic of the different material forms.

In Figure 8, the measured strength of the different materials is plotted along with the results from the models. The models discussed in the last section appear to do a good job of modeling all three material types. The parameters used in these models are presented in Table 3. In the buckling region, the compression strength does not seem to be affected much by either stitching or by matrix toughness since all three curves fall close together. The stitched composite does appear slightly stronger in this region, but this difference is due to the stitched laminate being slightly thicker because of the stitching. The buckling strength is especially sensitive to the thickness because of its influence on the bending moment of inertia.

In the small gage length region, the stitched laminate's strength is consistently about 20% below that of the baseline. This is assumed to be largely due to the stitches causing perturbations in the 0° plies. An increased fiber misalignment from 1.5° to 2.5° due to the stitching could have caused the observed drop in strength as indicated by the 3501-6 RT/DRY curve in Figure 7. Figure 9 shows fibers in a lamina curving around a stitch and shows that a 2.5° fiber misalignment is actually a conservative value. The failure of a stitched specimen with a 0.5 in gage length is shown in Figure 10. The photographs shows damage in the laminate before failure which is extending perpendicularly across the specimen. This damage is following the line of a stitch which lies just below the surface. This supports the assumption that stitching causes local misalignments of the 0° fibers and hence lowers the strength of the composite. After failure, the specimen appears to have failed in a 45° shear band. This post failure appearance is also typical of the longer stitched specimens that buckled, again showing that post failure appearance is not a good indication of the cause of failure.

The toughened matrix appears to cause a small increase in strength as shown in Figure 8. This is somewhat surprising since the lower stiffness of the 8551-7 matrix shown in Figure 6 causes the fiber collapse model to predict a lower strength for this material. The difference may be due to a difference in fiber misalignment angles. The baseline material is a resin transfer molded uniweave. The small transverse weave of the uniweave is intended to curve around the tows in the primary direction, but a small amount of crimp may still take place. Also, during the RTM process, when resin is pumped through the dry fiber material, fibers may tend to move somewhat therefore affecting the fiber alignment. The fibers in the toughened matrix material may therefore be straighter than that of the unstitched uniweave. A change in fiber misalignment angle from 1.5° to 1.0° would account for this difference in strength as indicated by the horizontal distance between the 3501-6 and 8551-7 RT/DRY curves of Figure 7. The tape material may also be more uniform as indicated by the low slope of the size effect model curve in Figure 8. This might indicate better control of the processing of the tape material.

The failure of the tape material appears very similar to that of the baseline material. Occasionally near failure, a progression of delaminations were seen in the toughed and baseline materials, as shown in Figure 11. The photographs of the progressive failure gives insight into

how the brooming failure develops. However, brooming is not believed to be the true cause of failure. The models worked equally well for the baseline, toughened, and stitched composite materials even though the progressive delamination failure was never seen in the stitched material. Also, for the shortest gage lengths, failure in the toughened and base line laminates would occasionally develop as a shear band similar to that seen for the stitched composites. The change in strength in this region of the baseline and toughened matrix composites was similar to that of the stitched material where no transition in failure appearance was seen. The progressive delaminations were therefore believed to be caused by misaligned fibers which collapsed and then caused the delaminations. Therefore, stitching or tougher matrix systems are not expected to affect compression strength due to their increased delamination toughness but may affect it due to their influence on fiber alignment and fiber support.

The strength results from the $(0/45/0/-45/90/-45/0/45/0)_S$ laminates are shown in Figure 12. The trends are similar to those for the quasi-isotropic laminate. In the buckling region, the stitched panel appears slightly stronger than the baseline or toughened panels due to the increased thickness of the panel. In the nonbuckling region, a 20% decrease in strength is seen and again is assumed due to increased fiber misalignment from stitching. The strength of the toughened matrix material is again in the range of the untoughened baseline material. The appearance of the failure was also similar to that seen for the quasi-isotropic laminates of the different materials. A larger change in strength with gage length is seen for the toughened tape material than the baseline uniweave material. This is the opposite trend from that seen for the quasi-isotropic specimens and would indicate that the tape material had a larger distribution of flaws than the uniweave.

The buckling strength of the $(0/45/0/-45/90/-45/0/45/0)_S$ laminate is significantly below that of the quasi-isotropic laminate at the same gage length. This is due to the sensitivity of buckling strength to specimen thickness. The excellent fit of the model to the data in both cases indicates that the strength in this region is truly governed by the global buckling response. The rotational spring stiffness β was changed for the modeling of the thinner laminates to 4000 in-lb/rad, because the thinner laminates did not provide as much bending constraint at the grip as the thicker laminate. The shear modulus for the $(0/45/0/-45/90/-45/0/45/0)_S$ laminates was calculated using the laminate analysis to be 0.75 Msi.

In the non-buckling region, one might expect the critical stress in the 0° plies, $\sigma^\circ_{0.5}$, for the same material to be the same for the different laminate types. Figure 13 plots $\sigma^\circ_{0.5}$ for the different materials and the different laminates. The figure shows that the strengths of the 0° plies in the $(0/45/0/-45/90/-45/0/45/0)_S$ laminates are consistently 15% below that from the quasi-isotropic laminate. Although surprising, this could be due to the $(0/45/0/-45/90/-45/0/45/0)_S$ laminate having a 0° ply on the outside of the laminate which may be more critical than an embedded 0° ply.

EFFECT OF HOT/WET CONDITIONS

Each material and both types of laminates were tested under hot/wet conditions as described earlier in this paper. The moisture content in each material and for each laminate is recorded in Table 2. The stitched material absorbed significantly more moisture than either the unstitched or the toughened matrix material. This was probably due to the additional resin content in this material and due to the glass stitch material allowing more moisture absorption. Another reason the stitched material's moisture content may have been higher was that even after the 45-day soak, the

specimens were not completely saturated. The stitched material was more nearly saturated because it absorbed moisture much quicker, possibly due to the resin rich stitches wicking moisture to the interior of the laminate. The 8551-7 tape material absorbed less moisture than the 3501-6 uniweave. The thinner $(0/45/0/-45/90/-45/0/45/0)_S$ laminates had larger % moisture contents than the thicker quasi-isotropic laminate after the 45 day soak. This also may be due to differences in saturation level with the thinner laminate being more nearly saturated. The material for the hot/wet tests was assumed completely saturated and compared using saturated elevated temperature matrix properties.

The compression strengths of the quasi-isotropic laminates and of the $(0/45/0/-45/90/-45/0/45/0)_S$ laminates are presented in Figures 14 and 15, respectively. The trends in both cases look similar to those seen under ambient conditions, and the model strength curves fit the data well. The parameters used in generating these curves are presented in Table 3. The buckling strength curves were practically unaffected by the change in test environment. The buckling strength is primarily a function of the laminate stiffness which, as shown by the measured modulus data in Table 2, is essentially unchanged. The laminate stiffness is mainly controlled by the stiffness of the fibers which should not be affected by the hot/wet conditions. The stitched laminate again appears a little stronger in the buckling region because it is slightly thicker. In the nonbuckling region, the stitched laminate compressive strength was again almost 20% lower than the baseline unstitched uniweave. The reduction was slightly less than 20% for the quasi-isotropic laminate and slightly more for the $(0/45/0/-45/90/-45/0/45/0)_S$ laminate. The toughened matrix material is 13% and 19% higher than the baseline material under the hot/wet conditions for the quasi-isotropic and $(0/45/0/-45/90/-45/0/45/0)_S$ laminates, respectively. This is different from the ambient conditions where they were about the same. The similarity in strength for these materials at ambient conditions is postulated to be due to compensating factors: straighter fibers and a more compliant matrix in the tape material. It is not surprising that under hot/wet conditions the strengths would no longer be the same since the hot/wet environment would have a different effect on the two matrix materials.

To better evaluate the effect of the hot/wet conditions, the $\sigma^0_{0.5}$ for each material and each laminate were compared for the ambient and hot/wet conditions. These results are shown in Figure 16. Both the baseline and the stitched materials had about a 30% drop in strength due to the hot/wet conditions for both laminates. The drop in strength for the toughened matrix material was only about 20%.

Figure 6 also shows the shear response of the 3501-6 and 8551-7 matrix material under hot/wet conditions. The hot/wet matrix properties of the two materials were used in the fiber collapse model to predict the strengths of the 0° ply. These predictions are shown in Figure 7. Assuming fiber misalignment angles in the 1-3 degree range, these predictions suggest that a 50% drop in strength from the room temperature tests should be expected for the baseline and stitched materials, and a 35% drop should be expected for the toughened matrix material. This predicted reduction is significantly larger than the measured reduction, but the prediction that the effect would not be as large for the toughened matrix composite was correct. The predicted reduction may be greater than the measured reduction because the ambient specimens were assumed to be completely dry and the hot/wet specimens were assumed to be completely saturated. Neither condition was strictly true, so the changes in matrix properties due to moisture were over estimated. The moisture effect however should be smaller than the effect of temperature [22, 24].

The strength under hot/wet conditions of the 0° ply in the quasi-isotropic laminate again was consistently higher than in the $(0/45/0/-45/90/-45/0/45/0)_S$ laminate. Although not noted on Figure 16, $\sigma^0_{0.5}$ for the two baseline material laminates differed by 13% under hot/wet conditions. This

is consistent with the 14% difference found under ambient conditions, as was shown in Figure 13, and again may be due to the $(0/45/0/-45/90/-45/0/45/0)_S$ laminate having 0 external plys. The difference in $\sigma^o_{0.5}$ between the two laminates was 20% for the stitched material and only 8% for the toughened matrix material under hot/ wet conditions as compared to differences at ambient conditions of 15% and 13%, respectively. The discrepancy between the ambient and hot/wet values for the stitched and toughened materials may simply be due to experimental scatter.

CONCLUDING REMARKS

The effect of the trade-off between stitching and toughened matrix systems on the compression property of composite laminates was determined at both ambient and hot/wet conditions and for a large range of unsupported gage lengths. The compressive strength of a stitched uniweave composite with a brittle epoxy (3501-6) and of an unstitched tape composite containing a toughened epoxy (8551-7) were compared to a baseline material made of unstitched uniweave with the brittle epoxy matrix. This comparison was made for two laminates: a 48-ply quasi-isotropic laminate and a thinner 18-ply $(0/45/0/-45/90/-45/0/45/0)_S$ laminate which contained a larger portion of 0^o plies.

If a compression specimen was long enough to buckle, the important material parameters were the laminate stiffness and thickness as indicated by the buckling model. The stitched material which had a slightly reduced modulus from the baseline material actually carried more load because of the laminate's increased thickness. No effect of the hot/wet environment was observed when buckling governed failure.

When the test specimens were short (<3.5 inches), the specimens failed before buckling occurred. The strength of the composite was not constant in this region but increased as the gage length decreased. This increasing strength was believed to be due to a random distribution of flaws within the material which causes larger specimens to have a lower strength on average. The critical flaw was assumed to be misaligned fibers. A model that predicts strength based on the fiber misalignment angle and the matrix nonlinear shear stress-strain curve was used to predict strengths. The predicted results agreed well with measured values.

An observed 20% reduction in the strength of the stitched material from that of the baseline materials was attributed to a small increase in fiber misalignment caused by the stitching. The strength of the toughened tape material was approximately the same as the baseline material but the similarity in strength is believed to be due to compensating effects of straighter fibers and a lower modulus matrix. The resistance to delamination gained by stitching or by increased matrix toughness is not believed to influence compression strength. Delaminations that were observed during the failure of the baseline and toughened tape materials were believed to develop after failure was initiated by the collapse of misaligned fibers. The effect of stitching and of the toughened matrix was approximately the same for both quasi-isotropic and $(0/45/0/-45/90/-45/0/45/0)_S$ laminates but the strength of the critical 0^o plies was calculated to be 15% higher for the quasi-isotropic laminate, on average.

The hot/wet environment caused a reduction in strength for all materials, but the effect was somewhat larger for the baseline and stitched materials which had the more brittle matrix. The decrease in strength was around 30% for these materials and only 20% for the toughened matrix material. The smaller effect on the toughened matrix composite was predicted by the model. The effect of moisture was the same for both laminates.

Although this paper shows that the compression strength is adversely affected by stitching (if buckling does not cause failure), it is only one of many properties which must be evaluated when choosing a material system. The results of this study also indicate that care must be taken when comparing compression data because strength values can change with gage size. The results also showed that the appearance of a failed specimen is not a good indication of the cause of compression failure. Finally, the 30% decrease in strength due to stitching showed just how sensitive the compression strength is to fiber misalignment.

REFERENCES

1. *Toughened Composites: SYMPOSIUM ON TOUGHENED COMPOSITES, ASTM STP 937*, Johnston, N.J., Ed., American Society for Testing and Materials, Philadelphia, 1985.

2. Dow, M.B.; Smith, D.L.; and Lubowinski, S.J.: "An Evaluation of Stitching Concepts for Damage-Tolerant Composites," *Fiber-Tex 1988 Conference Proceedings,* NASA CP-3038, 1989, pp. 53-73.

3. Jang, B.Z.; Shih, W.K.; and Chung, W.C.: "Mechanical Properties of Multidirectional Fiber Composites," *Journal of Reinforced Plastics and Composites*, Vol. 8, November 1989, pp. 538-464.

4. Lubowinski, S.J.; Guynn, E.G.; Elber, W.; and Whitcomb, J.D., "Loading Rate Sensitivity of Open-Hole Composite Specimens in Compression," *Composite Materials: Testing and Design*, Garbo, S.P., Ed., American Society for Testing and Materials, Philadelphia, 1990, pp. 457-476.

5. Berg, J.S.; and Adams, D.F.: "An Evaluation of Composite Material Compression Test Methods," *Journal of Composites Technology & Research*, Vol. 11, No. 2, Summer 1989, pp. 41-46.

6. Tan, S.C., "Stress Analysis and the Evaluation of Celanese and IITRI Compression Test Specimens," *Composite Materials in Transition,* Proceeding of the American Society for Composites, E. Lansing, Michigan, June 1990, pp. 827-838.

7. Wisnom, M.R.: "Effect of Shear Stresses in Indirect Compression Tests of Unidirectional Carbon Fiber/Epoxy," *AIAA Journal*, Vol. 29, No. 10, October 1991, pp. 1692-1697.

8. Cano, R.J.; and Dow, M.B.: "Properties of Five Toughened Matrix Composite Materials," NASA TP-3254, October 1992.

9. "Strain Gage Applications with M-Bond AE-10/15 and M-Bond GA-2 Systems," Instruction Bulletin B-137-15, Micro-Measurements, Raleigh, NC, 1979.

10. Lauraitis, K.N.; and Sandorff, P.E.: "The Effect of Environment on the Compressive Strengths of Laminated Epoxy Matrix Composites," AFML-TR-79-4179, Wright-Patterson Air Force Base, Ohio, December 1979.

11. Wung, E.C.J.; and Chatterjee, S.N.: "On the Failure Mechanisms in Laminated Compression Specimens and the Measurement of Strengths," *Journal of Composite Materials*, Vol. 26, No. 13, 1992, pp. 1885-1914.

12. Timoshenko, S.: *Theory of Elastic Stability*. New York: McGraw-Hill Book Co., Inc., 1936, p. 140.

13. Newmark, N.M.: "A Simple Approximate Formula for Effective End-Fixity of Columns," *Journal of the Aeronautical Sciences.*, Vol 16, No. 2, AIAA, Easton, PA, 1949, p. 116.

14. Murri, G.B.; Salpekar, S.A.; and O'Brien, T.K.: "Fatigue Delamination Onset Prediction in Unidirectional Tapered Laminates," *Composite Materials: Fatigue and Fracture, Vol. 3, ASTM STP 1110*, O'Brien, T.K., Ed., American Society for Testing and Materials, Philadelphia, 1991, pp. 312-339.

15. Odom, E.M.; and Adams, D.F.: "Failure Mode of Unidirectional Carbon/Epoxy Composite Compression Specimens," *Composites*, Vol. 21, No. 4, July 1990, pp. 289-296.

16. Weibull, W.A.: "A Statistical Distribution Function of Wide Applicability," *Journal of Applied Mechanics*, Vol. 18, 1951, p. 293.

17. Hitchon, J.W.; and Phillips, D.C.: "The Effect of Specimen Size on the Strength of CFRP," *Composites*, Vol. 9, 1978, pp. 119-124.

18. Adams, D.F.; and Lewis, E.Q.: "Influence of Specimen Gage Length and Loading Method on the Axial Compressive Strength of a Unidirectional Composite Material," *Experimental Mechanics*, March 1991, pp. 14-20.

19. Haeberle, J.; and Matthews, F.L.: "Studies on Compressive Failure in Unidirectional CFRP using an Improved Test Method," *Developments in the Science and Technology of Composite Materials,* J. Füller et. al., Eds. Proceedings of the 4th European Conference on Composite Materials, Elsevier Applied Science, Stuttgart, FRG, September 1990, pp. 517-521.

20. Wisnom, M.R.: "The Effect of Specimen Size on the Bending Strength of Unidirectional Carbon Fibre-Epoxy," *Composite Structures*, Vol. 18, 1991, pp. 47-63.

21. Wisnom, M.R.: "The Effect of Fibre Misalignment on the Compressive Strength of Unidirectional Carbon Fibre/Epoxy," *Composites*, Vol. 21, No. 5, September 1990, pp. 403-407.

22. Adams, D.F.: "A Micro Mechanics Analysis of the Influence of the Interface on the Performance of Polymer Matrix Composites," *Journal of Reinforced Plastics and Composites*, Vol. 6, January 1987, pp. 66-88.

23. Richard, R.M.; and Blacklock, J.R.: "Finite Element Analysis of Inelastic Structures," *AIAA Journal*, Vol. 7, No. 3, 1968, pp. 432-438.

24. Coquill, S.L.; and Adams, D.F.: "Mechanical Properties of Several Neat Polymer Matrix Materials and Unidirectional Carbon Fiber-Reinforced Composites," NASA CR-181805, April 1989.

25. Camponeschi, E. T., Jr.: "Lamina Waviness Levels in Thick Composites and Its Effect on Their Compression Strength," *Composites: Design, Manufacture, and Application,* Tsai, S.W. and Springer, G.S., Eds., Proceedings of the Eighth International Conference on Composite Materials (ICCM/8), SAMPE, Honolulu, July 1991, No. 30-E, pp. 1-13.

26. Gipple, K.: "A Comparison of the Compression Response of Thick (6.35mm) and Thin (1.60 mm) Dry and Moisture Saturated AS4/3501–6 Laminates," DTRC-SME-90/74, David Taylor Research Center, Bethesda, MD, October 1990.

Table 1. AS4/3501-6 Lamnia Properties [26]

E_{11} (Msi)	16.6
E_{22} & E_{33} (Msi)	1.5
ν_{12} & ν_{13}	0.33
ν_{23}	0.47
G_{12} & G_{13} (Msi)	0.87
G_{23} (Msi)	0.55

Table 2. Measured Laminate Properties

	Thickness		**Density**	**V_f**	**Modulus**		**% Moisture**	
	in.		lb/in^3	%	Msi		%	
		Std. Dev.			Ambient	Hot/wet	Ambient	Hot/wet
Baseline								
Quasi-Isotropic	0.255	0.010	0.0579	62.3	7.18	7.23	0.17	0.69
$(45/0/-45/90/-45/0/45/0)_S$	0.100	0.004	0.0581	63.6	9.71	9.71	0.43	1.41
Stitched								
Quasi-Isotropic	0.291	0.003	0.0577	54.1	6.47	6.54	0.51	1.33
$(45/0/-45/90/-45/0/45/0)_S$	0.114	0.001	0.0578	58.5	8.69	8.64	0.58	1.63
Toughned Matrix								
Quasi-Isotropic	0.268	0.004	0.0561	57.9	6.63	6.84	0.17	0.52
$(45/0/-45/90/-45/0/45/0)_S$	0.102	0.002	0.0553	60.4	9.18	9.39	0.34	0.95

Table 3. Strength Model Parameters

	Buckling Model		Weibull Model				0° Strength	
	G_{12}	β	$\sigma_{0.5}$ (ksi)		m		$\sigma^{\circ}_{0.5}$ (ksi)	
	(MSI)	(in-lb/rad)	Ambient	Hot/wet	Ambient	Hot/wet	Ambient	Hot/wet
Baseline								
Quasi-Isotropic	.69	16,000	99.6	68.1	10.4	21.0	245	168
$(45/0/-45/90/-45/0/45/0)_s$	.75	4,000	118.0	82.0	15.2	22.6	210	146
Stitched								
Quasi-Isotropic	.69	16,000	80.1	56.7	8.8	18.7	197	139
$(45/0/-45/90/-45/0/45/0)_s$	.75	4,000	93.8	62.3	10.2	7.1	167	111
Toughned Matrix								
Quasi-Isotropic	.69	16,000	101.1	77.2	14.5	36.1	249	190
$(45/0/-45/90/-45/0/45/0)_s$	.75	4,000	121.4	97.7	6.5	15.3	216	174

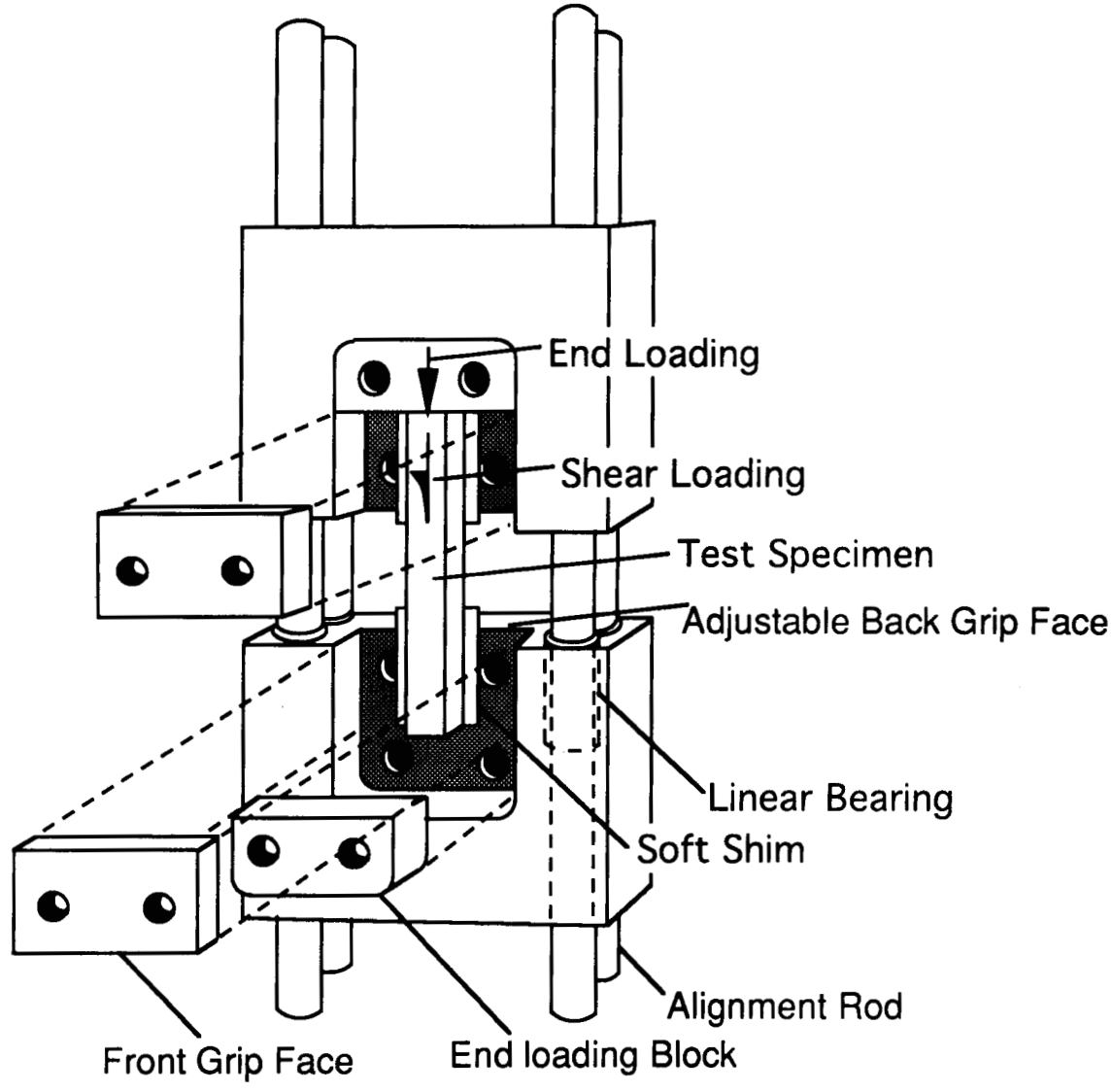

Figure 1. Linear bearing compression test fixture.

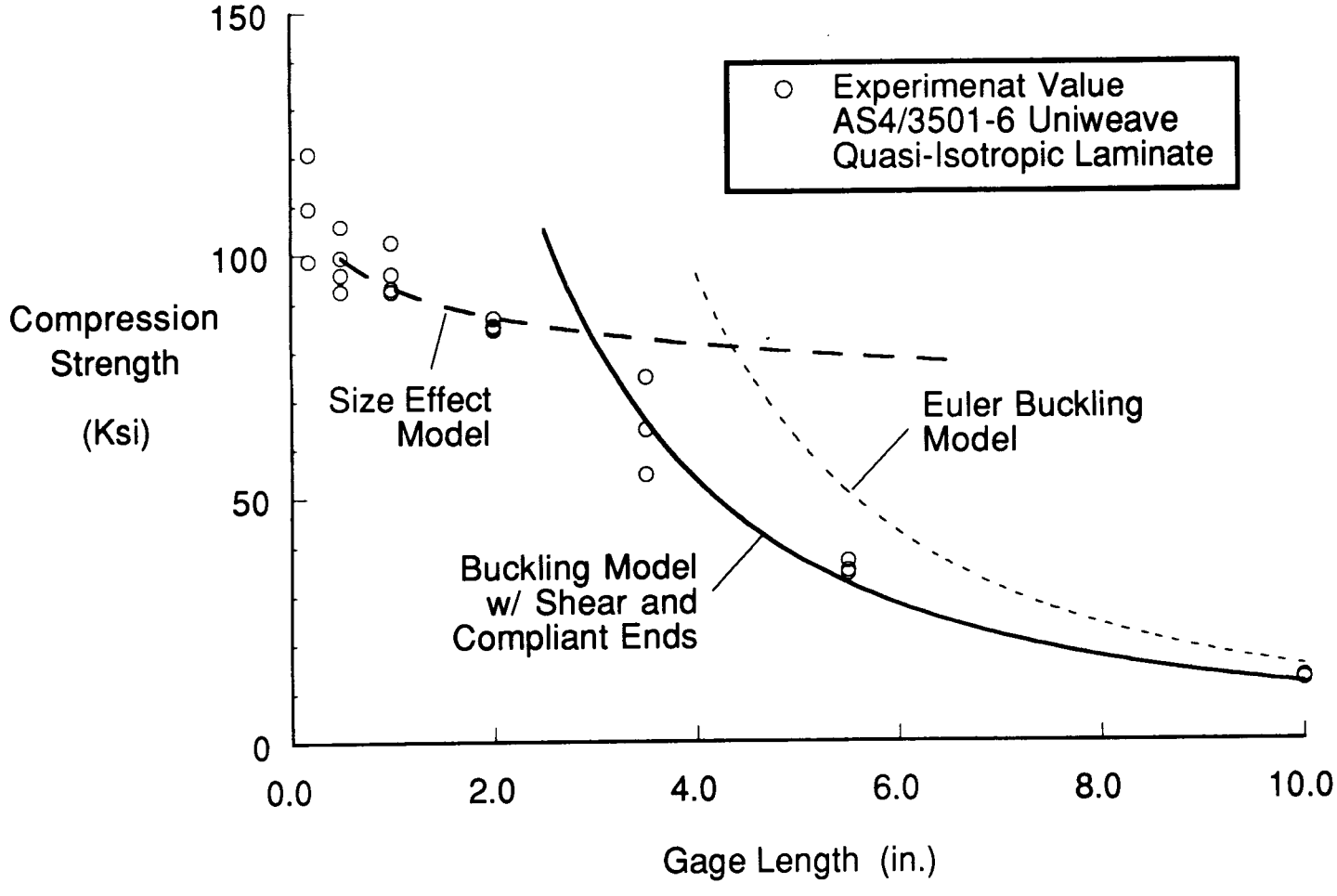

Figure 2. Compression strength models for quasi-isotropic baseline laminate.

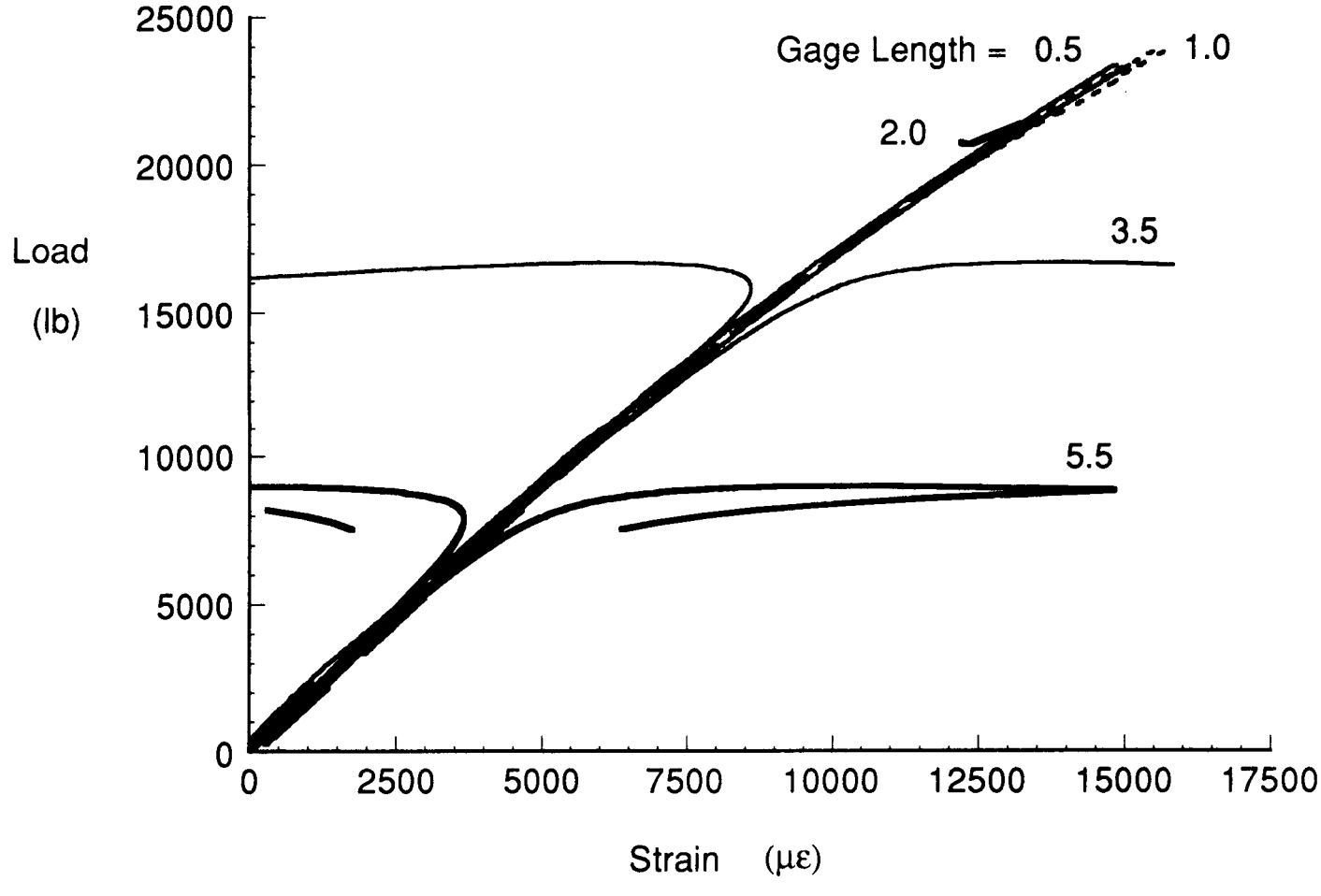

Figure 3. Loading response of baseline laminates at different gage lengths.

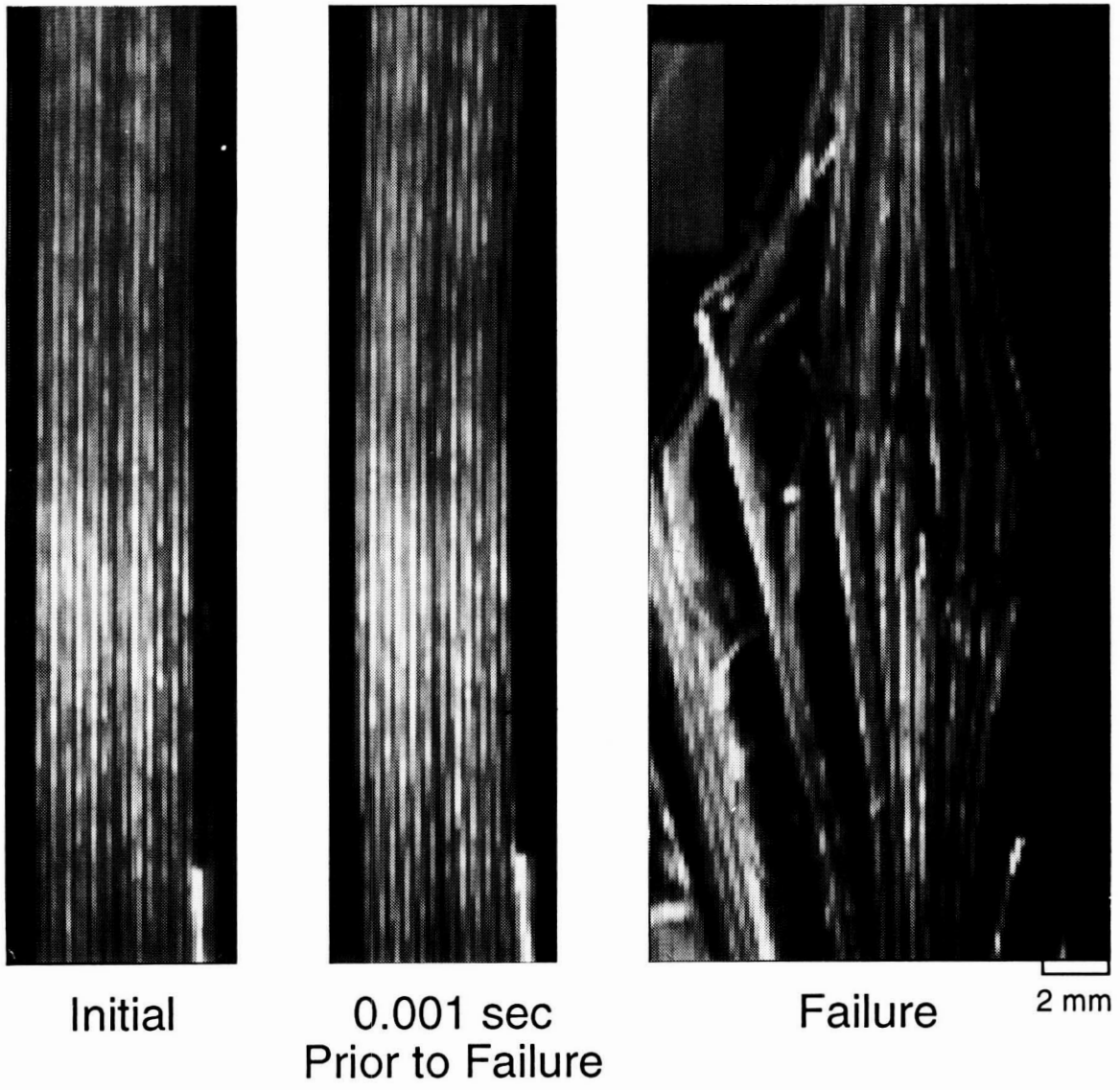

Figure. 4 Buckling failure of quasi-isotropic baseline laminate with a 3.5 in. gage length.

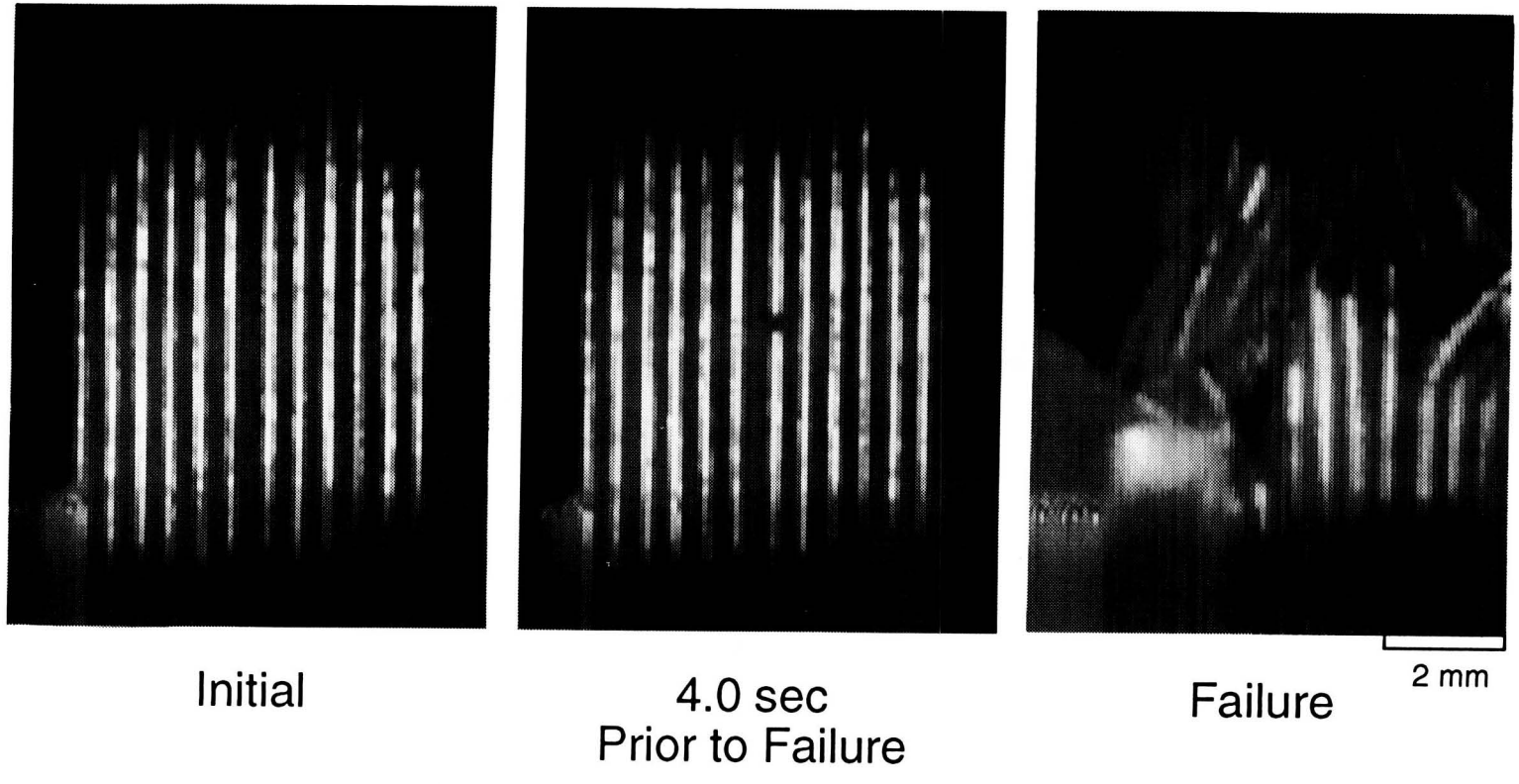

Figure. 5 Local failure in quasi-isotropic baseline laminate with a 0.5 in. gage length.

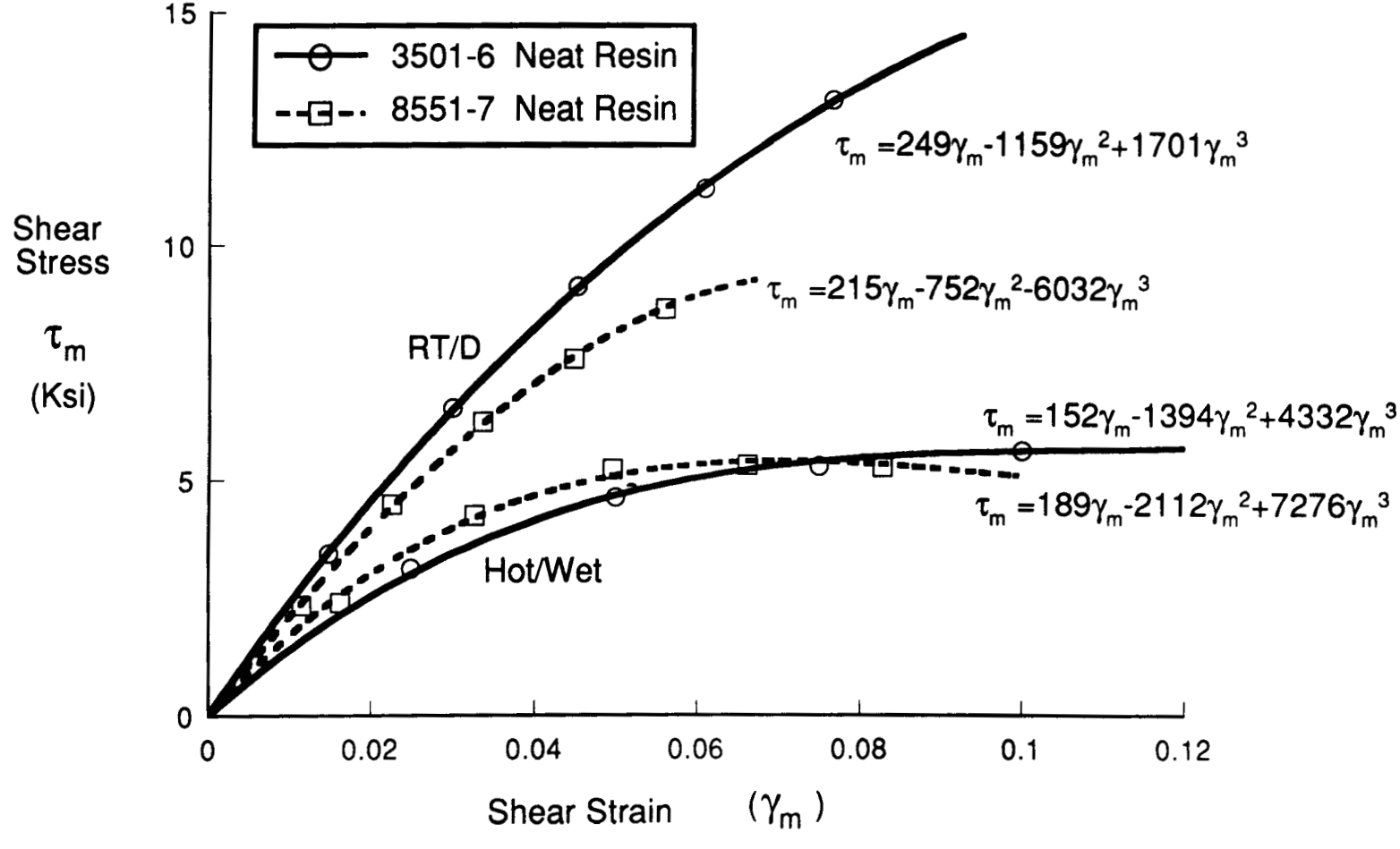

Figure 6. Shear response of 3501-6 [22] and 8551-7 [24] neat resins.

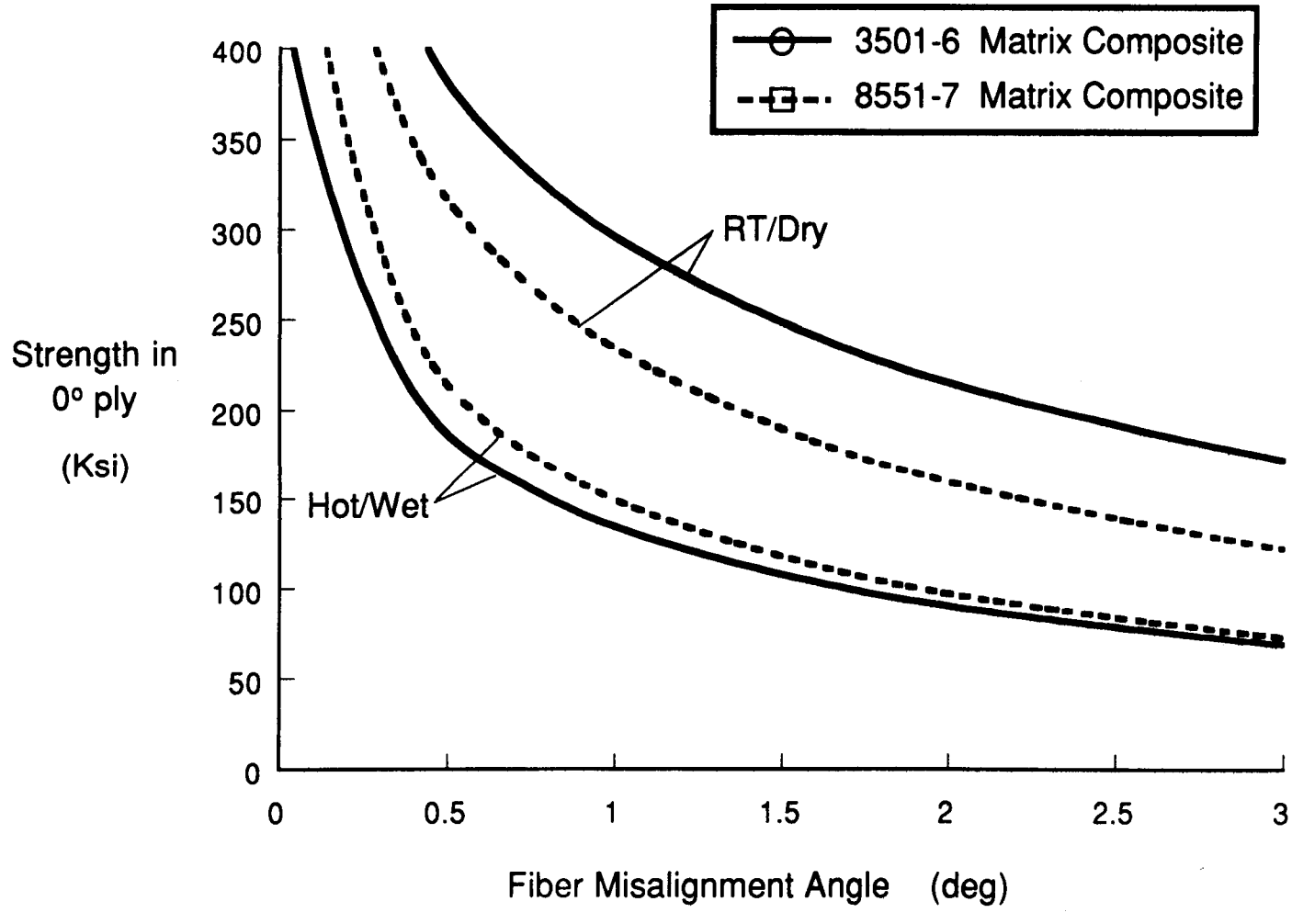

Figure 7. Strength predictions of fiber collapse model.

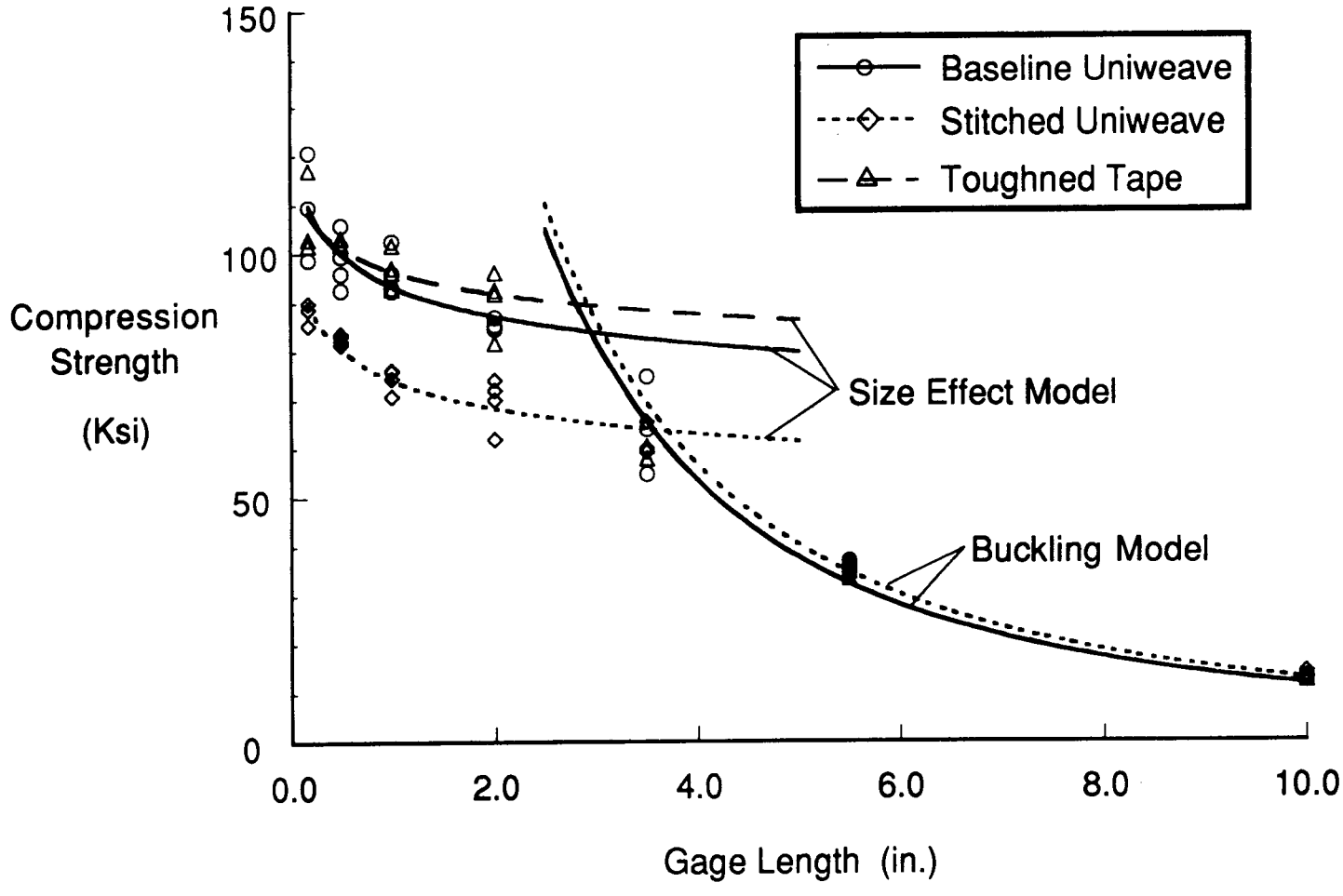

Figure 8. Compression strength of quasi-isotropic laminates under ambient conditions.

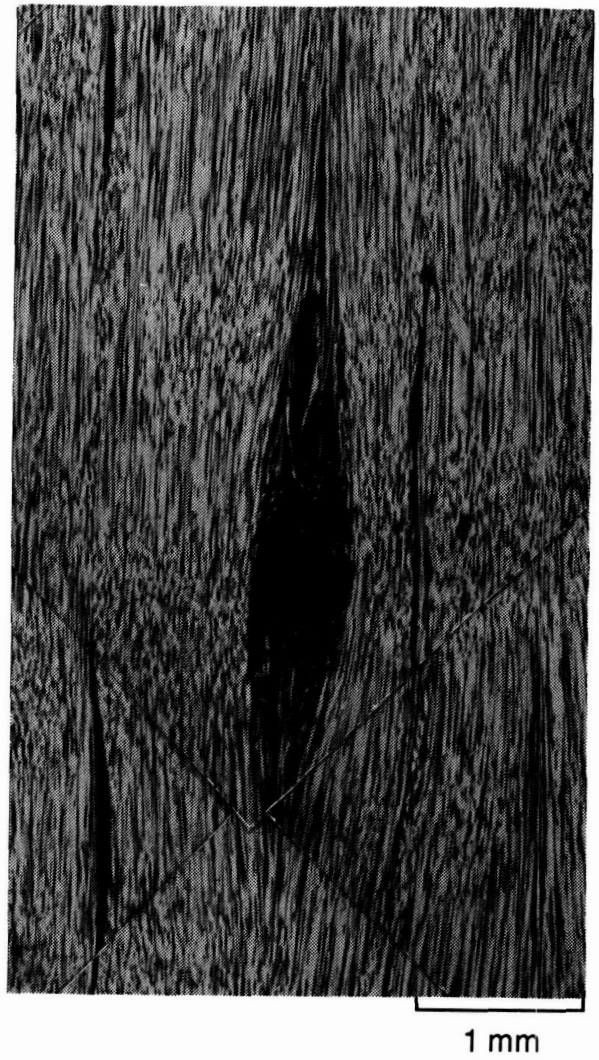

Figure. 9 Fiber orientation around a stitch.

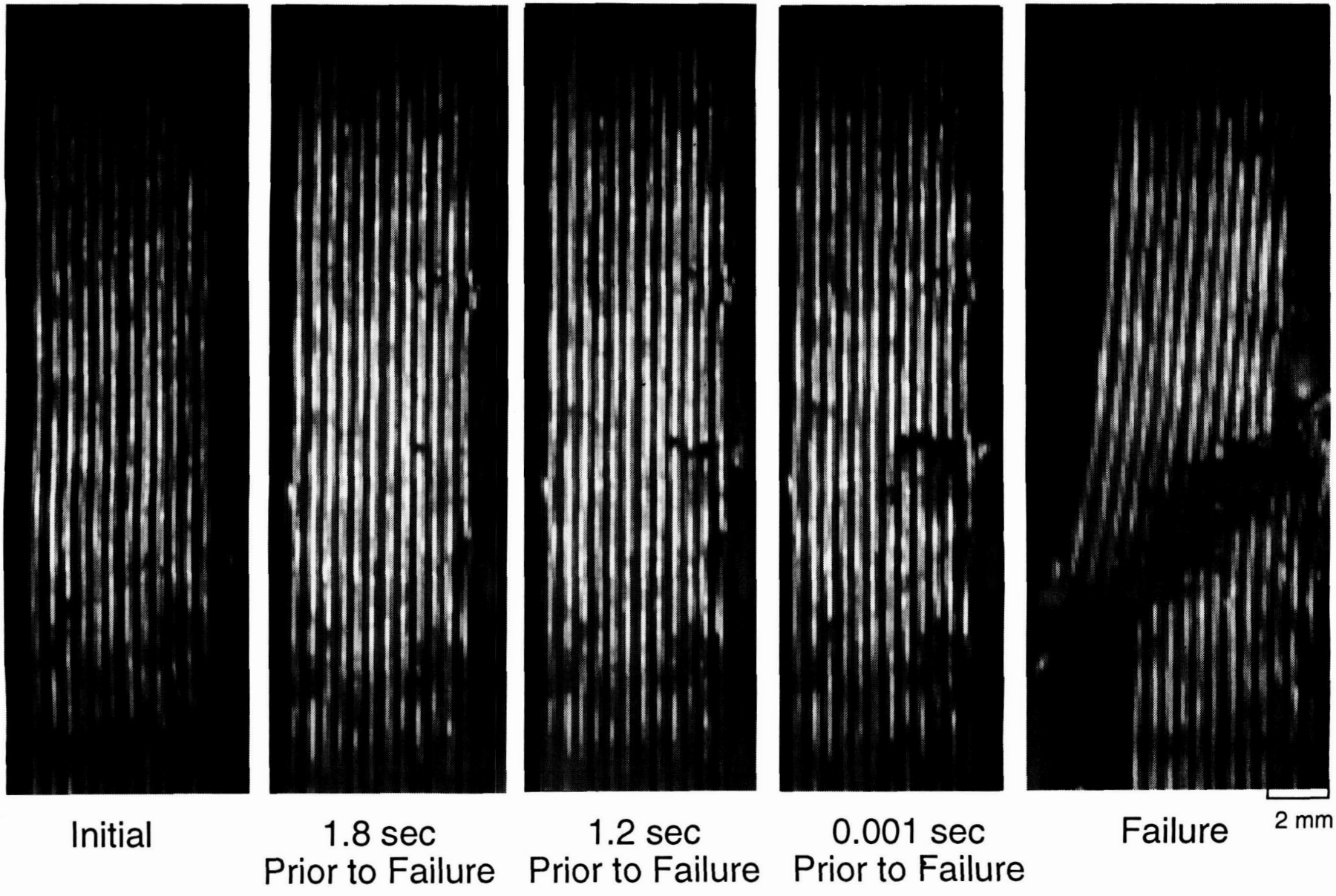

Figure. 10 Failure of quasi-isotropic stitched laminate with a 2 in. gage length

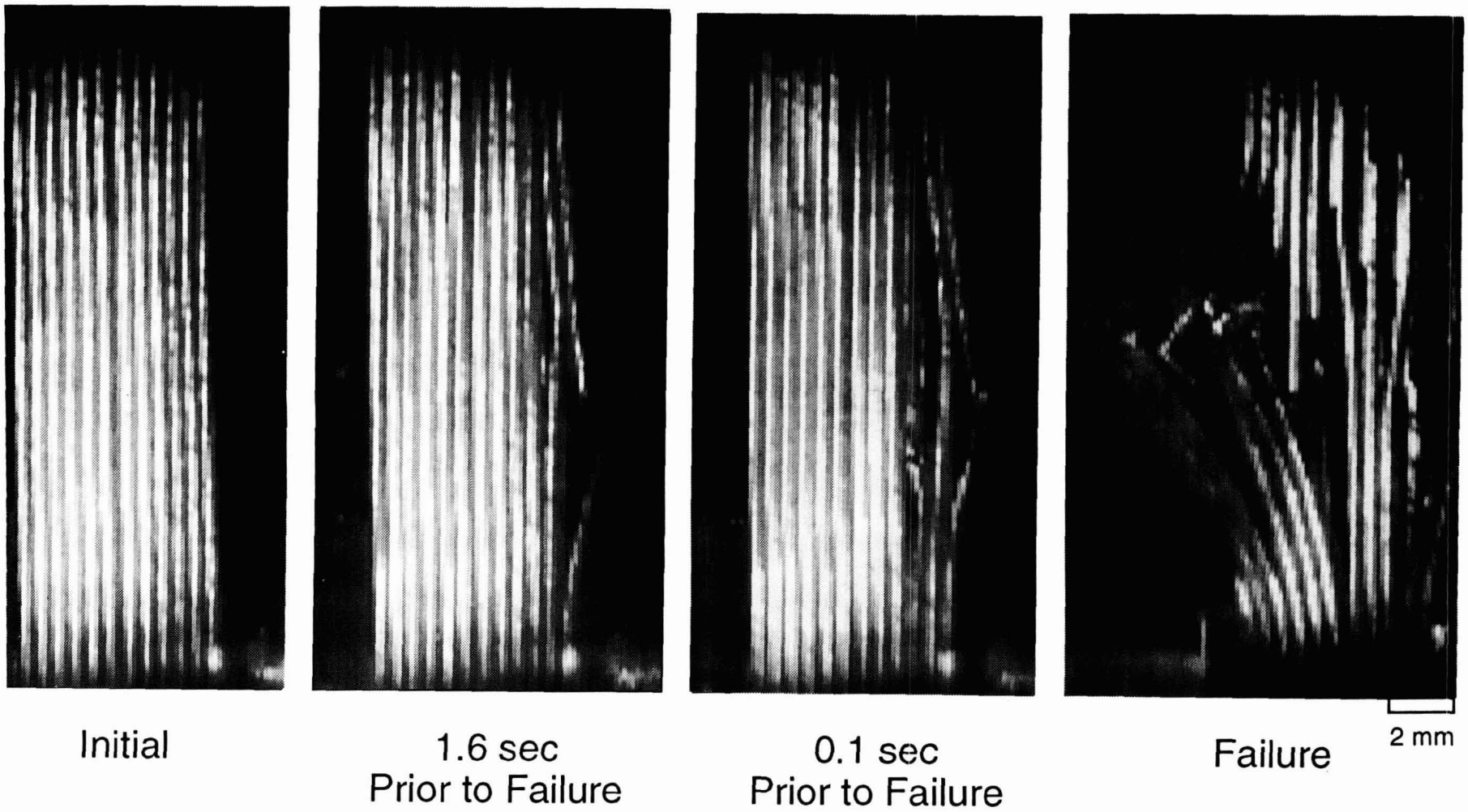

Figure. 11 Progressive delamination failure of toughened tape laminate with a 1 in. gage length

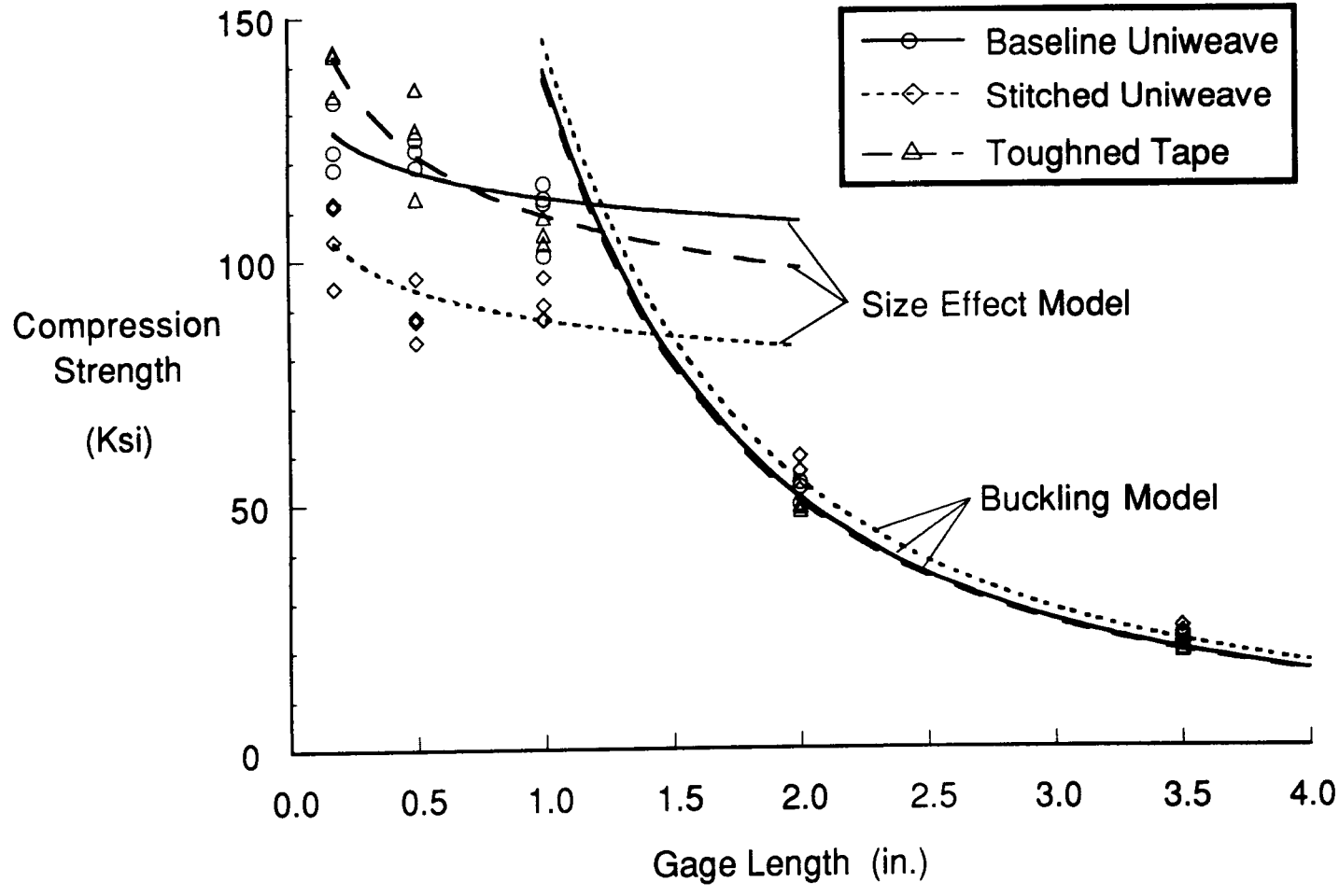

Figure 12. Compression strength of $(0/45/0/-45/90/-45/0/45/0)_s$ laminates under ambient conditions.

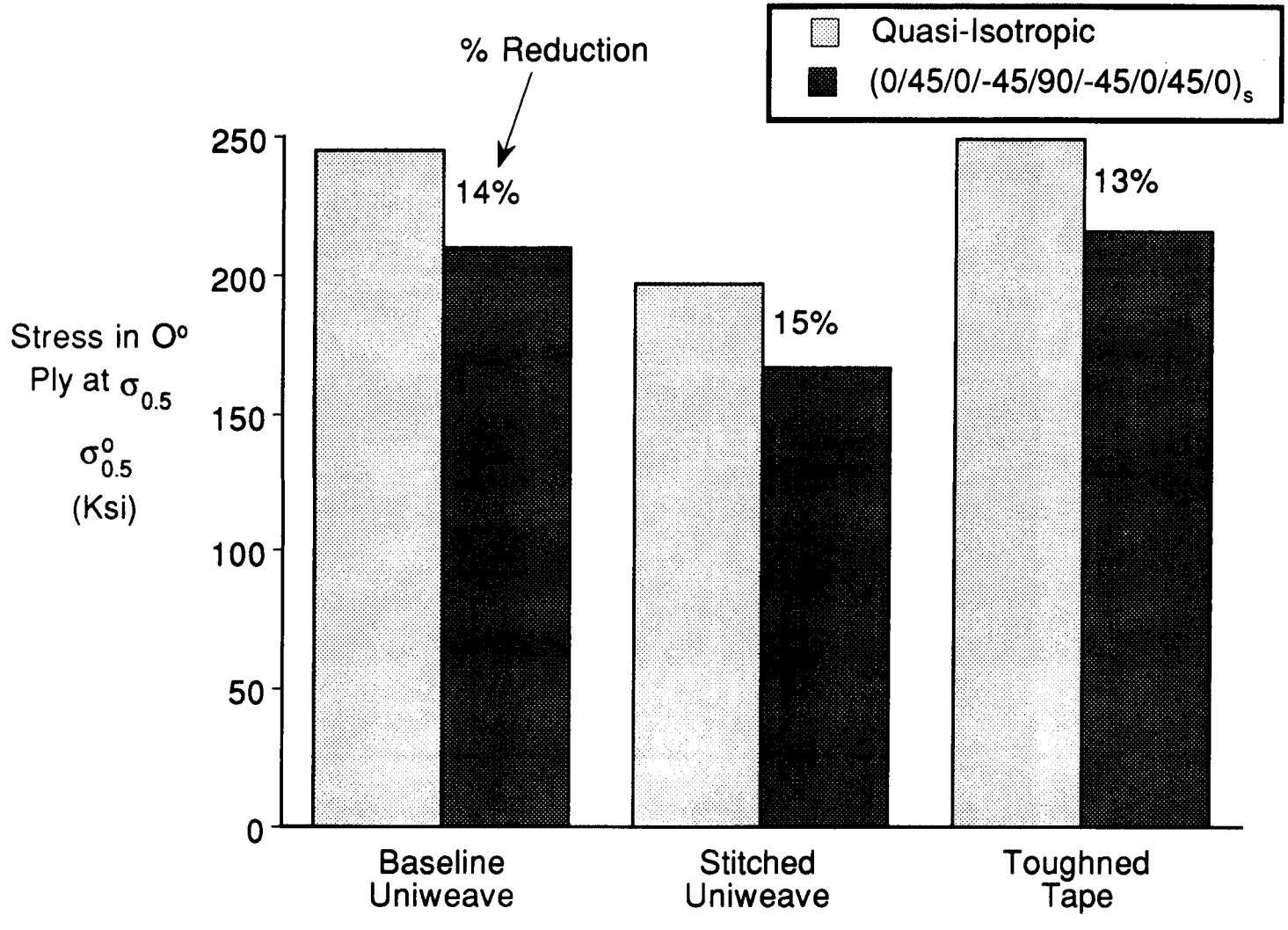

Figure 13. Comparison of the compression strength of different laminates.

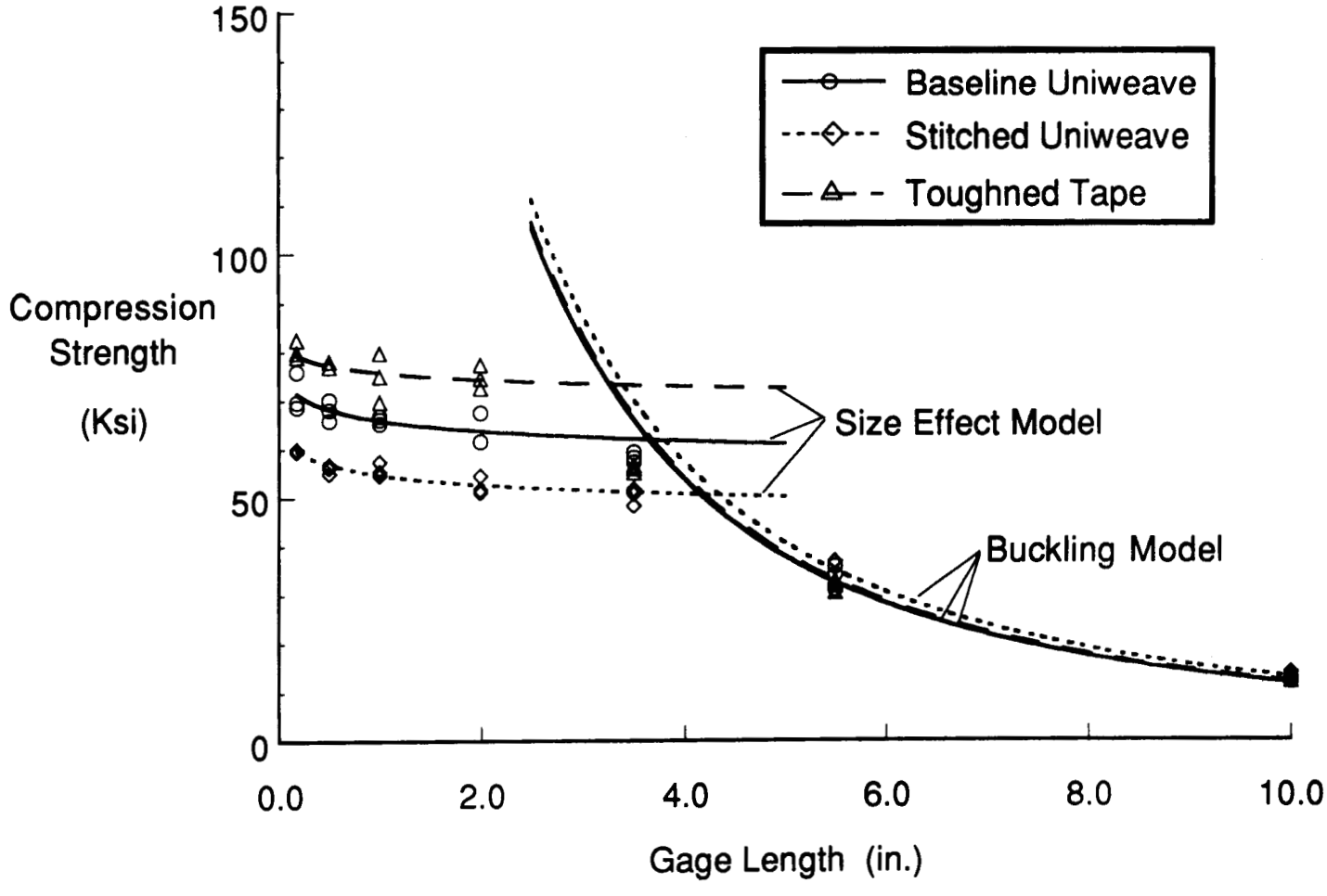

Figure 14. Compression strength of quasi-isotropic laminates under hot/wet conditions.

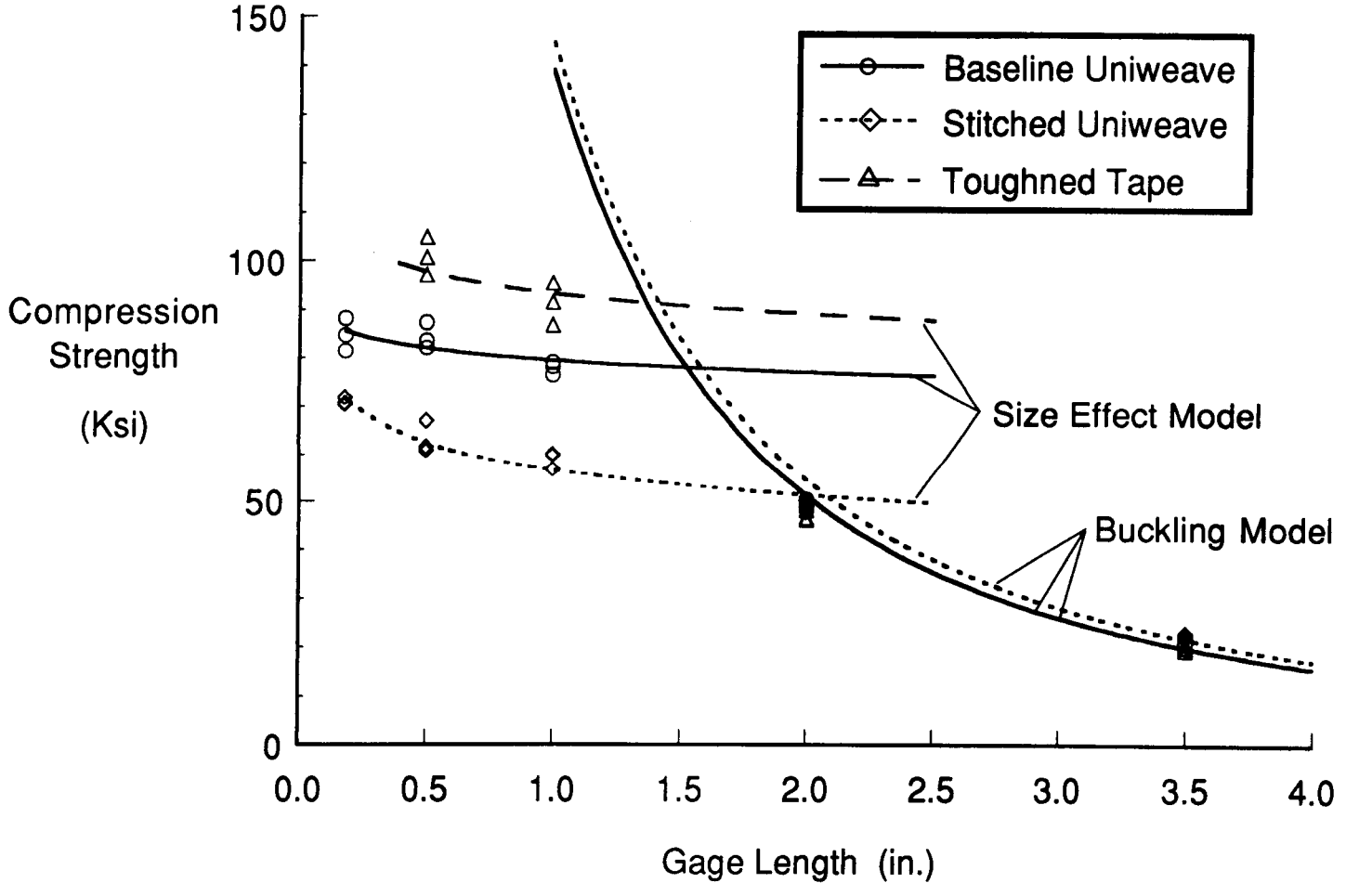

Figure 15. Compression strength of $(0/45/0/-45/90/-45/0/45/0)_s$ laminates under hot/wet conditions.

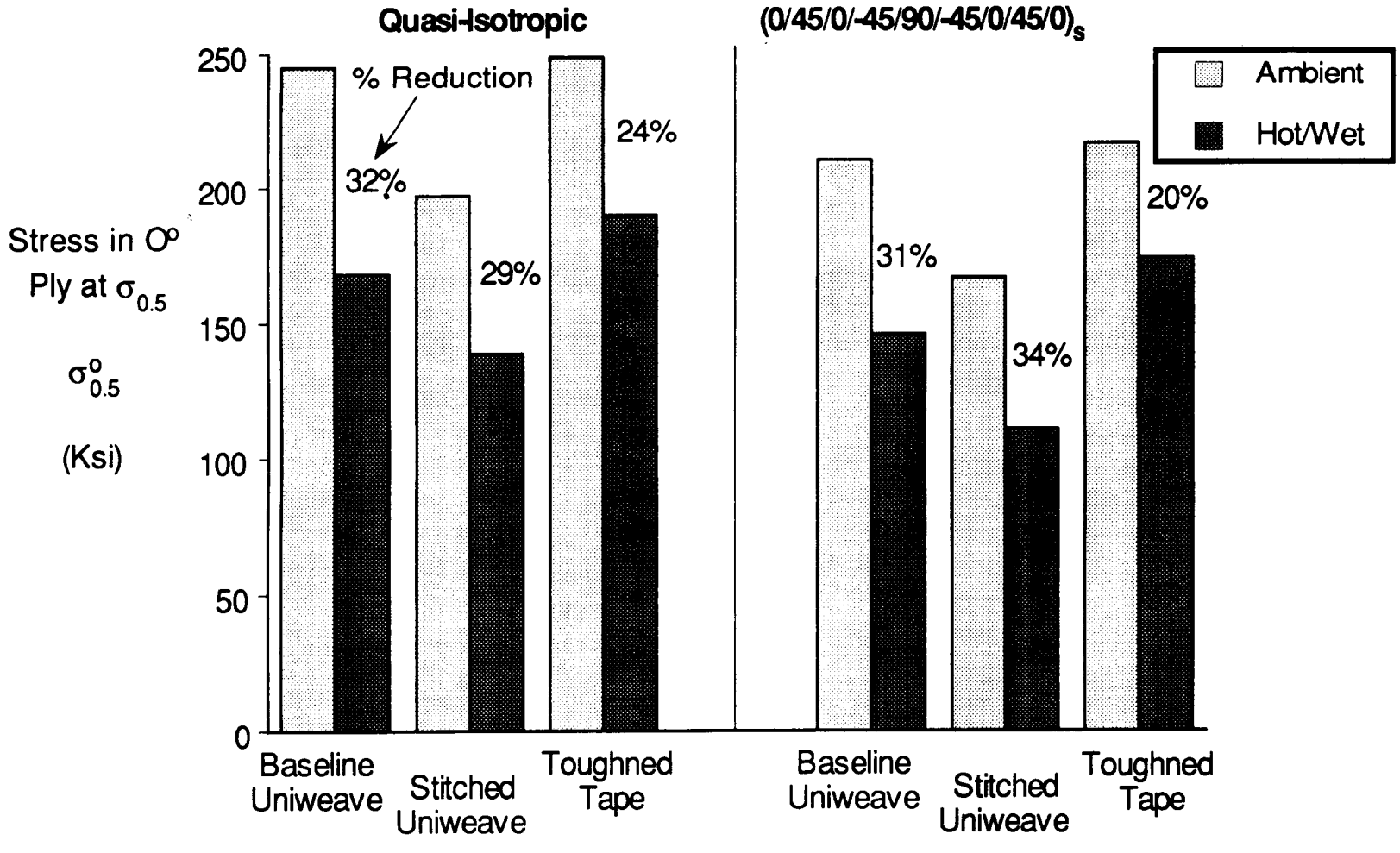

Figure 16. Effect of hot/wet conditions on compression strength.

TENSION STRENGTH, FAILURE PREDICTION AND DAMAGE MECHANISMS IN 2D TRIAXIAL BRAIDED COMPOSITES WITH NOTCH

Timothy L. Norman
Department of Mechanical and Aerospace Engineering
West Virginia University
Morgantown, WV

Colin Anglin
Department of Mechanical and Aerospace Engineering
West Virginia University
Morgantown, WV

SUMMARY

The unnotched and notched (open hole) tensile strength and failure mechanisms of two-dimensional (2D) triaxial braided composites were examined. The effect of notch size and notch position were investigated. Damage initiation and propagation in notched and unnotched coupons were also examined. Theory developed to predict the normal stress distribution near an open hole and failure for tape laminated composites was evaluated for its applicability to 2D triaxial braided textile composite materials. Four different fiber architectures were considered; braid angle, yarn and braider size, percentage of longitudinal yarns and braider angle varied. Tape laminates equivalent to textile composites were also constructed for comparison. Unnotched tape equivalents were stronger than braided textiles but exhibited greater notch sensitivity. Notched textiles and tape equivalents have roughly the same strength at large notch sizes. Two common damage mechanisms were found: braider yarn cracking and near notch longitudinal yarn splitting. Cracking was found to initiate in braider yarns in unnotched and notched coupons, and propagate in the direction of the braider yarns until failure. Damage initiation stress decreased with increasing braid angle. No significant differences in prediction of near notch strain between textile and tape equivalents could be detected for small braid angle, but the correlations were weak for textiles with large braid angle. Notch strength could not be predicted using existing anisotropic theory for braided textiles due to their insensitivity to notch.

INTRODUCTION

Textile composite materials are receiving recognition as potential candidate materials for increasing damage tolerance of structures. Design for damage has become especially important because of increased expected service life of aircraft. Textile composites offer through-the-thickness reinforcement which should aid in preventing propagation of damage. In addition to expected high damage tolerance, textile composite architecture can be tailored to suit strength and stiffness requirements. They also offer numerous options in material architecture and net shape geometry and enhance manufacturability of composites. Fibers and resins can be changed to optimize material performance. Typical textile composites include stitched, knitted, 2D and 3D woven and braided preform types. Although braider reinforcement increases damage tolerance, the performance of textile composites, e.g. strength, stiffness, toughness, is not understood. Open hole strength is often critical in design. Methodologies for characterizing textile material behavior, however, are currently not available. Specifically, no methodology is currently available to predict the effect of notch for textile composite materials.

In this investigation, our overall goal was to determine how open hole effects tension failure in 2D braided textile composite materials. We tested four 2D braided textile composite architectures with the following objectives:

- determine notch sensitivity
- determine notch position sensitivity
- evaluate applicability of anisotropic theory for strain and failure prediction
- document damage initiation and propagation mechanisms

Specifically, 2D braided textile composite materials with variations in percentage of 0 degree fibers, percentage of braider yarn fibers and braid angle yielding four distinct architectures were investigated to determine the effect of notch on strength. Notched and unnotched coupons were tested under static tension loading to failure to investigate the effects of hole size and hole placement on ultimate failure stress. Damage initiation and progression to failure were also characterized using radiographs and photomicrographs of polished cross-sections at specific load intervals. The normal strain distribution measured from the notched coupon with three different open hole sizes were compared to predictions made from the approximate solution proposed by Konish and Whitney [ref. 1] for anisotropic materials. The point stress failure criteria [ref. 2] was also evaluated for prediction of failure in notched textiles. The approximate solutions were evaluated as potential design tools for 2D braided textile composites with open hole. Tape laminates equivalent to textile composites were constructed for comparison to the textile composites.

MATERIALS AND METHODS

Materials and Specimen Preparation

Four distinct triaxially braided materials were constructed from AS-4 fabric impregnated with Shell 1895 epoxy resin. Braid angle, yarn and braider size, percentage of longitudinal yarns, or volumetric proportion of longitudinal yarns to total yarn content, and braider angle varied. A description of the triaxial braid pattern is provided by Masters et al. [ref. 3]. The nominal braid geometry and layup configuration is given in Table 1. In the table, the following nomenclature has been adopted in order to describe the layup:

$$[0_{XXk}/\pm\theta_{XXk}]\ Y\%\ \text{Axial}$$

where XX indicates the yarn size, k indicates thousands and Y indicates the percentage of axial yarns in the preform.

The 30.48 cm X 60.96 cm plates of nominal 2.54 mm thickness were machined into notched and unnotched coupons. Three different coupon sizes were machined: 2.54 cm wide unnotched and notched, 5.08 cm wide notched and 10.16 cm wide notched. Notch sizes were chosen to maintain a coupon width to hole diameter equal to 4 (W/D = 4). This criterion yields hole sizes of 6.35 mm, 12.7 mm and 25.4 mm for 2.54 cm, 5.08 cm and 10.16 cm wide coupons, respectively. Gage length to width ratio (L/W) was 4 for 2.54 cm and 5.08 cm wide coupons and was 2.25 for 10.16 cm wide coupons. Tape laminates of equivalent material and layup geometry were designed at NASA Langley and fabricated at West Virginia University Composite Materials Laboratory. The equivalent laminates were made from AS4/3501-6 prepreg tape and were designed to have equivalent total areal weights, cross-ply angle equal to braid angle, unit ply consisting of braider and longitudinal plies, equivalent number of textile layers (unit plies) and were designed to be as symmetric as possible (Table 1). Specimens of dimensions approximately the same as the textiles were fabricated.

Table 1. 2D braided textile and tape equivalent laminates.

2D Braided Material		Tape Equivalent Laminate
Type	Braid Material	Layup Geometry
LSS	$[0_{6k} / \pm 45_{15k}]12\%$	$(45 / -45)_2 / 0 / (45 / -45)_3 / 0 / (-45 / 45)_3 / 0 / (-45 / 45)_2$
LLS	$[0_{36k} / \pm 45_{15k}]46\%$	$45 / -45 / 0_3 / (45 / -45)_2 / 0_4 / (-45 / 45)_2 / 0_3 / -45 / 45$
SLL	$[0_{30k} / \pm 70_{6k}]46\%$	$(70 / -70 / 0_2)_2 / 0 / 70 / -70 / -70 / 70 / 0 / (0_2 / -70 / 70)_2$
LLL	$[0_{75k} / \pm 70_{15k}]46\%$	$70 / -70 / 0_3 / (70 / -70)_2 / 0_4 / (-70 / 70)_2 / 0_3 / -70 / 70$

Specimens of all material types were mounted with strain gages to measure remote strain and near notch normal strain distribution. For unnotched coupons, strain gages were mounted in the center of each coupon. Remote strain gages (MM CEA-13-500UW-120) were mounted in the center of the coupon half way between the notch and the end tabs. These strain gages measured 4.6 mm in width and 12.7 mm in length which satisfied our criterion that the gage be at least as long as 2 times the unit cell length (10.5 mm). A total of five strain gages were mounted adjacent to the circular hole to measure the normal strain distribution. CEA-13-015UW-120 gages were used for 2.54 cm width specimens and EA-13-031DE-120 gages were used for 5.08 cm and 10.16 cm width specimens. One Gage was placed on each side of the specimen as close to the notch as possible, approximately 0.9 mm. A third gage was place at approximately 4.6 mm for 2.54 cm and 5.08 cm specimens and 4.9 mm for 10.16 cm specimens away from the notch. A fourth gage was placed mid-way between the hole and the specimen edge and a fifth gage was placed at 2.54 mm from the specimen edge.

Experimental Procedure

Coupons were clamped between the grips of a servo-hydraulic testing machine (Interlaken, Minneapolis, Minn). An extensometer with a 2.54 cm gage length was mounted to the coupon on the opposite side of the coupon adjacent to the strain gage. This allowed comparisons between the strain gage and the extensometer. Coupons were subjected to a static tension load at a displacement rate of 0.254 mm/min while load, stroke and extensometer and strain gage strain were recorded. There were three different coupon groups for braided textile and tape equivalents: Load to failure, nondestructive evaluation (NDE) and destructive evaluation coupons. Load to failure coupons were loaded until catastrophic failure occurred and used as failure allowables. Notched and unnotched NDE coupons measuring 2.54 cm in width were loaded to designated load levels, removed from the testing machine and radiographed. The failure loads of these coupons were not included in the average of load to failure coupons. Coupons with widths measuring 5.08 cm and 10.16 cm were radiographed at specified intervals while mounted in the machine using a portable X-ray machine available at Langley Research Center. Notched and unnotched destructive evaluation coupons were loaded to 50%, 75% and 95% of the failure stress. Longitudinal, transverse and 45° cross sections were removed from coupons with a diamond blade sectioning saw. The sectioned composites were embedded in an epoxy-resin mount and polished using a

Buehler Ecomet 2 grinder-polisher (Buehler Inc., Lake Bluff, ILL.). Photomicrographs were taken using an Olympus (Lake Success, N.Y.) dissecting research microscope.

Method of Analysis

The presence of notches in a laminate creates the problem of stress concentrations around the cutouts. The approximate normal stress distribution away from the hole can be obtained through the use of the extended isotropic solution [refs. 1, 2, 4]:

$$\frac{\sigma(\xi)}{\sigma_o} = 1 + \frac{\xi^{-2}}{2} + \frac{3\xi^{-4}}{2} - \frac{K_T - 3}{2}(5\xi^{-6} - 7\xi^{-8}) \qquad (1)$$

where $\xi = x/R$ which is the distance from the center of the hole divided by the hole radius, $\sigma(\xi)$ is the stress at position ξ, and σ_o is the remote stress. Assuming the plate infinite when compared to the hole size

$$\sigma_{\theta\theta}\big|_{r=R} = f(\theta)\sigma_o \qquad (2)$$

where R is the hole radius and $f(\theta)$ is defined as

$$f(\theta) = \frac{E_\theta}{E_1}\Big[-(\cos^2\phi - (q+k)\sin^2\phi)q\cos^2\theta + ((1+k)\cos^2\phi - q\sin^2\phi)\sin^2\theta - k(1+q+k)\sin\phi\cos\phi\sin\theta\cos\theta\Big] \qquad (3)$$

where ϕ is the load angle, θ is the angle at which $\sigma\theta\theta$ is measured and $E\theta$, k, p and q depend on the material laminate properties E_1, E_2, G_{12} and v_{12}. The stress concentration factor, K_t, is the maximum value of $f(\theta)$. A computer program for calculating laminate stresses and strains using lamination theory was modified to include the extended isotropic solution.

RESULTS

Notch Sensitivity

Net failure stress of notched and unnotched textile and tape equivalent coupons have been normalized to 60% fiber volume fracture according to the relation $\sigma_{net\ (corr)} = \sigma_{net} * v_f/0.6$, where σ_{net} is the measured net stress, v_f is the measured fiber volume fraction and $\sigma_{net\ (corr)}$ is the corrected net failure stress. LLS tape laminates exhibit significant notch sensitivity at small notch sizes but the sensitivity lessons with increasing notch size. For the same architecture, the textile appears roughly notch insensitive and have approximately the same strength at all notch sizes. For the LLS textiles, there is no significant difference in notched and unnotched failure strengths, however, the notched textile data indicated slightly greater strength than the tape laminates. SLL tape exhibited greater notch sensitivity than the textiles at smaller notch sizes. The textile and tape equivalent have approximately the same notch failure strength at all notch sizes but the tape has higher unnotched strength. LLL tape exhibited significantly greater notch sensitivity than the LLL textile (Fig. 1). The textile and tape 1" hole specimens have approximately the same failure strength. In summary, in three of four architectures, the tape laminates exhibited greater

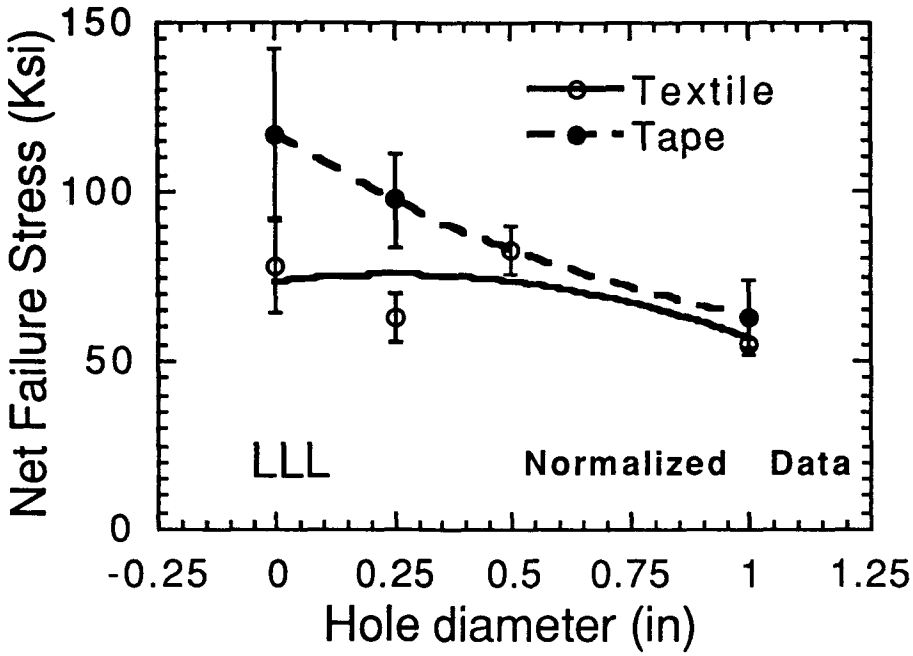

Fig. 1 Net failure stress for textile and tape equivalent LLL specimens.

notch sensitivity than the textiles. Even though the strength of the tape equivalents was greater initially, the strengths of the notched textiles and tape equivalents were approximately the same for the largest notch size tested. In the other case, the notch sensitivity was roughly equivalent.

Statistical analysis was used to detect significant differences in failure strength of the different architectures. The data were analyzed using two way ANOVA. The design variables were the combinations (LSS, LLS, SLL and LLL) and hole size. All combinations were not included in the test matrix making it difficult to attribute reason for significance among all combinations, but were enough to make the following comparisons:

- braid yarn size had no significant effect on stress ratio (notched strength to unnotched strength)
- axial yarn size had no significant effect on stress ratio
- braid angle had a significant effect on stress ratio.

Using the statistical analysis, optimum combinations according to hole size in terms of strength ratio were determined (Fig. 2). Based on the average strength for hole size, average failure strength:

- for the 0.25" hole LLL was significantly ($p > 0.05$) less than the other architectures
- for the 1.0" hole SLL was significantly less than the other architectures
- for the 0.5" hole LSS was significantly less than the other architectures
- for the 0.5" hole LLL was significantly greater than the other architectures

These optimum combinations provide a guideline for design of notched textile composites with the four architectures tested.

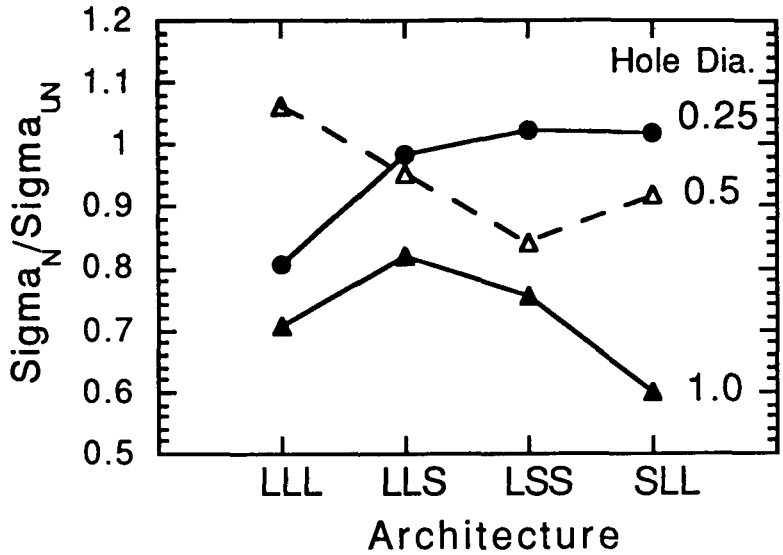

Figure 2. Architecture effect on hole size.

Notch Position Sensitivity

The coefficient of variation (COV) is defined as the standard deviation divided by the mean net failure stress. It was proposed earlier that COV could be used as an indicator of notch position sensitivity (i.e. if notched coupons exhibited larger COV than unnotched coupons for holes that are randomly placed, that it was an indication of notch position sensitivity). Using this criteria for the textiles alone, the LSS textile architecture was not sensitive to notch position whereas the LLS textile architecture was. This criteria was applied to the tape equivalents, which exhibited a similar trend. Because tape laminates should not be notch position sensitive (due to microscopic homogeneity), we concluded that variation of COV observed between architectures was a function of material geometry and not notch position sensitivity. Thus, our criteria was not valid measure of notch position sensitivity.

Near Notch Strain Predictions

Remote strain of the textile and tape equivalent materials was multiplied by the stress ratio corresponding to the position (ξ) of each gage location from which predicted strain-stress curves were generated. Measured strain-stress curves at each gage location were compared to predicted curves. An analysis of the slopes for observed vs. predicted was also performed. Results for LSS and LLS textile architectures indicated very good fits of the lines to the data. The trend line should be 0.00 + 1.00x, and both approximate that quite closely. The fit is a little better for the equivalent laminated material (seen in larger R^2), and correspondingly there is greater variability

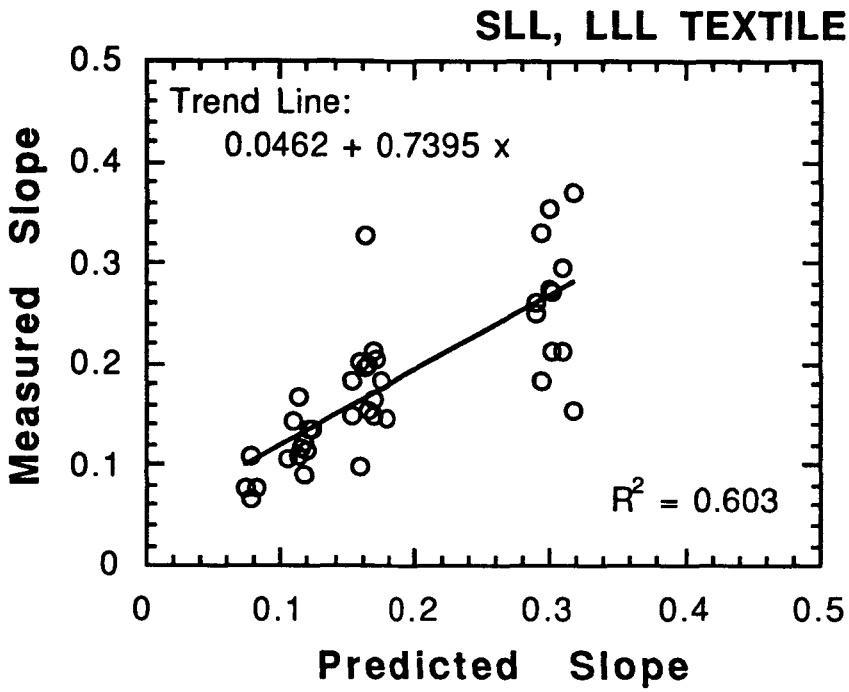

Figure 3. Correlation between measure and predicted near notch strain-stress curve.

from the trend line for braided textile (seen in larger error variance), but the differences weren't significant. Correlations for the slopes of SLL and LLL architectures (Fig. 3) were not as good as LLS and LSS, but were within an acceptable range. Measured and predicted slopes correlated significantly better for the tape equivalents than the braided textiles, with the Rsquare for the tape equivalents roughly equal to that of the LLS and LSS architectures. These data suggests that accuracy of predictions of near notch strain decreases with increasing braid angle for textiles.

Failure Prediction

Applicability of existing notch failure theory developed for anisotropic materials was tested for textile composites. Using the point stress failure theory developed by Whitney and Nuismer (1974), a characteristic distance d_o is calculated from experimentally measured notched and unnotched failure strengths. d_o is the distance between the edge of the notch and some point away from the notch where the stress is equal to the (unnotched) strength. Accurate near notch stress predictions for LSS and LLS architectures and to a lessor degree the SLL and LLL architectures supports the use of the point stress criteria.

Using the same stress concentration factor calculated for the near notch strain predictions described above along with the notched and the unnotched strength, d_o was calculated. As is seen by the notched failure data normalized by the unnotched data for the LLL architecture (Fig. 4), textiles are less notch sensitive than tape equivalents as indicated by large values of do for the

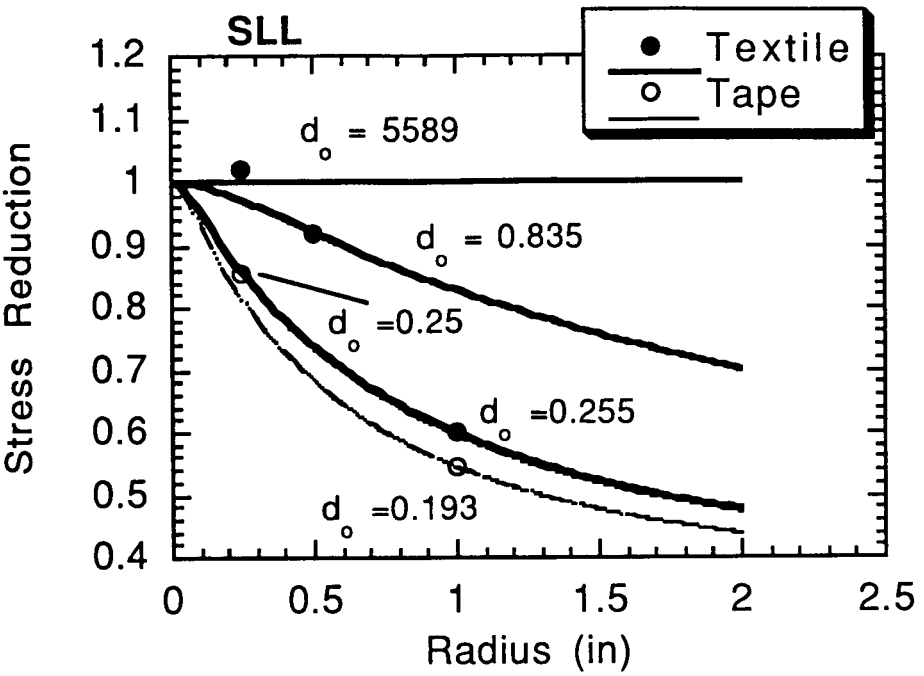

Figure 4. Point stress failure criteria for tape and textile coupons.

textiles and by the area under the stress ratio vs. hole radius curves (the textiles exhibit significantly greater d_o values and greater area under the curves than the tape equivalents). Values of d_o are unreasonable and physically unrealistic at small notch sizes for the textiles but are within an acceptable range for the tape equivalents.

Damage Initiation and Propagation Mechanisms

Radiographs and photomicrographs were used to determine damage initiation stress, damage growth mechanisms, crack locations and general failure characteristics. Only a summary of damage mechanisms is given here. A detailed discussion will be provided in a final report submitted to NASA at a later date.

Damage initiation stress of 1" notched and unnotched textiles coupons was determined using the radiographs of specimens taken at small intervals of loading (Fig. 5). The initiation stresses were normalized to the ultimate failure stress of the notched and unnotched coupons. The data in the figure indicates that damage initiation level and the difference between notched and unnotched initiation stress decreases with increasing braid angle.

Two dominate damage mechanisms were observed in notched textiles: braider yarn cracking and longitudinal yarn splitting. Longitudinal yarn splitting occurred near the notch for longitudinally dominated architectures and was associated with shear lag effect. Braider yarn cracking occurred along the coupon edge (in notched and unnotched) and along the notch edge. Crack density increased with little to no cracking observed in the longitudinal yarns until failure. One hypothesis for failure (ref. 5) is that braider yarn cracking increases in density and impinge upon the longitudinals. With many stress concentrations along the length of the longitudinal, the

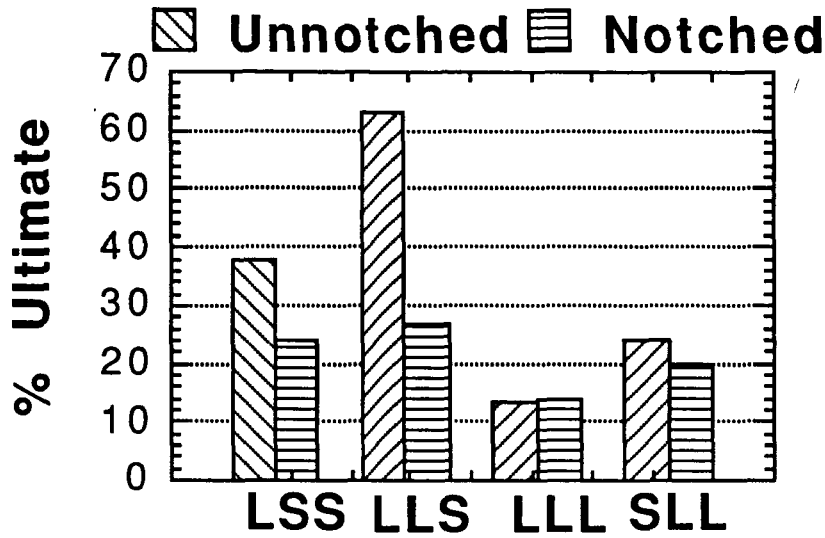

Figure 5. Damage initiation stress for textile 1" coupons.

yarn eventually fractures at some critical value. At the time of this report, damage studies have not been completed for the SLL and LLL architectures.

DISCUSSION AND CONCLUSIONS

For tension loading, which was the only loading considered, the textile composites exhibited notch insensitivity. In three of four cases, there was no reduction in failure strength for small notch sizes, and a relatively small reduction for larger notch sizes when compared to tape laminates. Even though the unnotched tape laminates where stronger than the unnotched textiles, after an open hole was placed in the coupons, the materials had roughly equivalent strengths. This is important since often open hole strength influences design, and, consequently, the textile structure can be designed for strength with less notch "knock-down" factor currently considered for tape laminates. Textiles composites structures can be designed for other desirable features, e.g. net shape fabrication, damage tolerance, with less penalty for open hole strength.

The notched textile composites also exhibited delamination suppression. It has been well documented that tape laminates have low damage tolerance due to weak lamina interface. This was demonstrated in our study radiographically and in photomicrographs. The longitudinal cracking in 0° plies of tape laminates that occurred near the notch due to shear transfer, or shear lag, propagated to the 0/±45 interface and then propagated in the form of delamination to the hole edge. Radiographs and photomicrographs of the textile indicated that longitudinal cracking near the notch due to shear lag was found in the longitudinal yarns and propagated to the outside perimeter of the yarn but did not propagate beyond its own interface, as there is no "ply interface" for propagation to occur. This may be a factor in the apparent notch insensitivity observed in this study. On a larger scale, delamination is a common failure mechanisms for large cutouts in composite structure. Our results suggests that use of textile composites may be beneficial for composite structure with cutouts that are large were delamination plays a role in failure.

In summary, the following conclusions have been made concerning the materials tested in this study:

- Generally speaking, unnotched tape equivalents are stronger than braided textiles but exhibited greater notch sensitivity.
- Notched textiles and tape equivalents have roughly the same strength at large notch sizes.
- Notch position sensitivity could not be tested by COV.
- No significant differences in prediction of near notch strain between textile and tape equivalents could be detected for small braid angle, but the correlations were weak for textiles with large braid angle.
- Notch strength could not be predicted using existing anisotropic theory for braided textiles.
- Damage initiation stress decreases with increasing braid angle.
- Braider yarn cracking dominates failure process.

ACKNOWLEDGMENT

The authors would like to thank the National Aeronautics and Space Administration for their support of this work under grant No.NAG-1-1381. The authors would also like to thank Mr. C.C. (Buddy) Poe of Langley Research Center and Dr. John Masters of Lockheed Aircraft Co. for their invaluable discussions and support.

REFERENCES

1. Konish, H. J. and Whitney, J. M. 1975. J. Composite Materials, 9:157-166.

2. Whitney, J. M. and Nuismer, R. J. 1974. J. Composite Materials, 8:253-265.
3. Masters, J. E., Foye, R. L., Pastore, C. M. and Gowayed, Y. A. 1993. Journal of Composites Technology and Research, 15:112-122.
4. Lekhnitskii, J. E. 1963. Theory of Elasticity of an Anisotropic Body. San Francisco, CA: Holden-Day.
5. Norman, T. L. and Patrick, M. 1994. J. Comp. Tech. & Res., *in press.*

EXPERIMENTAL INVESTIGATION OF TEXTILE COMPOSITE MATERIALS USING MOIRÉ INTERFEROMETRY

Peter G. Ifju

University of Florida
Aerospace Engineering, Mechanics & Engineering Science Department
Gainesville, FL 32611-6250

ABSTRACT

The viability as an efficient aircraft material of advanced textile composites is currently being addressed in the NASA Advanced Composites Technology (ACT) Program. One of the expected milestones of the program is to develop standard test methods for these complex material systems. Current test methods for laminated composites may not be optimum for textile composites, since the architecture of the textile induces nonuniform deformation characteristics on the scale of the smallest repeating unit of the architecture. The smallest repeating unit, also called the unit cell, is often larger than the strain gages used for testing of tape composites. As a result, extending laminated composite test practices to textiles can often lead to pronounced scatter in material property measurements. It has been speculated that the fiber architectures produce significant surface strain nonuniformities, however, the magnitudes were not well understood. Moiré interferometry, characterized by full-field information, high displacement sensitivity, and high spatial resolution, is well suited to document the surface strain on textile composites. Studies at the NASA Langley Research Center on a variety of textile architectures including 2-D braids and 3-D weaves, has evidenced the merits of using moiré interferometry to guide in test method development for textile composites. Moiré was used to support tensile testing by validating instrumentation practices and documenting damage mechanisms. It was used to validate shear test methods by mapping the full-field deformation of shear specimens. Moiré was used to validate open hole tension experiments to determine the strain concentration and compare then to numeric predictions. It was used for through-the-thickness tensile strength test method development, to verify capabilities for testing of both 2-D and 3-D material systems. For all of these examples, moiré interferometry provided vision so that test methods could be developed with less speculation and more documentation.

INTRODUCTION

Advanced textile composite materials are currently being evaluated as potential structural materials for aircraft at the NASA Langley Research Center. Textile composites have the potential for distinct advantages over laminated composites including, net-shape fiber preform production, which increases the potential for automation. Additionally, they can be made to incorporate through-the-thickness reinforcement for increased interlaminar stiffness, strength and impact damage reduction. Textile composites can be produced via braiding, weaving, knitting or stitching of yarns made from advanced fibers such as carbon, aramid and glass. The polymer matrix is introduced through resin transfer molding, thin film adhesives or powder coating of the yarns. Fiber reinforcement can be made to form a three dimensional sub-structure to give desired properties in prescribed directions. The geometry of the sub-structure also called the fiber architecture forms a repeating pattern, the smallest of which is called the unit cell. For some architectures the volume of the unit cell can be quite large and the exposed area at the specimen surface can be larger than strain gages used for testing of laminated composite materials. If strain

variations exist over the area of the unit cell, significant problems may arise if standard mechanical testing practices used for homogeneous materials are extended to textile composites.

Some of the basic questions that are of paramount importance to the textile composites testing community are, how much variation in strain exists over the unit cell, how much variation exists amongst neighboring unit cells and how do the variations affect the mechanical property characterization for such materials. Even though laminated composites are not homogeneous on the fiber scale, they are over the bondable resistance strain gage scale. Textile composites, however, are not homogeneous over the strain gage scale since the fiber architecture or substructure is on the same scale as strain gages. Additionally, it was found that using smaller gages led to increased scatter in material property measurements [1]. These finds suggest strain variations on the surface of textile composites, although the magnitudes of these variations could not be documented since strain gages average the strain over the region they span and hence do not have adequate spatial resolution. This is where a full-field method such as moiré interferometry [2] with high spatial resolution and strain sensitivity can play a significant role in the understanding of how much variation occurs on the surface of textile composites. Moiré interferometry is a well established experimental technique currently in its second decade of use. Its sensitivity, spatial resolution and full-field capabilities have provided the basis for a "marriage" between the technique and composite materials.

While moiré interferometry is limited to 2-D surface measurements, it can still be very useful in documenting various behaviors in order to guide and give "vision" to the experimentalist whose goal is to develop standard test methods for textile composites and other such innovative materials. This paper gives examples of how moiré interferometry was used in the Advanced Composites Technology (ACT) Program. Four material behaviors were investigated using moiré interferometry; in-plane tension, in-plane shear, through-the-thickness tension, and open-hole tension.

MATERIALS TESTED

Two categories of textile composites were evaluated in these studies, 2-D triaxial braids and 3-D woven composites [3]. The yarns were composed of AS4 graphite fibers and the matrix was Shell 1895. The composite panels were manufactured via resin transfer molding. Figure 1 illustrates the fiber architectures for the materials tested. Panels with significantly different mechanical properties were made by varying the yarn sizes and braider yarn directions. Table I lists all of the 2-D braids and 3-D weaves that were tested in the NASA Langley effort.

The 2-D triaxial braids are referred to as 2-D since they are composed of layers with no reinforcement interconnecting the layers. They are triaxial since the yarns are oriented in the plane along three directions: the braiders oriented at $+\alpha$ and $-\alpha$ and the axials oriented at 0°. The braids were of a 2/2 pattern where the braider yarns oriented at $+\alpha$ continuously pass over two $-\alpha$ yarns and then under two $-\alpha$ yarns. The 3-D woven materials have in-plane reinforcement aligned in the 0° and 90° direction with the through-the-thickness reinforcement either interconnecting successive layers or traversing the entire thickness. Three through-the-thickness yarn architectures were investigated; orthogonal interlock (OS-n), layer-to-layer interlock (LS-n) and through-the-thickness interlock (TS-n).

MOIRÉ INTERFEROMETRY

Moiré interferometry is an optical experimental technique. It is characterized by high in-plane displacement sensitivity, full-field capabilities, high spatial resolution and high signal to noise ratio. The method involves replicating a very high frequency (30,480 lines per inch or 1200 lines per mm) crossed-line diffraction grating on the surface of the test specimen. The

grating is thin, typically about 0.001 inches, and deforms freely with the specimen. A laser based moiré interferometer is then used to interrogate the deformed moiré grating. The resulting output is a fringe pattern that represents the displacements on the specimen surface, Since a crossed-line grating is used, both the displacements in the x direction (U-field), and the displacements in the y direction (V-field) can be obtained. The displacement sensitivity of the technique is determined by the frequency of the specimen grating. In these studies a standard sensitivity of 0.417 μm per fringe order was used. From the two displacement fields, the normal strains ε_x and ε_y and the shear strain γ_{xy} can be evaluated. In general, the strain is proportional to the frequency of the fringe pattern. For instance the normal strain ε_y is calculated by determining the y spacing of the fringes in the V-field pattern, then multiplying by a constant of proportionality which is dependent on the grating frequency used. Simplistically, areas of dense fringes correspond to areas of high strain.

TENSILE TESTING OF 2-D TRIAXIAL BRAIDS

A series of tensile tests were performed on the braided textile architectures in Table I. Moiré interferometry was used to determine the displacement fields on the surface of specimens loaded in both the axial and transverse directions. All of the specimens were 1.5 inches wide and nominally 0.125 inches thick with the moiré fringe patterns taken in the middle of the specimens. The moiré patterns represent the full width (1.5 inches) and a height of 1.33 inches. The specimens were loaded in a 10,000 lb. capacity screw driven testing machine.

For comparative purposes a tensile test was performed on a unidirectional laminated composite specimen, to illustrate the amount of nonuniform behavior of the textile materials. The AS4/3501-6 laminated composite was loaded along the fiber direction. Figure 2 shows the displacements in the loading direction (V-field) and the displacements in the orthogonal direction (U-field). The V-field pattern contains evenly spaced horizontal fringes where the points on any fringe have been displaced vertically with respect to the points on a neighboring fringe. The displacement field represents uniform tension. Since the spacing of the fringes is constant throughout the fringe pattern the strains are also constant or uniform. The U-field fringe pattern illustrates the horizontal displacements. The pattern shows that there is uniform Poisson contraction. Again, the deformation is constant throughout. By contrast, the deformation fields on the surface of the textile architectures are much more nonuniform. The following sections will display the moiré interferometry fringe patterns for the four architectures loaded in both the axial (parallel to the axial yarns) and transverse (perpendicular to the axial yarns) directions.

(SLL) Small Braider Yarns, Large Axial Yarn percentage, Large Braid Angle

Axial Loading

The moiré interferometry fringe patterns for the axially loaded SLL braid at a nominal stress level of 12 ksi are pictured in Fig. 3. The V-field fringe pattern is the displacement field in the direction of loading and the U-field is the fringe pattern in the orthogonal direction. From the V-field, the fringes are generally horizontal, however they are wavy and the fringe spacing is not uniform. The patterns display nonuniform strain. Additionally, the fringes vaguely form a repeating pattern. This repeating pattern follows the repeating pattern of the textile architecture although the faithfulness of the repetition was not strict. This means that nominally equivalent unit cells do not deform in an identical fashion. This is likely do to imperfections in the architecture, nesting effects, or variations in fiber volume. Hence to analyze the deformation of one unit cell would not yield a representative quantity. It is however important to note the a typical magnitude of variation within a representative unit cell. The variation of maximum

normal strain in the loading direction was typically about twice the value of the minimum normal strain.

The U-field fringe pattern for axial load has basically vertical fringes that contain abrupt jogs. The jogs in the fringes are a result of high shear strains between the braider yarns. The shear strains are restricted to the compliant resin rich region between the braider yarns and result from the relative motions of the braider yarns. The magnitude of these shear strains are on the same order as the magnitude of the applied normal strain.

The specimens were loaded up to 30 ksi. There were no cracks on the specimen surface at that load level.

Transverse Loading

The moiré interferometry fringe patterns for the SLL architecture at a nominal stress level of 6 ksi are illustrated in Fig. 4. From the patterns it is immediately evident that the strains are not uniform on the surface of the specimen. There does, however, appear to be a repeating pattern. The V-field shows that the normal strain in the loading direction varies along the length of the specimen. The variation is not confined to the unit cell but forms a global material response. By analyzing the deformation on the surface, the specimen would appear to be made of compliant and stiff materials arranged in series along the loading direction. Areas of lower strain are located above the cross-over regions of the braider yarns, whereas the areas of high strain were located above the braiders between the cross-over regions. The maximum strains were on the order of twice the minimum strain on the surface. This behavior was unexpected and counterintuitive. Since the braided materials have random nesting, one would expect the behavior to be dependent on the nesting. Moreover, it is not believed that the strain variation is present through the entire thickness. If this were the case, large through-the-thickness shear strains must exist in the specimen.

In addition to the cyclic normal strain variation there are also large shear strains present between the braider yarns. This can be seen by the abrupt jogs in the fringes between the braider yarns. The shear strain between the braider yarns are on the order of the applied average normal strain. The high shear strains also coincide with the zones of high normal strain and the combination or resolved maximum normal and shear strain are around twice the applied average normal strain.

The U-field fringe pattern consists of a series of sinusoidal fringes that snake up the length of the specimen. The period of the sinusoid matches that of twice the length of the unit cell. A cyclic pattern results as the braider yarns rotate in unison in a scissor action to accommodate the tensile load. The resulting rotation of the braider yarns act to deform the specimen in a sinusoidal shape.

Upon subsequent loading of the specimen, damage in two forms was evidenced. The first cracks, at around 18 ksi, were along the axial yarns, which, for the transversely loaded specimen, run perpendicular to the loading direction and are located under the braider yarns between the cross-over regions. The cracks could not be view on the surface, however the moiré patterns revealed them as anomalies in the otherwise repeating pattern. The second form of damage in the specimen was cracking along the direction of the braider yarns. The cracks were in the resin rich region between the braider yarns at the same locations where the combined normal and shear strains were highest. The third fringe pattern in Fig. 4 is the zero load pattern taken after unloading from 21 ksi tensile stress. The cracks are clearly visible in the displacement field.

The specimen also exhibits an edge effected zone. There is a distinct difference in the fringe pattern near the two sides of the specimen. The edge effected zone covers the entire length and penetrates into the specimen a distance equivalent to the width of one braider yarn.

(LLL) Large Braider Yarns, Large Axial Yarn Percentage, Large Braid Angle

The LLL braid is an architecture that was intended to be a scaled-up version of the SLL. The braid angle and the percentage of axial yarns are nominally the same. The two materials behave similarly in tension except that the LLL architecture in general had a more pronounce variation in strain. Additionally, damage was detected in the specimen at an earlier stress level.

Axial Loading

The fringe patterns for the axially loaded LLL specimen at the nominal stress level of 12 ksi are shown in Fig. 5. The patterns are similar in nature to those for the SLL architecture in that there is some trend in the repeatability of the deformation fields, but the faithfulness of repetition was not strict. Maximum strain within any unit cell was about twice that of the minimum strain value within the same unit cell. For some extreme cases the ratio was as high as 2.5. The U-field, as with that of the SLL specimen, displayed high shear strains between the braider yarns. Additionally, the edge effected zone was small.

The axial specimen was loaded until damage, in the form of cracking, was detectable. Cracking occurred at the 24 ksi stress level. The third fringe pattern in the group is the zero load pattern taken after the specimen was loaded to 28 ksi and then unloaded. In the pattern, cracks can be seen along the braider yarns.

Transverse Loading

The transversely loaded LLL specimen, pictured in Fig. 6, showed an alarming strain variation. The stress level pictured is nominally the same as that pictured for the SLL transversely loaded specimen, namely 6 ksi. As with the SLL specimen, the strain variation breached the confines of the unit cell and formed a global specimen response. The ratio of maximum strain to minimum strain within a typical unit cell was on the order of 4. The high strain regions had strains that were twice that of the average strain. The variation cycled with a period equal to twice the unit cell length.

The U-field fringe pattern shows the same trend as the SLL specimen. The braiders rotated in unison and high shear strain was present between them. The specimen takes on a sinusoidal shape as the braider yarns align with the tensile load.

The specimen also exhibits an edge effected zone on the two sides of the specimen. The edge effected zone runs the length of the specimen and permeates into the specimen a distance equivalent to the width of one braider yarn.

The third fringe pattern in the figure shows the damage in the specimen after it was unloaded from the 12 ksi stress level. In the pattern, cracks can be seen in the region where there are axial yarns running underneath the braider yarns. Small cracks appear as bulls eye patterns. The row of these patterns in the upper portion of the picture are small cracks on the surface which connect up with a crack in the axial yarn underneath. Cracking occurred at a much lower load level than for the SLL specimen.

Figure 7 shows the normal strain contours and the shear strain contours plotted on top of a small portion of the specimen. The strain contours were plotted using software developed by the IMB Corporation. Strain contours are plotted over an area with dimensions of one unit cell in the vertical direction, and two unit cells in the horizontal direction. High strain regions are distinguished by light shading and low strain regions are illustrated by dark shading. From the contour plot, the dark region corresponds to the braid cross-over region. The light shading

corresponds to the region where the axial yarns run underneath the braider yarns. The highest strain corresponds to the resin rich zones above where the axial yarns run. Cracking of the specimen corresponded with zones where the strain was highest.

In summary, the strain fields for the transversely loaded LLL specimen showed the same characteristic deformation patterns as the SLL, however the magnitude of the variation was more pronounced for the LLL architecture. Since the only major difference between the two architectures is the scale, it is believed that using larger yarns leads to more nonuniformity in strain. The two specimen types displayed nominally equal stiffness, hence the nonuniformities had no effect on the elastic properties. However, it is believed that early damage in the LLL specimen was a direct result of the strain nonuniformity.

(LLS) Large Braider Yarns, Large Axial Yarn Percentage, Small Braid Angle

The LLS fiber architecture was designed to have a large percentage of axial yarns and a relatively small percentage of braider yarns oriented at 45 deg. The braider yarns for this architecture experienced considerable crimp. As received, the specimens for this architecture appeared to have a less systematic fiber architecture. In other words the braid pattern was less orderly, possibly due to mishandling during processing of the specimen.

Axial Loading

The fringe patterns for the LLS specimen at the 12 ksi stress level are pictured in Fig. 8. From the V-field fringe pattern, a distinct repetitive pattern is not present. It is believed this is a result of the poor quality of the specimen material. Strain variations exist on the surface of the specimen, although the variations are not systematic. There are regions of very high normal and shear strain where the maximum strain were about twice the average applied normal strain. There was little or no edge effect detected in the specimen since the fringe pattern near the free edge is consistent with that of the interior.

The U-field, unlike the V-field, shows a distinct repeating pattern. In the pattern the fringes are jagged and reveal strong shear strain in the resin rich zones. Also in the pattern the fringe density is somewhat more dense than the LLL or the SLL specimens. Thus revealing a larger Poisson effect.

The specimen was loaded up to 30 ksi. There was no detectable damage in the specimen. The poor quality of the specimen did not seem to affect damage initiation for the axially loaded case. It is believed that the axial yarns carry the most significant part of the load and that the misalignment of the braider yarn had no deleterious effect.

Transverse Loading

The fringe patterns for the transverse case at the 6 ksi stress level are pictured in Fig. 9. In the pattern there are areas of very high tensile strain over the cross-over region on the specimen. The patterns is relatively systematic. There are also cracks in the specimen at this load level. Cracking was first detected at around 4 ksi. The U-field displays a rather random fringe pattern. Also there seems to be a region on both sides (free edge) of the specimen where the fringe pattern does not match that of the interior. Therefore, there is an edge effected zone.

The specimen was unloaded from the 9 ksi stress level and the fringe pattern in the third figure was taken at zero load. An alarming amount of cracking is present. The crack pattern is also random. It is believed that early cracking of the specimen was a result of two factors, fiber crimp and poor specimen quality.

(LSS) Large Braider Yarns, Small Axial Yarn Percentage, Small Braid Angle

The LSS architecture was similar to the LLS architecture in that the braider yarns were the same size and the braid angle was nominally the same. The axial yarn content of the LSS architecture was significantly lower since only 6k axial yarns were used rather than 36k yarns. Unlike the LLS specimen the quality of the specimen, as received, was quite good.

Axial Loading

Fringe patterns for the LSS specimens are presented in Fig. 10 at the 6 ksi stress level. The fringes are basically horizontal with higher density in the zones between the braider yarns. The location of the braiders is obvious from the pattern and the repeatability of the pattern is good. The pattern is consistent throughout the face of the specimen even near the immediate vicinity of the free edge. The maximum normal strain in the loading direction was typically about twice the minimum normal strain.

The U-field fringe pattern also shows remarkable repeatability. The pattern contains basically vertical fringes over the braider yarns and inclined fringes over the resin rich zones between the braiders. These inclined fringes signify high shear strain between the yarns. The magnitudes of the shear strains were on the order of the applied average normal strain.

Damage on the surface was not detected in the specimen until 18 ksi although many audible cracking sounds were detected by ear well before that load level.

Transverse Loading

Fringe patterns for the V-field are illustrated in Fig. 11 for the 6 ksi load level. They look very similar to the axially loaded specimen. This is because the axial yarns are small compared to the braider yarns. The architecture is braider yarn dominated and the braider yarn direction is 45 deg. If one would omit the axial yarns entirely the architecture would be symmetric about 45 degrees and the behavior would be identical for axial and transverse loading. Hence the similarity in the fringe patterns.

The U-field, however, unlike the axially loaded specimen displays some edge effects. This can be seen by the change in the otherwise consistent pattern. The edge effected region, as with previous specimen architectures, penetrates into the interior of the specimen a distance equivalent to the width of one braider yarn.

A portion of the V-field fringe pattern is shown in Fig. 12 along with the strain contours. The high strains are depicted in white and are located over the resin rich regions.

Strain Gaging

The moiré interferometry study provided vision into the behavior of the textile materials. From the amount of nonuniformity of strain in the fringe patterns, it is obvious that using small strain gages will produce more scatter in the measured average stiffness. The variation of strain is highly dependent on the architectural parameters as can be seen by the vastly different fringe patterns. To establish a rule of thumb for an optimized strain gage size is therefore not precise. It is the authors opinion that "bigger is better", strictly from a coverage stand point. Larger gages are more expensive, though, and problems due to heat dissipation will be more significant, therefore a balance should be draw. It is the authors opinion that the strain gage should be large enough to span the largest dimension of the unit cell and include at least

three whole unit cells.

Modeling

In order to model the physical behavior of these textile materials many assumptions must be made. A typical starting point is some of the models currently being implemented by the Textile Composites Working Group is a iso-strain assumption on the boundaries of the unit cell. From the moiré interferometry fringe patterns it is clear that along any line, including the boundaries of the unit cell, the strain was never constant. In fact, for the most part, the strains vary by at least a factor of 2, and sometimes by as much as 4. The ramifications of this are unclear, but the observations may be important to future refinements of the models.

General Observations

The moiré fringe patterns display significant strain variation on the surface of the architectures. Variations on the order of 2 and 3 were common for maximum and minimum strains. For some architectures that were loaded in the transverse direction the variation was as high as 4. A brief list of some general observations discussed earlier is supplied here.

- Large strain variations were present in all of the archtectures.
- The larger the yarns, the larger the magnitudes of the variations.
- Cracking occurred earlier in specimens with larger yarns.
- Transverse loading of braids with large braid angles caused cyclic global material behavior.
- Cracking occurred earlier in transversely loaded specimens.

SHEAR TESTING

A new in-plane shear test methodology, developed for laminated composite materials, was extended to textile composites. The methodology incorporates two recently developed advances: a new specimen and a special strain gage. When used together, they produce accurate and consistent shear characterization of laminated and textile composite materials. The "compact shear specimen" incorporates many of the advantages of the similar Iosipescu shear specimen but has a larger test section. A special strain gage called the "shear gage" integrates the shear strains across the entire test section of the specimen to obtain the average shear strain, regardless of the shear strain distribution in the test section.

The methodology was used to test both 2-D braided and 3-D woven textile composites. The entire shear stress-strain response, including the shear modulus and shear strength, was measured for nine textile composite architectures. The variation in shear modulus and shear strength were low and were comparable to the variation of tensile and compressive modulus for the respective materials. Moiré interferometry was used to compliment the test methodology. Enhanced x-rays were used to document the damage accumulated during failure of the specimens.

Introduction to Shear Testing

Shear characterization of textile composites is particularly challenging when considering that there is no standard test method that exists for laminated composites. Numerous test methods have been proposed and a considerable amount of research in shear testing of laminated composites has been performed [4]. At the present time, the Iosipescu specimen [5] is

the most used shear test specimen and has distinct advantages over other existing methods. The Iosipescu specimen was first developed for isotropic materials by Nicolae Isopescu in Romania and then extended to composite materials testing by Adams and Walrath [6,7] of The University of Wyoming. The Iosipescu specimen is a compact notched beam that has the potential to determine the entire shear response of laminates including both shear modulus and shear strength. Given the methods popularity, ASTM conducted a round robin study [8] to determine its feasibility as a standard test method for laminated composites. Among the nine laboratories participating in the study, the coefficient of variation for shear modulus was around 9% within each laboratory for each material system tested. The variation is substantially worse than the variation in tensile and compressive moduli for comparable materials. Therefore either laminated composites inherently exhibit more variability in shear properties compared to tensile properties or the test method, as it stands, does not produce adequate reliability.

Further investigation of the Iosipescu specimen revealed that the shear stress and shear strain distributions in the test section were not uniform and were dependent on the orthotropy of the material being tested [9-12], the specimen configuration and the loading condition. Additionally, it has been shown that twisting of the specimen can occur during loading, adding and subtracting shear strain on the two opposing faces of the specimen [12]. Both problems lead to inaccuracies in shear modulus when measuring the shear strain with a small centrally located strain gage rosette placed on one side of the specimen as recommended by Adams and Walrath. To obtain the shear modulus, the average shear stress (load divided by the cross-sectional area of the specimen) is divided by the local shear strain measured by the gage.

Recently, work at Virginia Polytechnic Institute and State University (VPI & SU) by the author in collaboration with Prof. Daniel Post and Micro-Measurements Division of the Measurements Group, Inc. [13-18] has addressed the problems associated with the nonuniform shear strain distributions and specimen twist. A special strain gage called the "shear gage" was developed that spans the entire test section of the Iosipescu specimen, thus integrating or averaging the shear strain. When gages are placed on both faces of the specimen, the nonuniform shear strains and complications resulting from twist are corrected. Along with developing the shear gage, another notched specimen called the "compact shear specimen" was developed that has similar advantages as the Iosipescu specimen yet has a larger test section. Shear gages were designed in two sizes: one to fit the test section of the Iosipescu specimen and one to fit the test section of the compact shear specimen.

A series of tests [13, 16] was conducted to determine the validity of the new gages on both the compact and the Iosipescu specimens. The results were impressive yielding a coefficient of variation in shear modulus within each material system of less than 2% for both specimen configurations. When compared to the 9% variation in the ASTM study, one can see the benefits of the new test methodology. Furthermore, there was no significant difference in the shear strength values between the compact shear specimen and the Iosipescu specimen.

Because of the success of the compact specimen and shear gage for laminated composite testing, the methodology was extended to the shear testing of textile composites. Although there was no significant difference between the performance of the compact and Iosipescu specimens for laminated composites, the larger test section of the compact specimen makes it more favorable for textile composites, which exhibit more fabric preform induced deformation nonuniformity.

Shear Test Methodology and Procedure

The compact shear specimen and loading fixture are illustrated in Fig. 13. The specimen is square (1.5 in. by 1.5 in.) with two 0.25 in. diameter semi-circular notches machined on opposing sides producing a 0.75 in. test section. The compact size of the specimen

makes it ideal for testing expensive materials such as composites or for extracting specimens from real structures for quality assurance tests. The compression loaded fixture grips both flanks of the specimen and was designed to accommodate specimens of various thickness (0.1 to 0.5 in.). It was also designed so that any twist that occurs in the early stages of loading is reduced as the specimen approaches failure.

The shear gage, illustrated in Fig. 13, is a +45°/-45° rosette that spans, vertically, the entire test section between the notches of the specimen. It integrates the shear strain in the test section which compensates for the nonuniform strain distributions. When gages are placed on both faces of the specimen, as in these tests, the deleterious effects of specimen twist on shear modulus are corrected. The shear strain values from the two gages were averaged and plotted against the average shear stress (load divided by the cross-sectional area between the notches of the specimen) to obtain the shear response.

A 20 kip hydraulic testing machine was used at a loading rate of 0.01 in/min., and the load and strain gages were monitored every 2 seconds during loading. The test section length and specimen thickness were measured with a micrometer for all specimens prior to testing.

The shear modulus was determined as the secant modulus from 1000 με to 2000 με. For the material systems tested the response was fairly linear over that range. The shear strength was determined from the maximum load divided by the original cross-sectional area of the test section. At the end of each test, the specimens were taken out of the fixture and doped with x-ray enhancing dye penetrant. X-rays were then taken to determine the damaged state.

In order to develop confidence in the test methodology, a 7075-T6 aluminum specimen was tested using the above procedure. The shear modulus of the aluminum was known in advance since it was back calculated from the modulus of elasticity and the poison's ratio. This procedure was used before testing of each material. The difference between the value obtained by the compact specimen and the back-calculated value was consistently less than 1%. This procedure is recommended to be a standard part of testing of exotic materials. If one can't determine the shear modulus for an isotropic material, it is not reasonable to have confidence in values obtained from complex materials such as textile composites.

Results

Full-Field Deformation Analysis

Moiré interferometry was used to investigate the shear deformation characteristics of the textile specimens. A brief review of the results will be discussed here in order to add validity to the current test methodology.

Three moiré fringe patterns of displacement over the compact specimen test section are shown in Fig. 14. All three patterns are horizontal displacement fields. The first pattern is for a cross-ply laminate, the second is for the SLL braid and the third is for the OS-1 weave. The first pattern contains basically horizontal fringes where all the points along one fringe have been displaced horizontally with respect to points along a neighboring fringe, thus signifying shear deformation. The shear strain is related to the fringe spacing in the vertical direction. The fringe spacing changes gradually over the entire test section therefore revealing a smooth distribution. By contrast, the fringe spacings for the two textile architectures vary significantly. The deformation fields contain repeatability that corresponds to the cyclic architecture of the textile preforms.

The shear strain distributions are influenced at two scales; the specimen scale and the micro-mechanical scale of the material. For laminates, the two scales are quite different where the test section of the specimen is 0.75 in. and the fiber diameter is on the scale of around 0.001

in. As a result, local strain nonuniformities over the fiber scale do not significantly influence the shear strain distribution across the test section. For textiles, however, the preform unit cell sizes are on nearly the same scale as the test section scale therefore nonuniformities over the unit cell significantly influence the strain distributions in the test section. This can be thought of as a local strain distribution caused by the repeating textile architecture superimposed over the global shear distribution of the specimen.

Since the shear strain gage integrates the shear strains across the entire test section, the entire strain distribution is averaged, including those influenced at the local and global scales. If only a small portion of the test section were instrumented, such as with the small gages commonly used on the Iosipescu specimens, neither local nor global distributions would be sufficiently sampled. This is because the gages would be to small to cover at least one repeating unit cell of the textile architecture. Additionally, they could not account for the global shear distribution.

Shear Stress-Strain Response

The shear stress-strain curves for the four braid and five weave architectures are presented in Figs. 15 and 16 respectively. A total of four weave specimens and six braid specimens are plotted for each material type tested. The weaves and the braids exhibit a fundamental difference in their shear response. The Braids are nearly linear all the way to failure, whereas the weaves are nearly linear up to around 1% shear strain and then become highly nonlinear and sustain load well past 8%. Many of the curves end prior to 8%, as a result of the strain gages detaching from the specimens as cracks developed under them.

Shear modulus values and coefficient of variation for each of the architectures is presented in Table II. The variation of shear modulus was generally low and equivalent to tensile and compressive moduli for the respective material systems

Shear modulus values for the braided architectures were higher than for the weave architectures. Since shear stress can be resolved as equal and opposite tension and compression in the +45° and -45° directions, it becomes apparent that the braids have yarns more closely aligned with the principle stress directions. The braid architectures with 45° braider yarn directions exhibited higher stiffness. Additionally, the braid with the highest percentage of 45° braider yarns exhibited the highest shear stiffness.

The shear stress strain response of the braids was mostly fiber dominated while that of the weaves was mostly matrix dominated as evidenced by the ductile flow of the material at higher load levels.

Shear Strength

The shear strength of composite materials is a difficult property to measure since this requires the specimen to be loaded in such a way that a state of pure and uniform shear exists in its entire test section. Additionally, the specimen must fail in the test section in a shear mode. These conditions cannot be strictly met, because the test section of flat coupon specimens such as the compact specimen and the Iosipescu specimen must have free edges where the shear stress must be zero. The shear stress from the free edge inward rises to form some distribution across the test section. Hence, with the given shear stress distribution, a gradient is present. Given this gradient, equilibrium holds only when gradients in the normal stresses exist. Thus, the state of shear stress across the test section can be neither uniform nor pure. Strictly speaking, a complex state of stress exists in the test section, but, for practical purposes, the state of stress is predominantly in the form of shear.

How much credibility should be associated with the shear strength values derived from

tests with flat coupons? This is not an easy question to answer. The authors opinion is that the values should be considered conservative and are more realistic for some architectures than others. This is because the shear stress distribution in the test section is a function of the orthotropy of the material being tested, the specimen geometry, and the loading conditions on the specimen. For some material systems, the state of stress in the test section is more uniform and pure than for others. This has been demonstrated for laminated composites using both experimental and numerical methods [9-12].

The shear strength values for the nine material systems is presented in Table II along with the coefficient of variation. It was found that the variation was generally less than 10% for the braids and less than 2% for the weaves. The braids exhibited a higher shear strength than the weaves, since, as with shear modulus, the yarns are more nearly aligned with the principle stress directions.

A postmortem inspection of all of the specimen types was conducted using enhanced x-rays to determine whether the failure was confined to the test section and in the form of shear. Figure 17 shows the x-ray micrographs for the nine textile architectures tested. Damage is evident by the dark areas. All of the specimens failed in the test section with the exception of the LSS braid which was dominated by +45°/-45° yarns. Therefore, the shear strength values for that material system are not considered accurate.

The weave architectures produced the most desirable failure with cracking evenly distributed and confined to the test section. Cracks were aligned in the 0°/90° directions in and between the yarns.

Concluding Remarks

The compact shear specimen and the shear gage together form a reliable means to determine the shear response of textile composite materials. The method is capable of determining shear modulus and strength for most textile materials with comparable repeatability as respective tensile moduli and strength. The specimen is small and can be efficiently used for material property characterization as well as quality assurance.

THROUGH-THE-THICKNESS TENSILE STRENGTH

One of the benefits of textile composite materials is the potential for improved through-the-thickness properties. Since traditional laminated composites have relatively low interlaminar properties, they are susceptible to delaminate from out-of-plane loads. Out-of-plane loads may be produced from loading such as impact loading or around structural details such as curved geometry, ply drops, or fasteners. Composites made from 2-D or 3-D textile preforms were expected to improve both the through-the-thickness tensile and shear strengths. In the 2-D materials, the improvement was expected due to the nesting and interaction of layers of textile preform. The 2-D braids that were tested were manufactured with six to ten layers. In the 3-D materials, direct reinforcement in the thickness direction was specifically included to improve these properties. With improved through-the-thickness properties, the susceptibility to damage from out-of-plane loads should be greatly reduced. Although the through-the-thickness tensile strength is an important material property for design purposes, it inherently is a difficult property to quantify.

In laminated composite materials, the through-the-thickness tensile strength can be approximated by the transverse-width strength measured from flat 90° specimens [19]. In textile

composites, however, the architecture of the preform is three dimensional with significantly different properties in all directions. Consequently, a novel test methodology was developed to measure through-the-thickness tensile strength. The methodology incorporates an "L" shaped specimen with a curved test section at the elbow. Through-the-thickness tension is induced in the test section by a moment applied through two couples created by a standard four-point-bending fixture as shown in Fig. 18. The through-the-thickness strain ε_r is maximum near the centerline or neutral axis of bending as shown in Fig. 19 where the distributions have been predicted based on anisotropic elasticity theory and later measured with moiré interferometry.

Several other through-the-thickness test methods have been proposed. In reference [20], a flatwise tension test was investigated where the specimen was loaded using aluminum shanks bonded to the upper and lower surfaces of the specimen. The radius was machined into the specimen to give a minimum area at the center. This type of test method was not used since failures were often at the bond line, extensive machining was required, and thick specimens must be used. Other test methods using "L" or "C" shaped specimens have also been proposed [19,21]. However, the proposed methods using the "L" shaped specimen and a four-point-bending fixture has several advantages over the other methods: use of a standard test fixture, simplified analysis, constant moment in the test section, and a self-aligning test configuration.

The maximum through-the-thickness stress in the test section was determined from the applied moment, elastic properties and the specimen geometry using a solution developed by Lekhnitskii [21]. The test configuration produces pure bending in the test section and thus the closed-form solution is easily implemented in a curved beam segment with cylindrical anisotropy. The radial and circumferential stresses were calculated at the instant of failure and the maximum radial (through-the-thickness) stress was determined.

To aid in the development of the test method, moiré interferometry was used to determine the state of strain along the edge of the test section. Textile composites have very nonhomogeneous properties through the thickness due to their coarse preform architectures. Consequently, very nonuniform displacement fields were expected. Initially, tests were conducted on 48-ply unidirectional laminates, where the fibers ran circumferentially around the test section. By comparing analytical predictions of strain and displacement, the test method could be verified using the unidirectional laminates. Moiré fringe patterns are shown in Fig. 20 for a laminated composite, a 2-D braided textile composite, and a 3-D woven textile composite, respectively. From the patterns, it can be seen that the displacement fields are markedly different for the three specimens. The laminated composite has a relatively uniform displacement field through the thickness. The 2-D and 3-D textile composites display serious nonuniformities due, in part, to the three dimensional substructure of the textile and to the edge effects.

The strain distributions for the laminated composite materials were extracted from the moiré fringe patterns and are plotted in Fig. 19. Both the radial (through-the-thickness) strain and the circumferential strain are plotted. The through-the-thickness strains generally agreed with, but were slightly higher than the predicted values. The differences between the experimental and predicted values was attributed to a distortion of the outer radius of the test section during the specimens manufacture. Since the laminated specimens were made over a male tool, the outer radius was slightly malformed with an increased thickness around the curved region. Never-the-less, the moiré study confirmed the stress distribution and the analysis methodology.

The failure modes for the three composite types was markedly different. The moiré fringe patterns provided an excellent method of detecting and documenting damage. The cracks are easily recognized in Fig. 20. The laminated composite failed by delamination between the plies. Often, the sublaminates formed by the initial delamination would also delaminate to form more sublaminates. The failure was initiated in the specimen in the region of the highest through-the-thickness stress, hence, it is believed that the test method is valid for laminated composites.

The 2-D braids also delaminated between the layers. However, the delaminations between the layers often followed a more tortuous path. In the moiré patterns, in general, high fringe density corresponds to high strain. The fringe patterns for the 2-D textile reveal zones of high shear strain. The strain in these regions were on the order of three or four times the ambient value. It is believed that failure initiated in these zones since the location of some of the cracks corresponded with regions of high shear strain. It could not be determined if the cracks initiated at the surface or in the interior of the specimen. Regardless, the failure mode was correct and confined to the location of highest radial stress. Therefore, it is believed that the test method is valid for 2-D textile composites. The values for through-the-thickness tensile strength were less than half those for tape composites. It is believed that this is due to the compliant zones which are analogous to the weak link.

Initial damage in the 3-D braids occurred very early in the loading and was made up of a series of radial cracks caused by the high circumferential stress along the inner radius. The radial cracks were easily detected with moiré. The radial cracks tended to shift the neutral axis of bending upward, thus changing the stress distribution. In other words, the specimen geometry was altered by the radial cracks. Final failure was caused by circumferential cracks around the test section. The failure strength of the 3-D materials were much lower than the 2-D and laminated materials. It is believed that the values obtained for the through-the-thickness strength for the 3-D textiles were not accurate and further studies are required.

OPEN-HOLE TENSION

One of the critical test methods that is used in the screening process of new material systems for aircraft structures is the open-hole tension test. Since many real structures are required to have holes, cut-outs for fasteners or through wiring and tubing, the test provides a means to evaluate the material in a realistic situation. Since it has been established that significant strain variations exist in tensile panels, it is of interest to document how the variations interact with a stress riser such as a hole.

A series of moiré interferometry tests were performed to determine the strain distributions in 2-D braided open hole tensile specimens. The main objectives were to determine the distribution and severity of the strain concentration, and to document damage initiation and progression. Two architectures were tested, both 2-D triaxial braids. Specimen I is the LLS architecture and specimen II is the LLL architecture. The tensile loads were applied in the direction of the axial yarns. Both specimens were 50.8 mm (2.00 in.) wide and had a nominal thickness of 0.32 mm (0.13 in.), with a hole diameter of 9.53 mm (0.375 in.).

Figures 21 and 22 show the moiré interferometry fringe patterns around the vicinity of the hole for the LLL and LLS. In the immediate vicinity of the hole there are serious strain concentrations for both arhcitectures.

Figure 23 shows the displacement fields around the hole for specimen I. The strain concentration is evidenced by high fringe gradients near the hole. The graph shows the ε_y strain distribution along the horizontal centerline of the specimen. Both of the specimens are represented. The two specimens, and also a Finite Element Method (FEM) solution for an isotropic material, exhibit a similar global response. The braided materials, however, show a higher strain concentration. In a series of tests with different specimens, the concentration factors varied between 3 and 6, depending upon the location of the hole with respect to the unit cell. The highest strain were located within 0.05 in. of the hole.

In axial tension experiments on the braided materials without holes, the maximum ε_y

strain was about twice that of the average ε_y strain. These strain variations occurred within each unit cell. The strain concentration factors found in the moiré interferometry tests are sensitive to the position of the hole relative to the unit cell. When the hole boundary coincides with the compliant part of the unit cell, the strain concentration rises.

The first cracks initiate at the regions of high strain in the immediate vicinity of the hole. As the load level increased, cracks propagated from the hole along the braid angles. The onset of cracking did not lead to catastrophic failure of the specimen; instead, cracking occurred over an extended load range. The first cracks, which occurred in the braider yarns, were detected well before half of the ultimate load. The axial yarns continued to carry a major part of the tensile load. Figure 24 shows the fringe pattern of an enlarged region of specimen II where a crack had formed. Surface cracks occurred between braider yarns and followed paths along the junctions between two braider yarns. In each case, the surface crack would terminate at the intersection of the next axial yarn, which acted as a temporary crack stopper. Subsequent loading would produce crack extension until global failure occurred. Surface cracks are illustrated in the figure, but in some cases the first crack occurred in the interior layer of fabric.

From the moiré experiments it was revealed that the initiation of cracking occurred at the location of high strain concentrations. Additionally, cracking occurred at a relatively early load level. The specimen, however, did not fail as a result of the initial crack and could carry considerable additional load, even though the crack density increased significantly. This suggests that the material was not damage resistant yet was quite damage tolerant for static loading.

CONCLUSIONS

Moiré interferometry can serve as valuable tool to provide vision in the test method development of novel material systems such as textile composites. It can provide information on the strain variations on the surface, which in turn, can guide in the instrumentation process. Moiré interferometry can document damage mechanisms to validate the correct use and application of test methods.

REFERENCES

[1] Masters, J. E., Ifju, P. G., and Fedro, M. J., "Development of Test Methods for Textile Composites," *Proceedings for the FiberTex Sixth Conference on Advanced Engineering Fibers and Textile Structures for Composites*, NASA CP-3211, Drexel University, Philadelphia, PA, 1992.

[2] Post, D., Han, B. and Ifju, P. G., "High Sensitivity Moiré, Experimental Analysis for Mechanics and Materials," *Springer-Verlag*, New York, NY, 1994.

[3] Scardino, F., "An Introduction to Textile Composites and Their Structures," Textile Structural Composites, Chou, T. W. and Ko, F. K., editors, *Elsevier Science Publishing Co.*, New York, NY, 1989.

[4] Lee, S. and Munro, M., "Evaluation of In-Plane Shear Testing for Composite Materials by the Decision Analysis Technique," *Composites*, 17(1):13 (Jan. 1986).

[5] Iosipescu, N., "New Accurate Method for Single Shear Testing of Metals," *Journal of Materials*, Vol. 2, No. 3., Sept. 1967, pp 537-566.

[6] Adams, D. F. and Walrath, D. E., "The Iosipescu Test as Applied to Composite Materials," *Experimental Mechanics*, Vol. 23, No. 1, March 1983, pp 105-110.

[7] Adams, D. F. and Walrath, D. E., "Current Status of the Iosipescu Shear Test Method," *J. Comp. Mat.*, 21, (1987) pp. 494-507

[8] Wilson, D. W., "Evaluation of the V-Notched Beam Shear Test Through an Interlaboratory Study," ASTM Subcommittee D30.03 Report, 1990.

[9] Walrath, D. E. and Adams, D. F., "Analysis of the Stress State in an Iosipescu Shear Test Specimen," Rep. UWME-DR-301-102-1, Department of Mechanical Engineering, University of Wyoming, Laramie, WY, NASA Grant NAG-1-272, June 1983.

[10] Pindera, M-J., Ifju, P. and Post, D., "Iosipescu Shear Characterization of Polymeric and Metal Matrix Composites", *Experimental Mech.*, 30, 1, (1990) pp. 101-108.
[11] Wang, S. S. and Dasgupta, A., "Development of Iosipescu-Type Test for Determining In-Plane Shear Properties of Fiber Composite Materials: Critical Analysis and Experiment," Rep. No. UILU-ENG-86-5021, Department of TAM and Aeronautical and Astronautical Engineering, Univ. of Ill., 1986.
[12] Ho. H., Tsai, J. Morton, J. and Farley, G. L., "Experimental Investigation of the Iosipescu Specimen for Composite Materials," *Exp. Mech.*, Vol. 31, No. 4, (Dec 1991). pp. 328-336.
[13] Ifju P. G., "The Shear Gage: for Reliable Shear Modulus Measurements of Composite Materials," *Exp. Mech. (accepted for publication).*
[14] Ifju P. G., and Post, D., "A Special Strain Gage for Shear Testing of Composite Materials," *Proceedings of SEM Spring Conference on Experimental Mechanics,* Milwaukee, Wisconsin, June 1991.
[15] Ifju, P. G., "Evaluation of a New Electrical Resistance Shear Strain Gage Using Moire Interferometry," *Proceedings of SPIE Conference on Photomechanics*, San Diego, California, August 1991.
[16] "Strain Gages for Shear Modulus Testing of Composite Materials," Micro-Measurements Division, Measurements Group, Inc., Supplimental Data Sheet for Strain Gage Catalogue.
[17] Ifju, P. G. and Post, D., "The Shear Gage and Compact Shear Specimen for Shear Property Measurements of Composite Materials," *VA Tech, Center for Composite Materials and Structures Report Series*, CCMS-92-19, (1992).
[18] Ifju, P. and Post, D., "A Compact Double Notched Specimen for In-Plane Shear Testing", *Proceedings of SEM Spring Conference on Experimental Mechanics*, Boston, Massachusetts, May 1989
[19] Jackson, W. C. and Martin, R. H. "An Interlaminar Tensile Strength Specimen," Composite Materials: Testing and Design (Eleventh Volume), ASTM STP 1206, E. T. Camponeschi, Jr., Ed., *American Society for Testing and Materials,* Philadelphia, December 1993. pp. 333-354.
[20] Lagage, P. A. and Weems. D. B., "A Through-the-Thickness Strength Specimen for Composites," Test Methods for Design Allowables for Fibrous Composites:, 2nd Volume, ASTM STP 1003, C. C. Chamis, Ed., *American Society for Testing and Materials*, Philadelphia, 1989, pp. 197-207.
[21] Hiel, C. C., Sumich, M., and Chappell, D. P., "A Curved Beam Test Specimen for Determining the Interlaminar Strength of a Laminated Composite," *Journal of Composite Materials*, Vol. 25, July 1991, pp. 854-868.
[22] Lekhnitskii, S. G., "Anisotropic Plates," *Gordon and Breach Science Publishers*, New York, 1968, pp. 95-101.

Table I Description of the textile preform architecture of the braided and woven materials under investigation

2-D Braids	Braid angle (deg.)	Braider yarn size (thousands)	Axial yarn size (thousands)
LLL	70	15 k	72 k
SLL	70	6 k	30 k
LLS	45	15 k	36 k
LSS	45	15 k	6 k
3-D Weaves	**0° yarn size (thousands)**	**90° yarn size (thousands)**	**Out-of-plane yarn size (thousands)**
OS-1	24 k	12 k	6 k
LS-1	24 k	12 k	6 k
LS-2	12 k	6 k	3 k
TS-1	24 k	12 k	6 k
TS-2	12 k	6 k	3 k

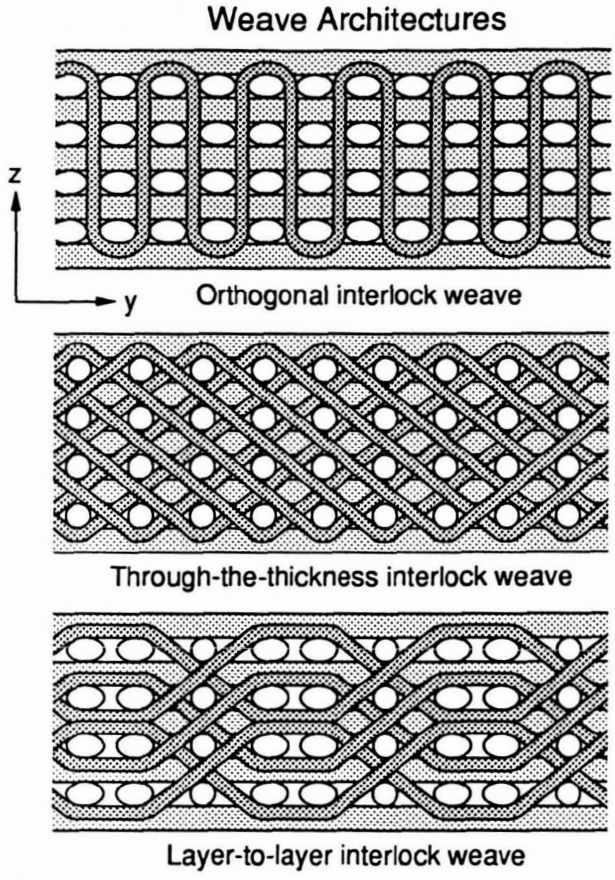

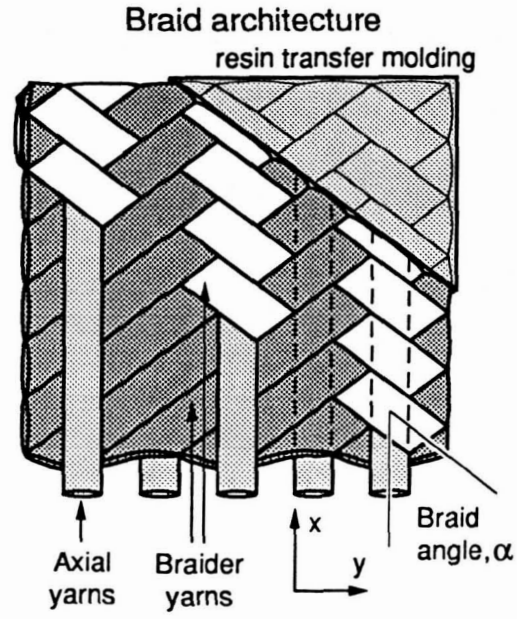

Fig. 1 Weave and braid architectures that were tested. The weaves were 3-D with reinforcement through-the-thickness while the braids were 2-D with no yarns interconnecting the layers of fiber preform.

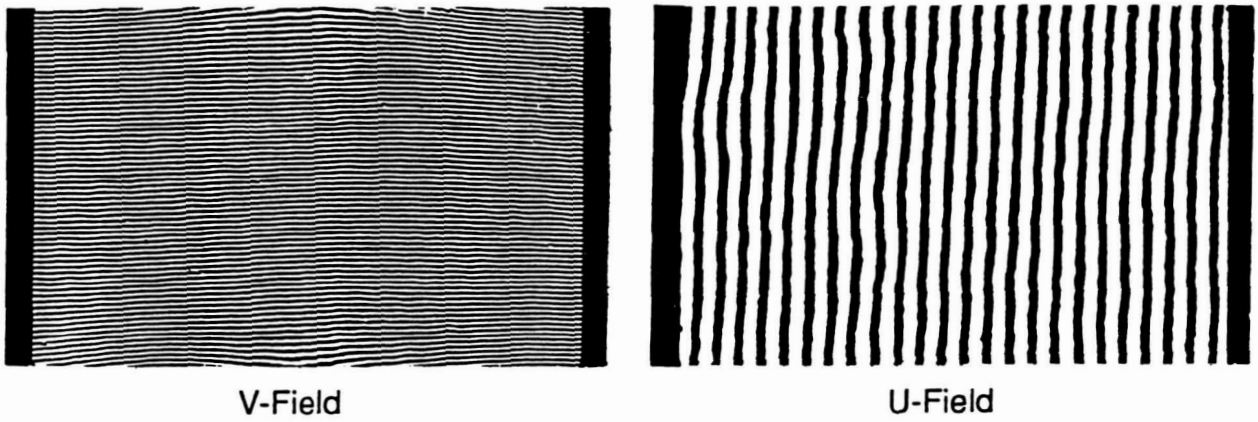

Fig. 2 Moiré interferometry fringe pattern for an unidirectional AS4/3501-6 tension specimen.

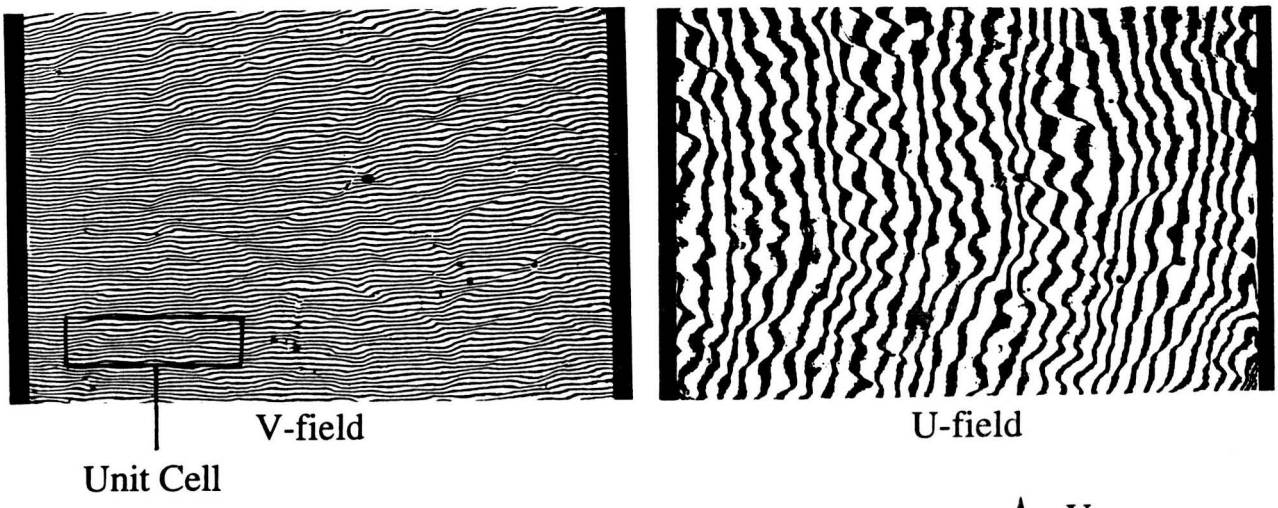

Fig. 3 Moiré fringe patterns for the SLL specimen with axial load at the 12 ksi stress level.

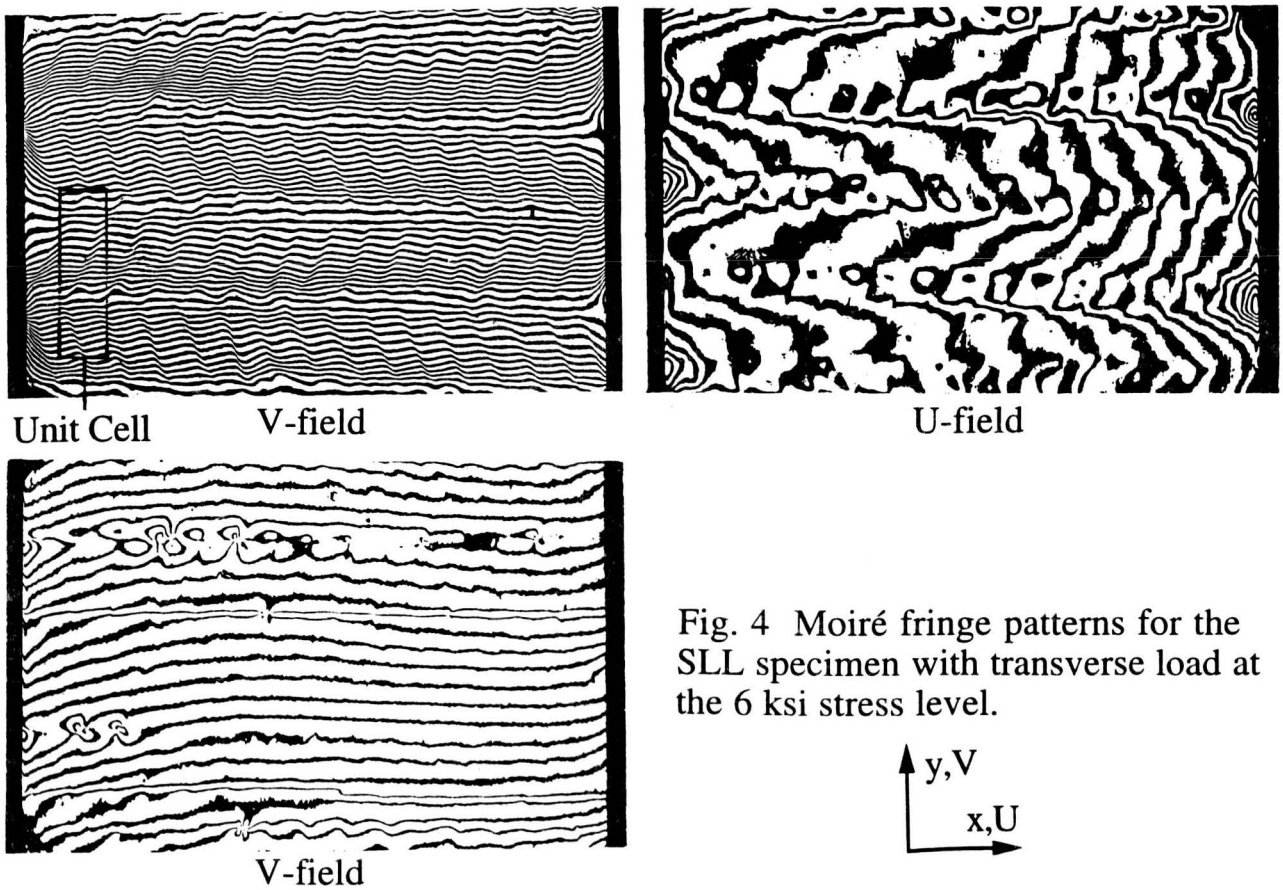

Fig. 4 Moiré fringe patterns for the SLL specimen with transverse load at the 6 ksi stress level.

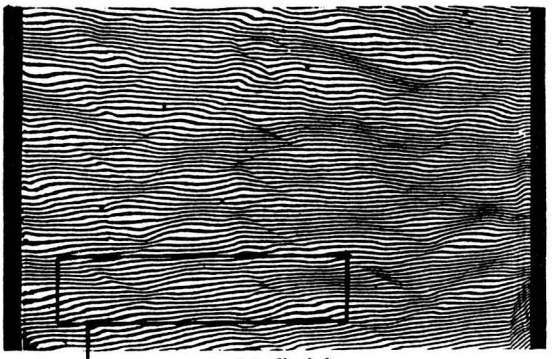

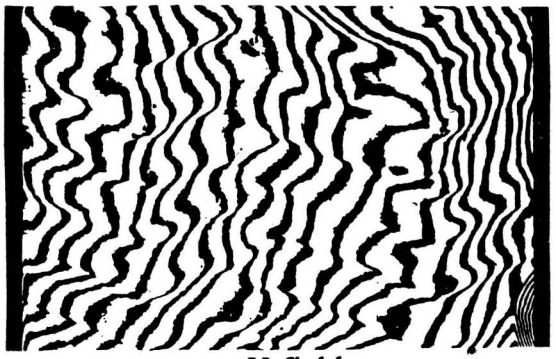

Fig. 5 Moiré fringe patterns for the LLL specimen with axial load at the 12 ksi stress level.

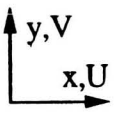

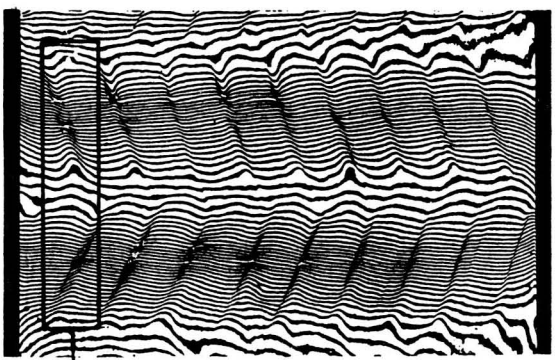

Fig. 6 Moiré fringe patterns for the LLL specimen with transverse load at the 6 ksi stress level.

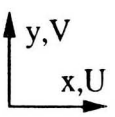

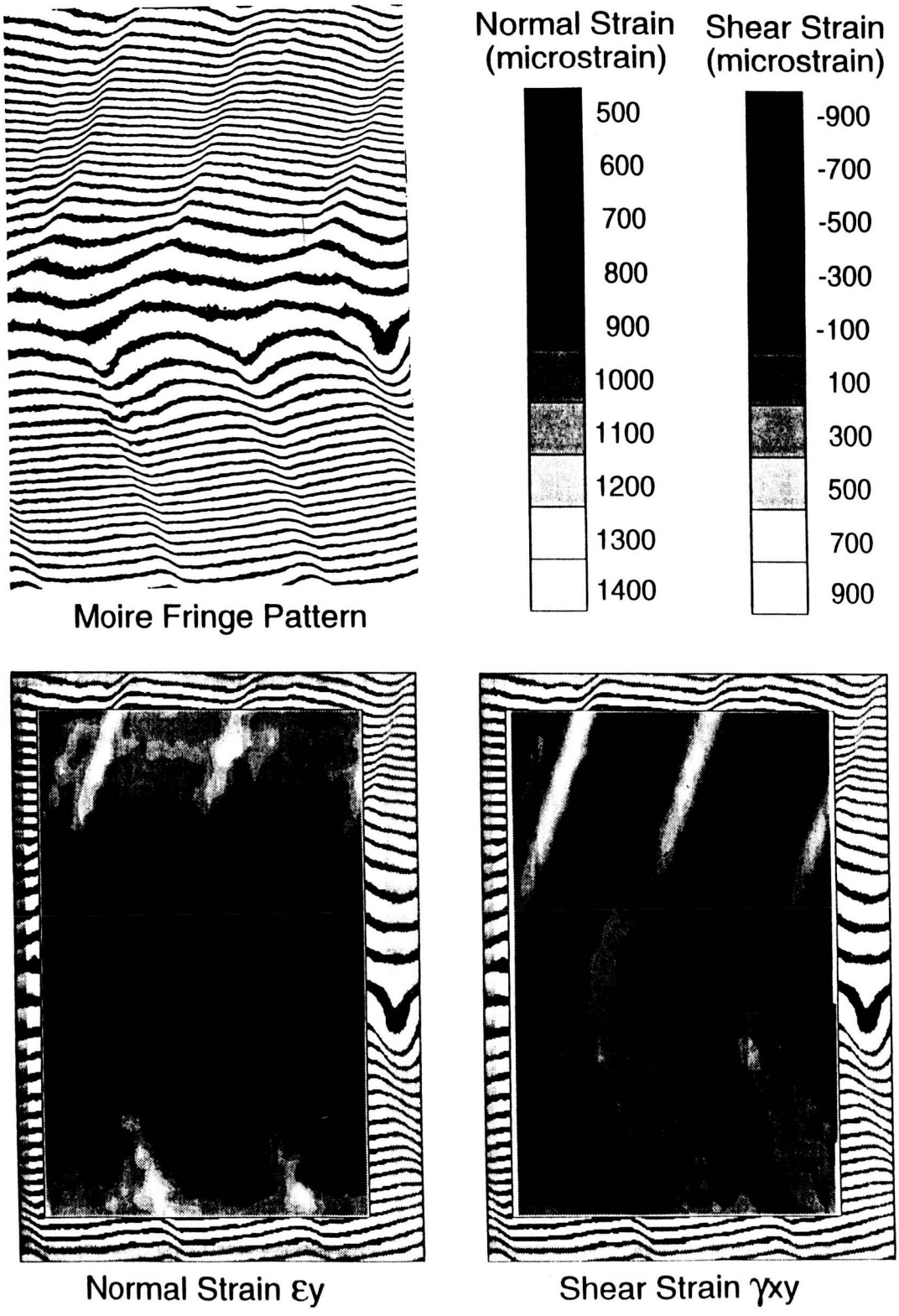

Fig. 7 Strain fields for the LLL, transverse loaded specimen.

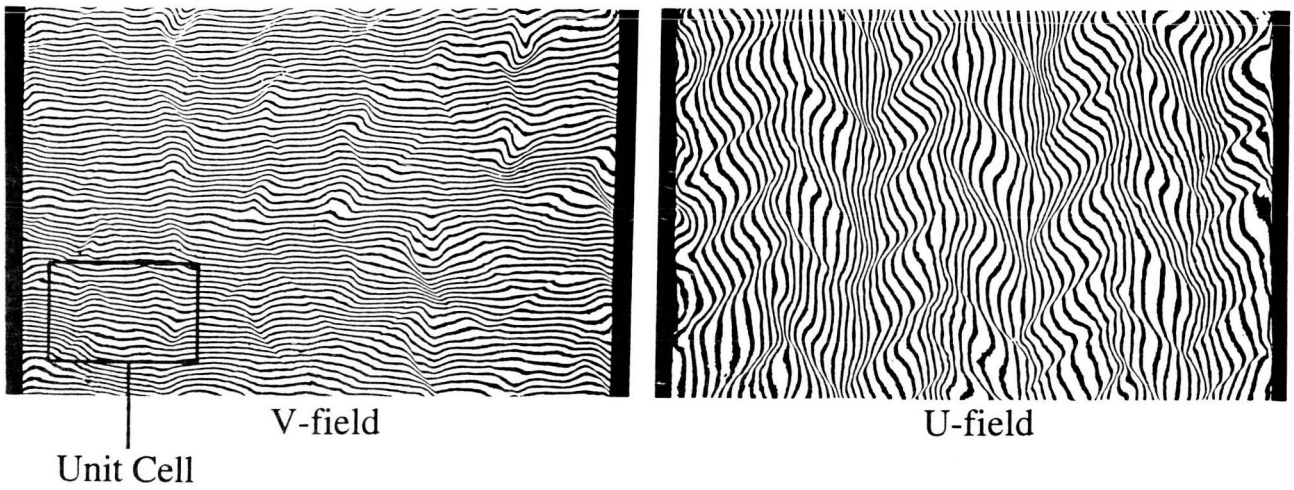

Fig. 8 Moiré fringe patterns for the LLS specimen with axial load at the 12 ksi stress level.

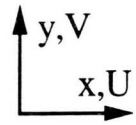

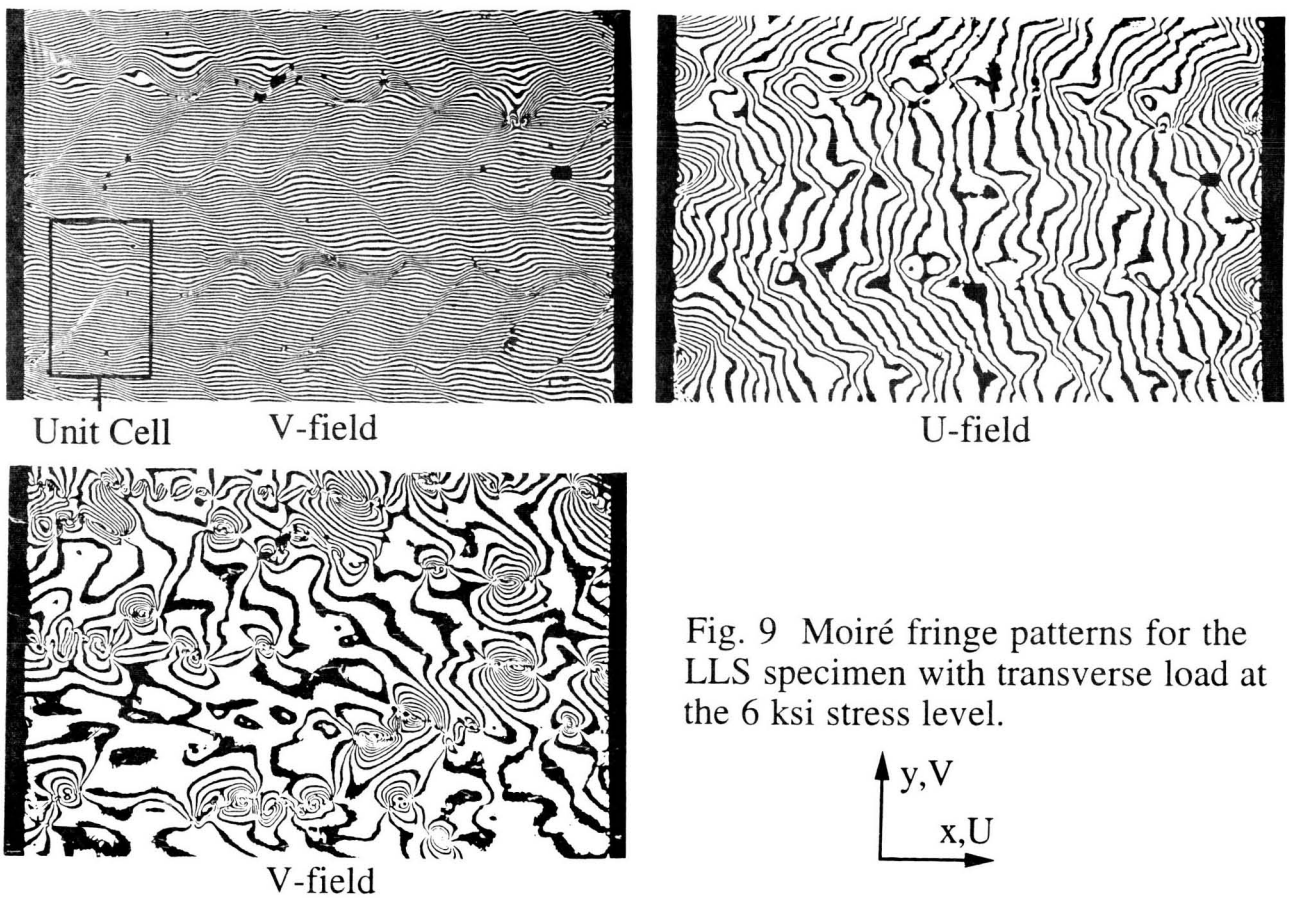

Fig. 9 Moiré fringe patterns for the LLS specimen with transverse load at the 6 ksi stress level.

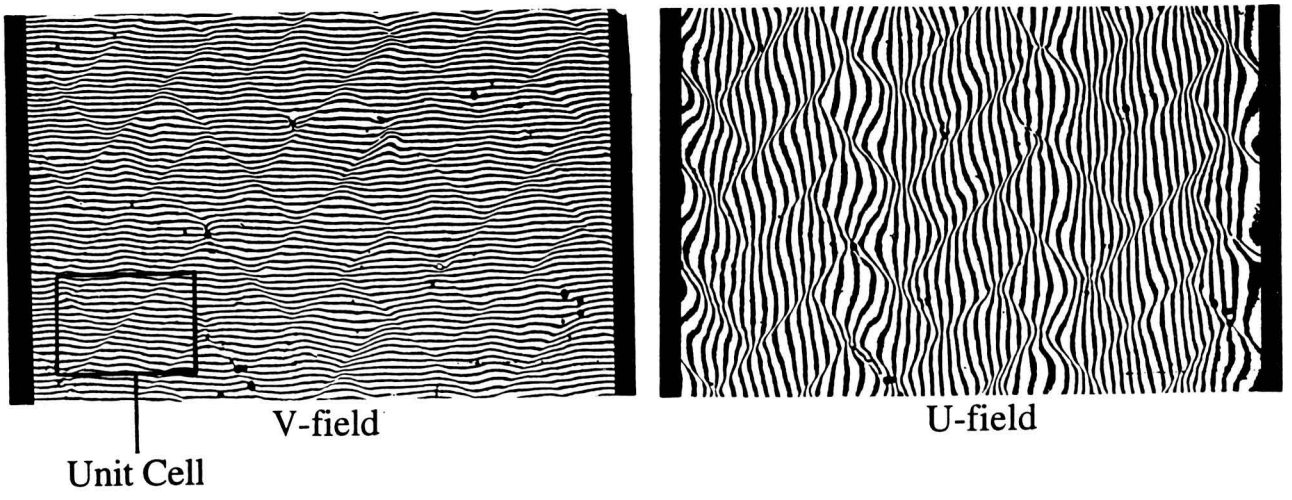

Fig. 10 Moiré fringe patterns for the LSS specimen with axial load at the 6 ksi stress level.

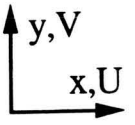

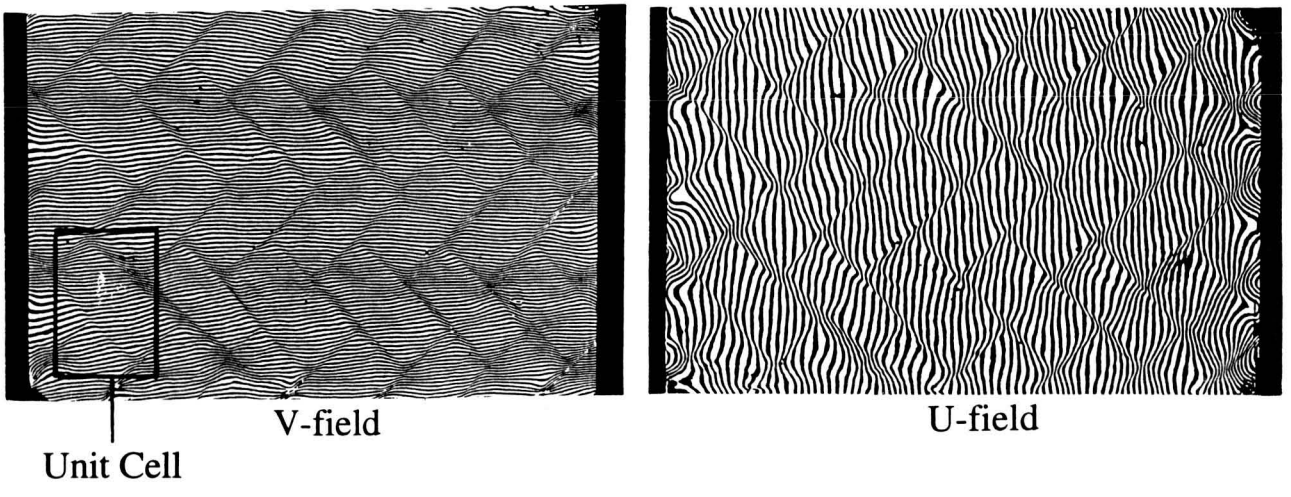

Fig. 11 Moiré fringe patterns for the LSS specimen with axial load at the 6 ksi stress level.

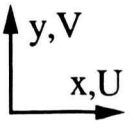

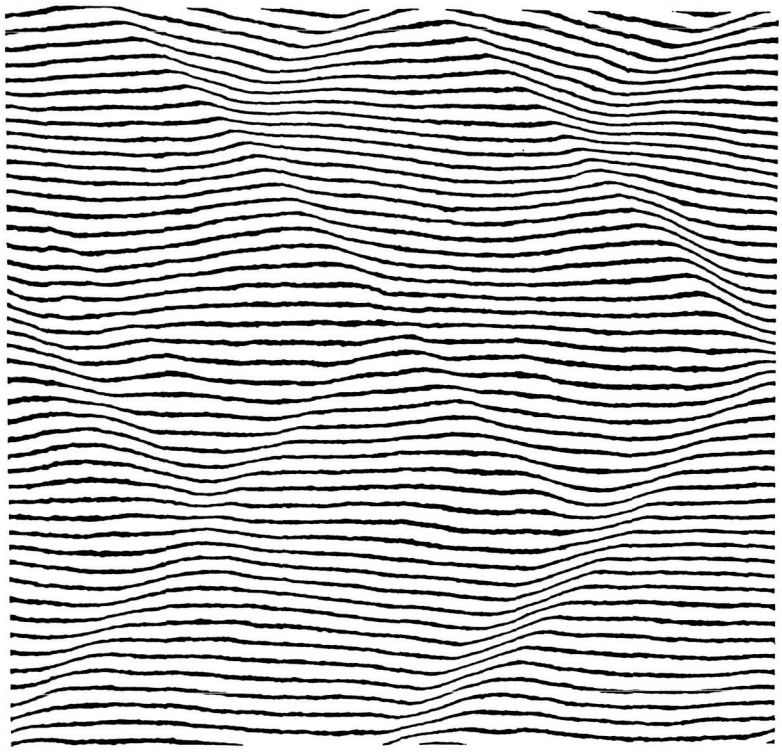

Moire Fringe Pattern

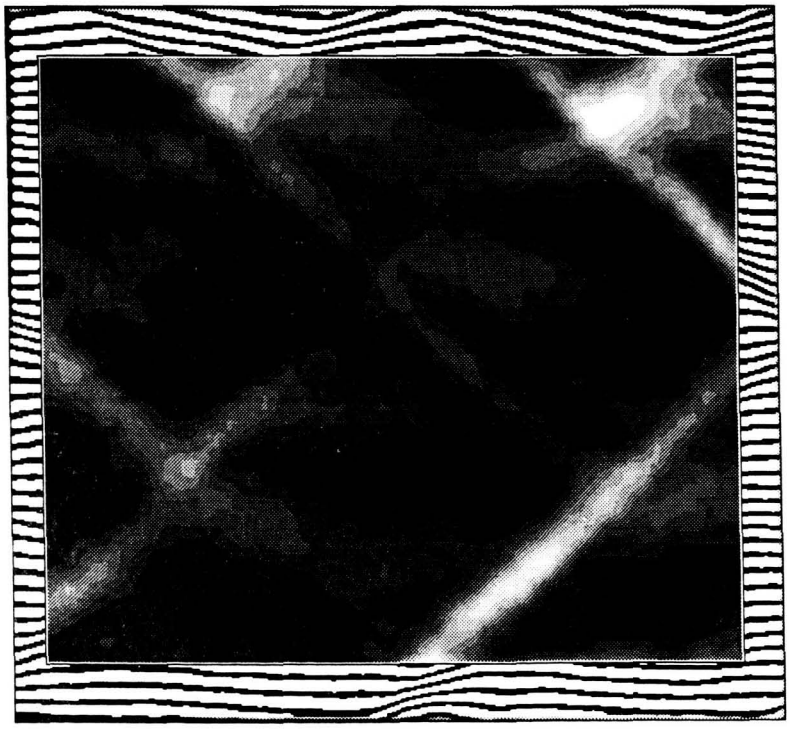

Normal Strain εy

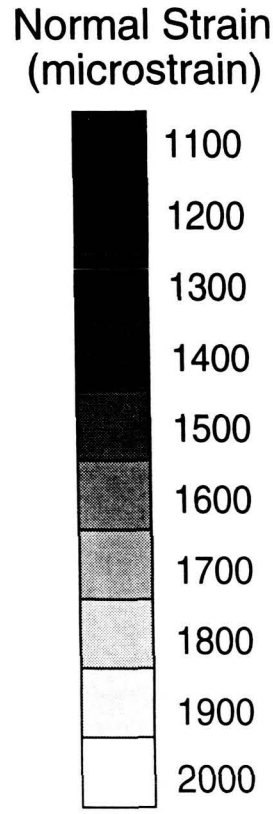

Fig. 12 Strain field for the LSS, transverse loaded specimen.

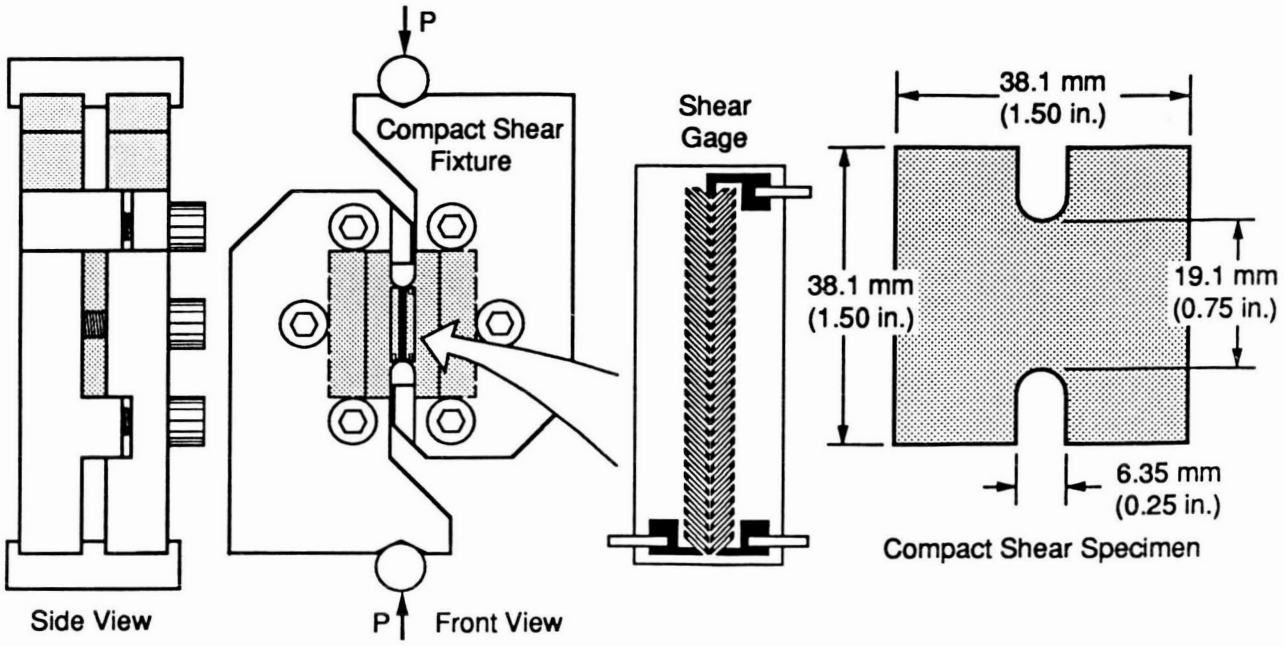

Fig. 13 The compact shear specimen, loading fixture and shear gage.

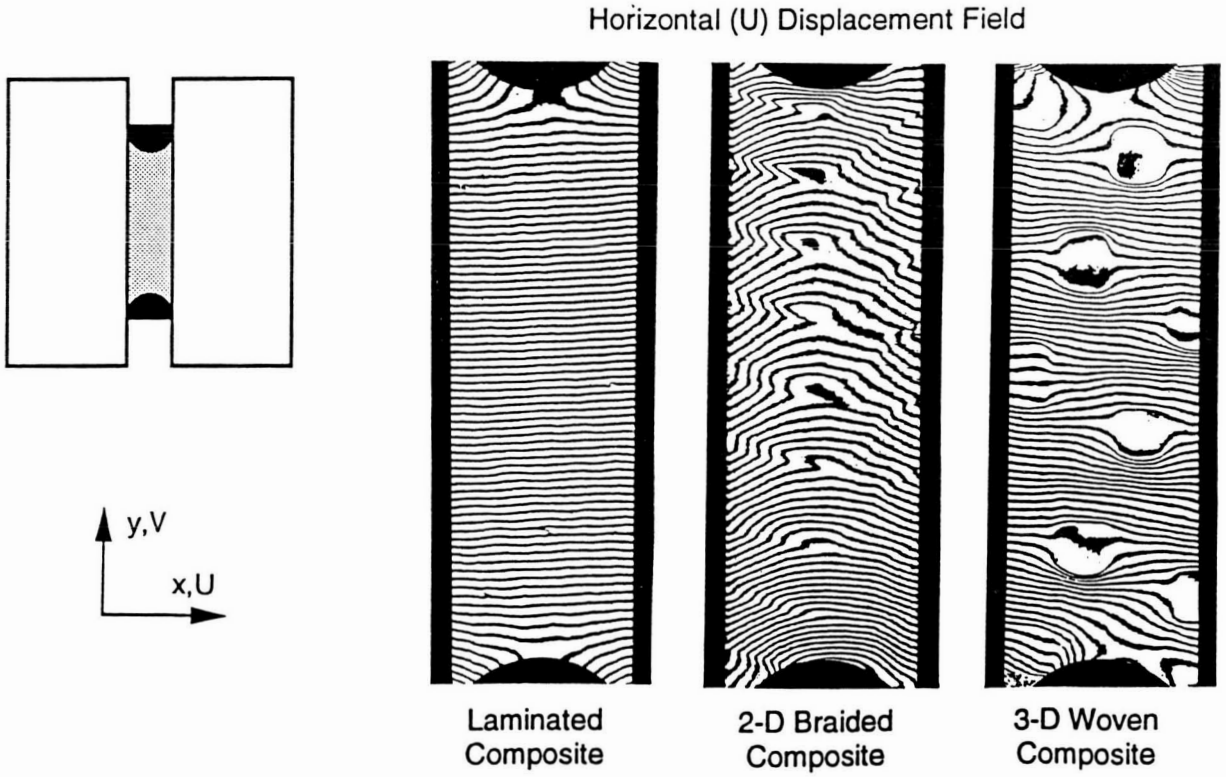

Fig. 14 Moiré interferometry fringe pattern for laminated, 2-D braided and 3-D woven. specimens.

Table II Shear modulus, shear strength and coefficient of variation values for the materials tested.

	Material	Shear modulus (GPa)	(Msi)	Coefficient of variation (%)	Shear strength (MPa)	(ksi)	Coefficient of variation (%)
Braids	LLL	11.0	1.60	3.5	136	19.7	4.1
	SLL	11.7	1.70	3.4	125	18.1	5.0
	LLS	17.0	2.46	3.0	141	20.4	10.6**
	LSS	27.9	4.05	3.9	141*	20.5*	6.2
Weaves	OS-1	5.03	0.73	3.9	70.3	10.2	2.6
	LS-1	6.21	0.90	6.4	71.0	10.3	2.6
	LS-2	5.79	0.84	4.7	73.1	10.6	1.5
	TS-1	5.58	0.81	2.3	80.7	11.7	2.7
	TS-2	5.65	0.82	6.9	77.2	11.2	0.8

* Specimens did not fail in test section

** One specimen failed prematurely

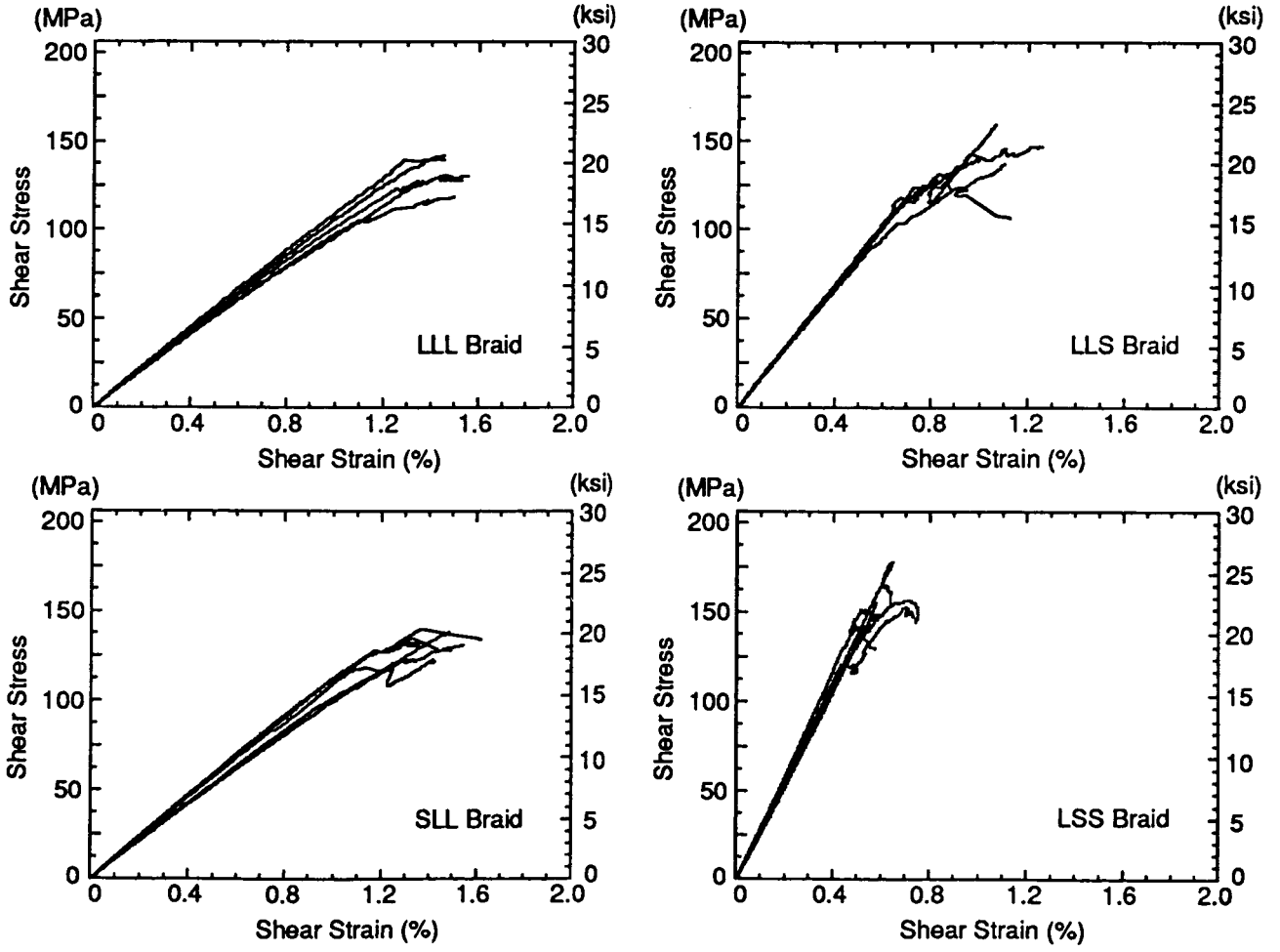

Fig. 15 The shear stress-strain response of the 2-D braid architectures.

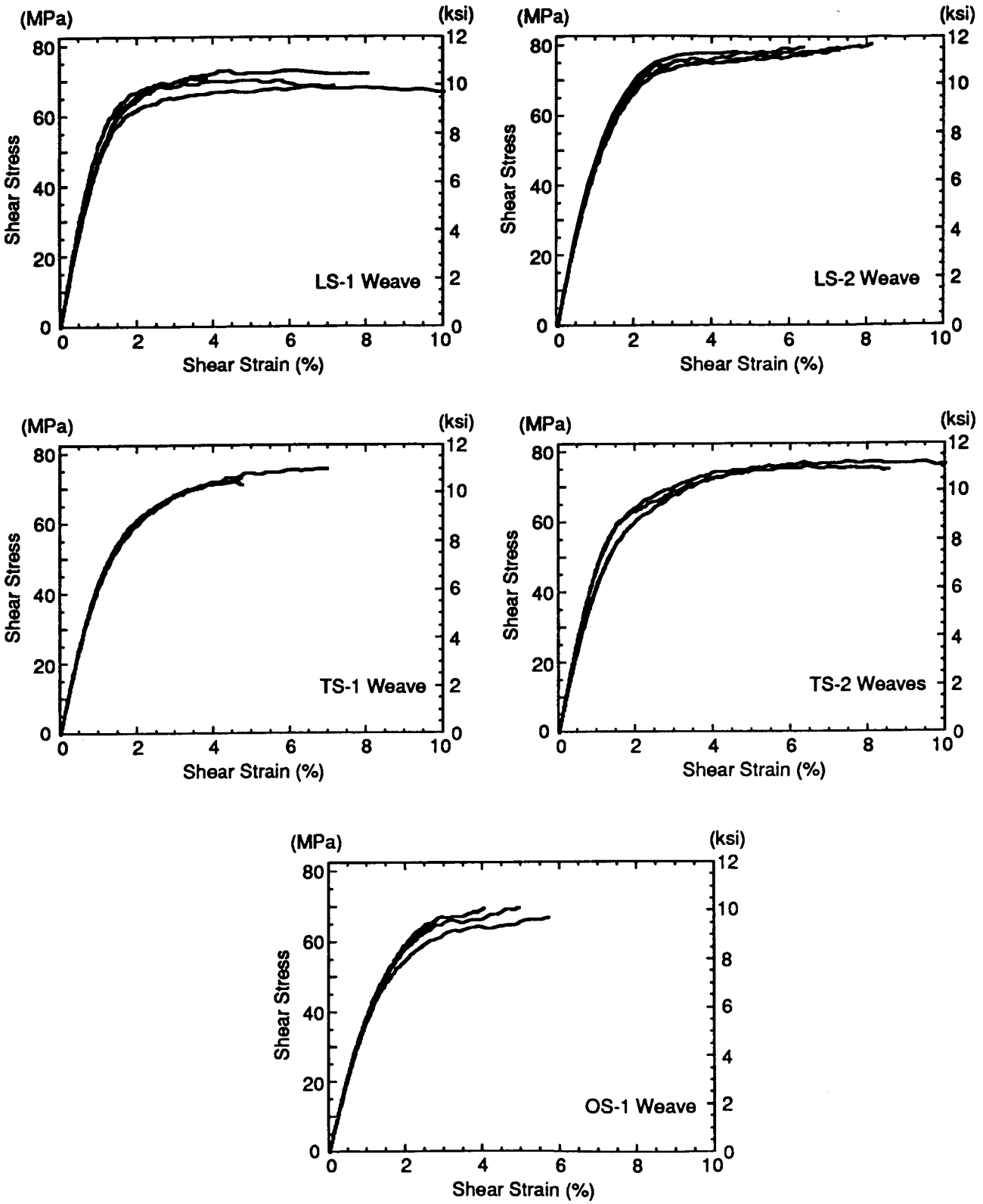

Fig. 16 The shear stress-strain response of the 3-D weave architectures.

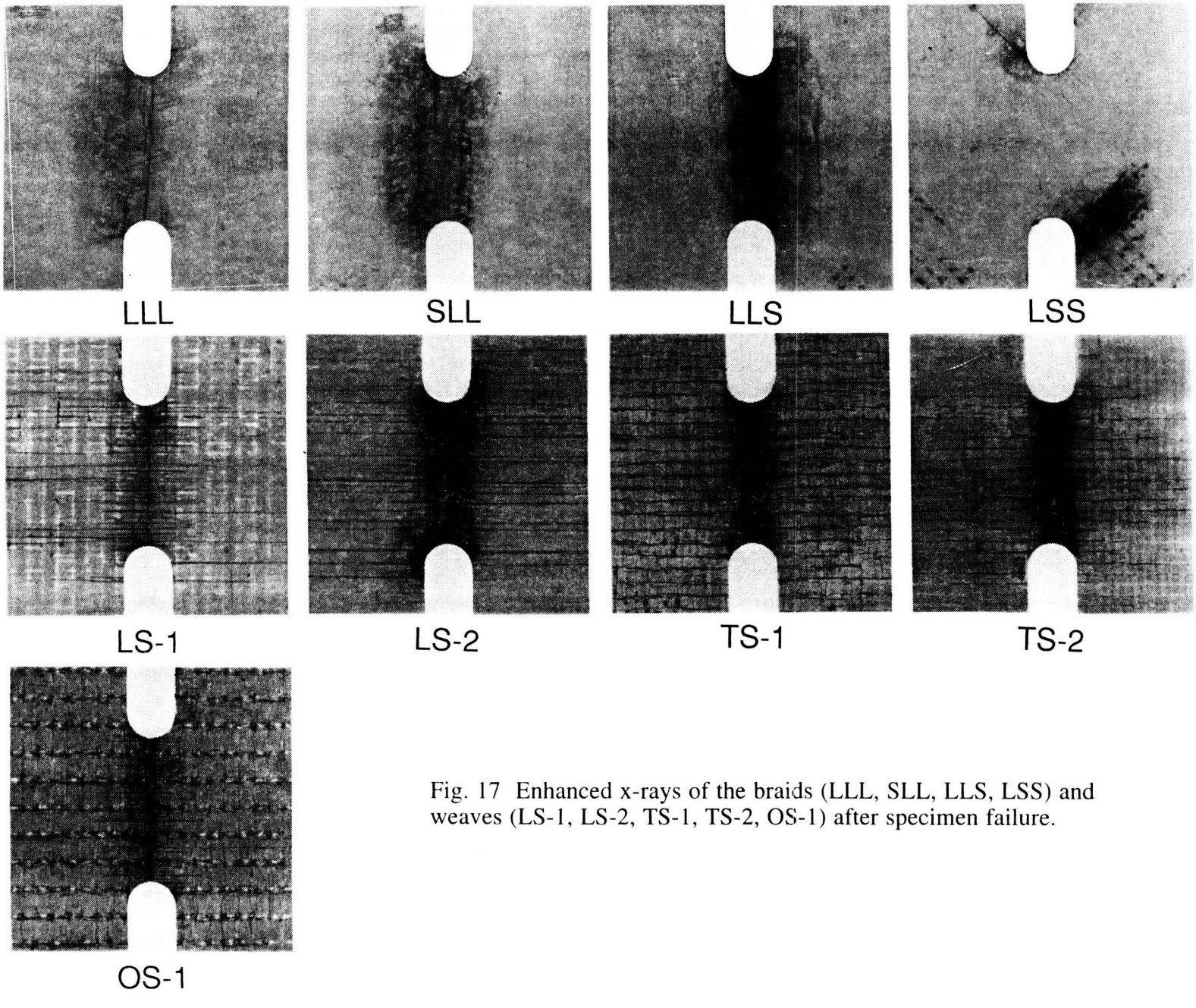

Fig. 17 Enhanced x-rays of the braids (LLL, SLL, LLS, LSS) and weaves (LS-1, LS-2, TS-1, TS-2, OS-1) after specimen failure.

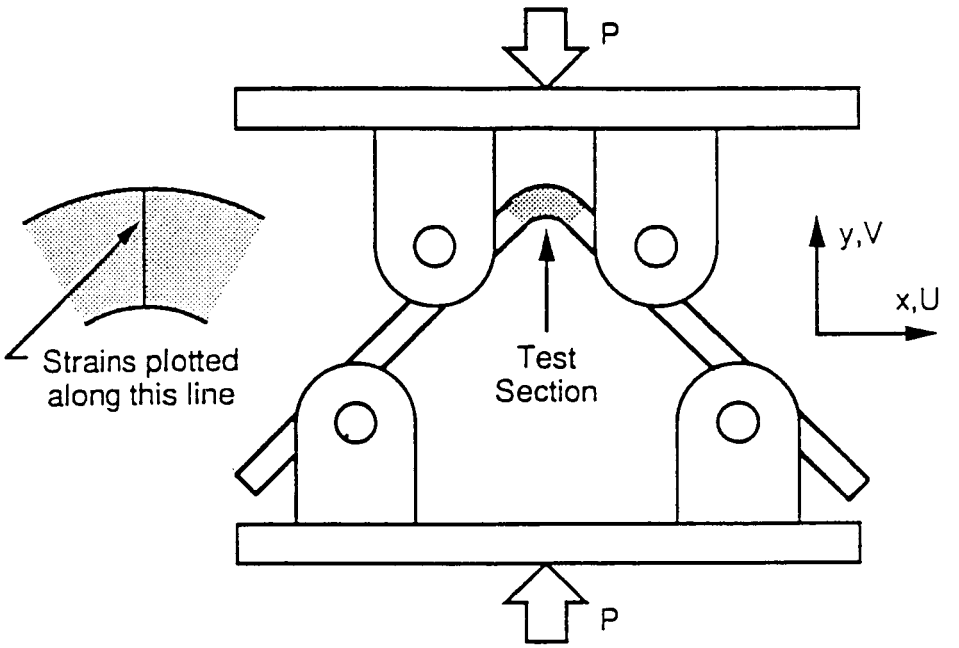

Fig. 18 The through-the-thickness tensile test loading fixture and specimen.

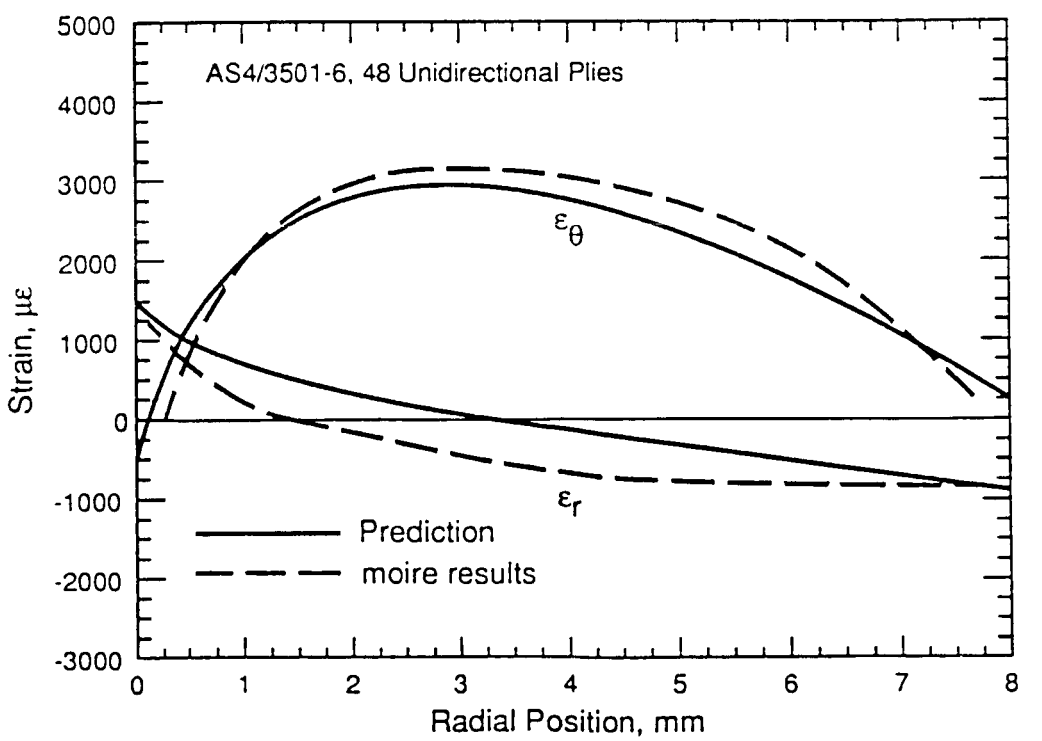

Fig. 19 Strain distributions on the edge of the through-the-thickness tensile specimen.

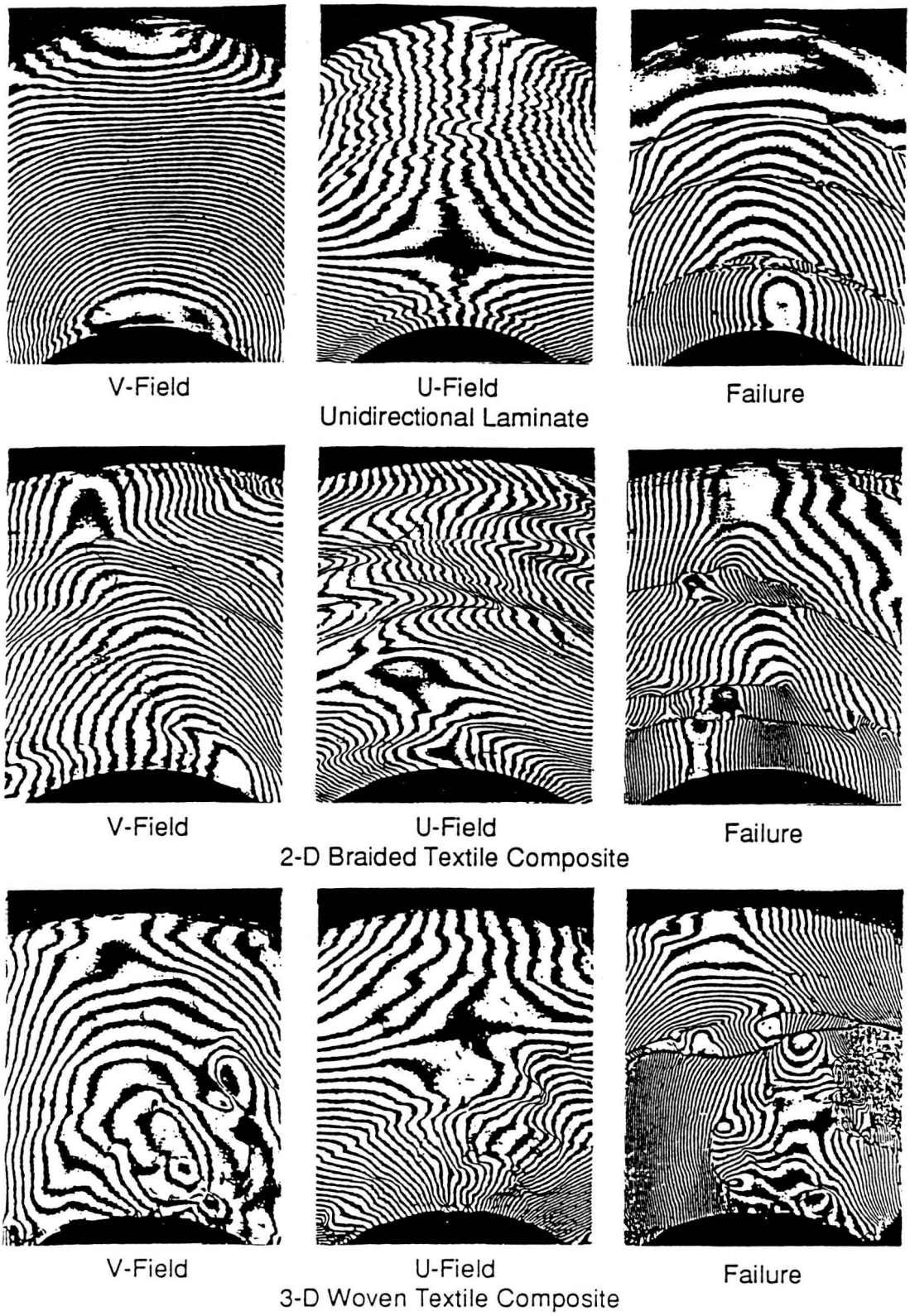

Fig. 20 Moiré interferometry fringe patterns of through-the-thickness tensile test for laminated, 2-D braided and 3-D woven composites.

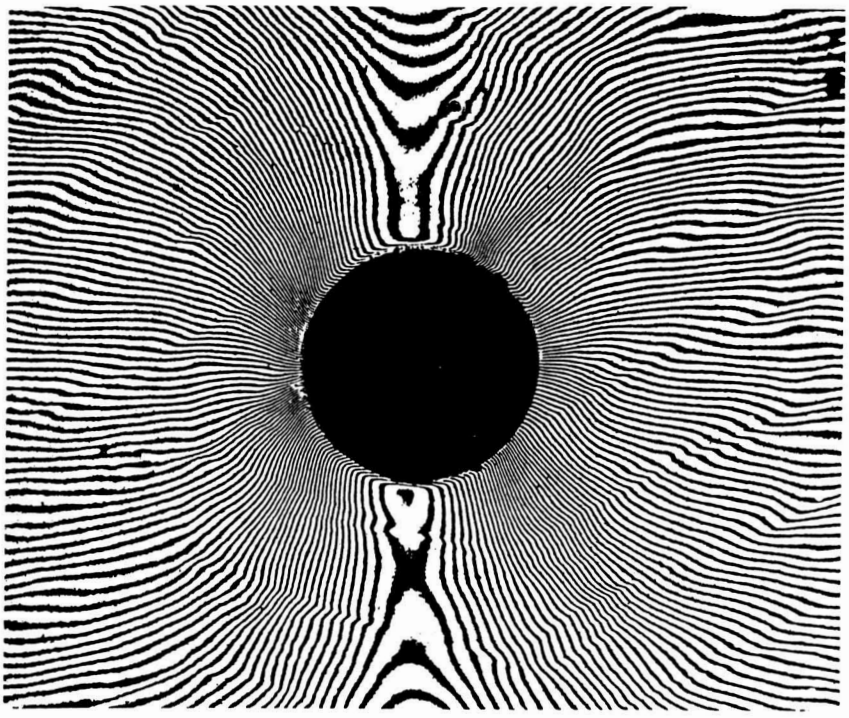

V-Field

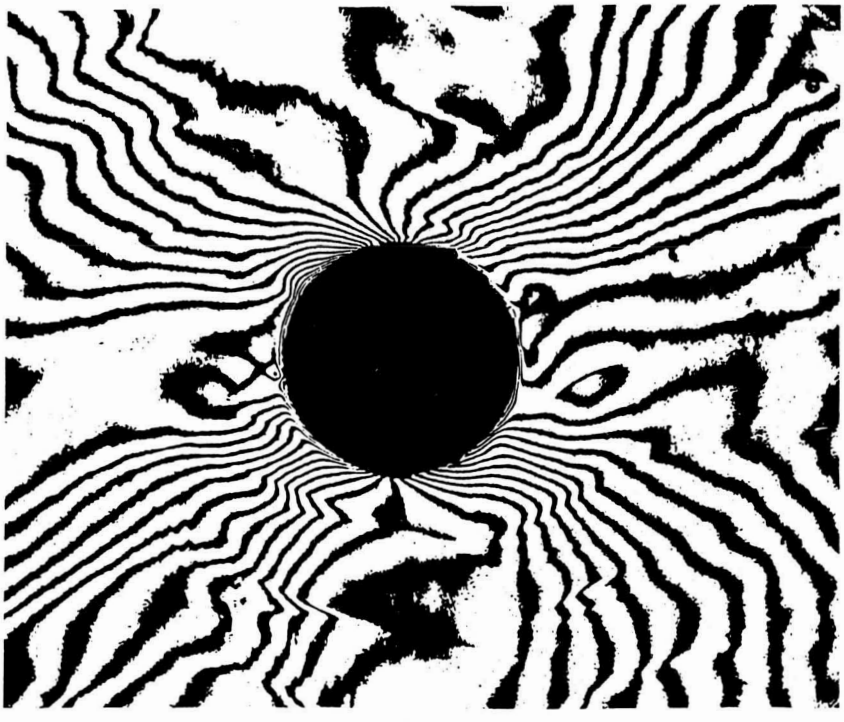

U-field

Fig. 21 Moiré interferometry Displacement fields for the LLL Open-Hole tension specimen.

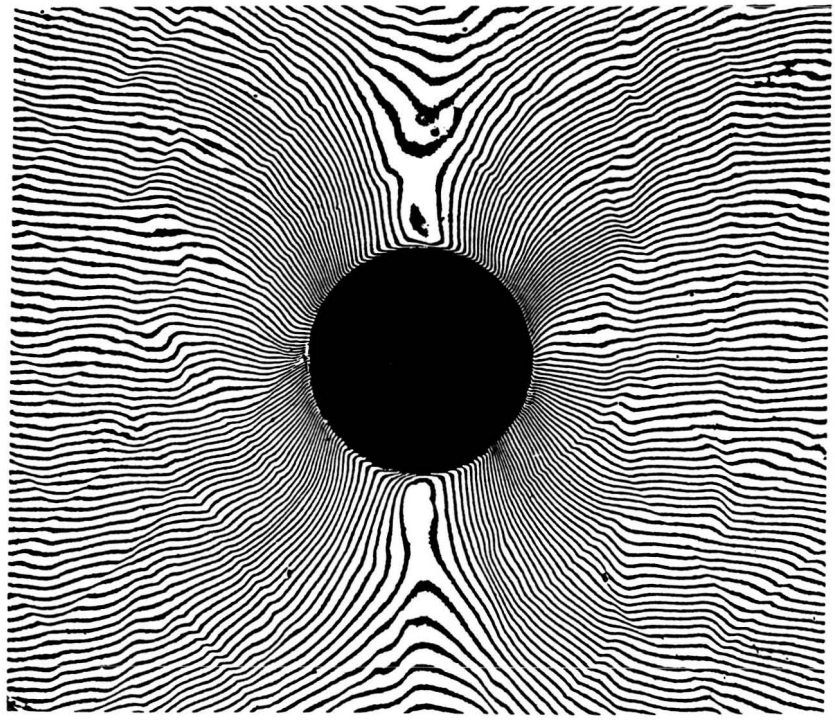

V-Field

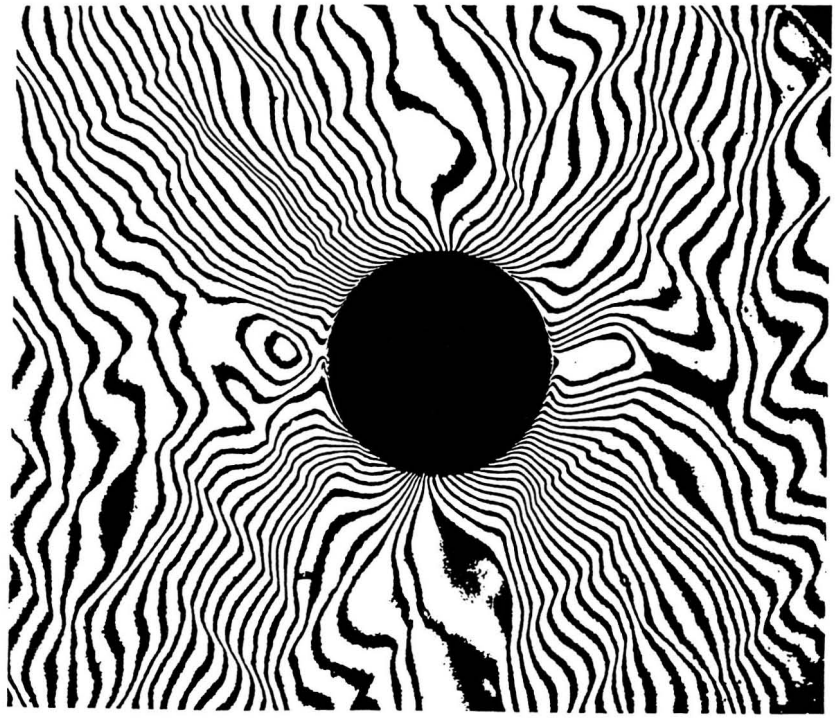

U-field

Fig. 22 Moiré interferometry Displacement fields for the LSS Open-Hole tension specimen.

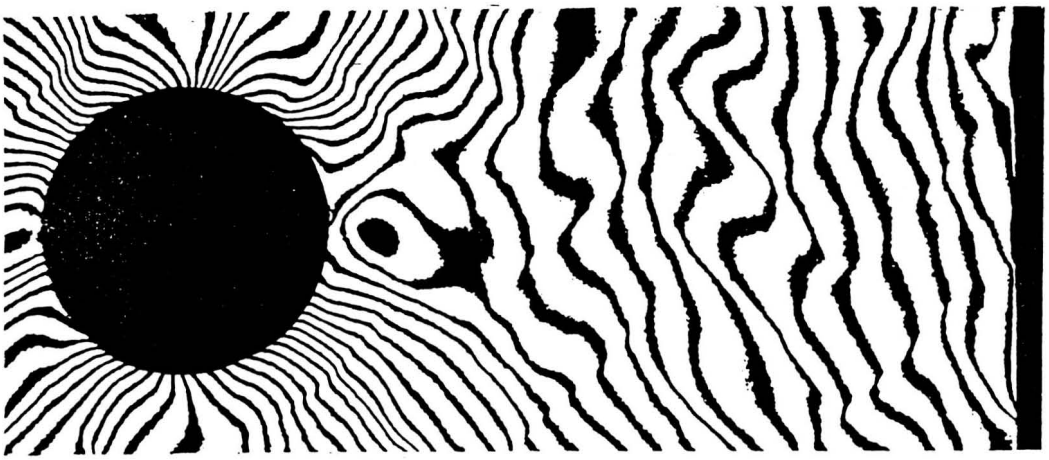

u displacement field for specimen I

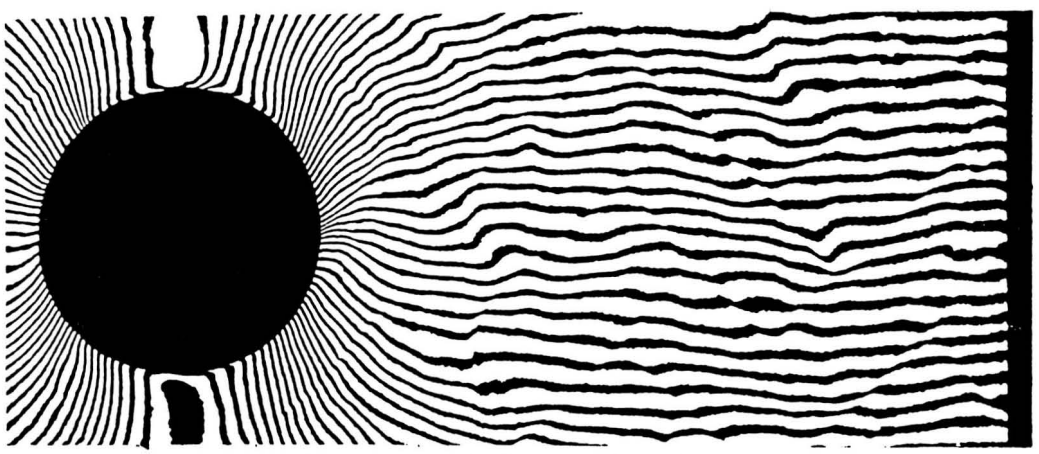

v displacement field for specimen I

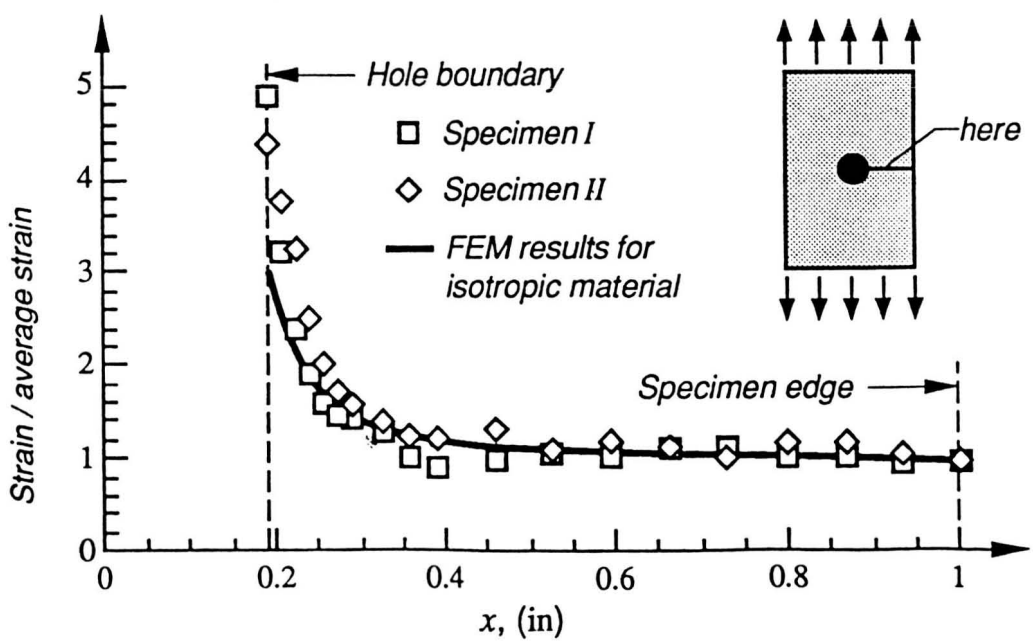

Fig 23 Moiré patterns for the LSS specimen and strain plot for both the LLL and LSS specimens.

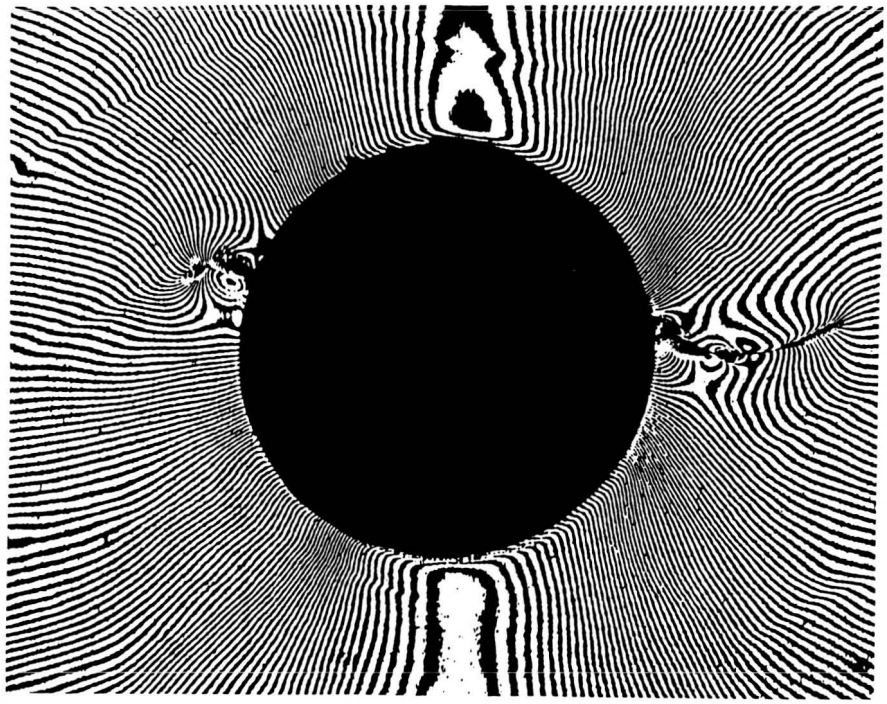

LLL Specimen

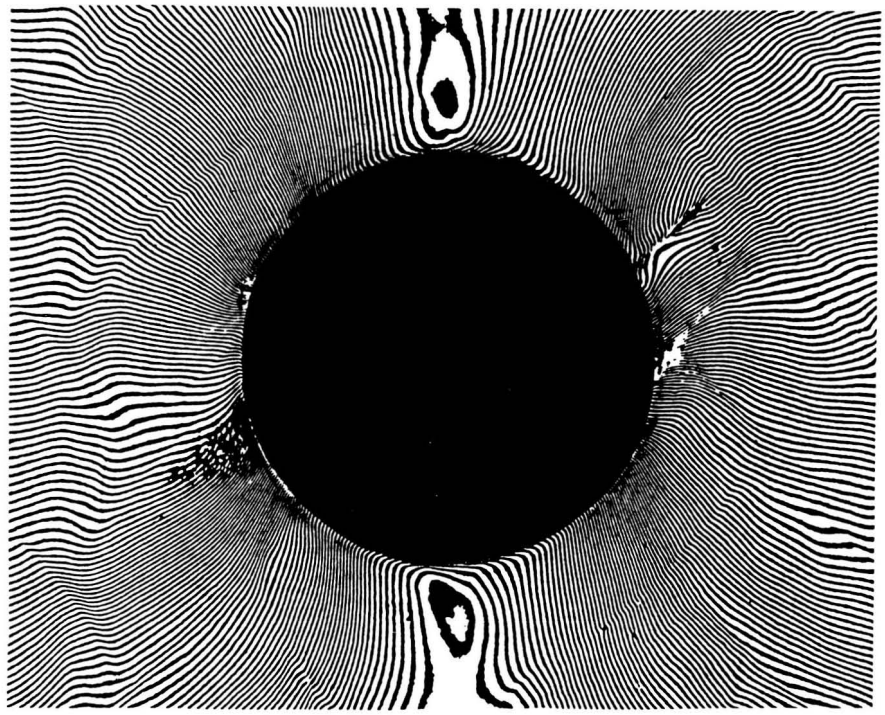

LSS Specimen

Fig. 24 Cracking can be seen at the location of the hole.

Multiaxial Stiffness and Strength Characterization of 2-D Braid Carbon/Epoxy Fiber Composites

S. R. Swanson and L. V. Smith
Department of Mechanical Engineering
University of Utah
Salt Lake City, Utah 84112

ABSTRACT

Textile preforms are currently being considered as a possible means for reducing the cost of advanced fiber composites. This report presents the results of a study of the stiffness and strength of carbon/epoxy 2-D triaxial braid fiber composites under general conditions of biaxial stress loading. A comprehensive investigation into the in-plane stiffness and strength properties of 2-D braids has been carried out, using tubular specimens of AS4/1895 carbon fiber/epoxy made with the RTM process. The biaxial loadings involved both compression-compression and tension-tension biaxial tests. The results showed that failure under biaxial loading could be based on procedures similar to those developed for laminates, using critical strain values in the axial and braid direction fibers, but with degraded strength properties because of the undulating nature of the fiber paths. A significant loss of strength was observed in the braid directions.

INTRODUCTION

This is a final report on a three year program to measure the biaxial stiffness and strength properties of 2-D triaxial braid carbon fiber/epoxy materials, using cylindrical specimens. Four different sets of braid architectures were studied, using biaxial tension and biaxial compression tests. This final report summarizes the entire project. The results have also been presented in papers in the open literature which have been submitted or already published, which in some instances provide additional detail. The work on stiffness models, an experimental study of the effects of strain gage size, and comparison of theoretical and experimentally measured stiffness has been reported [1]. The failure properties of the braids under biaxial compression loading was reported in [2], along with comparisons with a maximum strain failure criterion. Similar results for the biaxial tension experiments were given in [3]. The details of the design of the biaxial tension

specimen and test fixture have been submitted for publication in [4]. The correlations of braid architecture with observed stiffness and strength in biaxial compression have been reported in [5], and submitted for publication in [6] in expanded form including both the biaxial compression and tension results. An examination of the micro-mechanics parameters affecting the strength of the braids has been submitted for publication in [7]. An overview paper comparing braid and lamination biaxial strength properties has been presented in abstract form in [8], and submitted for publication in [9]. An overview of selection of parameters for 2-D triaxial braids has been published in [10]. An overview of the strength properties of braids has been given in [11], and submitted in expanded form in [12].

Braided preforms are being considered along with other textile form composites for structural applications, because of possible advantages in through-the-thickness strength, increased damage resistance, and cost savings through increased automation in manufacturing. Braided materials would be expected to exhibit some loss of in-plane stiffness and strength relative to conventional laminates, particularly in the braid fibers because of the undulating fiber path. However little detailed information has been available to assess the trade-offs in properties.

Two-dimensional braiding enjoys a long history, where it was automated over a century ago [13]. The interlacing yarns, which travel in a serpentine path, form braiders which are oriented at an angle to the length of the braid. Two-dimensional structures made solely from these braider yarns are termed biaxial braids. A triaxial braid may be produced by introducing axial, also called fixed, yarns in the braiding process. The undulation of the braid yarns tends to enclose the axial yarns. In terms of laminated composites, the final structure will then have a $[0/\pm\theta]$ orientation, as illustrated in Fig 1. Braid size and angle can be chosen to provide even coverage of the axial (fixed) yarns. If this is done, the braided structure will have nearly straight axial yarns, and braider yarns with a high degree of undulation.

The development of braiding as a technique for advanced fiber composite structures has been described in recent work [14,15]. Processing parameters have been considered by Popper [16] and Ko, Pastore, and Head [17]. Braiding of fiber composites is one of the possible forms of textile

processes, and may be used in conjunction with resin transfer molding (RTM) techniques.

The development of stiffness models for textile materials including braids has been considered by a number of authors, including [18-24]. Information on the strength properties of textiles has been presented by Ishikawa and Chou [25], Ko [26] , and by Crane and Camponeschi [27].

The objective of the work reported here was to investigate the biaxial stiffness and strength properties of 2-D triaxial braid materials. The need for biaxial strength properties is clear, as even simple loadings produce multiaxial stresses in the various fiber directions in a braid or a laminate. However biaxial tests have proved to be relatively difficult to perform on fiber composite materials, because of experimental problems associated with stress concentrations in the specimen at load introduction locations. Experimental specimens and procedures have been developed in our laboratory, based on the use of tubular specimens. An overview of the experimental techniques used in previous tests on laminates is given in [28]. The procedures employed at present involve combinations of compressive axial loading and external pressure on tubular specimens to achieve biaxial compression loading, and tensile axial loading combined with internal pressure to achieve biaxial tension. Braided composites are often constructed at least initially as tubular preforms, and thus it is convenient to use tubular specimens in experimental studies. Tubular specimens are advantageous for reasons of relative freedom from end and edge effects. It is intended that the failure data obtained will be applicable to general structural applications.

Relatively little information is available in the literature on the strength properties of braided composites. However, strength data are important in proposed applications for strength critical structures. Ishikawa and Chou [25] presented results in which a threadwise analysis was extended to study the "knee behavior" in the stress-strain curve of woven fabric composites. They assumed that nonlinearities in the stress-strain relationship were a result of matrix cracking. Results of their study did improve correlation with the non-linear stress-strain curve, but were not used to predict ultimate failure. Ko [26] used the concept of an average cosine of the braid yarn path and the rule of mixtures to predict the ultimate failure strength of three-dimensionally braided composites, and obtained results useful for preliminary design studies. Crane and Camponeschi [27] published

significant experimental results involving tension, compression and flexure loading on three-dimensionally braided test specimens.

Experimental results for textile composites found in the literature have all involved uniaxial loading environments. Structural applications of braided composites may result in complex loadings, however, which complicate the assessment of strength. The present study attempts to add to the data base by reporting the results of failure tests on braided carbon/epoxy composites under biaxial compression loading, and provide sufficient architecture description to allow independent comparisons.

In the present work, biaxial failure tests were carried out on 2-D triaxial braids with four different sets of architectures. Correlation is given between measured stiffness properties and predictive models. Results of biaxial compressive testing of triaxially braided specimens will be shown in both strain and stress space. A review of the maximum fiber-direction strain failure criterion will be presented, and applied to the present data. Failure modes of the specimens that provide justification for using a maximum fiber-direction strain failure criterion will be discussed. Rules are developed so that strength critical design can be carried out with the braid materials. Correlations between the microstructure and failure properties will be discussed, and simplified analyses of the microstructure will provide insight into how braid parameters affect braid strength.

EXPERIMENTAL TEST PROGRAM

Preforms were produced by Fiber Innovations Inc. by braiding dry AS4 yarns in a regular (or 2-step) braid pattern over a mandrel. The 2-D triaxial braid combines straight axial yarns with $\pm\theta$ braid yarns, as illustrated in Fig 1. The preform (still on the mandrel) was then resin transfer molded (RTM) with a low viscosity resin system, Shell 1895. The RTM process produced specimens with good surface finish and dimensional repeatability. Specimens were fabricated in two sizes, a smaller size for the biaxial compression tests and a larger size for the biaxial tension tests. The biaxial compression specimens had a nominal inside diameter of 53 mm (2.09 in.), a nominal wall thickness of 3.24 mm (0.128 in) and were produced in 760 mm (30 in) lengths. The biaxial tension specimens had a nominal inside diameter of 96.8 mm (3.81 in), a wall thickness of 3.30 mm (0.130 in), and were also fabricated in 760 mm (30 in) lengths. The braiding parameters are listed in

Table 1. The braid architectures are designated as A, B, C, D in this report, which corresponds to the LSS, LLS, SLL, LLL designation, respectively.

Prior to being sent to the University of Utah, the specimens were inspected ultrasonically for porosity by the Boeing Co. The ultrasonic equipment was calibrated to a control specimen before each inspection. Since the absolute porosity of the control specimen was not known, the results from these inspections were used as a comparative tool only. These results, along with visual inspection of the specimen surfaces, indicated that porosity was not entirely uniform from specimen to specimen. Comparison of the experimental failure data provided no clear correlation between low mechanical performance and porosity. This suggested that although porosity varied from specimen to specimen, its magnitude was low enough in these specimens not to influence their mechanical properties.

The compression specimens were then cut to 223 mm (8.78 in) lengths, and the tension specimens cut to 330 mm (13 in) lengths. The ends were wet wrapped with fiberglass cloth, then cured in a mold to produce net shape reinforced molded endtabs.

Comparisons of the measured braid angle to the target were performed for each architecture. It was assumed that the braid angles of the outside braided layer was representative of the interior layers. Average braid angles were obtained with the assistance of a single braid tracer yarn, and were taken from the tangent of the average tracer yarn spacing in the axial direction and the specimen circumference. An approximate indication of the local extreme braid angles was found by tracing each braider yarn path around the circumference for 51 mm (2.0 in.) in the axial direction. This pattern was then laid flat, and the braid angles were measured using a protractor.

BIAXIAL COMPRESSION TESTS - A photograph of the specimen is given in Fig 2, and the biaxial compression apparatus is illustrated in Fig 3. The specimens were loaded in one of three ways. Uniaxial testing was achieved through either axial compression or radial pressure and combinations of these loads were used for biaxial compression. An axial compression test consisted of attaching steel end grips to the endtabs of the specimen to prevent endtab brooming failure during a test. This assembly was then placed in a load frame and loaded at 1.3 mm/min (0.05 in./min) to failure.

Compressive radial pressure tests were conducted by placing the specimen inside a steel thick walled cylinder and pressurizing the external surface of the specimen with hydraulic fluid, as illustrated in Fig 4. The endtabs of the specimen were machined to provide a hydraulic seal with the fixture. A synthetic liner around the specimen shielded it from the hydraulic fluid during a test. Although this test applied pressure in the radial direction only, the specimen was also subjected to an axial load that is a result of pressure acting on the tapered surface of the endtab. It is for this reason that the stresses from the radial pressure tests do not exactly fall on the hoop direction axis in the biaxial stress plots that will be presented later.

Biaxial testing was performed by combining these two loading environments at a controlled ratio. This was achieved by amplifying the electronically measured hydraulic pressure signal and slaving a load frame to it. In this manner a constant ratio of axial to hoop stress (σ_a/σ_h) was maintained throughout the test.

BIAXIAL TENSION TESTS - The biaxial tension tests were performed by applying internal pressure and axial tension to a cylindrical specimen, as illustrated in Fig 5. Pure axial tests were performed by placing the apparatus in a load fixture and loading in displacement control to failure. Pure hoop tests were performed by connecting the split cores, and pressurizing the specimen with hydraulic fluid to failure. Biaxial tests were performed by combining the two loading conditions. To maintain a constant ratio of axial to hoop stress, the pressure was monitored electronically. The electronic pressure signal was amplified according to the desired stress ratio, and used to drive a servo-controlled load frame in load control.

The specimen is similar to that used previously in laminate tests, but significant changes were made to the end grip configuration to accommodate the higher axial loads desired for the present program. The higher loads were necessitated both by the thicker wall thickness of the braid specimens, as well as to increase the range of test conditions. The design of the end grip regions is very important in conducting biaxial tests with tubular specimens, and considerable time and effort went into the design used in this program.

Biaxial Tension Load Fixture - The apparatus shown in Fig. 5 has been designed to load the specimen in the hoop direction by pressurization of the specimen. This can be accomplished in one of two ways. By connecting the

split cores, pressurization subjects the specimen to loading in only the hoop direction. With the split core not connected, pressurization produces a biaxial test, where the ratio of the axial to hoop average stress is 0.5.

Threaded attachments at either end of the apparatus allows connection to a load frame where any ratio of axial to hoop stress can be achieved. A constant ratio of axial to hoop stress was produced by monitoring the hydraulic pressure electronically. A load frame, in load control, was slaved to the signal coming from the pressure transducer which was amplified according to the desired stress ratio. This setup has worked well in past experiments, and proved adequate for these tests with the following exception. High stress ratios (axial to hoop) required large amplification of the pressure transducer signal. This can cause noise sensitivity, or allow the test to go unstable. Instability occurs when an increase in load causes the hydraulic pressure to increase from the Poisson effect of the specimen. This difficulty is easily avoided by controlling the pressure and axial loading independently. Further testing details implemented to induce gage section failure will be described in the discussion of endtab design.

Endtab Design and Analysis - Although the biaxial tension apparatus has been used in a number of previous investigations on laminates, it was desirable to carry out a redesign of the specimen for the present braid tests. As mentioned above, the changes were made to permit higher axial loads to be applied to the specimen without endtab failure, to accommodate the greater thickness of the braids specimens as well as to expand the range of biaxial stresses that could be applied. Fig. 5 depicts a cross-sectional view of the new fixture and specimen that has been developed to study composite cylinders in biaxial tension. A major feature is the use of a tapered region as used previously by Groves et al. [29]. The axial force on the tapered region introduces radial compression into the bond line between endtab and specimen, much as in an endtab for a tensile coupon. This increases both the bond and structural strength of the endtab. The key issues are the optimum design of the geometry and materials of the endtab to accomplish the dual objectives of minimizing the stress concentrations under both hoop and axial loading, and also transmitting a sufficiently high axial force.

Various endtab geometries were examined using finite element analysis. Three parameters controlling the shape and loading of the endtab were studied: endtab length, endtab thickness, and grip length. For a given

endtab geometry, the maximum stresses in the endtab are determined from the axial strength of the specimen. Specimen thickness and fiber orientation, therefore, have a dominant effect in the design process of the endtab.

The primary purpose of the endtab is to smoothly introduce load into the gage section. Finite element analysis showed a stress concentration in the specimen at the intersection of the endtab with the gage section. The magnitude of the stress concentration is controlled by the modulus and angle of the endtab. Although the modulus is determined by the endtab material, the angle can be chosen to minimize the stress concentration. There are practical limits on how small the angle of the endtab can be, however. Due to deformation of the endtab, it tends to slip in the grips during a test. Having a sufficiently large endtab angle reduces this tendency.

The final parameter controlling the geometry of the endtab is consideration of specimen pressurization. Since the endtabs are firmly fixed in the grips, pressurizing the gage section induces bending, or axial, stresses in the endtab region of the specimen. Increasing the length of the endtab outside of the grip region will reduce these effects. These parameters and numerous endtab geometries were considered in selecting the endtab geometry. The endtab has an ID equal to the OD of the specimen, which for the tests results given later was 103 mm (4.05 in), a length of 127 mm (5.0 in), a maximum thickness of 25 mm (1.0 in), and a grip length of 64 mm (2.5 in).

Finite element analysis showed that this geometry produced a stress concentration at the intersection of the endtab and gage section of 1.05. A comparison was made between the stress concentration induced by the cylindrical specimen and a flat uniaxial specimen. The same composite material properties were used in both models and typical fiberglass properties were used for the endtab in the uniaxial specimen. An endtab thickness of 6.3 mm (0.25 in) was used for the uniaxial specimen. Since ASTM 3039 does not specify an endtab angle, various angles were investigated for the uniaxial specimen. An angle of 15°, 30°, and 45°, for example, produced stress concentrations of 1.1, 1.2, 1.25 respectively. Although the stress concentration of the cylindrical specimen is less than the uniaxial specimen for the angles considered, it does not prove that the cylindrical endtab will produce an acceptable gage section failure. Based on the results of uniaxial specimens, the magnitude of the cylindrical specimen stress concentration is probably

acceptable. As is suggested in ASTM 3039 for uniaxial tension testing, gage section failure should be verified through experimental testing.

Finite element analysis of this endtab design was conducted with the specimen subjected to an axial load of 548 kN (123 kips). A stress concentration on the surface of the endtab, where it exited the grip region, was observed. Due to its relative small size, however, it was assumed that local yielding of the endtab would reduce the magnitude of the stresses in this region. The area of the endtab outside of the grip region was found to be primarily in tension, where tensile stresses of approximately 44 MPa (6.4 ksi) were observed. The area of the endtab inside the grip region was primarily in compression, where compressive stresses of approximately 16 MPa (2.3 ksi) were found. The maximum shear stresses at the interface of the composite and endtab were found to be 17 MPa (2.5 ksi) outside of the grip area, and 22 MPa (3.2 ksi) inside the grip area. Since the advertised strength of many structural epoxies exceeds these stresses, and the grip is expected to improve the endtab shear strength, this endtab design was selected for further study.

Endtab Material Selection - The neat epoxy endtab used previously by Groves et al. [29] was cast from DER 332 (Dow Chemical) resin and T442 (Texaco Chemical) hardener. This is an unfilled system that has been used for filament winding and has a room temperature pot life of nearly 8 hours. Casting the endtab from an epoxy in one step offers cost savings over previous endtab designs using combinations of materials, such as in our previous work [28]. The initial intent of this study was to follow this concept. Various epoxy systems were investigated, with varying degrees of success and failure.

Because of the thickness and size of the endtab, cure induced exotherms as well as shrinkage were of concern. These were addressed by selecting systems with relatively long pot lives and fillers designed to minimize shrinkage. Although these systems were successful at minimizing shrinkage, the fillers tended to reduce the bond strength of the epoxy and made the endtab more brittle. During an axial test, for example, portions of the endtab outside the grip area would often violently crack away from the specimen. At higher loads the endtab began debonding from the composite cylinder.

A series of toughened epoxy systems was investigated in the hope that a toughened endtab would conform to the circular grips by yielding rather

than cracking. Dog bone specimens were cast of each system, and loaded in uniaxial tension to failure. From these tests results a system high in toughness and strength was selected and used in the endtab. This system performed much better than the filled systems used initially. Where cracking of the endtab outside of the grip area initiated around 100 kN for the filled systems, the toughened endtab withstood loads of 300 kN before cracking initiated. Further, the toughened system did not debond from the composite during the test.

Although the toughened epoxy improved the endtab performance, it was necessary to have the endtab withstand loads in excess of 600 kN without cracking. In an attempt to significantly strengthen and toughen the endtab, fiberglass cloth was wet wrapped around the cylinder. To avoid machining, the fiberglass endtab was cured in the same mold used for the neat resin endtab. Although this combination proved adequate for this study, the endtab was resin rich, and high in void content. Higher loads might be achieved using a fiberglass prepreg cured in an autoclave. Since the fiberglass significantly stiffened the endtab, the geometry was tapered outside of the grip area as shown in Fig 6. This effectively reduced the endtab angle, making the stress concentration of the fiberglass endtab comparable with the neat resin endtab.

Endtab Design for Combined Load Testing - Initially it was anticipated that one endtab geometry would be used for all tests. Partial debonding of the fiberglass endtab during axial tests required developing an endtab specifically for axial testing, however. The increase in bond strength resulting from the grip induced compressive loading of the endtab is apparently significant. Only the portion of the endtab outside of the grip region was observed to debond. This may be a result of tensile radial stresses between the endtab and composite. Although they are small in magnitude, they were observed to affect the bond strength significantly.

To avoid the abrupt changes in load resulting from the partial debonding of the fiberglass endtab, a modified endtab geometry was investigated. The geometry of the modified endtab involved removing the material of the endtab that was debonding, as shown in Fig. 7. The endtab depicted in Fig. 7 was therefore used to test specimens in axial tension.

As shown in Fig 5, there is a small region between the hydraulic seal and the grip where the specimen is loaded by the axial force but not by the

internal pressure loading. Since biaxial stress typically strengthens composite laminates [19-22], depending on the layup, areas of high uniaxial stress such as this in a nominally biaxial test may be weak links in the specimen. The initial biaxial tests were carried out with the split cores connected. As the grips were pulled apart, the region between the bottom seal and grip (in the figure) increased. This produced an increasing area of material subject to high uniaxial axial stress. Accordingly, some of the specimens tested in this manner failed in this area of the endtab. The problem was remedied in two ways. First, the seals were modified, so that the region between the seal and grip was reduced from approximately 12.7 mm (0.5 in.), to 6.3 mm (0.25 in.). Second, subsequent biaxial tests were carried out with the split cores disconnected. This prevented the region from increasing during the test. The total axial load on the specimen is of course the total of the axial component due to the internal pressure, and the superposed axial loading from the axial force test machine. Biaxial tests conducted in this manner exhibited acceptable gage section failures.

STIFFNESS OF BRAID MATERIAL

Strain Measurement - Strain was measured using electric resistance strain gages bonded to the surface of the specimen. Three gages were mounted in each of the hoop and axial directions. The measured strains from these gages were averaged. A study on strain gage size showed that out of a 3.2 mm (0.12 in), 6.4 mm (0.25 in), and 13 mm (0.50 in) gage, the 13 mm by 4.4 mm (0.50 in. by 0.18 in.) rectangular strain gage, mounted with the 13 mm direction parallel to the direction of desired strain, produced satisfactory strain measurements. A summary of the strain gage size study is shown in Fig 8.

Typical measured stress-strain curves are shown in Figs 9-11, measured in uniaxial compression loading in the axial and hoop direction. The tension loadings gave similar response, although the compression test results were somewhat more nonlinear. A summary of the measured axial and hoop moduli is given in Tables 2 and 3 for the compression and tension tests.

Models - A basic requirement of design with braided materials is to be able to predict the stiffness. Three models available in the literature were compared with the experimental data. The models, in increasing degree of complexity, were as follows. The first, classical lamination theory, treats the braid as if it were a laminate that is characterized by the fiber volume fraction

and the amount of fibers in the ±θ braid and axial directions, and thus totally ignores the through-the-thickness component of the fiber path. The second model has been termed a three dimensional classical lamination theory model. It is based on a through-the-thickness angular transformation of properties, assuming a simple saw-tooth braid fiber undulation with a constant crimp angle (the through-the-thickness angle). The third model, termed the fiber inclination model, uses assumptions similar to the 3D lamination theory model, but models the braid fiber path as a series of in-plane and through-the-thickness segments, and combines these segment properties to predict average braid stiffness. More detail on these models has been given in Smith and Swanson [1].

All of the models investigated require input properties for the axial and braid yarns. The starting properties were based on known material lamina constants for AS4/3501-6, which is believed to be similar to the AS4/1895 system used at present. These properties are listed in Table 4, and correspond to a fiber volume fraction, v_f, of 0.60. It may be noted that carbon fiber exhibits stiffening in tension, with a secant modulus at high strain levels on the order of 10 or 15% higher than at low strain levels. The value for E_1 given corresponds to a low strain value, and is lower than values often listed for AS4/3501-6 in the literature, which presumably are taken at higher strain levels. These values must be adjusted for the lower v_f of the braids used at present, which had v_f approximately equal to 0.50. To accomplish this, fiber and matrix properties were found that corresponded to the lamina properties. These properties were then adjusted for v_f by using the usual rule of mixtures for modulus E_1, and the Halpin-Tsai relations [30] for the transverse and shear moduli.

The fiber volume fractions for the braids were obtained by using three different methods. The first estimate was obtained by measuring and weighing samples, and using known fiber and matrix densities. Although in general agreement with the other two methods, this technique was believed to be the least accurate. The second method was to weigh the specimen before and after the matrix was removed using acid digestion. The third method was to calculate a theoretical v_f based on the specimen dimensions and the known fiber content based on the number of fibers in the yarn, the size of the yarns, and the geometric factors of the braid and average crimp angles. These

later two methods agreed well. The theoretical calculations were then used in subsequent calculations to obtain model material properties.

The theoretical calculations for v_f were based on the following equations.

$$V_f = \frac{V_a + V_b}{V_t} \tag{1}$$

$$V_a = N_l N_a Y_a A_t \tag{2}$$

$$V_b = N_l 2 N_a Y_b A_t \frac{1}{2}\frac{1}{\cos(\beta)}\left\{1 + \frac{1}{\cos(\theta)}\right\} \tag{3}$$

where V_a and V_b are the volumes of the axial and braid yarns, N_l is the number of layers, N_a is the number of axial yarns, Y_a is the size of the axial yarn relative to a 6k yarn, A_t is the area of a 6k yarn, taken as 0.235 mm^2 =3.64 10^{-4} in^2, Y_b is the size of the braid yarn relative to a 6k yarn, β is the braid angle, and θ is the crimp angle.

As mentioned above, the first model is based on classical lamination theory and thus needs no further explanation. The braid yarns are assumed to be characterized only by the braid angle, and fiber volume fraction. The second model adds a transformation in the-through-the-thickness direction of the braid yarns. In this model it is assumed that the braid yarns follow a simple zig-zag pattern and so the braid yarn path can be characterized by the crimp angle and the braid angle, as well as the overall fiber volume fraction.

The average crimp angles for each architecture were calculated according to the following geometric relationships. The undulation amplitude, Au, was assumed to be equal to the composite thickness divided by the number of braided layers comprising it. The wavelength of undulation, Pu, was found according to:

$$P_u = \frac{\pi\phi}{N_a \sin\beta} \tag{4}$$

where ϕ is the nominal tube diameter, N_a is the number of axial yarns, and β is the average braid angle. The crimp angle, θ, is found as the tangent of the undulation amplitude and half of the wavelength as:

$$\theta = \tan^{-1}\left(\frac{2A_u}{P_u}\right) \tag{5}$$

The values for each architecture are listed in Table 5.

As described in [1], the stiffness of the braid yarns can be described by a transformation T_2 through the crimp angle to the in-plane direction, and an in-plane transformation T_3 through the braid angle to the overall global coordinates. The three-dimensional braid material stiffness matrix is then given by

$$\overline{Q}_{XYZ} = T_3^{-1} T_2^{-1} [Q_{123}] T_2 T_3 \tag{6}$$

The third model employed is based on the fiber inclination model (FIM) of Chou et al. [21,24]. In this model the path of the braid yarn within the unit cell is idealized as a series of straight segments. In [24] averaging of the compliances of the segments is then employed to form a three-dimensional compliance matrix that is then inverted to form the stiffness matrix for the braid, and then combined with the axial yarns using lamination theory. A slightly different approach will be used here, but it will be seen that under usual conditions the difference is not significant. The point of difference is that instead of starting with the assumption of averaging compliances, a more physically based procedure will be employed. Following what has been entitled a "mechanics of materials" approach to stiffness [30], and generalizing to n materials, two forms of combining moduli can be defined as

$$\frac{1}{E_s} = \sum \frac{v_f}{E} \tag{7}$$

for a summation of elements in series, and

$$E_p = \sum v_f E \qquad \text{or} \qquad \frac{1}{E_p} = \sum \frac{1}{v_f E} \tag{8}$$

for a summation of elements in parallel.

These rules are used in the elementary procedures for micromechanics predictions of properties [30]. It is also well-known that these rules correspond to the Voight and Reuss lower and upper bounds respectively, and also represent averaging of compliances and stiffness. Applying these ideas to the unit cell, the model for E1 would be obtained by considering the yarn segments within the unit cell to be in series and thus the compliance averaging to be most appropriate. Similarly the shear modulii would follow

similar rules. However the transverse modulii and minor Poisson's ratios would follow the rules for parallel elements, and thus would follow the averaging of Eqn 8. Thus it would appear that the averaging of material properties within the unit cell should most appropriately follow a mixture of both stiffness and compliance averaging. As a practical matter, however, the calculation of the transverse modulus E_2 is very insensitive to the averaging rule, and for moderate crimp angles E_2 can be taken as being constant. Also for constant E_2 the compliance term containing the ratio

$$\frac{-\nu_{21}}{E_2} = \frac{-\sum l\nu_{21}}{E_2 \sum l} = -\frac{\sum(\nu_{21}/E_2)}{\sum l} \tag{9}$$

can thus be obtained by using compliance averaging. Thus under these circumstances compliance averaging can be used for all of the terms, as in the fiber inclination model.

An illustration of the geometric parameters used for the fiber inclination model is given in Fig 13.

The comparisons of the models with the experiments are shown in Figs 14 and 17 for the axial modulus, Figs 15 and 18 for hoop modulus, and Figs 16 and 19 for Poisson's ratio, for the compression and tension loadings respectively. It can be seen that all of the models give a good prediction for the axial modulus, and that the fiber inclination model gives a good prediction for all of the properties. Even the simplest model, that of classical lamination theory that completely neglects the crimp angle effects, can give a reasonable prediction for braids with low crimp angles.

The major parameters influencing the stiffness are the fiber volume, the braid angles, and the percentage of fibers in axial and braid directions. Higher crimp angles decrease the in-plane stiffness in the braid direction, and this effect is well predicted by the fiber inclination model.

FAILURE STRENGTH RESULTS

Biaxial Compression Results - Approximately ten specimens of each of the four architectures were tested. To determine baseline axial and braid maximum fiber strains, three specimens were tested in axial compression and three under radial pressure. The remaining specimens were tested at various biaxial stress ratios to provide experimental verification of the maximum

strain failure envelope. The measured stresses and strains at failure are listed in Tables 6-9.

Maximum strains in the braid direction were found by transformation of strains obtained in the specimen coordinate system. Although measured average braid angles were close to the target values presented in Table 1, extreme values varied by approximately $\pm 5^{o}$ from that target. Braid fibers with an orientation that causes them to reach a critical strain first should have a dominating effect on the failure process. Using the largest measured braid angle in constructing the biaxial failure envelopes can be justified by considering a radial pressure test, where failure is controlled by the braid yarns. In such a test, fibers with a large braid angle will reach their maximum strain before fibers with a small braid angle. If the fibers that reach their critical strain first initiate failure, as the maximum strain failure criterion assumes, the braid angle of these fibers should be used in coordinate transformations that determine their maximum strain.

Evidence that failure is dominated by the fibers may be observed through examination of the specimen fracture surfaces. If failure is determined by a maximum strain in either the axial or braid direction, then braid and axial failure modes should be apparent in the failure surfaces. Observations of the failed specimens revealed three common failure geometries: axial, braid and biaxial. Axial failure was observed as a line or crack traversing the circumference of the specimen at random axial locations in the gage section, as shown in Fig 20. Random location of the failure zone suggests that the gage section experiences uniform stress, and failure occurs in the weakest gage section location.

Braid failure may be described as a line or crack traversing the axial direction nearly the entire length of the gage section, as shown in Fig 21. The inside and outside diameter failure areas looked very different for braid dominated failure. The outside of the failure surface showed little evidence of failure. The small crack that was visible on the outside of the specimen was difficult to detect photographically. The inside of the specimen showed more clearly evidence of failure. The specimen in Fig 21 shows the inside failure area.

Biaxial failure may be described as a combination of the two previously discussed modes and was observed in some specimens where the axial and braid strains reached their critical values simultaneously, as shown in Fig 22.

These three modes of failure support the use of a fiber-direction failure criterion, since only fiber dominated failure modes have been observed.

More evidence of the mechanism controlling failure can be found from a slightly closer examination of the failure surfaces. If the fibers are dominating failure, then they should all break at the fracture surface. Sections taken from fractured regions showed that all fibers did indeed break at the fracture surface.

Biaxial Tension Results - As mentioned previously strain was measured using common electric resistance strain gages bonded to the surface of the specimen. Many of the tension specimens experienced matrix cracking during the tension tests. Matrix cracking became severe enough for many specimens that the strain gage measurements were affected. For these specimens the failure strain was determined by extrapolation from the applied load and initial strain readings.

The stress-strain response of these materials was relatively linear, although slight non-linear softening was observed toward failure. Although softening was observed in both the hoop and axial directions, it was generally more apparent in the axial direction. Specimens retested after being loaded to near failure exhibited a lower initial modulus, indicating that the softening is not elastic, and may be a result of matrix cracking. Linearity in the hoop direction is not unexpected, since failure in this direction occurs at lower stresses and strains than the axial direction. At these stresses and strains, for example, the axial stress-strain response is very linear.

Tables 10-13 contain the results for the biaxial tension failure tests of all four architectures. The failure stresses and strains are listed for each test in both the axial and hoop directions. Although a range of biaxial stress ratios was examined, the specimens were observed to fail in one of two ways. The failure modes were termed axial and hoop, because they were first observed from the pure axial and hoop tests. The failure mode is also listed in the tables, and is necessary in order to properly evaluate the maximum fiber direction strain failure criterion. Examples of specimen failures are given in Figs 23 and 24. The failure strains are shown in Figs 25 and 26 as a function of braid architecture.

CRITICAL STRAIN FAILURE CRITERION

It has been found in previous work on failure of carbon/epoxy laminates that a maximum fiber-direction strain criterion has great utility in correlating failure under biaxial stress loading [32-35]. It is useful to consider the application of similar ideas to braided specimens. The approach that will be taken here is to consider the in-plane strain values in the direction of the braider and axial yarns. In the case of the braider yarns, this direction is not that of the fibers, since the braider yarns have a varying out-of-plane crimp orientation as they undulate over and under the axial yarns.

The tabulated failure results have been plotted in strain space for each of the architectures in Figs 27-30. A maximum fiber direction strain failure envelope, correlating the data, is also presented in each figure. The experimental data generally appear to follow the trend of the critical strain failure criterion, although scatter exists in the data.

The failure envelopes shown in Figs 27-30 were constructed from the uniaxial results, and used to predict failure for the biaxial tests. Two uniaxial axial tests were performed for each architecture. The axial failure strain was measured directly from these tests and averaged to determine an axial failure strain for each architecture. Three uniaxial hoop tests were performed for each architecture. The braid failure strains were determined by transforming the strains in the measured hoop and axial direction. As was noticed previously in the compression studies, the failure envelope was observed to be quite sensitive to the assumed braid angle. Although the average braid angle for each architecture was close to the braiding target, local extremes were observed to vary by as much as 5°. This presents difficulties in systematically constructing the failure envelopes since failure tends to be controlled by extremes rather than averages. For consistency, the method of determining the braid angle for braid failure strain transformations in the compressive studies was used for the tension tests also. The values used to construct the failure envelopes are listed in Table 14.

The failure data have been plotted in stress space in Figs 31-34. The failure envelopes are also shown in these figures. The failure criterion was transformed into stress space using the initial measured stiffnesses (secant stiffnesses for the compression tests) of each architecture, which are tabulated in Tables 2 and 3.

In computing the stress failure envelope from the critical strain values from the compression tests, the secant stiffness properties at failure were used to transform the failure envelope into stress space. This provided a slightly better fit with the experimental data than using the initial elastic modulii. Due to matrix cracking in the tension tests, many of the failure strains were extrapolated, while others were averaged from fewer than three strain gages. Therefore the initial elastic properties were used for the tension tests. It is believed that this has only affected the results between approximately 5% and 10% and should not be considered as a significant deterrent from the utility of this approach.

It may be noted that although the biaxial compression and tension failure data are plotted together here, the braid architectures differ somewhat between the compression and tension specimens. However these differences were much smaller than the differences between architectures, and it provides additional insight to plot the data together, as was done here.

It can be seen from the results presented here that there is a significant loss of strength in the braid direction. For example, the braid failure strains are much lower than the axial failure strains in both compression and tension. More discussion of this will be given later.

Although the maximum fiber-direction strain failure criterion appears to correlate the failure results of the current study, its utility is dependent on the fibers dominating failure. Architectures with a smaller braid angle than was considered in this study, for instance, may experience a hoop failure that is dominated by the matrix, rather than the fibers. In such a failure mode, matrix properties and conditions would likely have more relevance to failure than fiber strain. However practical fiber composites are designed to take advantage of the high fiber strengths, and in typical applications the failures will be fiber dominated as in the present experiments.

MICROMECHANICS ANALYSIS

The failure results given above show a large reduction of strength in the braid direction. Certainly some reduction in strength in the braid direction would be expected, given the undulation of the braid yarn path in addition to the lower fiber volume fraction of the braids relative to typical laminates. However it is believed that additionally the inhomogeneous

nature of braid preforms contributes to this loss of strength due to local variations. A discussion of this supposition is given in the following.

Experimental elastic strain measurements on the surface of braided composites verify that strain is not uniform but is a function of position within the repeating unit cell. This has been demonstrated in strain gage studies in which the effect of strain gage size and position on the measured strain have been examined. In our study of strain gage size, strain varied by a factor of 2.5 over the surface of a specimen.

A more precise indicator of surface strain gradients is the Moire fringe measurements reported by Naik, Ifju, and Masters [31]. The largest strain gradients were noted in transverse strain measurements on specimens loaded in the transverse direction. The ratio of maximum to average strain was reported as 1.3 and 1.9 for architectures close to the C and D architectures of the present study. These strain concentrations would be expected to directly affect the braid strength.

Insight into the causes of these observed surface strain variations can be obtained from models of the microstructure. Two models will be examined in the following. The first is a very simple idealization of a single braid layer, and is based on the difference between the compliance of the regions where the braid yarns go over and under the axial yarns as compared to the regions between the axial yarns. The second model is a finite element analysis using a 2-d generalized plane strain assumption. While this is a very simple finite element model as compared to the real 3-d geometry, it does give additional insight into the braid yarn strain concentrations.

The single layer analytical model is illustrated in Fig 35, where the axial yarns are shown along with the regions between the axial yarns. The basic idea here is that the two regions have different compliances, and thus exhibit different transverse strains when loaded in the transverse direction. The compliances were calculated using the three-dimensional lamination theory presented previously, which includes a transformation in the crimp angle direction. To match the boundary conditions, a generalized plane strain condition in the axial direction was assumed, along with zero axial load. The stress in the axial direction required to sustain uniform strain in this direction may be found from Hooke's law to be

$$\sigma_a^t = \sigma_\theta \frac{\nu_{at}^b E_a^t - \nu_{at}^t E_a^b}{E_a^t (r_b - 1)/r_b - E_a^b} \tag{10}$$

for the combined axial and braid region, and

$$\sigma_a^b = \sigma_\theta \frac{\nu_{at}^b E_a^t - \nu_{at}^t E_a^b}{E_a^t - E_a^b r_b/(r_b - 1)} \tag{11}$$

for the regions between the axial yarns. From these the strain in the transverse direction can be found as

$$\varepsilon_\theta^i = \frac{-\sigma_a^i \nu_{at}^i}{E_a^i} + \frac{\sigma_\theta}{E_t^i} \tag{12}$$

The subscript represents the direction with t for transverse and a for axial. The superscript represents the material with t for combined axial and braid (triaxial), and b for material between these regions (biaxial), and i if the equation applies to both regions. The ratio of maximum to average strain was found to be 1.1 for the A and B architectures, and the ratio for the C and D architectures was between 1.2 and 1.3. This simple model does illustrate that the compliance differences can lead to strain concentrations, but would not be expected to be numerically representative of the actual condition in a multilayer braid.

As mentioned above, a more detailed numerical finite element model was also investigated. This model was based on a generalized plane strain analysis of a cross-section in the transverse direction with respect to the axial yarns. The cross-section employed is illustrated in Fig 36, which is motivated by the cross-section shown in Fig 37. The axial yarns were assumed to be elliptical in shape. The width of the axial yarn was the same as that used in the analytical model above, while the height was calculated to produce the desired percentage of axial yarn as given in Table 4. The distance from the composite edge to the axial yarn was measured for each architecture and used in positioning the yarns nearest the edges. Interior axial yarns were assumed to be equally spaced through the thickness. The braid yarns (in the $\pm\ \theta$ direction) and resin pockets were smeared into one material and surrounded the axial yarns in the model. The vertical edges of the model were assumed

to be lines of symmetry and the right edge was given a constant displacement. The material properties of the axial and braid yarns were found using the fiber inclination model discussed previously.

The results of this numerical approach were similar to the simple analytical model. The ratio of the maximum to average transverse strain fell between 1.1 and 1.2 for the A and B architectures, and 1.2 and 1.4 for the C and D architectures. The maximum strains from the numerical solution were slightly higher than from the analytical model, as would be expected since the numerical model does not average the extreme strains.

DISCUSSION

A number of features of the program will be addressed in the following discussion. These are the overall experimental approach, the stiffness models and measurements, the strength properties of the braid specimens, the correlation of strength with architecture, and implications for design with braids.

Experimental Techniques - The experimental techniques used in the present program have been developed in our laboratory in previous work on laminates. These techniques proved to be very successful in the present application to braids. The basic idea of using tubular specimens to achieve biaxial loads was quite successful. The key to this approach, as with all biaxial tests, is careful attention to end effects at the load introduction locations. As described above, the material and geometry of the specimen ends were redesigned to permit higher axial loads. The redesign proved to be very successful in that the axial loads required to produce axial failure in the specimens, with the increased wall-thickness appropriate for the braids, could be achieved. Also failures were typically located away from the end regions, indicating a lack of stress concentration at these locations. This redesign required very careful attention to materials selection and sizing, and quite a bit of time was required to carry out this task.

The tests performed in the present program were of two general types, either compression-compression or tension-tension. The tests were restricted to these types because of the overall limitation of the number of specimens available. Mixed tension-compression tests could have been performed, using either of the two specimen sizes used in the program.

Braid stiffness - The available experimental evidence indicates that significant strain variations occur with respect to position within the unit cell of braid specimens, even for multi-layer materials where the location of the unit cell for each layer does not coincide. The most direct evidence is the Moire measurements reported by Naik, Ifju, and Masters [31], and this evidence is supported by the variations in results with strain gage size reported here and by others. However using larger size strain gages and averaging over multiple gages appears to be an adequate procedure for obtaining average strains. The tension tests did show numerous strain gage failures at the higher strain levels. This has been observed previously in tests of laminates, and especially filament wound materials, and is believed related to microcracking.

In general the models showed excellent agreement with the measured braid stiffnesses. Even relatively simple models such as three-dimensional lamination theory with out-of-plane and in-plane coordinate transformations could give reasonable accuracy. However the more detailed fiber inclination model gave the best results. This model does require knowledge of the details of yarn geometry within the unit cell, however. The stiffness calculations are seen to be strongly dependent on the fiber volume fraction, and also on the average crimp angle for the braid yarns. Once the properties have been established for the unit cell using the above procedures, the overall material stiffness properties can be calculated using classical lamination theory.

Biaxial strength properties - The correlations developed above were based on a failure criterion that employed critical in-plane strains in the axial and braid directions. These correlations appear to be very successful and give a good representation of the experimental data. It should be noted that the in-plane strains are not the actual strains in the braid yarns, which differ because of the component of the braid yarn in the out-of-plane direction (yarn crimp) as well as strain concentrations due to braid yarn undulation. Thus the allowable strains are clearly empirical values that must be established by tests on the braid materials. However once these allowable strain values have been established in uniaxial tests in the axial and transverse directions, the failure envelopes can be constructed and failure predictions can be made.

It should be pointed out that the state-of-the-art in predicting failure under biaxial loading in laminates is very similar to the above. There is clear evidence in the literature that while laminate strength can be predicted on

the basis of critical fiber direction strains, the allowable strain values in laminates of high-strength fiber and high-toughness resin materials systems [36], and in laminate compression tests [37,38], can differ from those measured in coupon tests. Thus actual tests on laminates must be employed.

One of the major features seen in the present results is the low critical strain values in the braid direction. As shown in Fig 26, the critical in-plane strains in the braid yarns are on the order of 0.4% in all of the architectures, and in either tension or compression. The failure strains measured in the present experiments are in good agreement with those measured in axial and transverse direction coupon tests by Minguet and Gunther [39]. These critical failure strains are significantly lower than typical failure strains for AS4 fibers, which would be expected to be on the order of -1.0 to -1.3% in compression, and 1.4% in tension. Since the allowable stresses are obtained from the allowable strains and the material stiffness, the somewhat lower stiffness values in the braid direction due to lower fiber volume fraction and fiber crimp also contribute to lower strength in the braid direction. As a result the braid direction strengths are significantly lower than would be expected in comparable laminations, with an up to 70% strength loss. Whether or not this is a critical factor would depend on the particular application. However it is a major characteristic that must be taken into account in design with braids.

One of the reasons for the relatively low braid direction allowable strain is believed to be strain concentrations associated with the discrete axial yarns. As described above in the section on Micromechanics Analysis, it is believed that the difference in stiffness between the axial fiber regions and the braid yarn regions between the axial yarns gives strain concentrations in the braid yarns. The most direct evidence for this is the Moire results of Naik, Ifju, and Masters [31]. The finite element calculations presented above also support this conclusion. It is possible that this strain concentration could be minimized by changing the braid architecture, so as to spread out the axial yarns. This would involve smaller yarn bundles and a smaller unit cell, and more braid layers. Another alternative would be to combine other forms of fiber layup with the braiding process, such as pultrusion for the axial yarns.

Another factor likely involved in the braid strengths in both axial and braid directions is the accuracy of fiber path. Examination of braid cross-sections under the microscope has revealed a number of defects and irregularities in the fiber paths, both in axial and braid directions. For

example the wavy axial fibers shown in Fig 40 are believed to affect the compressive strength. Other examples of wrinkles in the yarns included defects adjacent to the mold line, and are possibly caused by the effects of RTM on fiber locations.

Efforts to correlate the strengths with the architecture were only marginally successful. As can be seen in Figs 25 and 26, the critical strain values were in most cases not strongly affected by the braid architecture. An exception is the low axial compression strains in the B architecture, which were believed to be correlated with the wavy axial yarns. It was reported by the authors in [5,6] that the degree of waviness could be generally correlated with the degree of coverage of the braid yarns, with a more open coverage contributing to wavy axial yarns.

SUMMARY AND CONCLUSIONS

Biaxial tension-tension and compression-compression tests have been carried out on four architectures of 2-D triaxial braid specimens, using tubular specimens. Good accuracy in comparisons between existing stiffness models and experiment was seen, with the primary variables affecting stiffness being the fiber volume fraction, relative amount of fibers in the axial and braid directions, and braid angle. The biaxial strength results show that the failure properties could be correlated by using critical failure strain values in the axial and braid direction fibers. The braid materials exhibited somewhat lower strengths in the axial directions and significantly reduced strengths in the braid direction fibers relative to laminates of similar fiber and matrix materials. Analysis of the microstructure indicates that stiffness variations in the transverse direction occur, because of the discrete axial yarns. These stiffness variations are believed to cause strain concentrations that contribute to the low braid failure strains.

ACKNOWLEDGMENTS

This research was performed under the sponsorship of the NASA Langley Research Center under grant no. NAG-1-1379. This support is gratefully acknowledged.

REFERENCES

1. Smith, L. V., and Swanson, S. R., "Response of Braided Composites Under Compressive Loading," Composites Engineering, 3 (12), 1165-1184 (1993).
2. Smith, L. V., Swanson, S. R., 1994. "Failure of Braided Carbon/Epoxy Composites Under Biaxial Compression," to appear in J. Composite Materials.
3. Smith, L.V., and Swanson, S.R., "Failure of Braided Composite Cylinders Under Biaxial Tension," to appear in J. Composite Materials (1994).
4. Smith, L. V., Swanson, S. R., 1994, Design of a composite specimen and fixture for biaxial tension testing," submitted to Experimental Mechanics.
5. Smith, L. V., Swanson, S. R., 1993. "Effect of Braid Architecture on the Strength of Braided Carbon Fiber Tubes Under Biaxial Compression," Proceedings of ASME WAM, AD-Vol.37/AMD-Vol. 179, pp. 285-296, New Orleans, Louisiana.
6. Smith, L. V., and Swanson, S. R., "Effect of Architecture on the Strength of Braided Tubes under Biaxial Tension and Compression," submitted to ASME J. Eng Mtls and Tech (1994).
7. Smith, L. V., and Swanson, S. R., "Micro-mechanics Parameters Controlling the Strength of Braided Composites," submitted to Composites Science and Technology (1994).
8. Swanson, S.R., and Smith, L.V., "Comparison of the Biaxial Strength Properties of Braided and Laminated Carbon Fiber Composites," Proc. Intl. Conf. on Composites Engineering, ICCE/1, Ed. D. Hui, pp 511-512, New Orleans, August 28-31 (1994).
9. Swanson, S.R., and Smith, L.V., "Comparison of the Biaxial Strength Properties of Braided and Laminated Carbon Fiber Composites," submitted to Composites Engineering (1994).
10. Smith, L.V., and Swanson, S.R., "Selection of Carbon Fiber 2D Braid Preform Parameters for Biaxial Loading," Composites: Design and Manufacture for Cost Effectiveness, MD-Vol 48, Proc. ASME Winter Annual Meeting, pp 33-44 (1994).
11. Smith, L.V., and Swanson, S.R., "Strength Design with 2-D Triaxial Braid Textile Composites," Proc. Amer.Soc. for Composites 9th Tech. Conf., Univ of Delaware, pp 727-734, Sept 20-22 (1994).
12. Smith, L.V., and Swanson, S.R., "Strength Design with 2-D Triaxial Braid Textile Composites," submitted to Composites Science and Technology (1994).
13. Brunnschweiler, D. 1953. "Braids and Braiding," *J. of the Textile Institute,* 44:666-686.
14. Chou, T.W., and Ko, F.K., eds, Textile Structural Composites, 3, Elsevier (1989).
15. Soebroto, H. B. and Ko, F. K., "Composite Preform Fabrication by 2-D Braiding," Proceedings of the Fifth Annual ASM/ESD Advanced Composites Conference, 307-316 (1989).

16. Popper, P., "Braiding," Handbook of Composite Reinforcements, VCH Publishers, Inc., 24-41 (1993).
17. Ko, F. K., Pastore, C. M. and Head, A. A., "Handbook of Industrial Braiding", Atkins and Pearce (1993).
18. Ishikawa, T., "Anti-Symmetric Elastic Properties of Composite Plates of Satin Weave Cloth," Fiber Science Technology, 15, 127-145 (1981).
19. Ishikawa, T. and Chou, T. W., "One-Dimensional Micromechanical Analysis of Woven Fabric Composites," AIAA J., 21, 1714-1721 (1983).
20. Ishikawa, T., Matsushima, M. and Hayashi, Y., "Experimental Confirmation of the Theory of Elastic Moduli of Fabric Composites," J. Composite Materials, 19, 443-458 (1985).
21. Yang, J. M., Ma, C. L. and Chou, T. W., "Elastic Stiffness of Biaxial and Triaxial Woven fabric Composites," 29th National SAMPE Symposium, 292-303 (1984).
22. Byun, J. H., Chou, T. W., "Modelling and Characterization of Textile Structural Composites: A Review," J. of Strain Analysis, 24, 253-262 (1989).
23. Yang, J. M., Ma, C. L., Chou, T. W., 1986, "Fiber Inclination Model of Three-Dimensional Textile Structural Composites," J. of Composite Materials, 20, 472-484.
24. Whitney, T. J. and Chou, T. W., "Modeling of 3-D Angle-Interlock Textile Structural Composites," J. Composite Materials, 23, 890-911(1989).
25. Ishikawa. T., Chou, T.-W. 1982. "Stiffness And Strength Behavior of Woven Fabric Composites," *J. of Materials Science*, 17:3211-3220.
26. Ko, F. K. 1986. "Tensile Strength and Modulus of a Three-dimensional Braid Composite," *ASTM STP 893*, 392-403.
27. Crane, R. M., Camponeschi, E. T. 1986. "Experimental and Analytical Characterization of Multidimensionally Braided Graphite/Epoxy Composites," *Experimental Mechanics*, 26:256-266.
28. Swanson, S. R., Christoforou, A. P., and Colvin, G. E. Jr., "Biaxial Testing of Fiber Composites Using Tubular Specimens," Experimental Mechanics, 28(3), 238-243 (1988).
29. Groves, S. E., Sanchez, R. J., and Feng, W. W., "Multiaxial Failure Characterization of Composites,"Proc. of Eighth Int. Conf on Composite Matls. ICCM/VIII, 37-B, 1-15 (1991).
30. Jones, R.M., Mechanics of Composite Materials, Hemishphere Pub Co. (1975).
31. Naik, R.A, Ifju, P.G., and Masters, J.E., "Effect of Fiber Architecture Parameters on Mechanical Performance of Braided Composites," Proc. 4th NASA/DoD Advanced Composites Technology Conf., Salt Lake City, 525-554 (1993).
32. Swanson, S. R. and Nelson, M. 1986. "Failure Properties of Carbon/Epoxy Laminates under Tension-Compression Biaxial Stress," *Proceedings of the Third Japan-U.S. Conference on Composite Materials*, Tokyo.
33. Swanson, S.R., and Qian, Y., "Multiaxial Characterization of T800/3900-2 Carbon/Epoxy," Composites Science and Technology, 43(2), 197-203 (1992).

34. Swanson, S. R., and Trask, B. C., "Strength of Quasi-Isotropic Laminates Under Off-Axis Loading," Composites Science and Technology J., 34(1), 19-34 (1989).
35. Colvin, G.E., and Swanson, S. R., "Characterization of the Failure Properties of IM7/8551-7 Carbon/Epoxy Under Multiaxial Stress," ASME J. Eng. Mat. Tech., 112, 61-67 (1990).
36. Swanson, S.R., "Biaxial Failure Criteria for Toughened Resin Carbon/Epoxy Laminates," Proc. Amer. Soc. for Composites 7th Tech. Conf. on Composite Materials, Pennsylvania State Univ., 1075-1083, October 13-15 (1992).
37. Colvin, G.E., and Swanson, S.R., "In-Situ Compressive Strength of Carbon/Epoxy AS4/3501-6 Laminates," ASME J. Eng. Mat. Tech. 115, 122-128 (1993).
38. Sohi, M.M., Hahn, H.T., and Williams, J.G., "The Effect of Resin Toughness and Modulus on Compressive Failure Modes of Quasi-Isotropic Graphite/Epoxy Laminates," Toughened Composites, ASTM STP 937, 37-60 (1987).
39. Minguet, P.J., and Gunther, C.K., "A Comparison of Graphite/Epoxy Tape Laminates and 2-D Braided Composites Mechanical Properties," NASA Contractor Report 4618, July (1994).

Table 1. Description of the triaxial braid architectures. Subscript on braid code indicates compression or tension specimen.

Braid code	Filament count		Fixed yarns (% of total)	Braid angle (degrees)	Number of axial yarns	Number of plies	Crimp Angle (degrees)
	Braider	Fixed					
A_c (LSS)	12k	6k	19	25	36	3	10.3°
B_c (LLS)	12k	36k	47	45	36	3	17.1°
C_c (SLL)	6k	36k	46	70	36	3	28.6°
D_c (LLL)	12k	66k	46	72	54	3	28.7°
A_t (LSS)	12k	9k	20	47	72	4	14.6°
B_t (LLS)	12k	27k	44	45	72	3	18.5°
C_t (SLL)	6k	33k	45	73	36	5	7.7°
D_t (LLL)	12k	54k	43	70	36	3	12.5°

Table 2. Average architecture elastic properties for biaxial compression specimens.

Architecture	Initial linear elastic properties			Secant elastic properties at failure		
	E_a (GPa)	E_h (GPa)	ν_{ah}	E_a (GPa)	E_h (GPa)	ν_{ah}
A	29.3	17.8	0.700	25.3	16.9	0.766
B	53.4	15.3	0.699	50.9	14.3	0.779
C	50.0	35.4	0.188	46.0	35.3	0.187
D	47.7	30.8	0.161	42.6	28.2	0.176

Table 3. Average initial tangent stiffness properties for biaxial tension specimens.

Braid Code	Axial modulus		Hoop modulus		ν_{ah}
	GPa	Msi	GPa	Msi	
A	31.8	4.61	22.1	3.21	0.62
B	57.3	8.31	15.7	2.27	0.68
C	50.6	7.34	51.9	7.53	0.15
D	49.3	7.11	42.3	6.13	0.20

Table 4. Lamina properties for AS4/3501-6 at v_f=0.6, used for model input.

Property	Value	
E_1	127 GPa	18.4 Msi
E_2	11.0 GPa	1.6 Msi
G_{12}	6.55 GPa	0.95 Msi
v_{12}	.28	.28

Table 5. Braid undulation parameters calculated from braid geometry. Subscript on braid code indicates compression or tension specimen.

Braid code	Crimp angle (degrees)	Undulation			
		Wavelength		Magnitude (peak to peak)	
		(mm)	(in.)	(mm)	(in.)
A_c	10.2	14	0.56	0.6	0.03
B_c	17.1	14	0.56	1.1	0.04
C_c	22.5	10	0.40	1.1	0.04
D_c	22.7	16	0.60	1.6	0.06
A_t	14.5	13	.50	.79	.03
B_t	18.5	13	.52	1.06	.04
C_t	7.7	20	.77	.64	.02
D_t	12.5	20	.78	1.06	.04

Table 6. Failure stresses and strains of the A architecture under biaxial compression.

Failure mode	Axial stress		Hoop stress		Axial strain (%)	Hoop strain (%)	Braid strain (%)
	(MPa)	(ksi)	(MPa)	(ksi)			
Axial	-282	-41.0	0	0	-1.13	0.84	0.01
Axial	-284	-41.2	0	0	-1.10	0.85	0.03
Axial	-274	-39.7	0	0	-1.08	0.85	0.04
Axial	-444	-64.5	-119	-17.3	-1.30	0.52	-0.24
Axial	-471	-68.3	-180	-26.1	-1.28	0.32	-0.36
Axial	-432	-62.8	-207	-30.0	-1.02	-0.12	-0.47
Braid	-213	-30.9	-198	-28.8	-0.28	-0.52	-0.42
Braid	-99.8	-14.5	-234	-33.9	0.31	-1.10	-0.51
Braid	30.2	4.38	-211	-30.6	0.71	-1.26	-0.43
Braid	29.1	4.22	-203	-29.4	0.69	-1.22	-0.41
Braid	28.1	4.07	-196	-28.4	0.78	-1.26	-0.40

Table 7. Failure stresses and strains of the B architecture under biaxial compression.

Failure mode	Axial stress		Hoop stress		Axial strain (%)	Hoop strain (%)	Braid strain (%)
	(MPa)	(ksi)	(MPa)	(ksi)			
Axial	-319	-46.3	0	0	-0.62	0.53	-0.01
Axial	-325	-47.2	0	0	-0.65	0.48	-0.05
Axial	-272	-39.5	0	0	-0.53	0.40	-0.03
Axial	-387	-56.2	-82.4	-12.0	-0.62	-0.07	-0.32
Biaxial	-362	-52.4	-138	-20.0	-0.47	-0.48	-0.47
Braid	-194	-28.2	-157	-22.8	-0.15	-0.80	-0.50
Braid	24.7	3.58	-173	-25.0	0.25	-1.24	-0.54
Braid	23.9	3.47	-167	-24.3	0.34	-1.22	-0.50
Braid	24.4	3.53	-170	-24.7	0.29	-1.10	-0.46

Table 8. Failure stresses and strains of the C architecture under biaxial compression.

Failure mode	Axial stress		Hoop stress		Axial strain (%)	Hoop strain (%)	Braid strain (%)
	(MPa)	(ksi)	(MPa)	(ksi)			
Axial	-569	-82.5	0	0	-1.38	0.21	0.12
Axial	-527	-76.4	0	0	-1.11	0.22	0.15
Axial	-450	-65.2	0	0	-0.96	0.19	0.12
Axial	-543	-78.7	-60.1	-8.71	-1.14	0.042	-0.08
Axial	-550	-79.8	-101	-14.6	-1.15	-0.10	-0.16
Biaxial	-424	-61.4	-164	-23.8	-0.81	-0.28	-0.32
Braid	-255	-37.0	-173	-25.1	-0.43	-0.53	-0.52
Braid	-94.4	-13.7	-145	-21.1	-0.13	-0.33	-0.32
Braid	21.1	3.05	-147	-21.4	0.10	-0.44	-0.41
Braid	22.0	3.19	-154	-22.3	0.096	-0.43	-0.40
Braid	21.5	3.12	-151	-21.9	0.092	-0.40	-0.37

Table 9. Failure stresses and strains of the D architecture under biaxial compression.

Failure mode	Axial stress		Hoop stress		Axial strain (%)	Hoop strain (%)	Braid strain (%)
	(MPa)	(ksi)	(MPa)	(ksi)			
Axial	-547	-79.4	0	0	-1.38	0.24	0.13
Axial	-576	-83.6	0	0	-1.35	0.24	0.13
Axial	-383	-55.5	0	0	-0.80	0.15	0.08
Axial	-369	-53.5	-35.1	-5.09	-0.79	0.038	-0.02
Axial	-380	-55.1	-99.5	-14.4	-0.78	-0.21	-0.25
Axial	-387	-56.1	-122	-17.7	-0.79	-0.25	-0.29
Biaxial	-352	-51.1	-186	-27.0	-0.64	-0.45	-0.47
Braid	-283	-41.1	-167	-24.2	-0.53	-0.47	-0.47
Braid	-151	-21.9	-165	-24.0	-0.27	-0.52	-0.51
Braid	24.0	3.48	–168	-24.4	0.11	-0.62	-0.57
Braid	22.5	3.27	-157	-22.8	0.12	-0.53	-0.48
Braid	23.9	3.47	-167	-24.2	0.11	-0.60	-0.55

Table 10. Failure properties of architecture A under biaxial tension.

Failure strength				Failure strain		Observed
Axial		Hoop		Axial	Hoop	failure
(Mpa)	(ksi)	(Mpa)	(ksi)	(%)	(%)	mode
348	50.5	0	0.0	1.10	-0.79	axial
345	50.0	0	0.0	1.14	-0.75	axial
0	0.0	261	37.9	-0.65	1.34	hoop
0	0.0	245	35.5	-0.61	1.26	hoop
0	0.0	231	33.4	-0.67	1.34	hoop
401	58.2	112	16.2	1.07	-0.29	axial
374	54.3	148	21.5	0.97	-0.03	axial
157	22.8	315	45.7	-0.11	0.98	hoop
410	59.5	307	44.6	0.67	0.68	axial

Table 11. Failure properties of architecture B under biaxial tension.

Failure strength				Failure strain		Observed
Axial		Hoop		Axial	Hoop	failure
(Mpa)	(ksi)	(Mpa)	(ksi)	(%)	(%)	mode
545	79.1	0	0.0	0.94	-0.64	axial
551	80.0	0	0.0	0.96	-0.66	axial
0	0.0	138	20.0	-0.15	0.81	hoop
0	0.0	152	22.0	-0.19	0.96	hoop
0	0.0	132	19.1	-0.17	0.86	hoop
602	87.3	54	7.8	0.98	-0.38	axial
609	88.3	72	10.5	0.99	-0.26	axial
620	90.0	97	14.1	0.99	-0.12	axial
68	9.8	136	19.7	-0.05	0.80	hoop
459	66.5	149	21.7	0.62	0.43	hoop

Table 12. Failure properties of architecture C under biaxial tension.

Failure strength				Failure strain		Observed
Axial		Hoop		Axial	Hoop	failure
(Mpa)	(ksi)	(Mpa)	(ksi)	(%)	(%)	mode
512	74.3	0	0.0	1.06	-0.12	axial
524	76.0	0	0.0	0.99	-0.14	axial
0	0.0	241	34.9	-0.06	0.49	hoop
0	0.0	219	31.8	-0.04	0.45	hoop
0	0.0	179	26.0	-0.03	0.35	hoop
512	74.3	65	9.4	1.07	-0.03	axial
463	67.2	130	18.9	0.95	0.15	hoop
102	14.8	205	29.7	0.15	0.40	hoop
239	34.7	153	22.2	0.42	0.26	hoop
209	30.3	133	19.2	0.38	0.21	hoop

Table 13. Failure properties of architecture D under biaxial tension.

Failure strength				Failure strain		Observed
Axial		Hoop		Axial	Hoop	failure
(Mpa)	(ksi)	(Mpa)	(ksi)	(%)	(%)	mode
360	52.2	0	0.0	0.74	-0.12	axial
419	60.7	0	0.0	0.86	-0.10	axial
0	0.0	173	25.1	-0.06	0.37	hoop
0	0.0	232	33.7	-0.08	0.56	hoop
0	0.0	185	26.8	-0.03	0.39	hoop
465	67.4	83	12.0	0.87	0.03	axial
390	56.6	111	16.1	0.86	0.11	axial
500	72.5	191	27.7	0.87	0.30	axial
87	12.7	175	25.3	0.12	0.34	hoop
313	45.3	182	26.4	0.71	0.41	hoop

Table 14. Parameters used for critical strain failure criterion. Subscript on braid code indicates compression or tension.

Braid Code	Critical Axial Strain, %	Critical Braid Strain, %	Extreme Braid Angle, Degrees
A_c	-1.10	-0.415	49
B_c	-0.6	-0.499	47
C_c	-1.118	-0.395	76
D_c	-0.80	-0.535	75
A_t	1.117	0.506	50
B_t	0.951	0.399	47.5
C_t	1.026	0.402	76
D_t	0.799	0.404	74.5

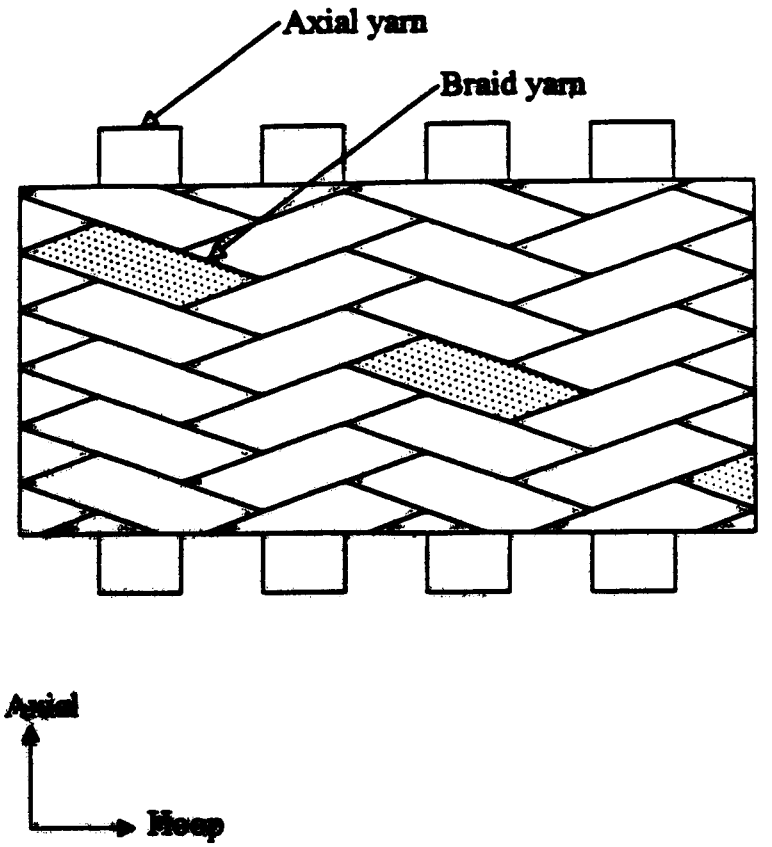

Fig 1. Illustration of 2-D triaxial braid, with axial and ±θ braid yarns.

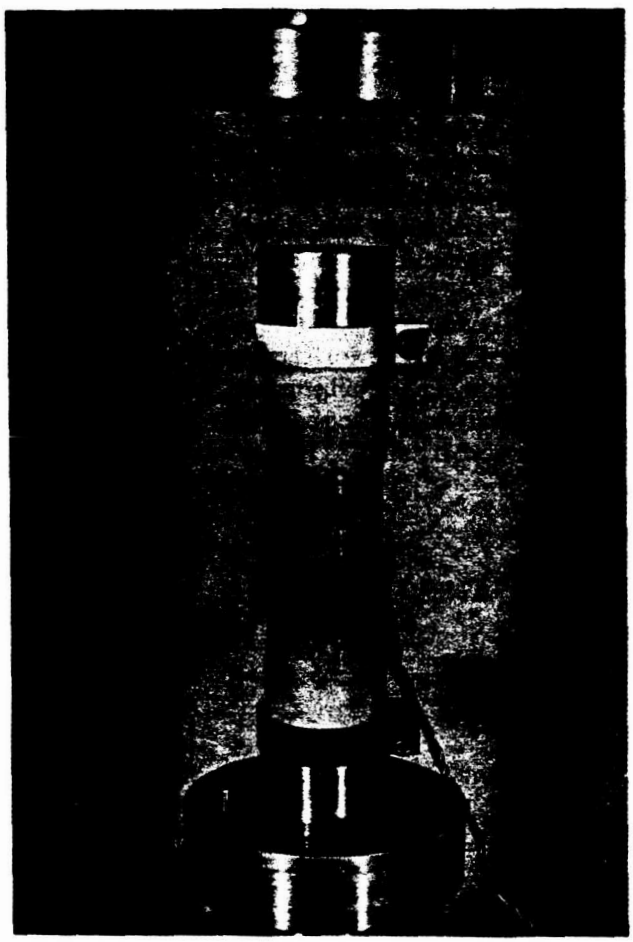

Fig 2. Compression specimen prepared for uniaxial compression test.

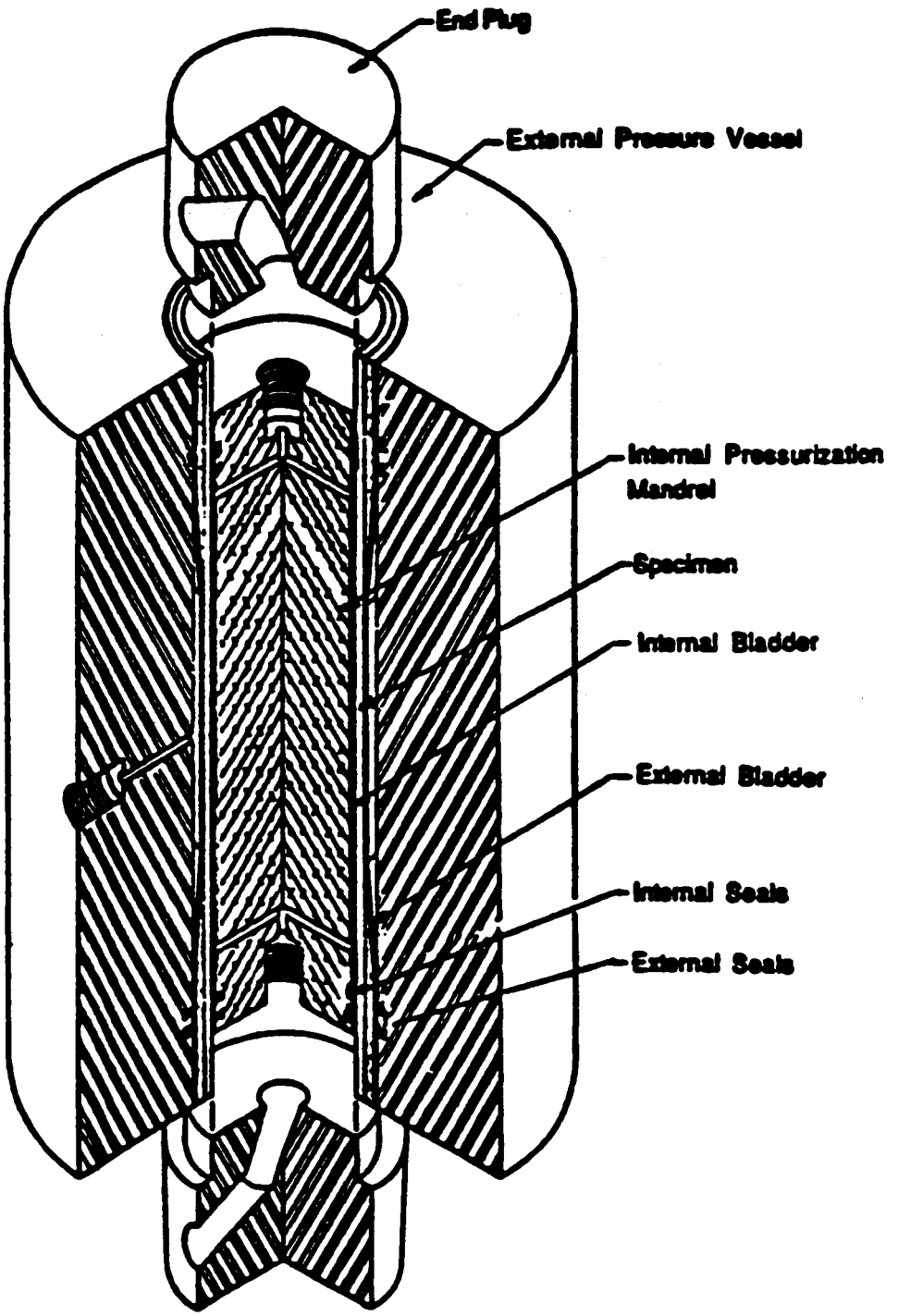

Fig 3. Biaxial compression apparatus.

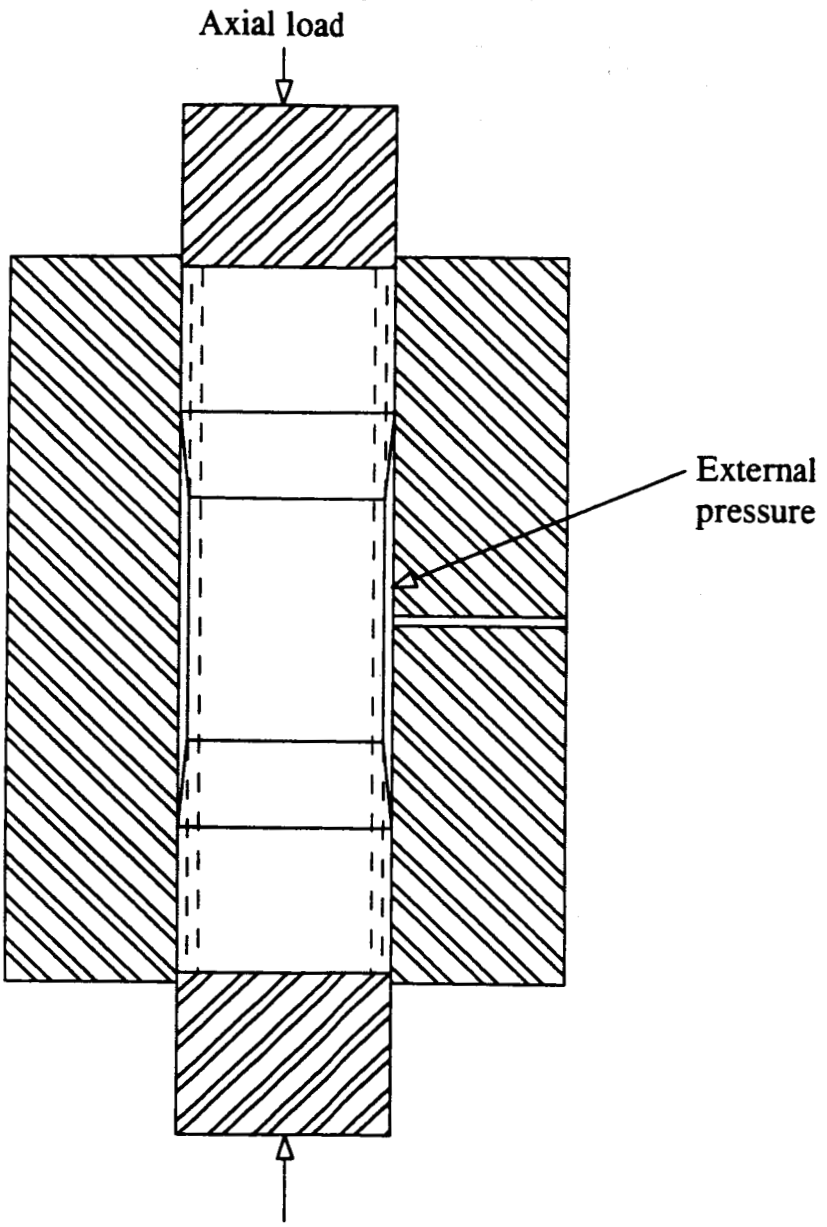

Fig 4. Illustration of external pressure and axial compression loading.

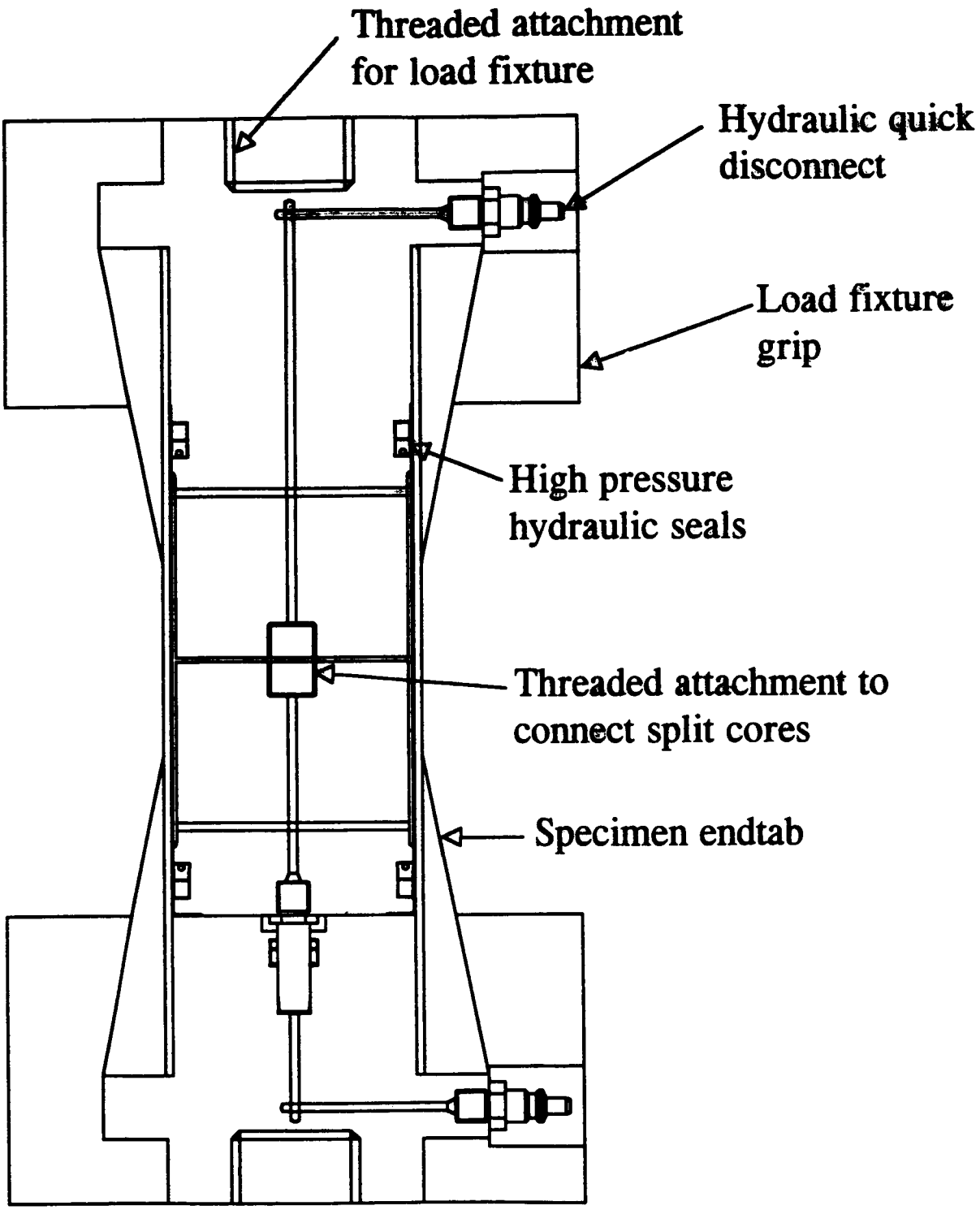

Fig 5. Schematic of biaxial tension apparatus.

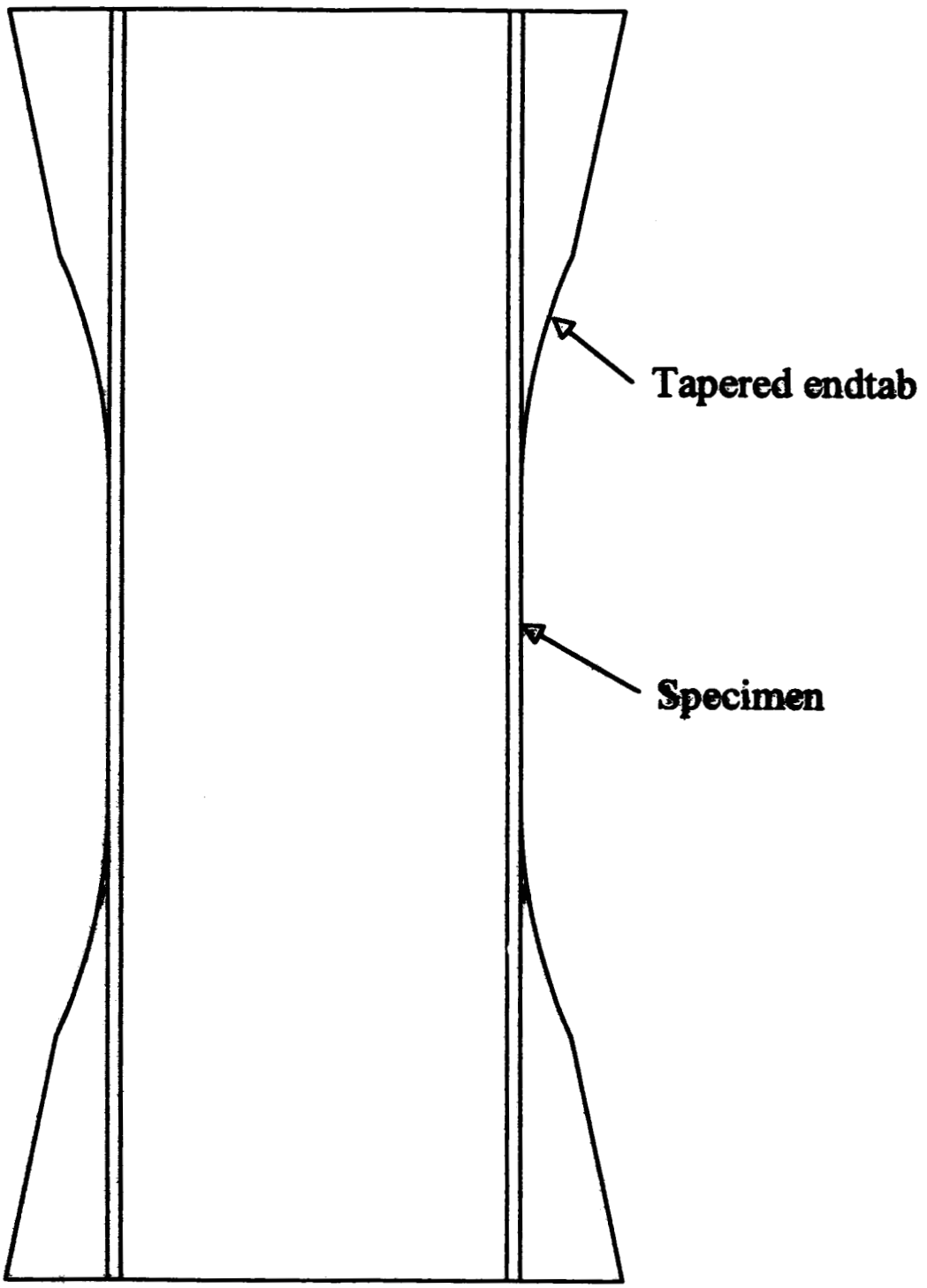

Fig 6. Biaxial tension cylindrical specimen.

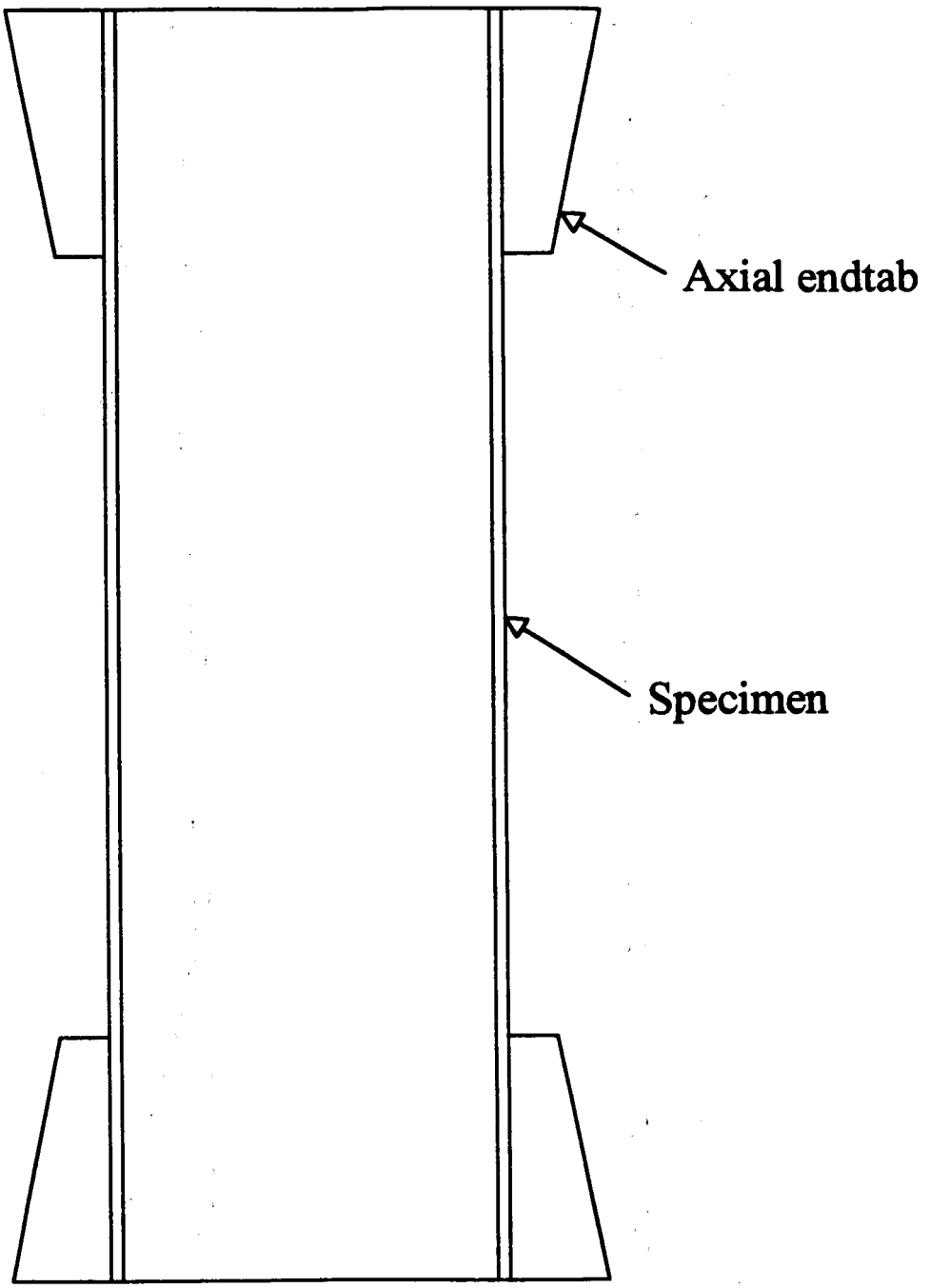

Fig 7. Biaxial tension cylindrical specimen, modified for high axial loads.

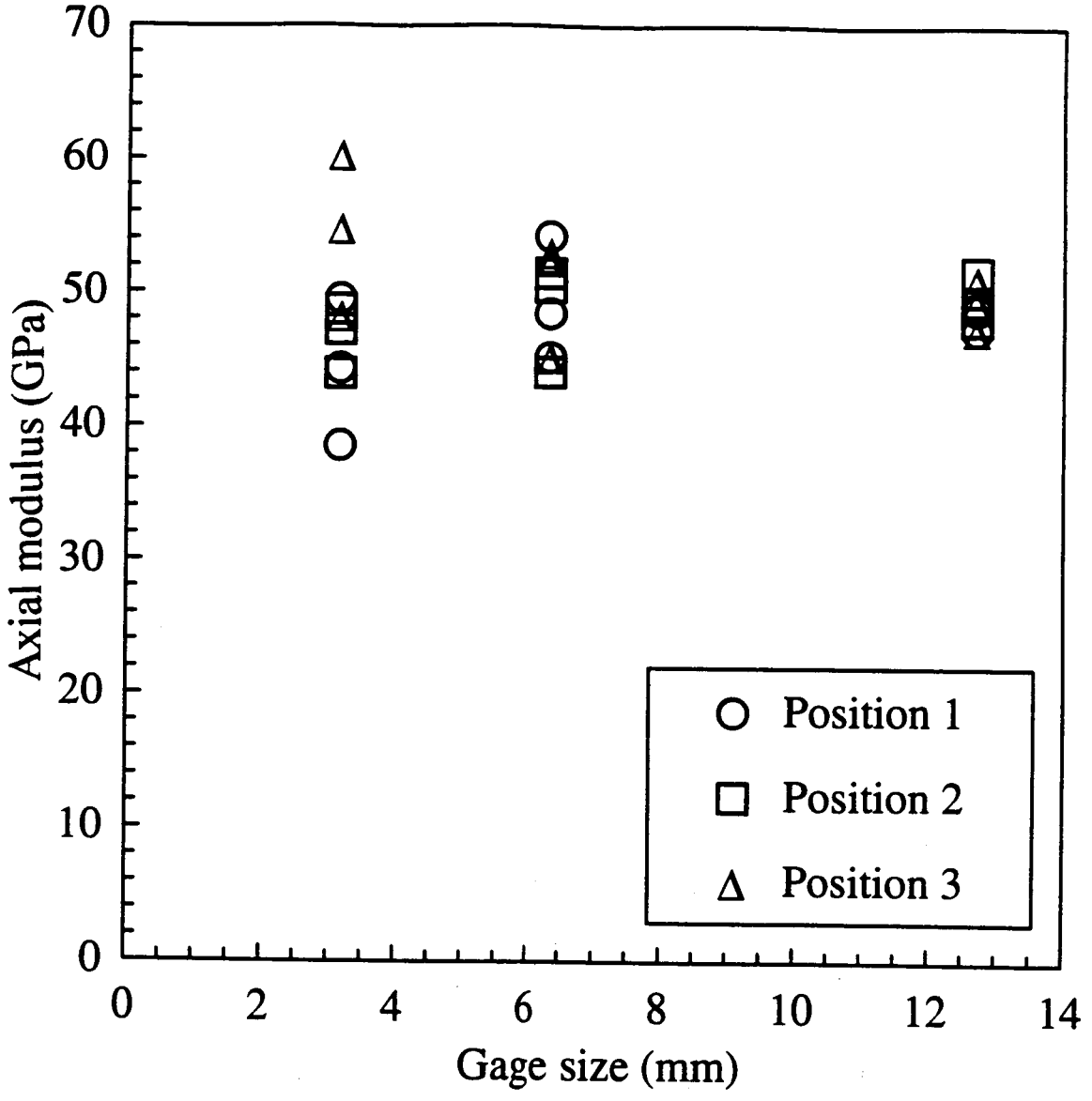

Fig 8. Strain gage size comparison, showing convergence of axial modulus with increasing strain gage size.

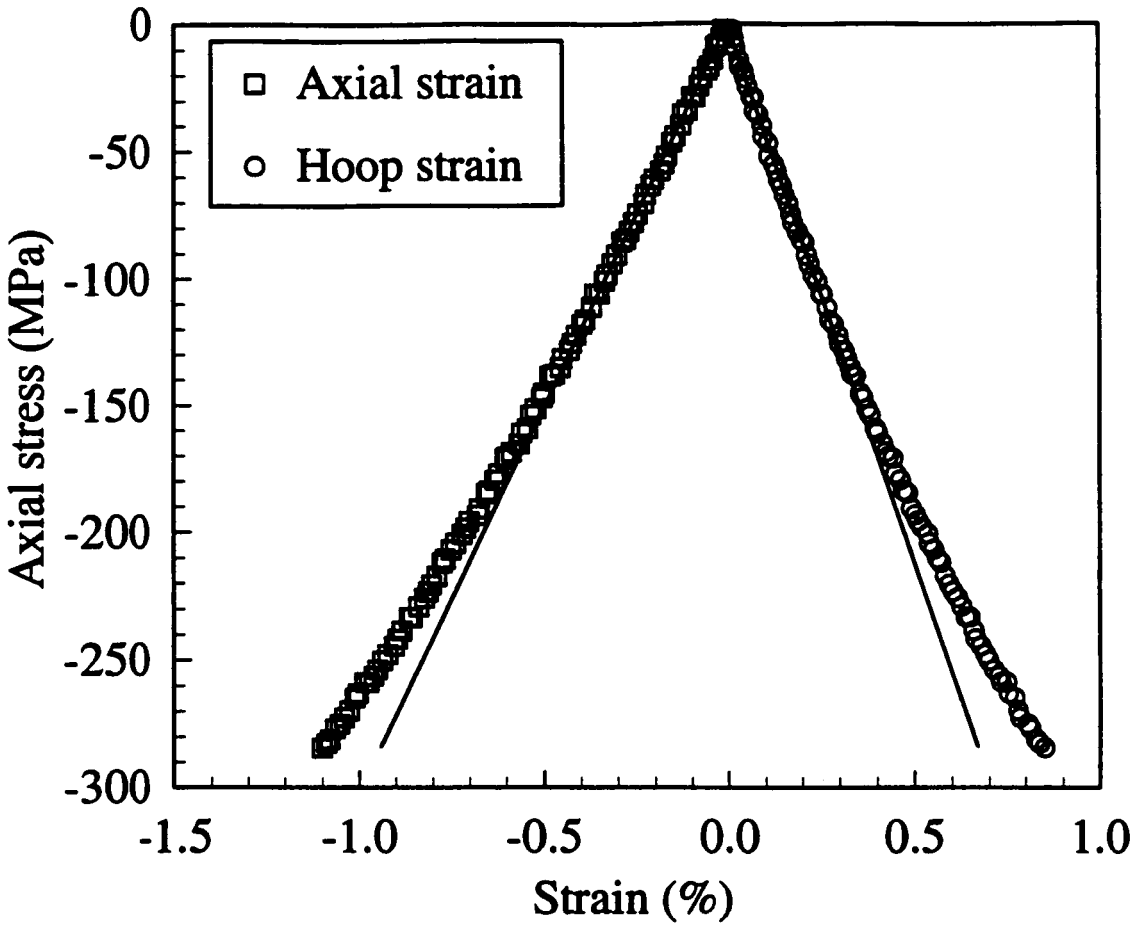

Fig 9. Uniaxial compression stress-strain response under axial loading of the A braid architecture.

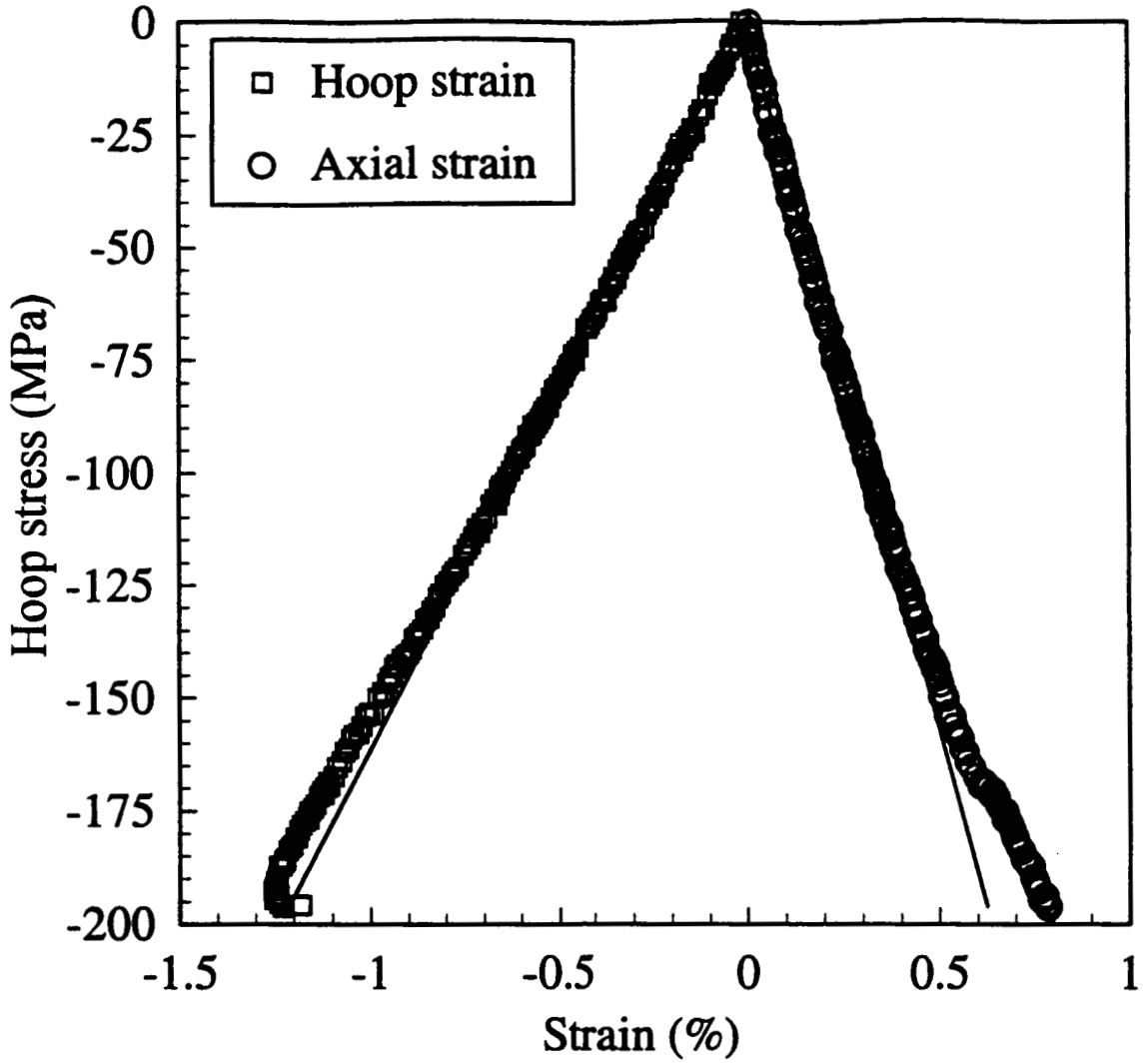

Fig 10. Uniaxial compression stress-strain response under hoop loading of the A braid architecture.

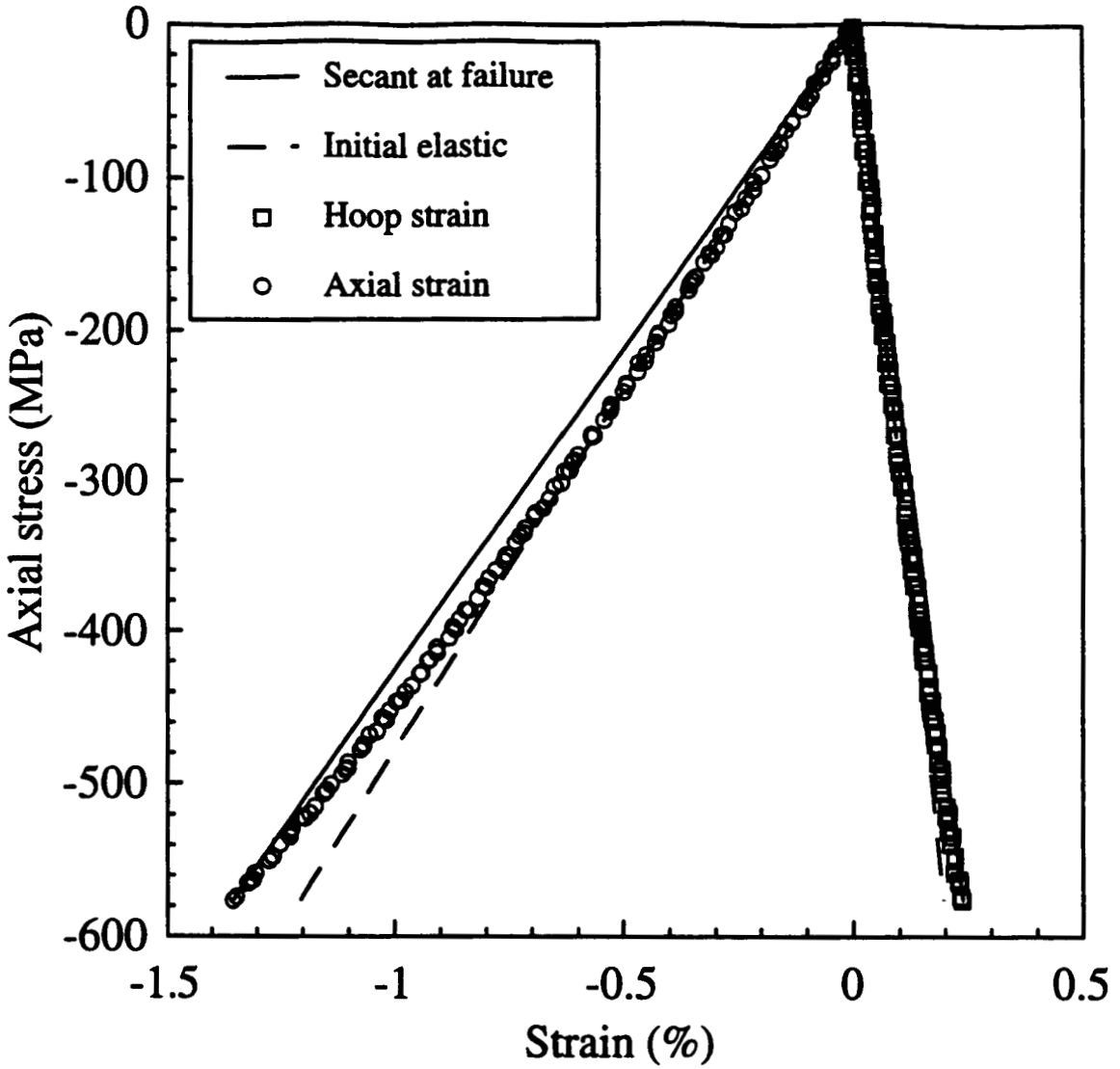

Fig 11. Uniaxial compression stress-strain response under axial loading, illustrating typical nonlinearity in compression, and use of secant modulus.

Fig 12. Microphotographs of polished sections showing braid undulation geometry.

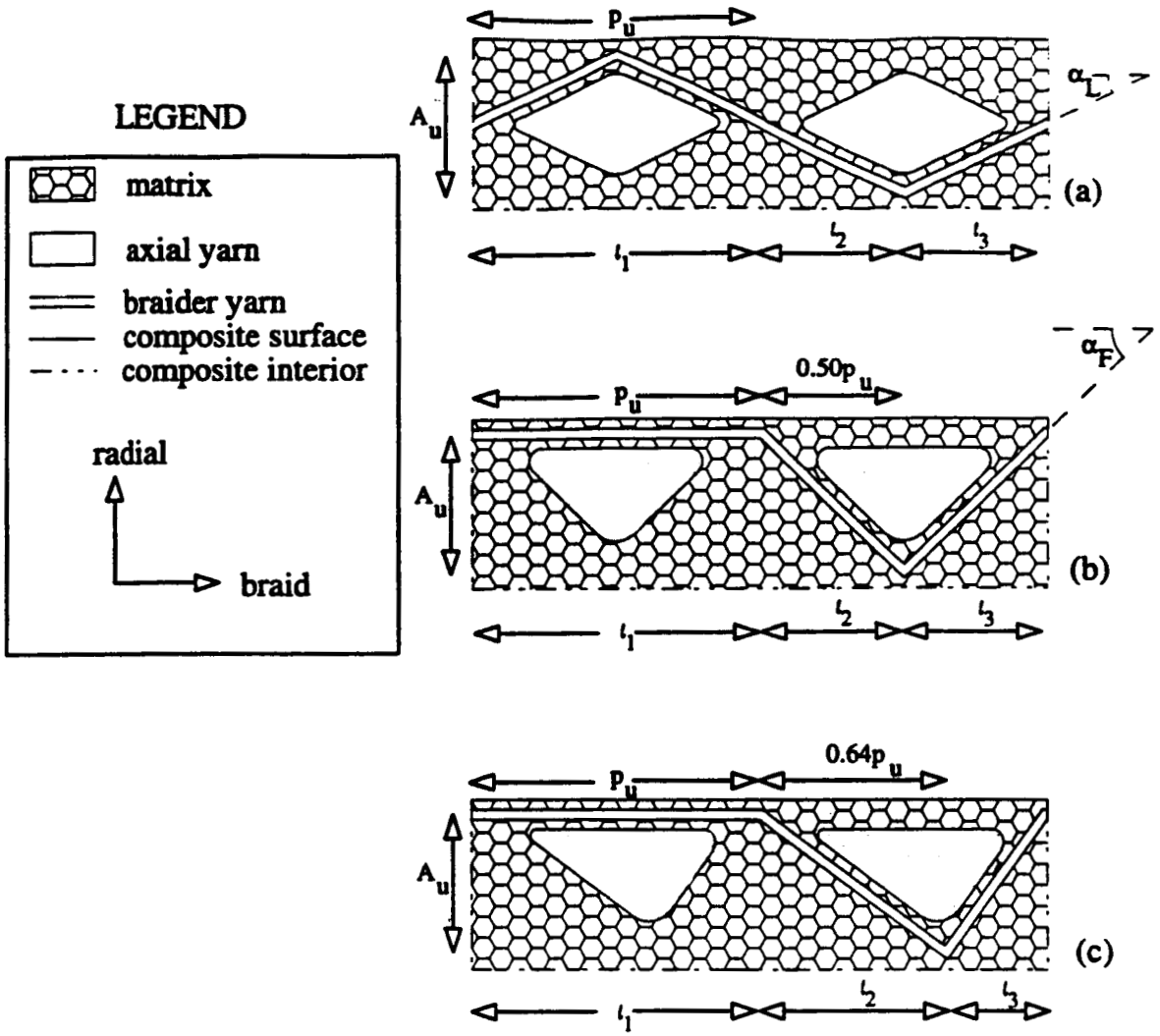

Fig 13. Schematic of sections taken parallel to the braid direction, showing the geometry assumed for the: a) 3-D classic lamination theory, b) the fiber inclination model, and c) experimentally measured geometry of the D architecture used for the fiber inclination model.

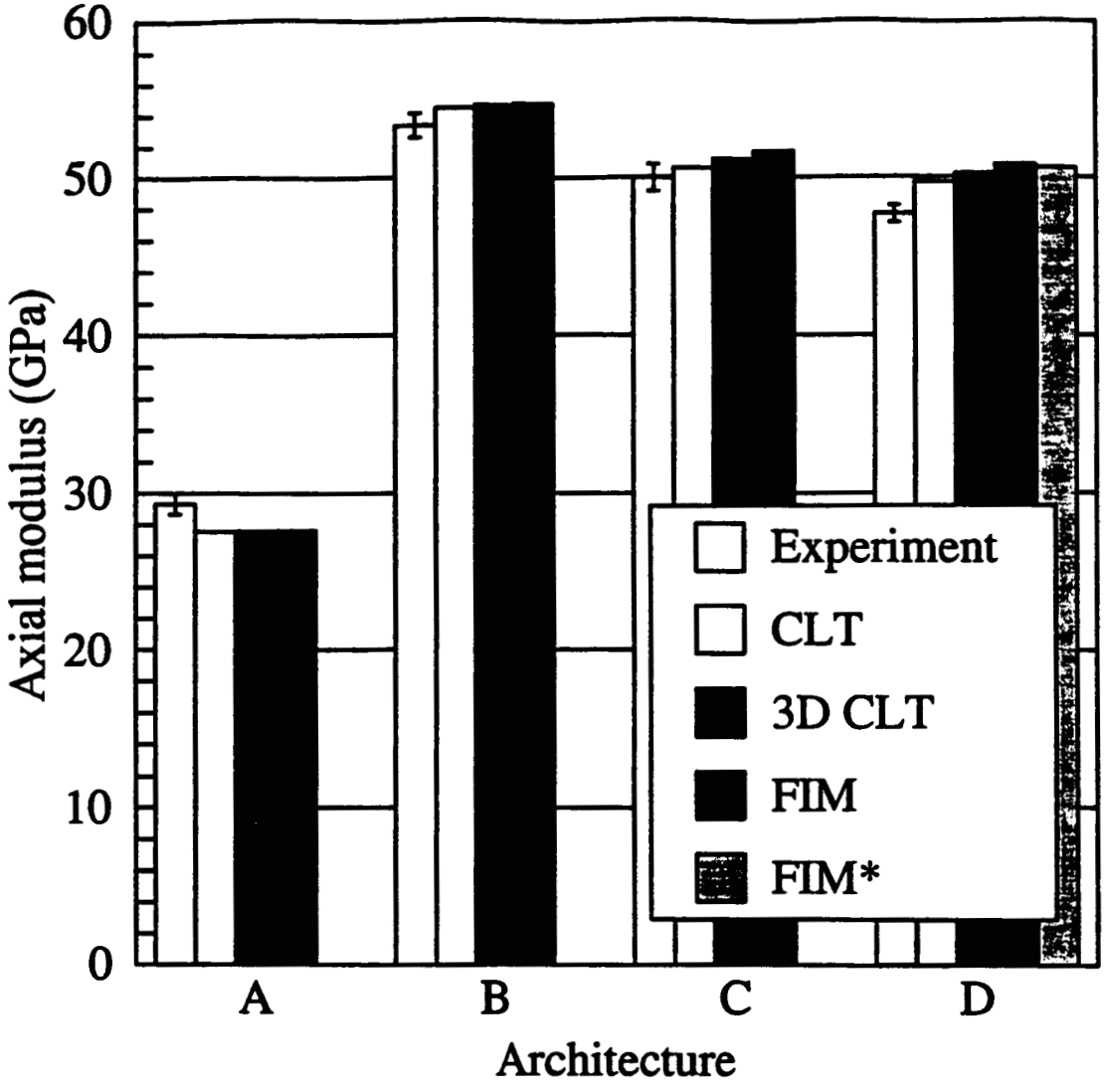

Fig 14. Comparison of models with experiment for axial modulus in compression specimens.

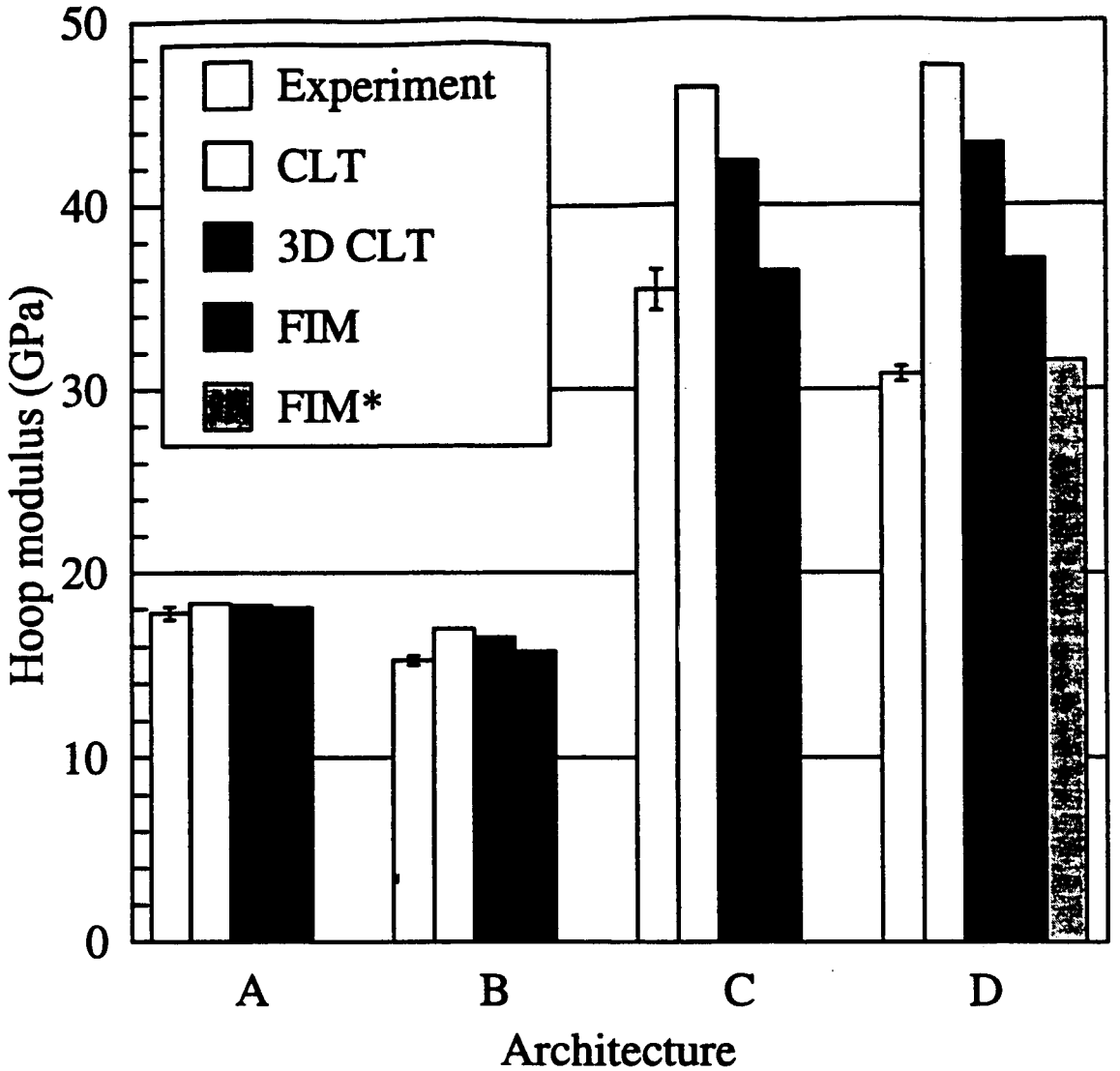

Fig 15. Comparison of models with experiment for hoop modulus in compression specimens.

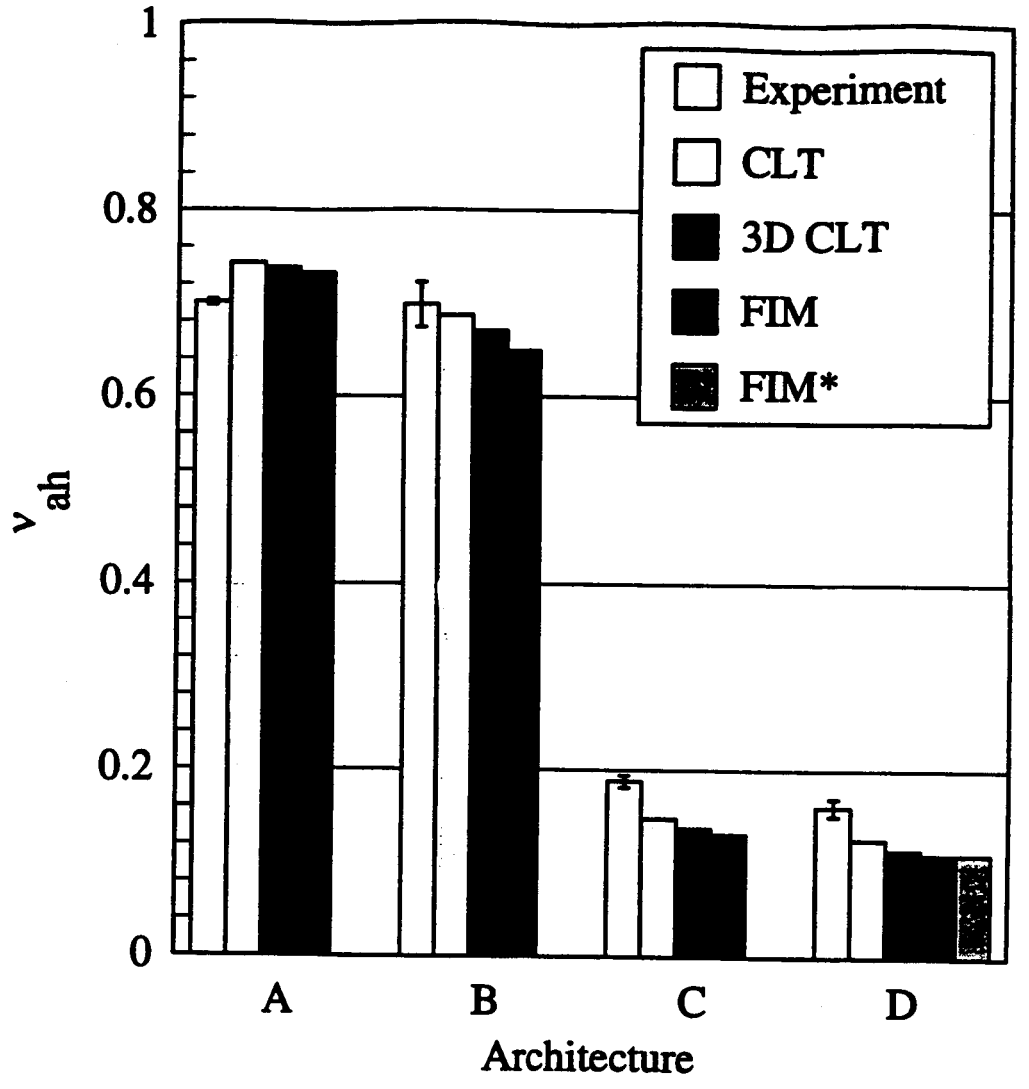

*With measured braid geometry

Fig 16. Comparison of models with experiment for Poisson's ratio in compression specimens.

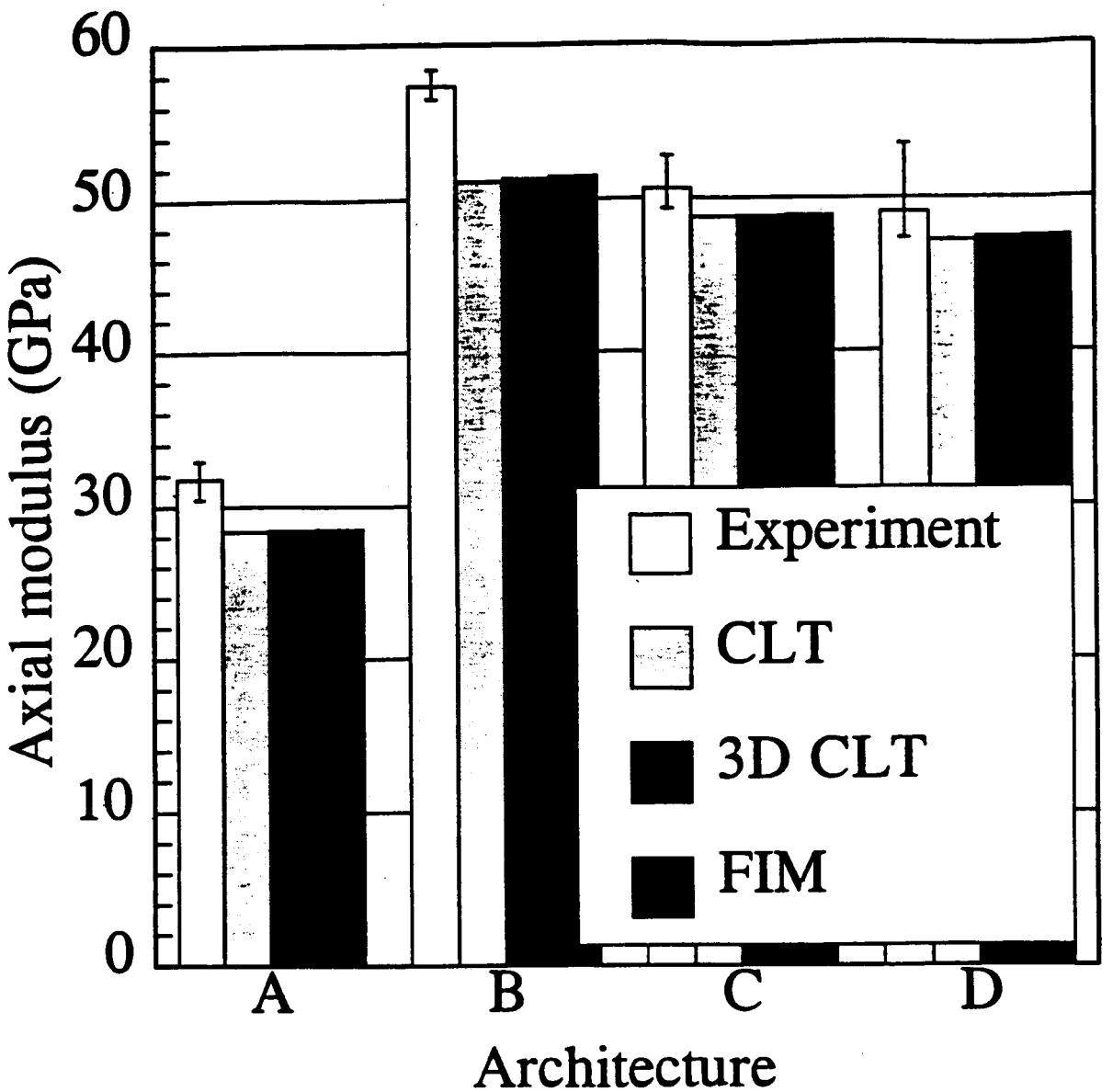

Fig 17. Comparison of models with experiment for axial modulus in tension specimens.

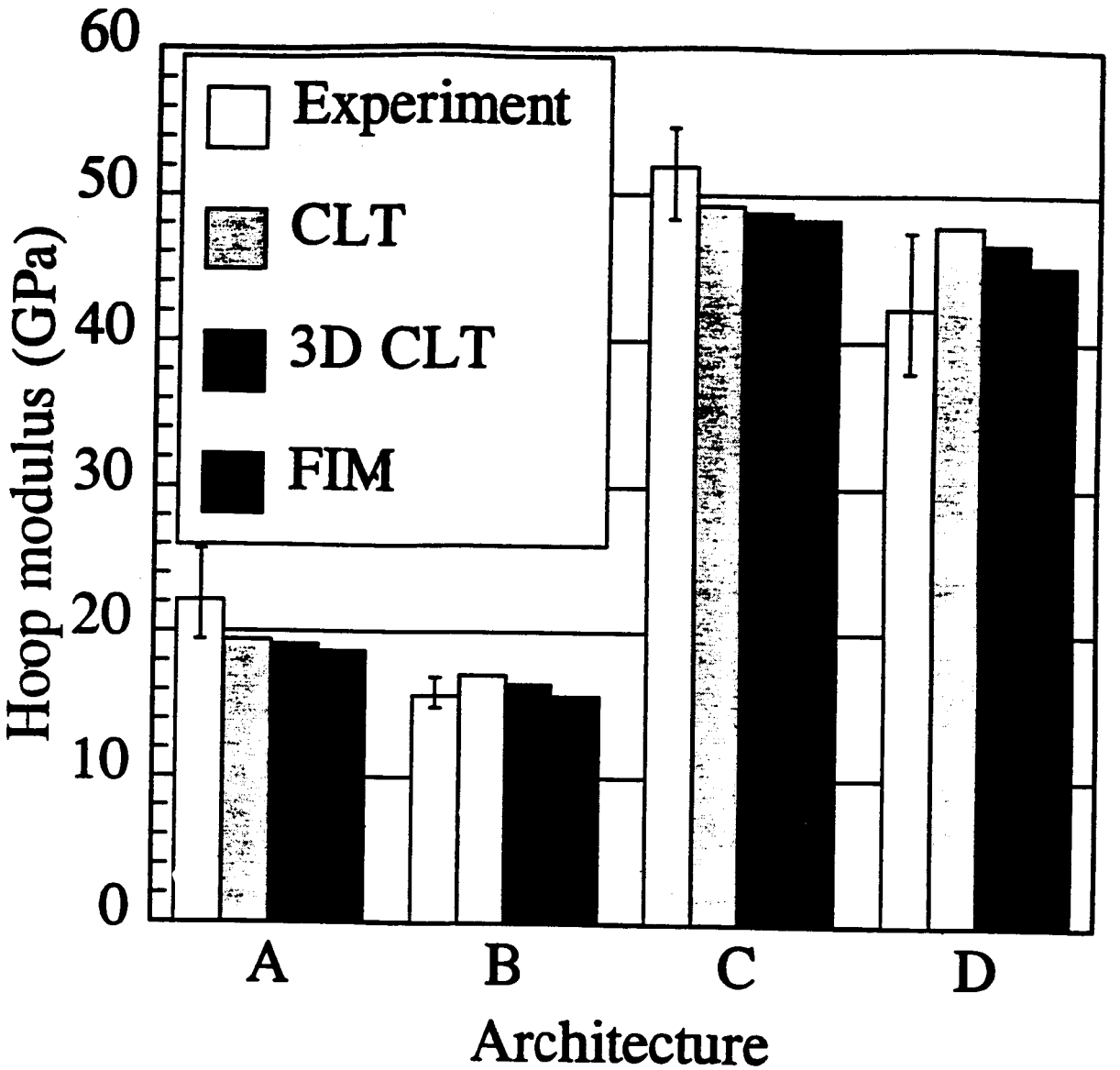

Fig 18. Comparison of models with experiment for hoop modulus in tension specimens.

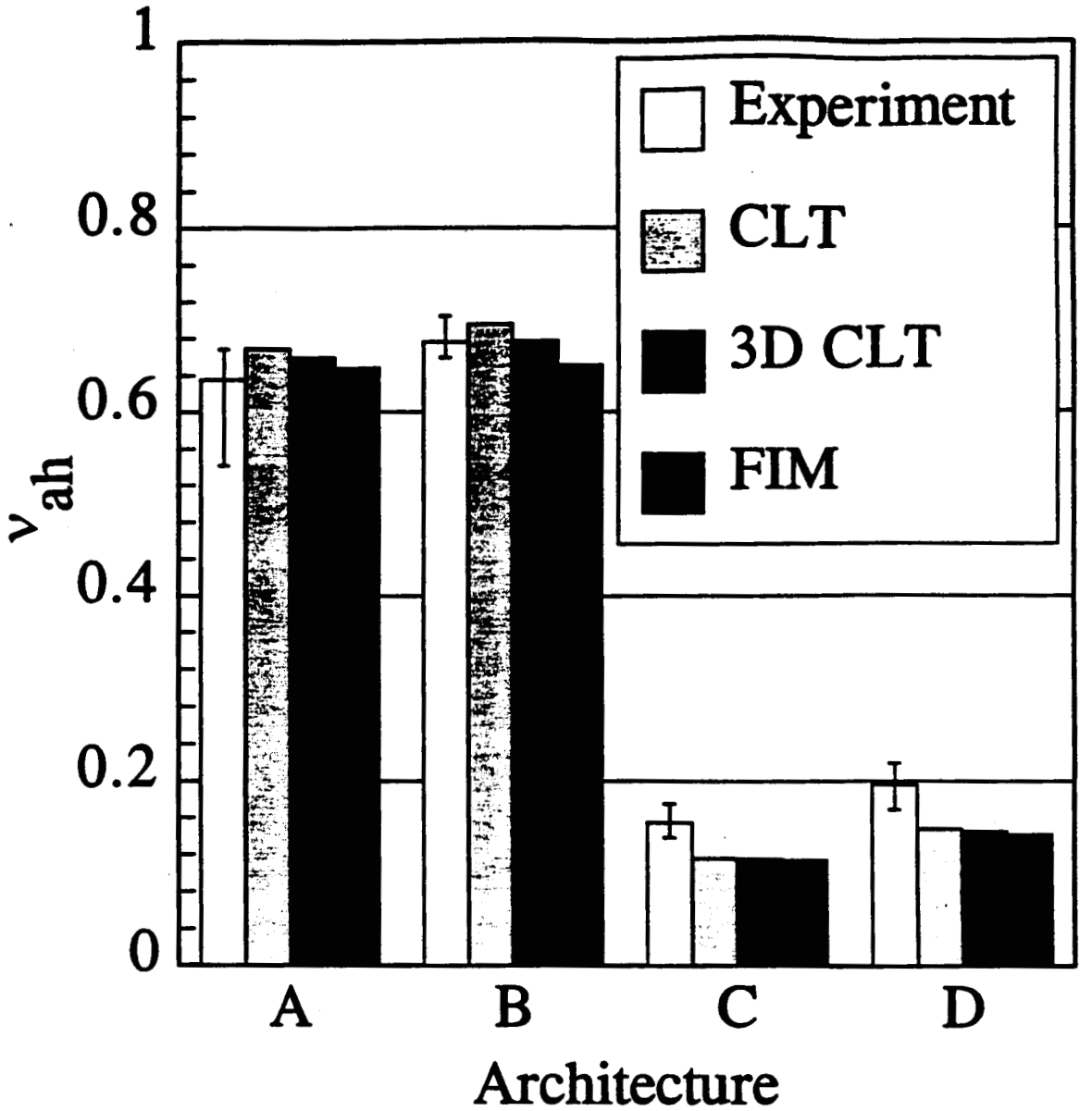

Fig 19. Comparison of models with experiment for Poisson's ratio in tension specimens.

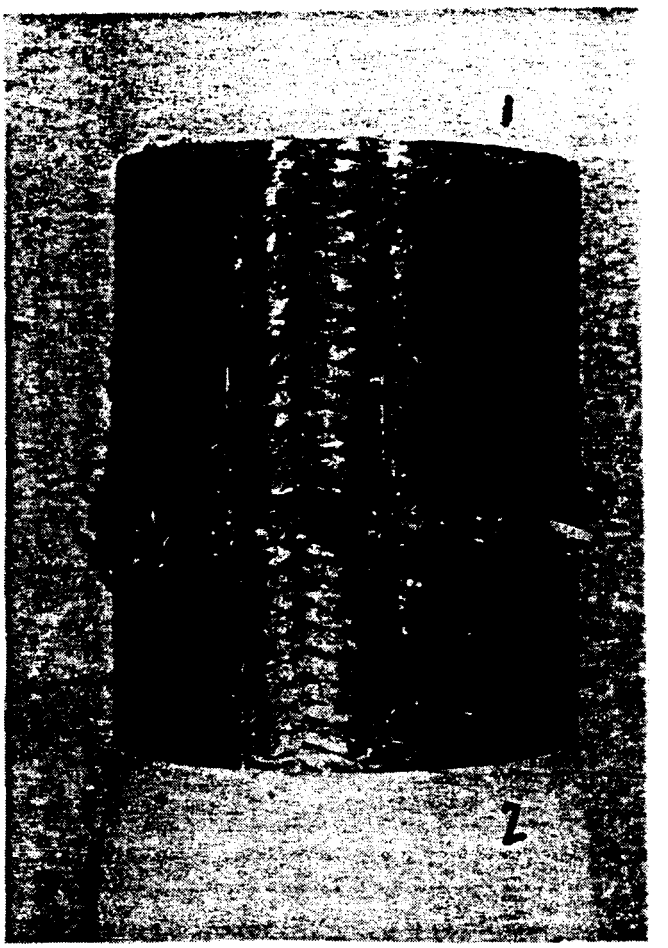

Fig 20. Failed specimen (D architecture) showing typical axial failure mode in compression.

Fig 21. Failed specimen (D architecture) showing typical braid failure mode in compression.

Fig 22. Failed specimen (C architecture) showing biaxial failure mode in compression.

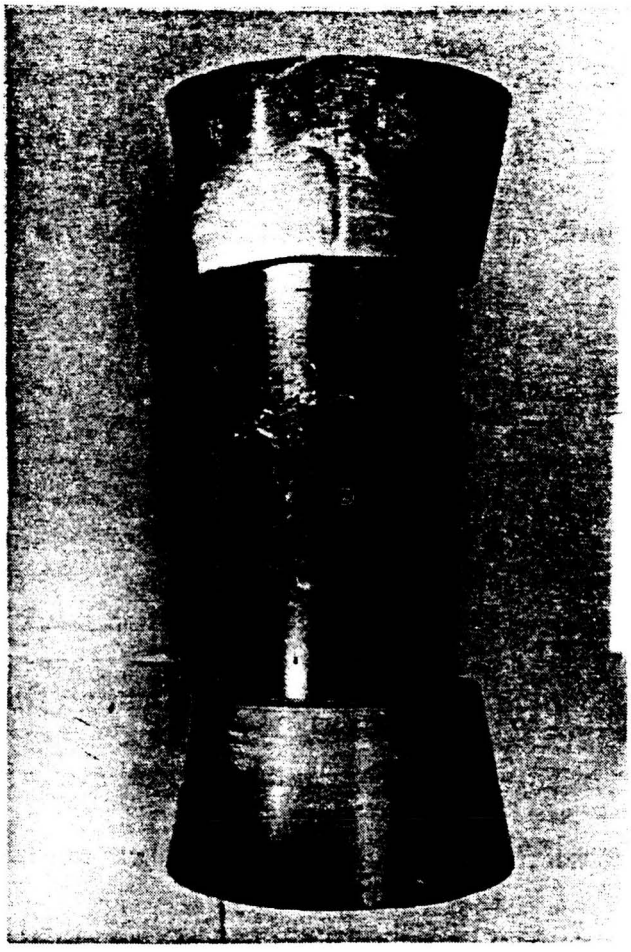

Fig 23. Example of axial tension failure.

Fig 24. Example of hoop tension failure.

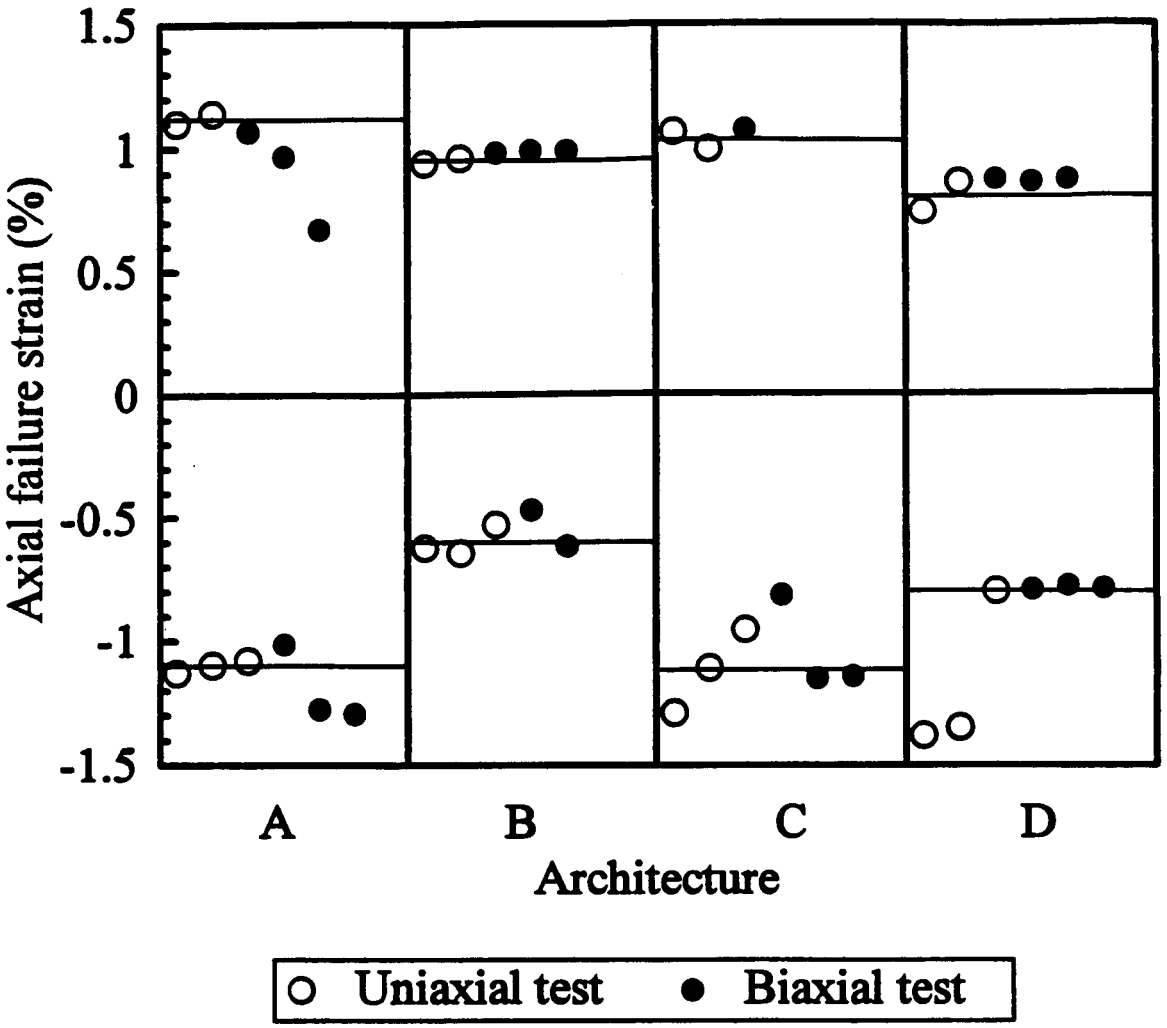

Fig 25. Measure axial direction failure strain for all specimens exhibiting an axial fiber failure mode in uniaxial and biaxial tension and compression tests.

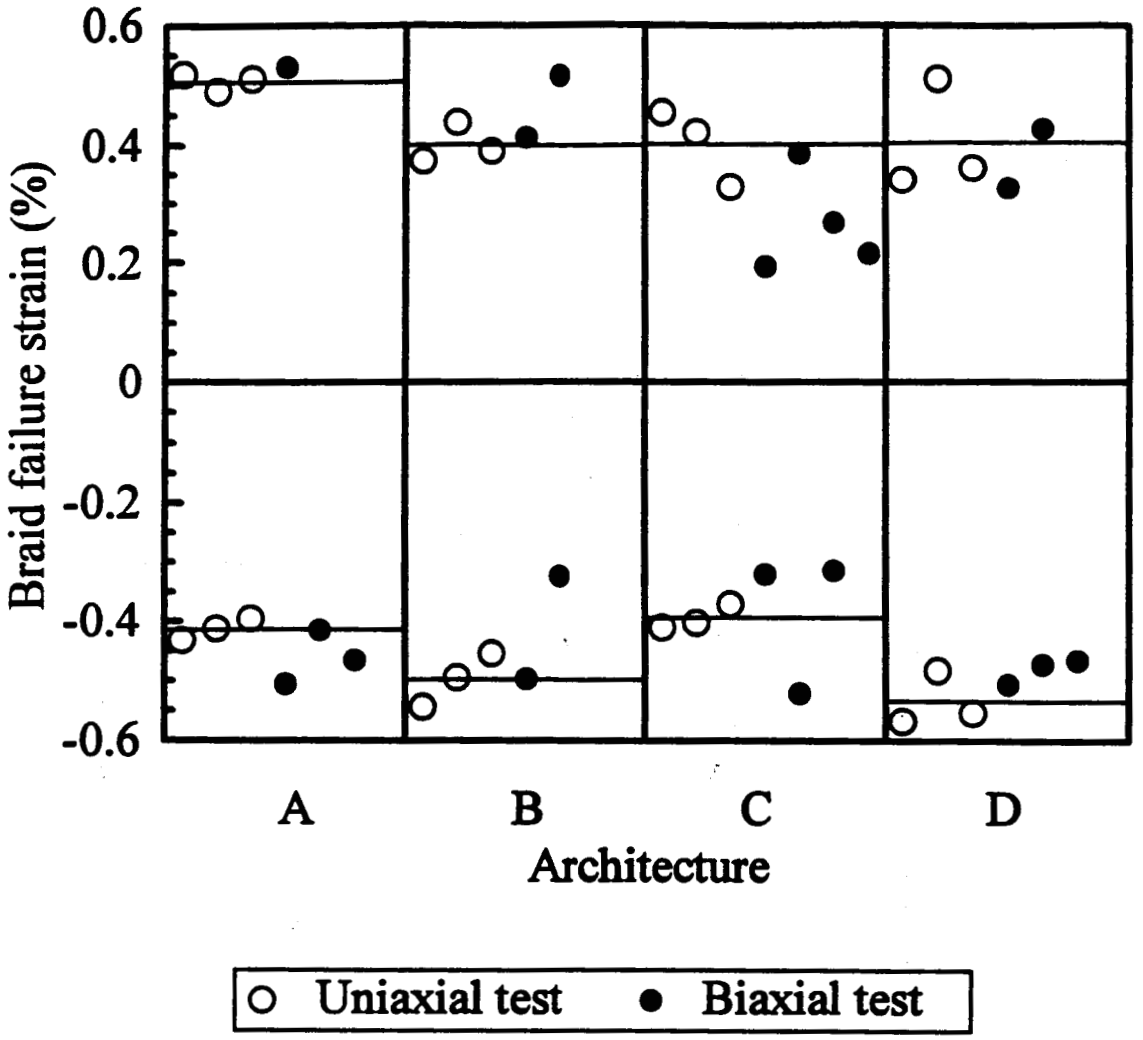

Fig 26. Measure braid direction failure strain for all specimens exhibiting a braid fiber failure mode in uniaxial and biaxial tension and compression tests.

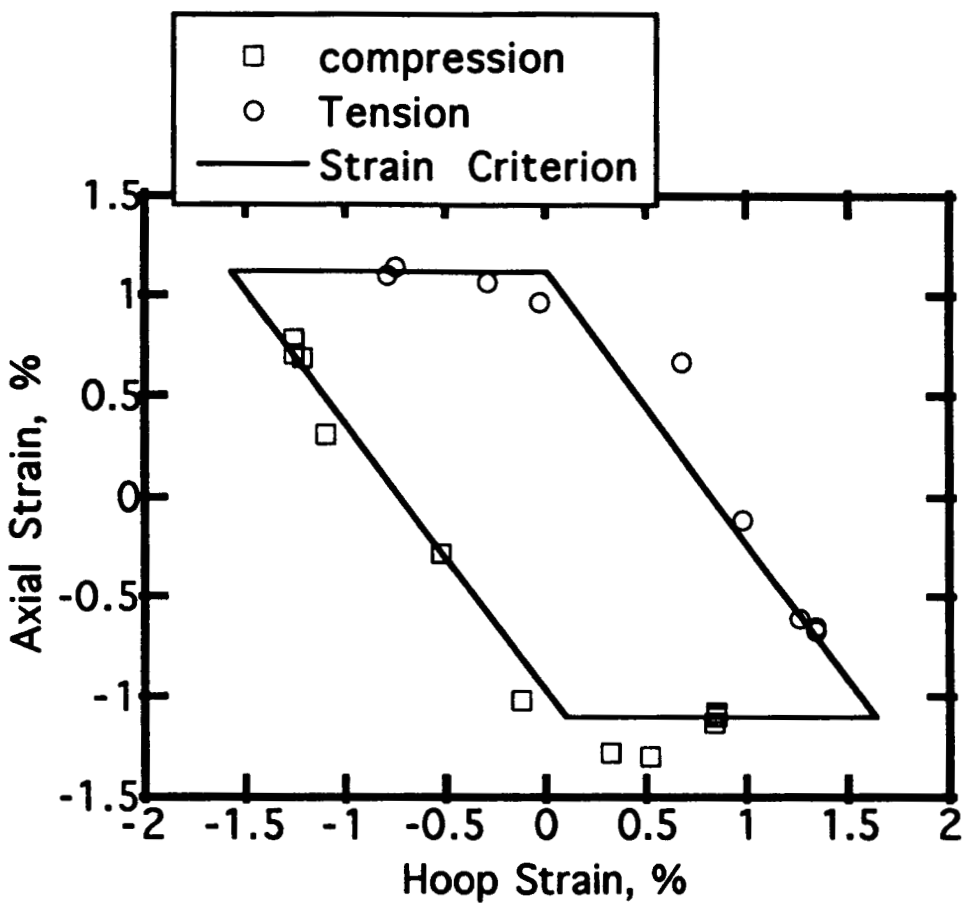

Fig 27. Biaxial loading failure envelope in strain space for 2-D triaxial braid, architecture A. Line is prediction based on the maximum fiber direction strain failure criterion.

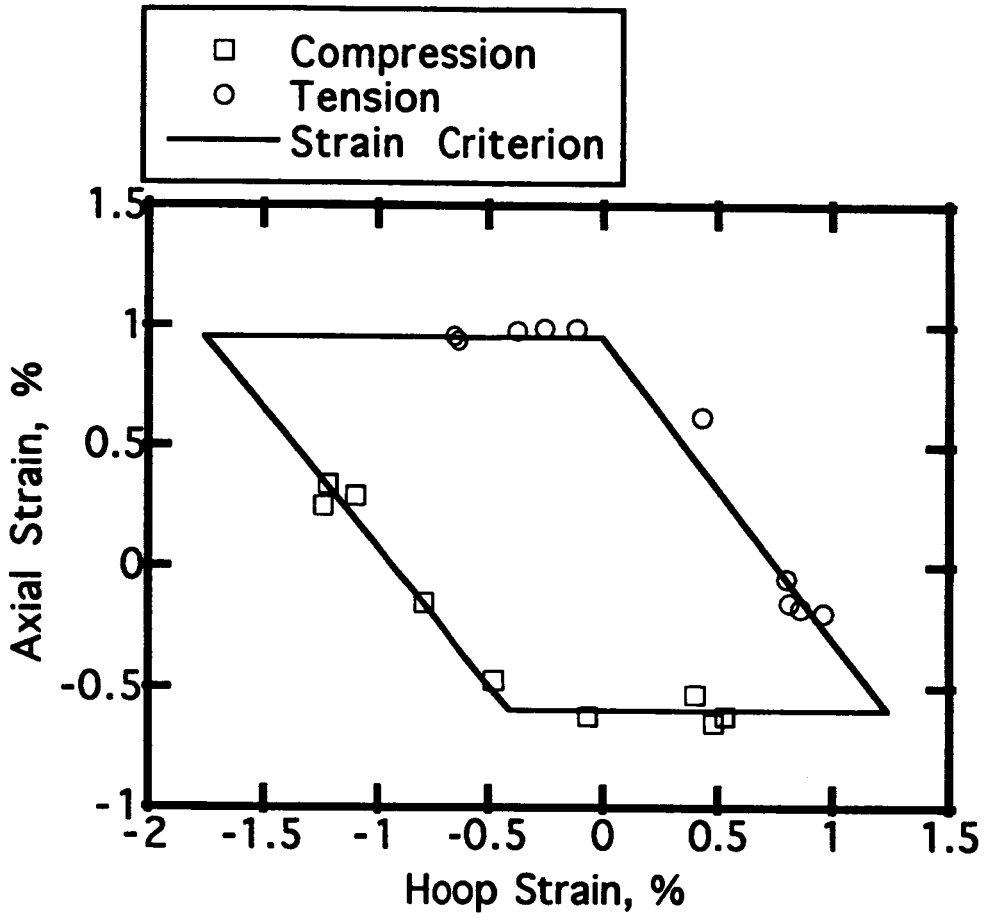

Fig 28. Biaxial loading failure envelope in strain space for 2-D triaxial braid, architecture B. Line is prediction based on the maximum fiber direction strain failure criterion.

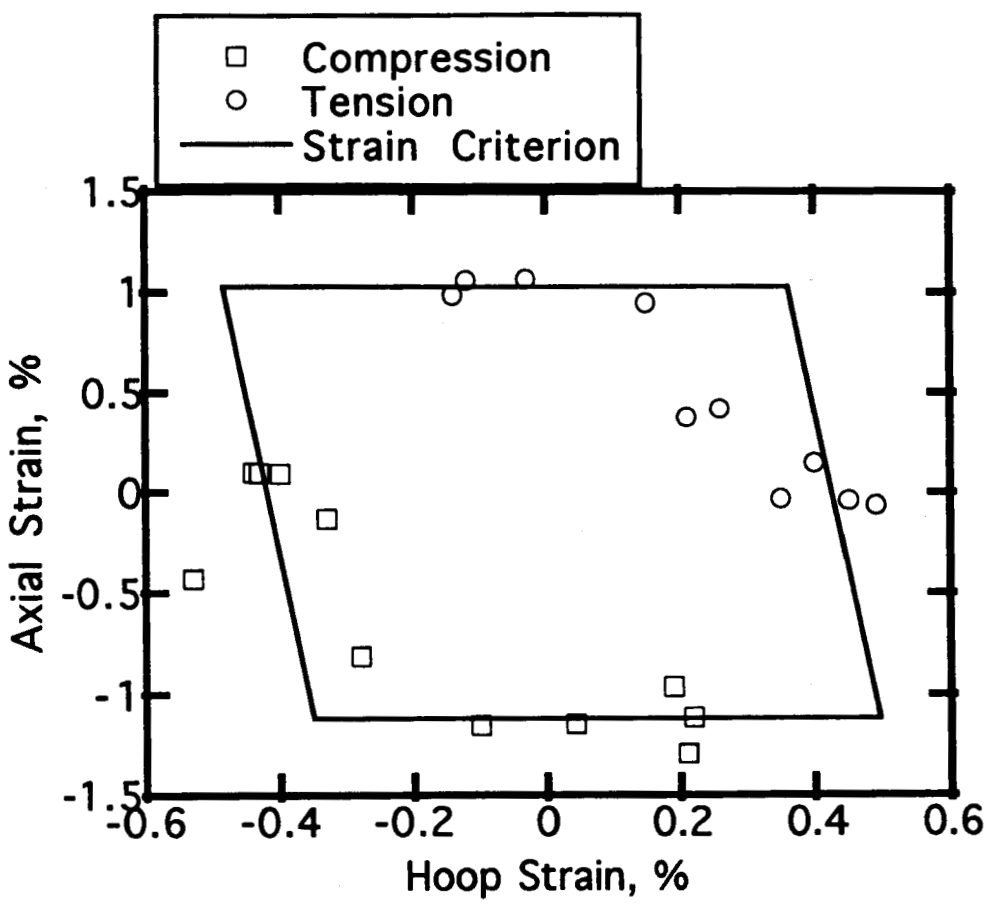

Fig 29. Biaxial loading failure envelope in strain space for 2-D triaxial braid, architecture C. Line is prediction based on the maximum fiber direction strain failure criterion.

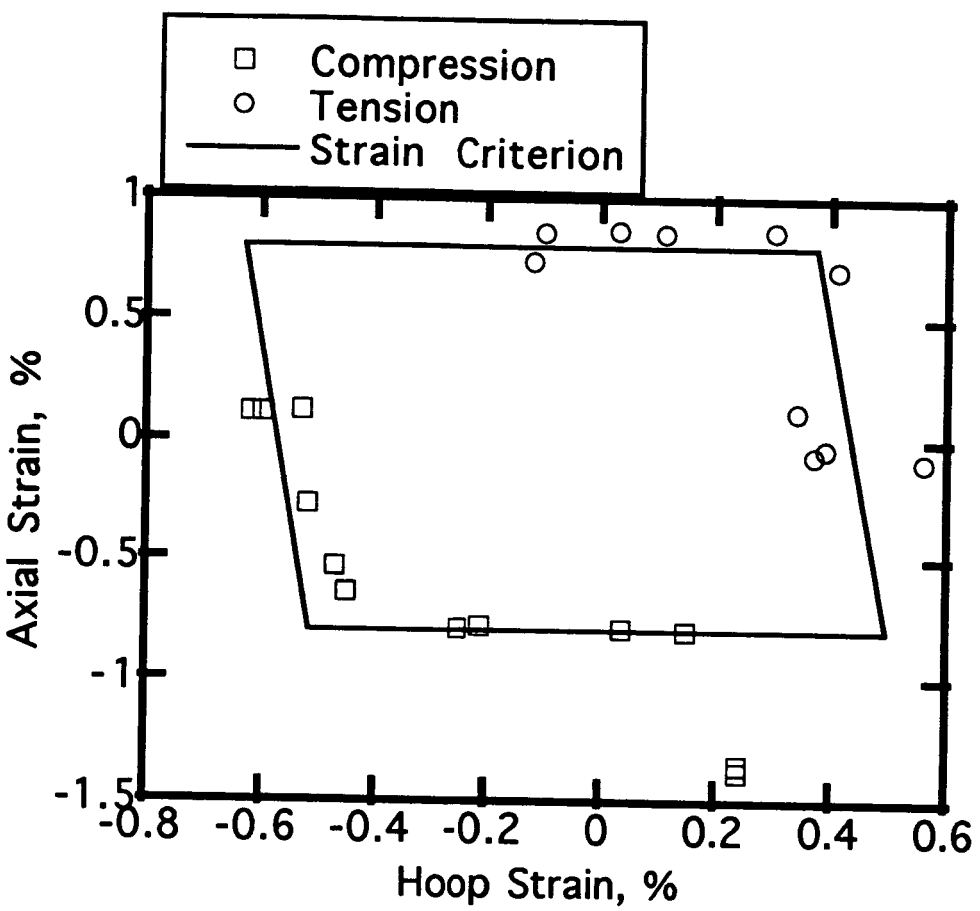

Fig 30. Biaxial loading failure envelope in strain space for 2-D triaxial braid, architecture D. Line is prediction based on the maximum fiber direction strain failure criterion.

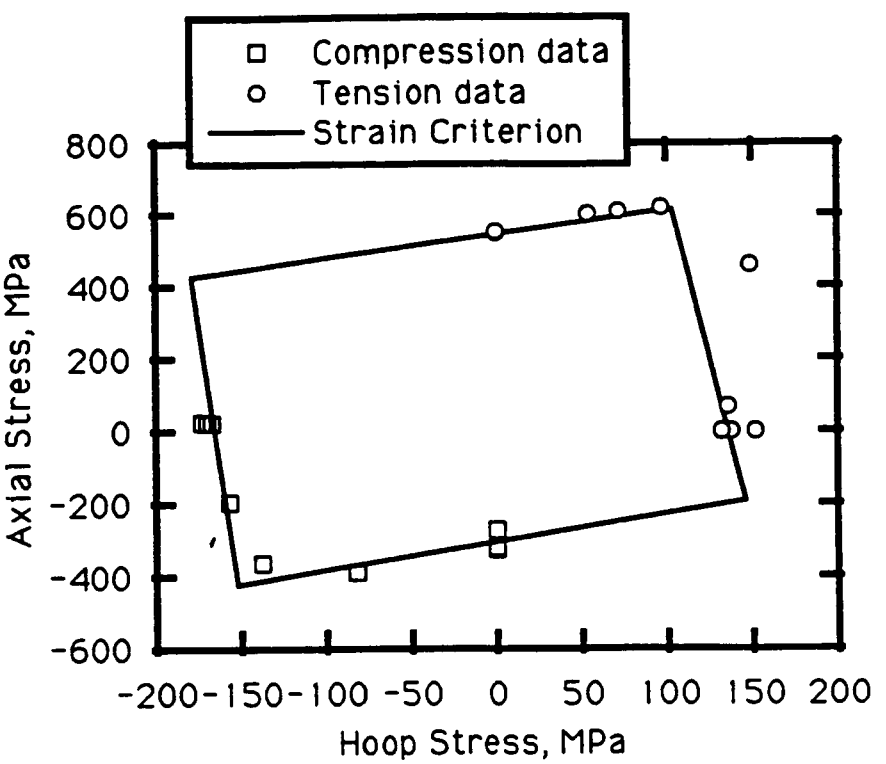

Fig 31. Biaxial loading failure envelope in stress space for 2-D triaxial braid, architecture A. Line is prediction based on the maximum fiber direction strain failure criterion.

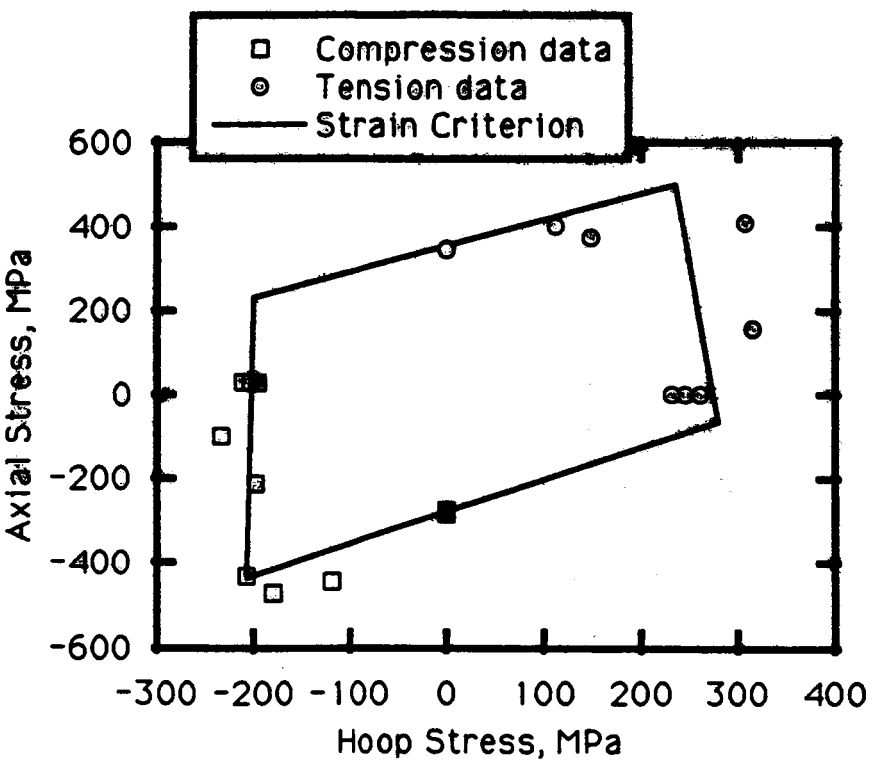

Fig 32. Biaxial loading failure envelope in stress space for 2-D triaxial braid, architecture B. Line is prediction based on the maximum fiber direction strain failure criterion.

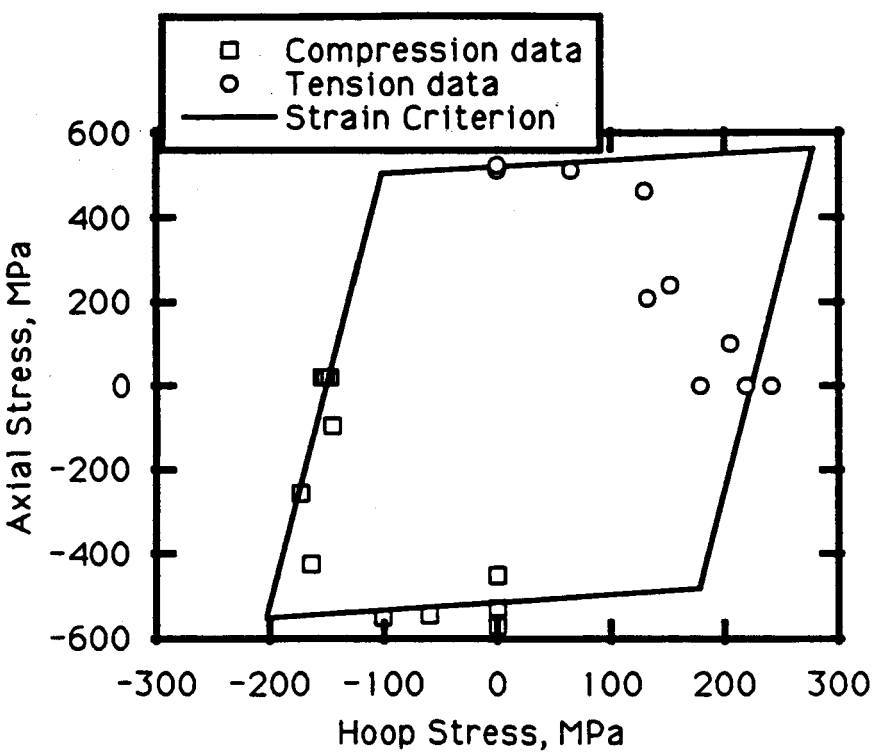

Fig 33. Biaxial loading failure envelope in stress space for 2-D triaxial braid, architecture C. Line is prediction based on the maximum fiber direction strain failure criterion.

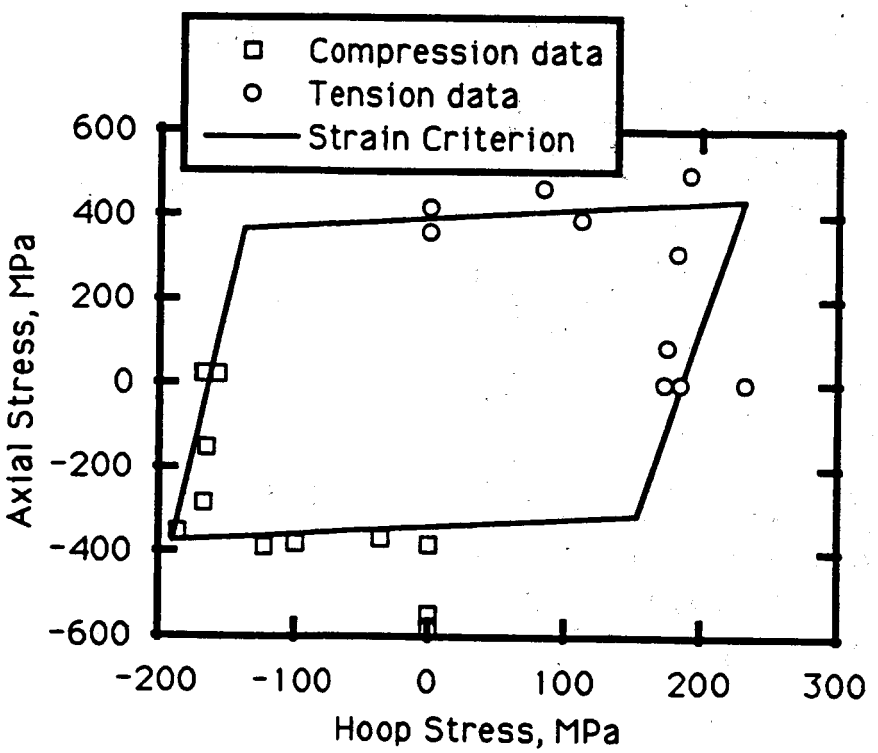

Fig 34. Biaxial loading failure envelope in stress space for 2-D triaxial braid, architecture D. Line is prediction based on the maximum fiber direction strain failure criterion.

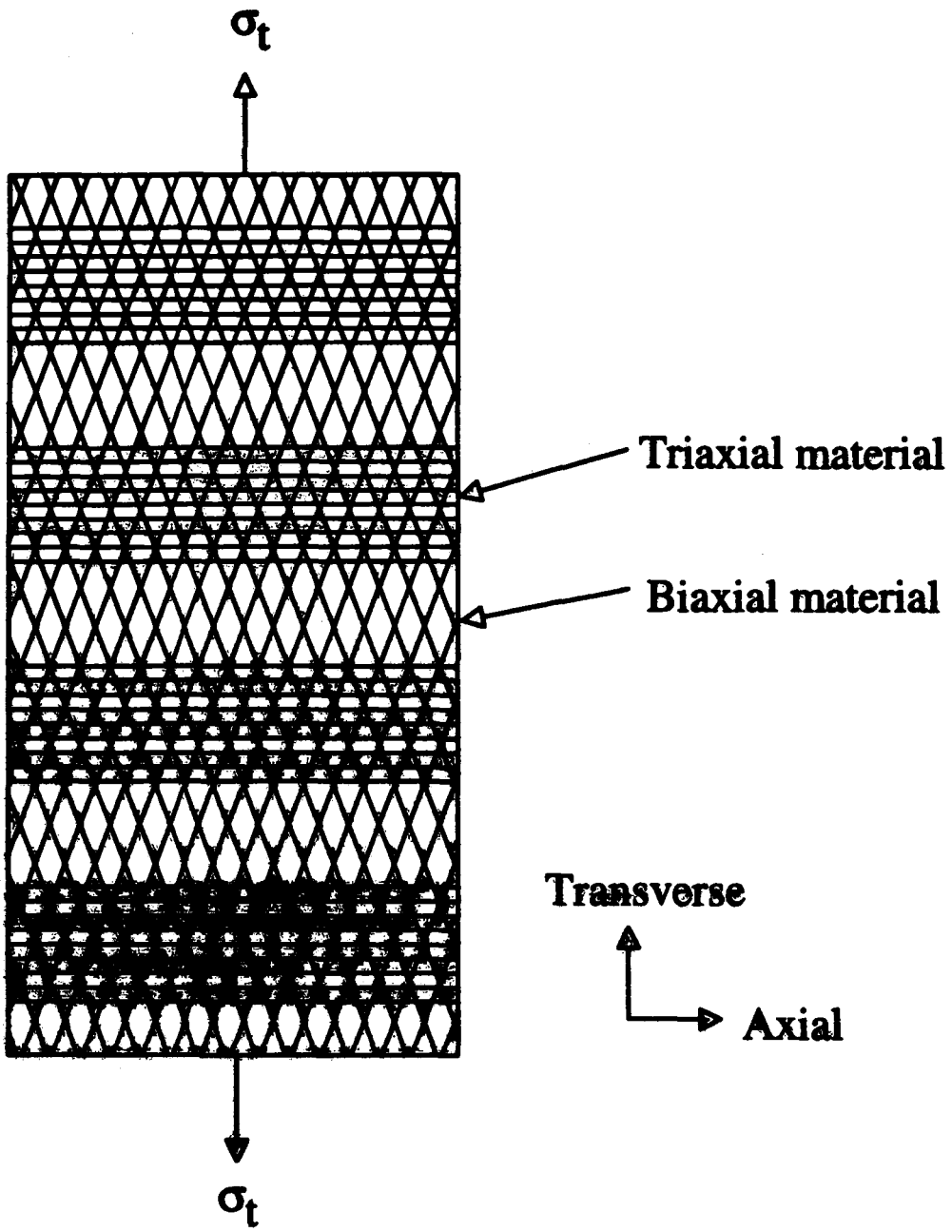

Fig 35. Fiber orientation assumed in the single-layer micro-mechanics model for strain concentration in the braid yarns due to stiffness variation.

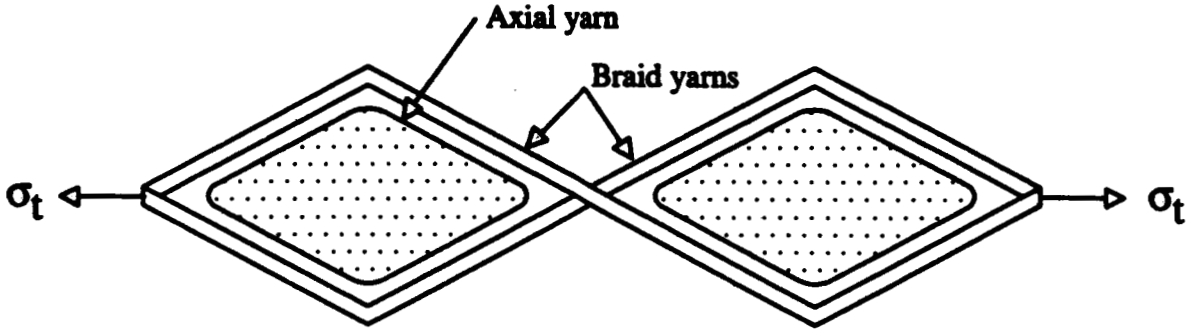

Schematic of one layer in a braided composite

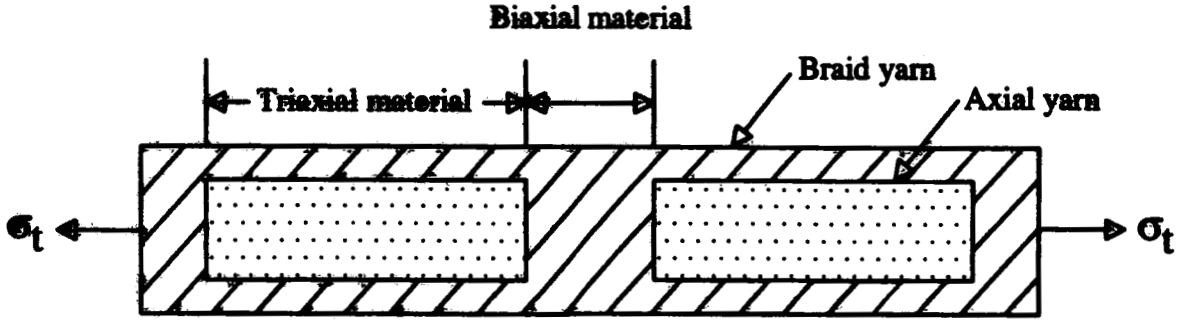

Geometry assumed by the analytical model

Fig 36. Through-the-thickness representation in the single-layer micro-mechanics model for strain concentration in the braid yarns due to stiffness variation.

Fig 37. Microphotograph of section normal to the axial yarns of the compression B architecture.

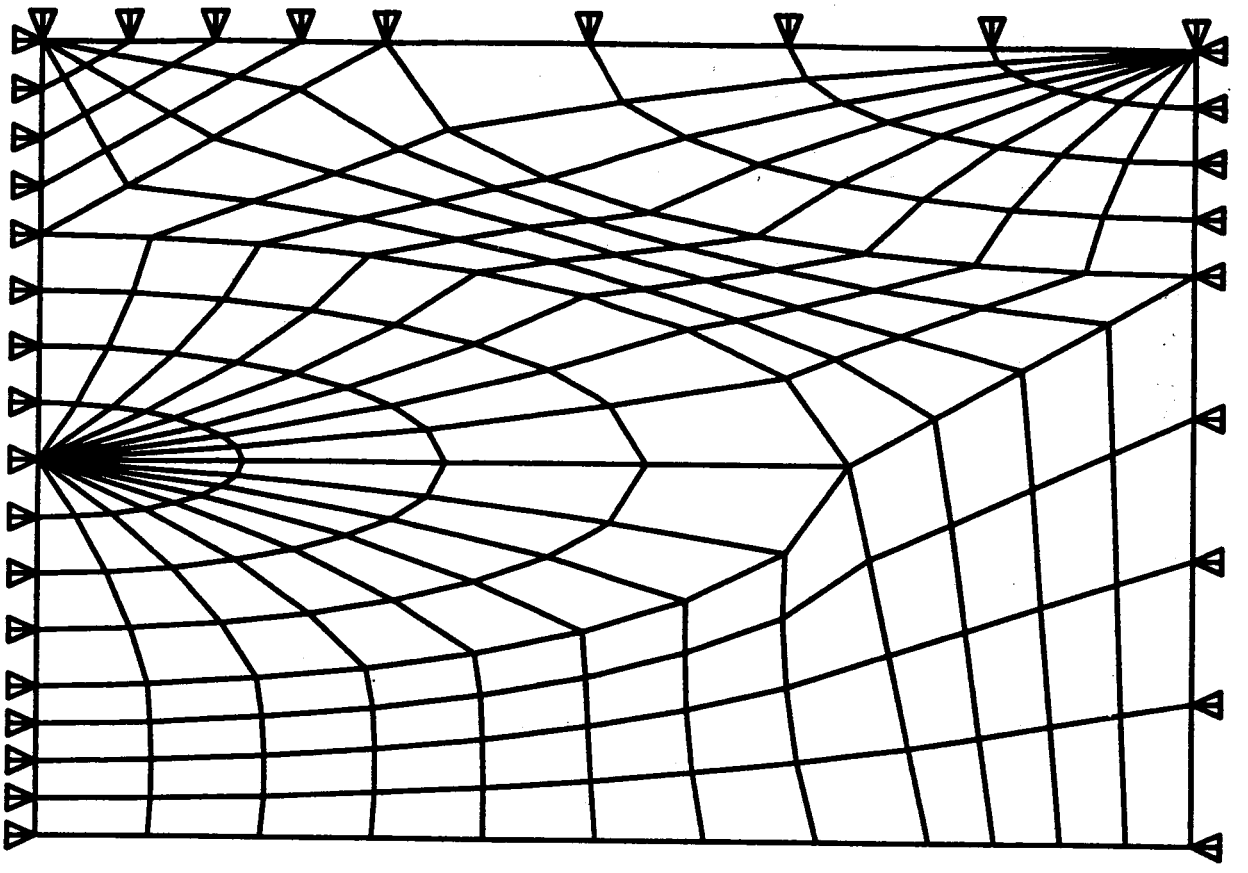

Fig 38. Finite element mesh of the compression B architecture, used in generalized plane strain model for strain concentration in the braid yarns due to stiffness variation.

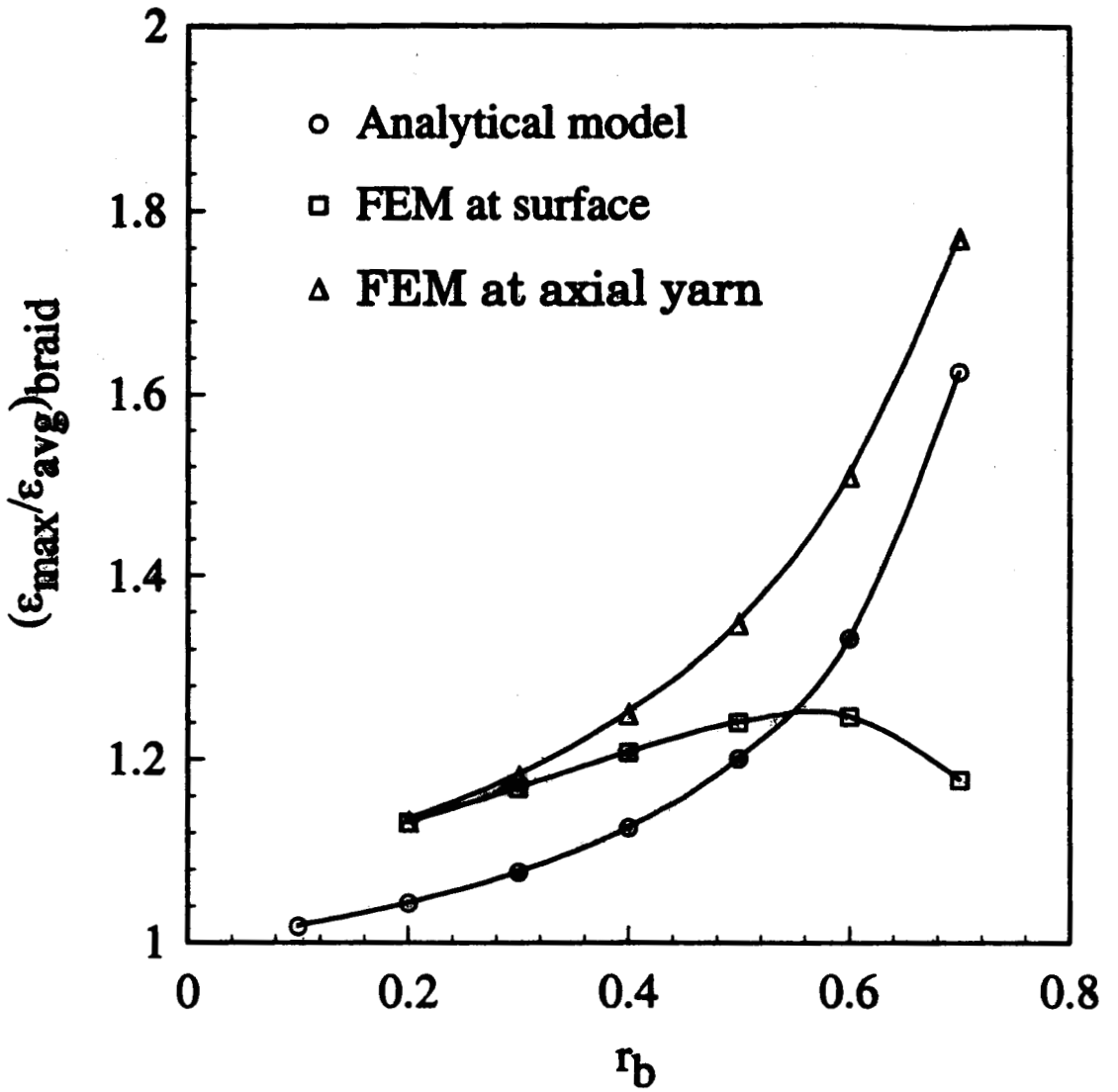

Fig 39. Comparison of the predicted strain concentration in the braid yarns due to stiffness variation, as predicted by the single-layer and finite element models. r_b is a braid geometrical factor, and varies between 0.22 and 0.62 for the braid architectures.

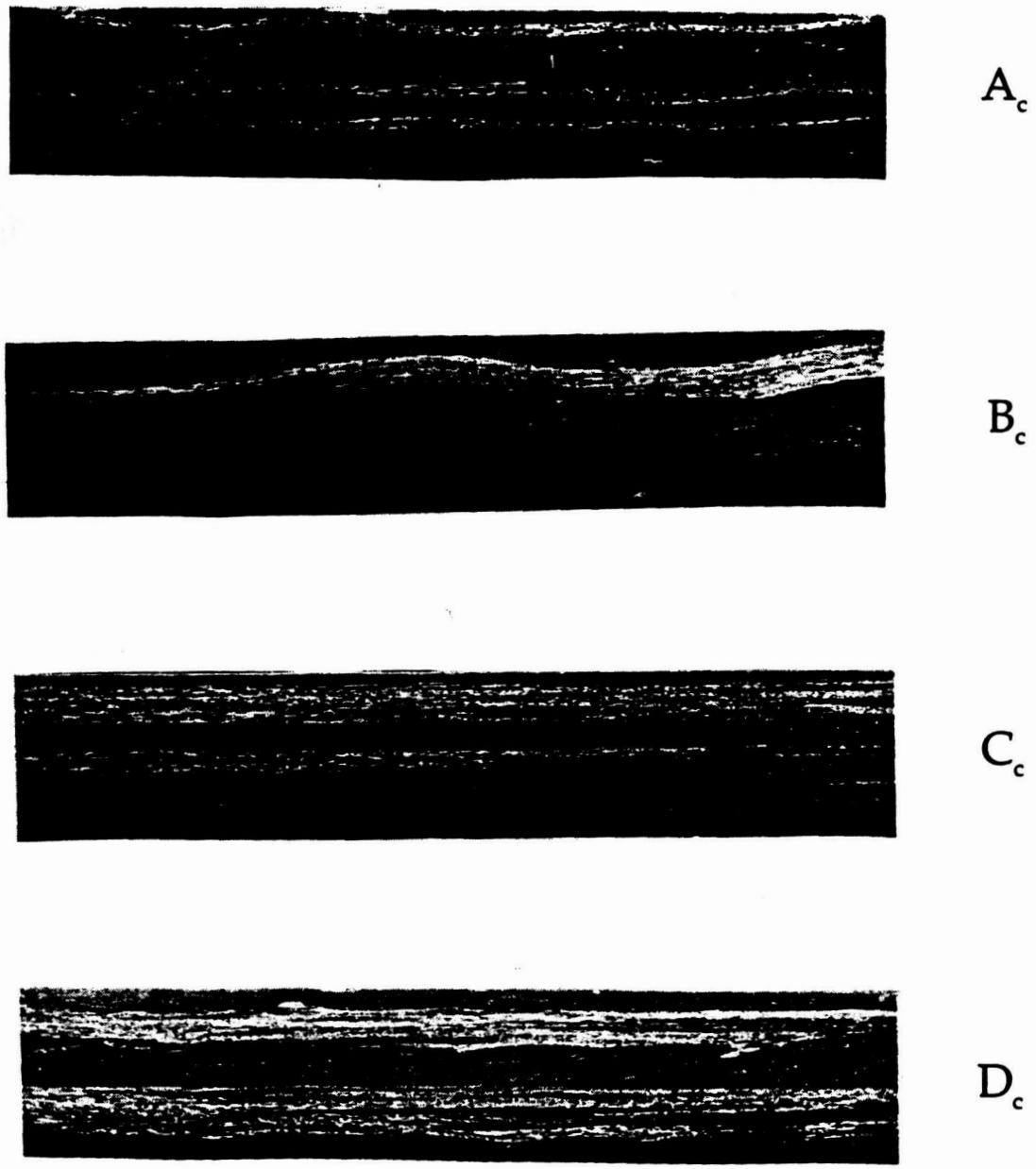

Fig 40. Microphotographs of polished sections showing axial yarns in compression specimens.

REPORT DOCUMENTATION PAGE

Form Approved
OMB No. 0704-0188

1. AGENCY USE ONLY *(Leave blank)*	2. REPORT DATE	3. REPORT TYPE AND DATES COVERED
	October 1995	Conference Proceedings

4. TITLE AND SUBTITLE
Mechanics of Textile Composites Conference

5. FUNDING NUMBERS
WU 510-02-1107

6. AUTHOR(S)
Clarence C. Poe, Jr. and Charles E. Harris

7. PERFORMING ORGANIZATION NAME(S) AND ADDRESS(ES)
NASA Langley Research Center
Hampton, VA 23681-0001

8. PERFORMING ORGANIZATION REPORT NUMBER
L-17532A

9. SPONSORING/MONITORING AGENCY NAME(S) AND ADDRESS(ES)
National Aeronautics and Space Administration
Washington, DC 20546-0001

10. SPONSORING/MONITORING AGENCY REPORT NUMBER
NASA CP-3311
Part 1

11. SUPPLEMENTARY NOTES

12a. DISTRIBUTION/AVAILABILITY STATEMENT
Unclassified–Unlimited
Subject Category—24

12b. DISTRIBUTION CODE

13. ABSTRACT *(Maximum 200 words)*

This document is a compilation of papers presented at the Mechanics of Textile Composites Conference in Hampton, Virginia, December 6–8, 1994. This conference was the culmination of a 3-year program that was initiated by NASA late in 1990 to develop mechanics of textile composites in support of the NASA Advanced Composites Technology Program (ACT). The goal of the program was to develop mathematical models of textile preform materials and test methods to facilitate structural analysis and design. Participants in the program were from NASA, academia, and industry.

14. SUBJECT TERMS
Weave; Braid; Stitch; Textile; Composite; Resin transfer molding; Test methods; Strengths; Thermo-elastic constants; Failure modes; Analysis

15. NUMBER OF PAGES
257

16. PRICE CODE
A12

17. SECURITY CLASSIFICATION OF REPORT	18. SECURITY CLASSIFICATION OF THIS PAGE	19. SECURITY CLASSIFICATION OF ABSTRACT	20. LIMITATION OF ABSTRACT
Unclassified	Unclassified		